Abstract

Heterogeneous photocatalytic oxidation has been extensively studied for environmental applications such as purification processes aimed to the removal of organic substances at room temperature both in water and in air. However, in recent years, photocatalytic processes have also been extended to the synthesis of organic compounds in mild conditions. This Ph.D. work has been focused on the application of heterogeneous photocatalysis for the removal of contaminants (azo-dyes and pesticides) and for the selective oxidation of benzene to phenol to explore its potential application in an industrial process. In particular, visible light active photocatalysts in powder form have been formulated, optimized through the coupling with β-cyclodextrins and studied in the degradation of water pollutants. Subsequently, the optimized photocatalysts were employed in the direct oxidation of benzene to phenol. Among the investigated photocatalysts, N doped TiO_2 (N-TiO_2) photocatalyst showed the highest benzene conversion than the other photocatalytic formulations.

Such photocatalyst was coupled with syndiotactic polystyrene in aerogel form (sPS) having a high affinity towards hydrophobic compounds (benzene) and a very low affinity towards hydrophilic compounds (phenol) in order to maximize the selectivity to phenol favoring its desorption from photocatalyst surface. Therefore, the selective photocatalytic oxidation of benzene in liquid phase is studied using visible active N-TiO_2 photocatalyst embedded into a monolithic syndiotactic polystyrene aerogel (N-TiO_2/sPS, 10/90 w/w) under UV or visible light irradiation with the aim to tune the selectivity towards the desired product. The experimental results evidenced that the presence of sPS allows to achieve a benzene conversion higher than 50% under both irradiation conditions at the spontaneous pH of the solution. In addition, N-TiO_2/sPS is able to enhance the phenol selectivity compared to N-TiO_2 in powder form that shows a very low selectivity to phenol in presence of UV light and no phenol production with visible light. A remarkable enhancement of both selectivity and phenol yield is achieved under visible light in acidic conditions because of the low affinity of phenol to the hydrophobic structure of sPS, facilitating the desorption of the produced phenol in the aqueous medium from N-TiO_2/sPS, and, consequently, inhibiting at a certain extent the phenol overoxidation reactions. The final phase of the PhD work was devoted to the formulation of transition metal oxides (V_2O_5, Fe_2O_3 and CuO) supported on N-TiO_2 and their dispersion in polymeric aerogels to increase both the benzene consumption rate and the production rate of phenol, maximizing, at the same time, selectivity and yield to the desired product under visible light. Cu/N-TiO_2 in powder form allowed to achieve a phenol yield after 10 hours of visible light, significantly higher than that observed with Fe/N-TiO_2 and V/N-TiO_2. Therefore, to further increase the yield and selectivity to phenol and the phenol production rate, Cu/N-TiO_2 photocatalyst was embedded in sPS aerogel. Then, the operating conditions (dosage of Cu/N-TiO_2/sPS, solution pH) were optimized. The best result so far not found in literature was obtained using Cu/N-TiO_2/sPS photoreactive aerogel in acidic conditions which reveals both benzene conversion and a phenol yield higher than 95% and a selectivity to phenol greater than 99 %, values achieved in a very short time of visible light irradiation (180 min) with very little formation of by-products. A possible reaction mechanism was also proposed, The developed photoreactive (Cu/N-TiO_2/sPS) solid phase represents a "proof of concept" that could allow a significant leap forward in the development of innovative green processes for the selective oxidation of aromatic hydrocarbons under mild conditions.

Abstract

L'ossidazione fotocatalitica eterogenea è stata ampiamente studiata per applicazioni ambientali quali processi di purificazione finalizzati alla rimozione di sostanze organiche a temperatura ambiente sia in acqua che in aria. Tuttavia, negli ultimi anni, i processi fotocatalitici sono stati estesi anche alla sintesi di composti organici in condizioni di temperatura ambiente e pressione atmosferica. Questo dottorato di ricerca si è concentrato sull'applicazione della fotocatalisi eterogenea per la rimozione di contaminanti (coloranti azoici e pesticidi) e per l'ossidazione selettiva del benzene a fenolo con lo scopo di esplorare la sua potenziale applicazione in un processo industriale. In particolare sono stati formulati fotocatalizzatori in polvere attivi da luce visibile , ottimizzati attraverso l'accoppiamento con β-ciclodestrine e studiati nella degradazione degli inquinanti presenti in acqua. Successivamente, i fotocatalizzatori ottimizzati sono stati impiegati nell'ossidazione diretta del benzene a fenolo. Tra i fotocatalizzatori studiati, il fotocatalizzatore TiO_2 (N-TiO_2) drogato con azoto ha mostrato la più alta conversione del benzene rispetto le altre formulazioni fotocatalitiche.

Tale fotocatalizzatore è stato accoppiato con polistirene sindiotattico (sPS) in forma di aerogel avente un'elevata affinità verso i composti idrofobici (benzene) e un'affinità molto bassa verso i composti idrofili (fenolo) al fine di massimizzare la selettività a fenolo favorendone il desorbimento dalla superficie del fotocatalizzatore. Pertanto, l'ossidazione fotocatalitica selettiva del benzene in fase liquida viene studiata utilizzando un fotocatalizzatore N-TiO_2 attivo nel visibile disperso in un aerogel di polistirene sindiotattico in forma monolitica (N-TiO_2/sPS, 10/90 w/w) sotto luce UV o visibile con l'obiettivo di regolare la selettività verso il prodotto desiderato. I risultati sperimentali hanno evidenziato che la presenza di sPS consente di ottenere una conversione del benzene superiore al 50% in entrambe le condizioni di illuminazione in condizioni di pH spontaneo della soluzione. Inoltre, l' aerogel N-TiO_2/sPS è in grado di migliorare la selettività del fenolo rispetto il fotocatalizzatore in polvere N-TiO_2 che mostra una selettività al fenolo molto bassa in presenza di luce UV e nessuna produzione di fenolo con luce visibile. Un notevole miglioramento sia della selettività che della resa a fenolo si ottiene sotto luce visibile in condizioni acide a causa della bassa affinità del fenolo alla struttura idrofobica di sPS, facilitando il desorbimento del fenolo prodotto nel mezzo acquoso dal composito N-TiO_2/sPS, e , di conseguenza, inibendo in una certa misura le reazioni di sovraossidazione del fenolo. La fase finale del dottorato è stata dedicata alla formulazione di ossidi di metalli di transizione (V_2O_5, Fe_2O_3 e CuO) supportati su N-TiO_2 e alla loro dispersione in aerogel polimerici per aumentare sia la velocità di consumo del benzene che la velocità di produzione del fenolo, massimizzando, allo stesso tempo, selettività e resa al prodotto desiderato sotto luce visibile. Cu/N-TiO_2 in polvere ha permesso di ottenere una resa a fenolo dopo 10 ore di luce visibile, significativamente superiore a quella osservata con Fe/N-TiO_2 e V/N-TiO_2. Pertanto, per aumentare ulteriormente la resa e la selettività a fenolo e la velocità di produzione del fenolo, il fotocatalizzatore Cu/N-TiO_2 è stato disperso nell'aerogel sPS. Quindi, sono state ottimizzate le condizioni operative (dosaggio di Cu/N-TiO_2/sPS, pH della soluzione). Il miglior risultato finora non riscontrato in letteratura, è stato ottenuto utilizzando l'aerogel fotoreattivo Cu/N-TiO_2/sPS in condizioni acide che rivela sia la conversione del benzene che una resa a fenolo superiore al 95% e una selettività a fenolo superiore al 99%, valori raggiunti in un tempo molto breve di irraggiamento della luce visibile (180 min) con formazione minima di sottoprodotti. È stato inoltre proposto un possibile meccanismo di reazione. La fase solida fotoreattiva (Cu/N-TiO_2/sPS) sviluppata potrebbe consentire un significativo passo in avanti nello sviluppo di processi sostenibili innovativi capaci di realizzare reazioni di ossidazione selettiva degli idrocarburi aromatici in condizioni miti (temperatura ambiente e pressione atmosferica).

UNIVERSITY OF SALERNO

DEPARTMENT OF INDUSTRIAL ENGINEERING

Ph.D. Course in Industrial Engineering
Curriculum in Chemical Engineering - XXXV Cycle

Ph.D. Thesis in

INNOVATIVE CATALYTIC FORMULATIONS FOR PHOTO-ASSISTED CHEMICAL REACTIONS

Supervisor
Prof. Vincenzo Vaiano

Ph.D. student
Antonietta Mancuso

Scientific Referees
Prof. Vincenzo Venditto
Prof. Diana Sannino
Prof. Maria del Carmen Hidalgo

Ph.D. Course Coordinator
Prof. Francesco Donsì

Academic Year 2022/2023

UNIVERSITY OF SALERNO

DEPARTMENT OF INDUSTRIAL ENGINEERING

Ph.D. Course in Industrial Engineering
Curriculum in Chemical Engineering - XXXV Cycle

Ph.D. Thesis in

INNOVATIVE CATALYTIC FORMULATIONS FOR PHOTO-ASSISTED CHEMICAL REACTIONS

Supervisor
Prof. Vincenzo Vaiano

Ph.D. student
Antonietta Mancuso

Scientific Referees
Prof. Vincenzo Venditto
Prof. Diana Sannino
Prof. Maria del Carmen Hidalgo

Ph.D. Course Coordinator
Prof. Francesco Donsì

Academic Year 2022/2023

“Il processo di una scoperta scientifica è, in effetti, un continuo conflitto di meraviglie.”

Albert Einstein

Alla mia famiglia

Acknowledgments

Eccomi qui, giunta alla fine di questo percorso accademico, che è iniziato in un periodo alquanto difficile segnato dallo sviluppo della pandemia Covid-19 che, tuttavia, non ha ostacolato il mio fervido desiderio di condurre ricerca. In primis, ringrazio me stessa per la determinazione che da sempre mi contraddistingue e che mi ha permesso di raggiungere questo obiettivo. Rivolgo un sincero grazie al mio tutor, il mio mentore, Vincenzo innanzitutto per avermi dato l'opportunità di entrare a contatto con il mondo della ricerca scientifica e, per avermi trasmesso la sua esperienza e passione. Grazie per avermi guidato in questi anni e per essere stato un punto di riferimento con preziosi consigli nei momenti di gioia o di sconforto. Ringrazio il prof. Venditto per aver reso possibile la collaborazione con lui e il Dipartimento di Chimica e Biologia e per aver partecipato al mio progetto di ricerca con forte interesse. Un ringraziamento speciale è rivolto ad Olga, la mia giovane prof, per avermi supportato, incoraggiato e aiutato con pratici e validi suggerimenti, per essere stata costantemente presente in qualità di coordinatrice e in particolare, come sorella, condividendo straordinari e indimenticabili viaggi di lavoro e non. Grazie al piccolo Fede per avermi strappato sempre un sorriso con la sua solarità, intelligenza e dolcezza. Ringrazio le colleghe del Lab.4 che hanno allietato le intense giornate di lavoro: Wanda, per i suoi consigli, la disponibilità e generosità; Morica per l'aiuto rivoltomi per le analisi dei test sperimentali; Raffa, compagna di pranzo e di fotocatalisi per le tante risate; Sara, la nostra madrelingua per la sua dolcezza; Ramona, per il suo spirito ribelle e Cristine per la sua simpatia e saggezza. Ringrazio tutti i colleghi del Lab T3: in particolare, la professoressa Sannino per la cortese collaborazione durante il mio percorso, Giusy, per gli utili consigli e la sua immensa gentilezza e Nicola con cui si è creato un sincero rapporto di fiducia e amicizia. La mia profonda e amorevole gratitudine è rivolta alla mia famiglia per il loro continuo e impareggiabile amore e aiuto. Grazie al mio compagno di vita, Andrea, per il suo amore e la sua costante partecipazione nella mia vita privata e lavorativa.

Publications list

1. A. Mancuso, O. Sacco, V. Vaiano, D. Sannino, S. Pragliola, V. Venditto, N. Morante, Visible light active Fe-Pr codoped TiO_2 for water pollutants degradation, Catalysis Today 380 (2021) 93–104

2. S. Mottola, A Mancuso, O Sacco, I. De Marco, V. Vaiano Production of hybrid TiO_2/β-CD photocatalysts by supercritical antisolvent micronization for UV light-driven degradation of azo dyes, The Journal of Supercritical Fluids 188 (2022) 105695

3. P. Franco, W. Navarra, Olga Sacco, I. De Marco, A. Mancuso, V. Vaiano, V. Venditto. Photocatalytic degradation of atrazine under visible light using Gd-doped ZnO prepared by supercritical antisolvent precipitation route. Catalysis Today 397-399 (2022) 240–248

4. A. Mancuso, V. Vaiano , P. Antico, O. Sacco, V. Venditto Photoreactive polymer composite for selective oxidation of benzene to phenol, Catalysis Today (2022), article in press (https://doi.org/10.1016/j.cattod.2022.09.020).

5. A. Mancuso, N. Morante, M. De Carluccio , O. Sacco, L Rizzo, M. Fontana, S. Esposito, V. Vaiano, .D. Sannino Solar driven photocatalysis using iron and chromium doped TiO_2 coupled to moving bed biofilm process for olive mill wastewater treatment. Chemical Engineering Journal 450 (2022) 138107.

6. A. Mancuso, O. Sacco, D. Sannino, S Pragliola, V. Vaiano Enhanced visible-light-driven photodegradation of Acid Orange 7 azo dye in aqueous solution using Fe-N codoped TiO_2 Arabian Journal of Chemistry (2020) 13, 8347–8360

7. A. Mancuso and G. Iervolino Synthesis and Application of Innovative and Environmentally Friendly Photocatalysts: A Review, Catalysts 2022, 12, 1074

8. O. Sacco, A. Mancuso, V. Venditto, S. Pragliola and V. Vaiano, Behavior of N-Doped TiO_2 and N-Doped ZnO in Photocatalytic Azo Dye Degradation under UV and Visible Light Irradiation: A Preliminary Investigation, Catalysts 2022, 12, 1208.

9. A. Mancuso, O. Sacco, D. Sannino , V. Venditto and V. Vaiano One-Step Catalytic or Photocatalytic Oxidation of Benzene to Phenol: Possible Alternative Routes for Phenol Synthesis? Catalysts 2020,10,1424.

10. A. Mancuso, W. Navarra, O. Sacco, S. Pragliola, V.Vaiano and V. Venditto. Photocatalytic Degradation of Thiacloprid Using Tri-Doped TiO_2 Photocatalysts: A Preliminary Comparative Study, Catalysts 2021, 11, 927

11. D. Sannino, · N. Morante, · O. Sacco, · A. Mancuso, · L. De Guglielmo, · G. Di Capua, N. Femia,· V.Vaiano Visible light-driven degradation of Acid Orange 7 by light modulation techniques, Photochemical & Photobiological Sciences, October 2022.

12. A. Mancuso, O. Sacco, V.Vaiano, D.Sannino, V. Venditto, S.Pragliola, N. Morante Visible Light Active Fe-N Codoped TiO_2 Synthesized through Sol Gel Method: Influence of Operating Conditions on Photocatalytic Performances CET, Chemical Engineering transaction VOL. 86, 2021

13. A. Mancuso , O. Sacco , V. Vaiano , B. Bonelli , S. Esposito, F.S.Freyria , N. Blangetti and D. Sannino Visible Light-Driven Photocatalytic Activity and Kinetics of Fe-Doped TiO_2 Prepared by a Three-Block Copolymer Templating Approach, Materials 2021, 14, 3105.

14. A. Mancuso, N. Blangetti, O. Sacco, F. S. S Freyria, B. Bonelli, S. Esposito, D. Sannino & V. Vaiano, Photocatalytic Degradation of Crystal Violet dye under Visible Light by Fe-Doped TiO_2 Prepared by Reverse-Micelle Sol–Gel Method. Nanomaterials 2023, 13(2), 270.

Contents

Index of figures

Index of tables

Abstract

Heterogeneous photocatalytic oxidation has been extensively studied for environmental applications such as purification processes aimed to the removal of organic substances at room temperature both in water and in air. However, in recent years, photocatalytic processes have also been extended to the synthesis of organic compounds in mild conditions. This Ph.D. work has been focused on the application of heterogeneous photocatalysis for the removal of contaminants (azo-dyes and pesticides) and for the selective oxidation of benzene to phenol to explore its potential application in an industrial process. In particular, visible light active photocatalysts in powder form have been formulated, optimized through the coupling with β-cyclodextrins and studied in the degradation of water pollutants. Subsequently, the optimized photocatalysts were employed in the direct oxidation of benzene to phenol. Among the investigated photocatalysts, N doped TiO_2 (N-TiO_2) photocatalyst showed the highest benzene conversion than the other photocatalytic formulations.

Such photocatalyst was coupled with syndiotactic polystyrene in aerogel form (sPS) having a high affinity towards hydrophobic compounds (benzene) and a very low affinity towards hydrophilic compounds (phenol) in order to maximize the selectivity to phenol favoring its desorption from photocatalyst surface. Therefore, the selective photocatalytic oxidation of benzene in liquid phase is studied using visible active N-TiO_2 photocatalyst embedded into a monolithic syndiotactic polystyrene aerogel (N-TiO_2/sPS, 10/90 w/w) under UV or visible light irradiation with the aim to tune the selectivity towards the desired product. The experimental results evidenced that the presence of sPS allows to achieve a benzene conversion higher than 50% under both irradiation conditions at the spontaneous pH of the solution. In addition, N-TiO_2/sPS is able to enhance the phenol selectivity compared to N-TiO_2 in powder form that shows a very low selectivity to phenol in presence of UV light and no phenol production with visible light. A remarkable enhancement of both selectivity and phenol yield is achieved under visible light in acidic conditions because of the low affinity of phenol to the hydrophobic structure of sPS, facilitating the desorption of the produced phenol in the aqueous medium from N-TiO_2/sPS, and,

consequently, inhibiting at a certain extent the phenol overoxidation reactions. The final phase of the PhD work was devoted to the formulation of transition metal oxides (V_2O_5, Fe_2O_3 and CuO) supported on N-TiO_2 and their dispersion in polymeric aerogels to increase both the benzene consumption rate and the production rate of phenol, maximizing, at the same time, selectivity and yield to the desired product under visible light. Cu/N-TiO_2 in powder form allowed to achieve a phenol yield after 10 hours of visible light, significantly higher than that observed with Fe/N-TiO_2 and V/N-TiO_2. Therefore, to further increase the yield and selectivity to phenol and the phenol production rate, Cu/N-TiO_2 photocatalyst was embedded in sPS aerogel. Then, the operating conditions (dosage of Cu/N-TiO_2/sPS, solution pH) were optimized. The best result so far not found in literature was obtained using Cu/N-TiO_2/sPS photoreactive aerogel in acidic conditions which reveals both benzene conversion and a phenol yield higher than 95% and a selectivity to phenol greater than 99 %, values achieved in a very short time of visible light irradiation (180 min) with very little formation of by-products. A possible reaction mechanism was also proposed, The developed photoreactive (Cu/N-TiO_2/sPS) solid phase represents a "proof of concept" that could allow a significant leap forward in the development of innovative green processes for the selective oxidation of aromatic hydrocarbons under mild conditions.

I Introduction

The health of the environment is a subject of continually growing interest to the public since the rapid industrialization and the population extension led a progressive accumulation of organic compounds. In this context, photocatalytic process represents an interesting alternative technology useful both in the field of water and air purification and as organic synthetic pathway. The need to develop chemical products and industrial processes that reduce or eliminate the use and generation of toxic substances that are both dangerous to human health and the environment is the goal of research efforts based on the principles of Green Chemistry. Heterogeneous photocatalysis is a technology extensively studied for abo
since Fujishima and Honda (1972) (Fujishima and [illegible]).
Photocatalysis, included in advanced oxidation processes (AOPs), comprises a large variety of reactions such us partial or total oxidations, hydrogen transfer, functionalization, rearrangements, dehydrogenation, mineralization, etc (Herrmann, 2005). It is a catalytic technique that draws its energy from the absorption of photons of light (solar or artificial), potentially making it very economical to use; a wide range of possible applications of the technology was found, such as water splitting (Fujishima and Honda, 1972), oxidation (Jiang et al., 2004) and the reduction (Joyce-Pruden et al., 1992). Much scientific interest has focused on the use of photocatalysis in wastewater remediation. Population explosion, expansion of urban areas increased adverse impacts on water resources, particularly in regions in which natural resources are still limited. The main causes of surface water and groundwater contamination are industrial discharges (even in low quantities), excess use of dyes, pesticides, fertilizers (agrochemicals) and land filling domestic wastes. The nature of water resources is worsening day by day because of the incessant accumulation of undesirable contaminants and chemicals in the water bodies. The wastewater treatment is based upon various mechanical, biological, physical and chemical processes. In fact, this is a combination of many operations like filtration, flocculation, chemical sterilization and the elimination of particles in suspension. The biological treatment is the ideal process (natural decontamination).

The physico-chemical processes (coagulation and flocculation) use various chemical reagents (aluminum chloride or ferric chloride, polyelectrolytes, etc.) and generate large amounts of sludge. Increasing demands for water quality indicators and drastic change regulations on wastewater disposal require the development of processes more efficient and more effective (ion exchange, ultrafiltration, reverse osmosis and chemical precipitation, electrochemical technologies). Each of these treatment methods has advantages and disadvantages. Water resources management exercises ever more pressing demands on wastewater treatment technologies to reduce industrial negative impact on natural water sources. Thus, the new regulations and emission limits are imposed and industrial activities are required to seek new methods and technologies capable of effective removal of heavy metal pollution loads and reduction of wastewater volume, closing the water cycle, or by reusing and recycling wastewater. Advanced technologies for wastewater treatment are required to eliminate pollution and may also increase pollutant destruction or separation processes. For this reason, photocatalysis has emerged as a technology effective and affordable for wastewater treatment also from an engineering point of view since it can operate in mild conditions (room temperature and atmosphere pressure). Indeed, photocatalytic destruction has allowed cleaning up waste streams using light and a catalyst, opening a new field in wastewater remediation (Senthurchelvan et al., 1996).Various types of hazardous organic contaminants, including organic dyes, pesticides, oils, phenols, fertilizers, pharmaceutical waste, hydrocarbons, phenols, and detergents, have also been found in various water bodies (Javadian et al., 2014, Dixit et al., 2015).This makes heterogenous photocatalysis an ideal technique to clean up contaminated water.

One of the applications of photocatalysis, up to now studied only to a limited extent and still under current investigation and development, is the use of the technique in the field of organic synthetic reactions (Reischauer and Pieber, 2021). This process can induce oxidation and reduction reactions, eliminating the need for expensive and dangerous solvents and chemicals. An advantage is that photocatalytic processes do not require some of the extreme conditions necessary for some organic synthesis processes and that again can have an effect on costs as well as safety considerations such as elevated temperatures and pressures. The photocatalytic technique is potentially much more selective and therefore the production of by-products is reduced. When the photocatalytic process based on semiconductor photocatalyst is coupled with a separation polymer system it is possible to obtain a synergic effect of organic compounds production by minimizing environmental and economic impacts. In this photocatalytic hybrid system, in fact, the radicals produced by the irradiation of the photocatalyst were exploited to perform partial or total redox reactions leading to selective organic products which can be separated by the polymeric substrate. The

photoreactive composite polymer in which the photocatalyst is dispersed constitutes a "green" technology, because it allows the reactions to be carried out in mild conditions, and to obtain the interest products in a single step by separating them from the reaction system with considerable savings in terms of time and costs in order to make this process very interesting for industrial application. The choice of an appropriate polymer having high affinity with reactant subtrate and the knowledge of the parameters influencing the photocatalytic process represent, therefore, an important step in the design of a phoreactive composite polymer. The main aim of this Ph.D. thesis was the development of visible light active photocatalysts for water pollutants removal and the formulation of a photoreactive polymer composite in monolithic form, for partial oxidation reactions of organic compounds in liquid phase. In Section I the basic fundamentals and the main application fields of photocatalysis are examined, with a wide overview on the current progresses and drawbacks present in literature. Section II reports a detailed presentation of polymeric substrates classifying the possible materials to use in the oxidation process. Finally, a review on the application and modelling of photocatalytic polymeric reactors is treated. Then, the experimental results obtained in this study on the photodegradation of organic compounds in water are presented in Section III. In particular, the photodegradation of two different contaminants, Acid Orange 7 and Thiachloprid, in water and the separation of the clarified solution is studied both using photocatalyst in powder form and photocatalyst coupled with β-cyclodextrine (β-CD). In Section IV, the direct synthesis of phenol through hydroxylation of benzene, is reported. The benzene hydroxylation using a monolithic polymeric aerogel in which photocatalyst is embedded is studied in Section V. An accurate discussion of the promising experimental results in terms of phenol yield and selectivity to phenol obtained by modifying some operative conditions is described in Section VI.

I.1Photocatalysis as a green process

Heterogeneous photocatalysis is part of the environmentally friendly advanced oxidation processes (AOPs) and has slowly provided the prelude for environmental remediation (Wang et al., 2022). Photocatalysis plays a central role in ecological balances. Solar radiation is the main source of energy on Earth that exceeds every conceivable need of humanity in the future (25,000–75,000 kWh per day and hectare).

In this perspective, photocatalysis can be defined as a “catalytic reaction involving the production of a catalyst by absorption of light” (Verhoeven, 1996). Figure 1 shows the proper placement of the fully occupied lower s-band called the valence band (VB), and the upper unoccupied band as a conduction band (CB) in semiconductors, making them materials suitable for light absorption and photocatalytic action. The s and p bands are so close in

electrical conductor that they overlap, thus making it very easy for electrons to be promoted into a higher energy level. In semiconductors and insulators the gap between VB and CB is called the band gap.

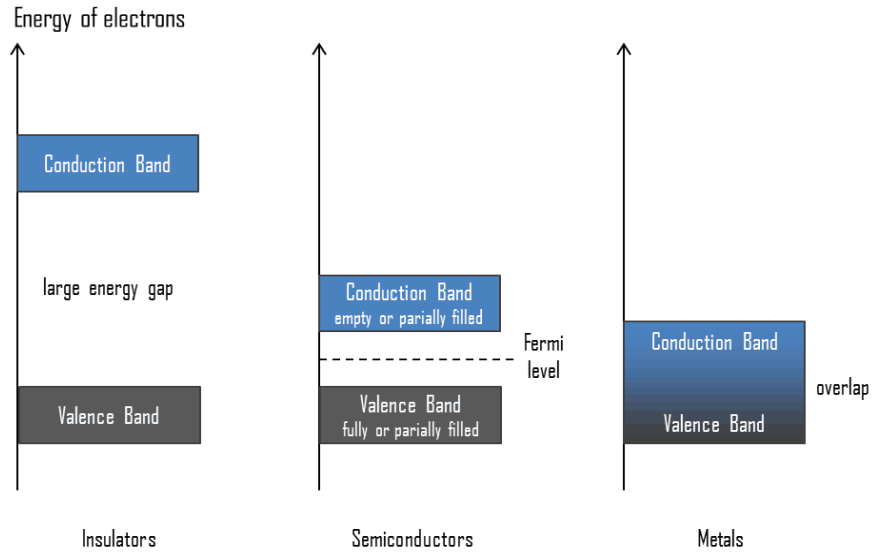

Figure I.1 *Valence band (VB) and Conduction band (CB) positions in metals, semiconductors, and insulators (Lazar et al., 2012)*

Heterogeneous photocatalytic reactions have many advantages, such as the use of solar light, which is a sustainable resource, a quick reaction rate and low energy consumption of heterogeneous photocatalytic oxidation; milder reaction conditions than those of traditional thermal catalysis, when compared with conventional treatment technologies (including adsorption, membrane separation, chemical sedimentation, and bioprocesses). To date, thousands of studies have been reported on the photocatalytic treatment of various pollutants, and new studies are being increasingly conducted in this regard. While it was not until the 1970s that this technique gained attention many examples of semiconductor photocatalysis had already been reported in the literature by the start of the century. Photocatalytic reactions constitute one of the emerging technologies for chemical transformations. In the late 1970s, the initial stages of this development were boosted by very attractive proposals concerning water splitting using UV energy (Fujishima and Honda, 1972)

Initial hopes were however, not fulfilled and in the early 1980s, when enthusiasm for the technology was declining, a new possible application

appeared, when it was reported that photocatalytic reactions could be utilised for environmental remediation (Haarstrick et al., 1996). Since then there have been a wide range of investigations on the abatement of air and water pollution; and pollution control remains as the most important target for applications and the main reason for research and development studies. The application for organic synthesis has however only been investigated to a limited extent (Cundall et al., 1976, Pincock et al., 1985, Fox and Dulay, 1993). Some syntheses process require the use of hazardous and expensive chemicals and procedures, with the production of hazardous by-products as is the case with the industrial process of multi-step cumene to obtain phenol. This translates into increased costs for the manufacturer due to additional safety requirements and the need for disposal and separation of unwanted products (Hjeresen et al., 2002). Although fine chemical production only accounts for about 5% of chemical production, it accounts for about 20% of profits (Blaser and Studer, 1999). Conventional industrial routes for many important organic chemicals typically require harsh operating conditions, such as high temperature and pressure. Thus, the development of photocatalytic synthesis routes which rely on light as an energy source to drive chemical reactions under much milder reaction conditions is highly desirable. Moreover, photocatalytic systems match the needs of green engineering in which fewer processing steps are achieved (Friedmann et al., 2016).

I.2 Foundamental of heterogeneous photocatalysis

Heterogeneous photocatalysis is a term which describes a process in which the photocatalyst is in a different phase with respect to the substrate. In this condition, the reaction scheme implies the previous formation of an interface between the photocatalyst in solid form and a liquid or a gas phase containing the reactants. Photocatalysis is generally defined as the change in the rate of a chemical reaction or its initiation under the action of ultraviolet, visible or infrared radiation in the presence of a substance, the photocatalyst, which absorbs light and it is involved in the chemical transformation of the reaction partners.

$$A + D \xrightarrow[light \geq E_{bg}]{semiconductor} A^- + D^+ \tag{1}$$

As in the case of catalytic reactions, heterogeneous photocatalytic reactions are composed of purely chemical and purely physical reaction steps. The main difference with a catalytic process is that, while in a catalytic process the catalyst is ready to operate, in photocatalysis the photocatalyst is "generated" and its activity maintained by the radiation absorption.

In a photocatalytic reaction, the following steps must be considered:
1. Diffusion of reactants to the photocatalyst surface through the boundary layer;
2. Diffusion of reactants into the pores;
3. Photoadsorption of reactants on the pore surface;
4. Photoreaction;
5. Photodesorption of products from the pore surface;
6. Diffusion of the products out of the pores;
7. Diffusion of the products away from the catalyst through the boundary layer

I.3 Mechanism

An ideal photocatalytic material should be highly photoactive, stable against photocorrosion, harmless, cheap and chemically inert and stable in a water environment during the reaction processes.
Moreover it should be active in both UV and visible region as sunlight is a costless, green and sustainable energy and its wavelength ranges from 280 to 4000 nm, with the UV photons which account for just a small percentage of the total energy (3–5%). The photogenerated pairs are the species eventually responsible for both the oxidation and reduction reactions occurring on the surface of catalyst; in fact, a photocatalyst must be able to photoadsorb simultaneously two reactants in different sites, one being reduced and the other oxidized, to guarantee the electroneutrality of the whole photocatalytic cycle. The semiconductor materials which have an empty energy region (band-energy structure), where no energy levels are available (Figure I.1). The region which extends from the top of the filled valence band to the bottom of the vacant conduction band is called band gap, Eg. The ability of a semiconductor to perform photoinduced electron-hole transfer to superficial species depends by the band energy positions of the semiconductor and the redox potential of the adsorbates.

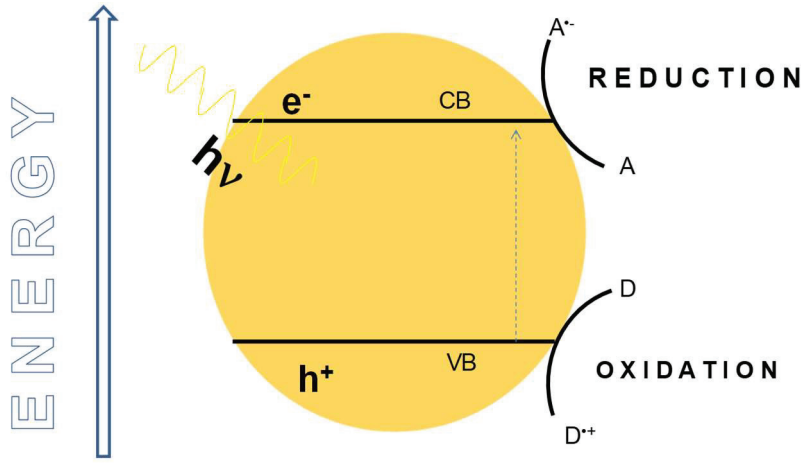

Figure I.2 *Illustration of the main processes occurring on a semiconductor photocatalyst under electronic excitation*

The preliminary step of the photocatalytic reactions is the radiation absorption by the catalyst.
The activation of a semiconductor photocatalyst is achieved through the absorption of a photon with a wavelength greater than the band gap energy which leads to the promotion of the electrons e^- from VB into CB, and in the simultaneous generation of positive holes h^+ in the VB (Shekofteh-Gohari et al., 2018, Mousavi et al., 2018). At this point, for the photocatalytic process to occur, the reagents must reach the outer surface of the photocatalyst, diffuse into the pores, photoadsorb and photoreact.
The photogenerated hole-electron pairs react with the molecules of reagents adsorbed on the semiconductor surface generating highly reactive radical species that are thus involved in oxidation and reduction processes of water pollutants (Fujishima, 1972). In particular, the reaction of either the photopromoted electron with a reducible adsorbed substrate (usually oxygen in aerated system) and/or the hole with an oxidizable adsorbed species can occur. By considering a semiconductor (SC), the heterogeneous photocatalytic process is a complex sequence of reactions that can be expressed by the following set of simplified equations (Linsebigler et al., 1995b)

a) Charge separation

$$SC + h\nu \longrightarrow e^-_{CB} + h^+_{VB} \qquad (2)$$

b) Bulk/surface separation

$$e^-_{CB} + h^+_{VB} \longrightarrow heat \quad (3)$$

c) Surface trapping

$$h^+_{VB} + \equiv Ti\text{-}OH \longrightarrow \equiv Ti\text{-}O^{\cdot} + H^+ \quad (4)$$

$$e^-_{CB} + \equiv Ti\text{-}OH \longrightarrow \equiv Ti^{\cdot} + OH^- \quad (5)$$

d) Surface recombination

$$e^-_{CB} \equiv Ti\text{-}O + H^{+\cdot} \longrightarrow \equiv Ti\text{-}OH \quad (6)$$

$$h^+_{VB} + \equiv Ti\text{-}OH \longrightarrow \equiv Ti\text{-}O^{\cdot} + H^+ \quad (7)$$

e) Interfacial charge transfer

$$Red_1 + \equiv Ti\text{-}O^{\cdot} \longrightarrow Ox_1 + \equiv Ti\text{-}OH \quad (8)$$

$$Ox_2 + H_2O + \equiv Ti^{\cdot} \longrightarrow Red_2 + \equiv Ti\text{-}OH \quad (9)$$

f) Back reaction

$$Red_2 + \equiv Ti\text{-}O^{\cdot} \longrightarrow Ox_2 + \equiv Ti\text{-}OH \quad (10)$$

$$Ox_1 + \equiv Ti^{\cdot} \longrightarrow Red_1 + \equiv Ti\text{-}OH \quad (11)$$

I.4 Photocatalytic reaction parameters

In photocatalytic process, various operating parameters affect the reaction path:

i. *mass of catalyst*: the initial rate of reaction was found to be directly proportional to the mass m of catalyst either in static, slurry or dynamic flow photoreactors (Figure I.3). This indicates a true heterogeneous catalytic regime. However, above a certain value of m, the reaction rate levels off and becomes independent of m. This limit depends on the geometry and on the working conditions of the photoreactor. These limits correspond to the maximum amount of photocatalyst (i.e.TiO_2) in which all the particles i.e. all the surface exposed are totally illuminated. For higher quantities of catalyst, a screening effect of excess particles occurs, which masks part of the photosensitive surface. For applications, this optimum mass of catalyst has to be chosen in order to avoid an unuseful excess of catalyst and to ensure a total absorption of efficient photons.

ii. *wavelength*: the variation of the reaction rate as a function of the wavelength follows the absorption spectrum of the catalyst (Figure I.2), with a threshold corresponding to its band-gap energy. For TiO_2 having E_G = 3.02 eV, this requires: λ 400 nm , i.e. near-UV wavelengths (UV-A). In addition, it must be checked that the reactants do not absorb the light to conserve the exclusive photoactivation of the catalyst for a true heterogeneous catalytic regime (no homogeneous or photochemical in the adsorbed phase). Since the solar spectrum contains 3–5% UV-energy, photocatalysis can be activated by solar energy.

iii. *initial concentration of reactant*: the kinetics follows a Langmuir–Hinshelwood mechanism confirming the heterogeneous catalytic character of the system with the rate r varying proportionally with the coverage θ as:

$$r = k\theta = k(KC/1+KC) \tag{12}$$

where k is the true rate constant; K is the constant of adsorption at equilibrium and C is the instantaneous concentration.
For diluted solutions (C < 10^{-3} M), KC becomes << 1 and the reaction is of the apparent first order, whereas for concentrations >$5\cdot10^{-3}$ M, (KC >> 1), the reaction rate is maximum and is of the apparent order (Figure I.). In the gas phase, similar Langmuir–Hinshelwood expressions have been found including partial pressures P instead of C. In some cases, such as in liquid alcohol dehydrogenation (Pichat et al., 1982) the rate follows variations including the square root of concentration:

$$r = k\left[K^{1/2}C^{1/2}/(1+K^{1/2}C^{1/2})\right] \tag{13}$$

This indicates that the active form of the reactant is in a dissociated adsorbed state. In other cases, such as in the photocatalytic degradation and mineralization of chlorobenzoic acids, a zero kinetic order was found, even at low concentrations. This was due to a strong chemisorption on titania with the saturation of the hydroxylic adsorption sites. For a maximum yield, reactions should be performed with initial concentrations equal to or higher than the threshold of the plateau.

iv. *temperature*: Because of the photonic activation, the photocatalytic systems do not require heating and are operating at room temperature. The true activation energy E_t, relative to the true rate constant $K = K_0 \exp(-E_C/RT)$ is nil, whereas the apparent

activation energy E_a is often very small (a few kJ/molhr) in the medium temperature range (20°C≤θ≤80°C).

However, at very low temperatures (-40°C≤θ≤0°C), the activity decreases and the activation energy Ea becomes positive (Figure I.). By constrast, at ‘‘high’’ temperatures (θ≥70-80°C) for various types photocatalytic reactions, the activity decreases and the apparent activation energy becomes negative (I.2c).

This behavior can be easily explained within the frame of the Langmuir–Hinshelwood mechanism described above. The decrease in temperature favors adsorption which is a spontaneous exothermic phenomenon. θ tends to unity, whereas KC becomes ≥1.

In addition, the lowering in T also favors the adsorption of the final reaction product P, whose desorption tends to inhibit the reaction. Correspondingly, there appears a term K_PC_P in the denominator of eq. 15. If P is the strong inhibitor, when gets:

$$K_PC_P >> KC \tag{14}$$

and the Langmuir–Hinshelwood equation becomes:

$$r = r\theta = kK(1 + KC + K_pC_p) \approx kKC / k_pC_p \tag{15}$$

where K_P is the adsorption constant of final product *P*. There results an apparent activation energy E_a equal to:

$$E_a = E_t + \Delta H_A - \Delta H_p \tag{16}$$

v. *radiant flux*: By definition, quantum yield is equal to the ratio between the reaction rate in converted molecules per second (or in moles per second) and the efficient incident photon flux in photons per second (or in Einstein per second (an Einstein is one mole of photons)). This is a kinetic definition, which is directly related to the instantaneous efficiency of a photocatalytic system. Its theoretical maximum value is equal to 1. It can vary over a wide range depending on the nature of the catalyst, the experimental conditions used (concentrations, T, m,…) and in particular, the nature of the reaction considered. Knowledge of this parameter is essential as it allows to compare the activity of different catalysts for the same reaction, to estimate the relative feasibility of different reactions and to calculate the energy yield of the process and its cost.

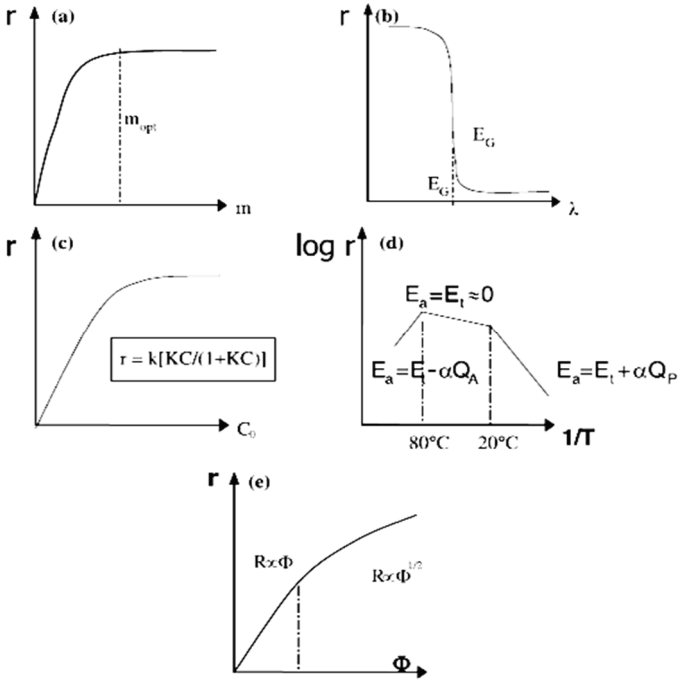

Figure I.3 *Influence of the different physical parameters on the kinetics of photocatalytic process: reaction rate r; (a): mass of catalyst m; (b): wavelength λ; (c): initial concentration c of reactant; (d) temperature T; (e) radiant flux ϕ.*

vi. *pH of aqueous solution*: The photocatalytic reaction is influenced by the pH of liquid medium. TiO_2 surface is positively charged in acidic condition. On the other hand, at pH higher than 7, TiO_2 surface is negatively charged (Konstantinou and Albanis, 2004, Bekkouche et al., 2004) according to the following reactions:

$$TiOH + H^+ \rightleftharpoons TiOH_2^+ \quad (17)$$

$$TiOH + OH^- \rightleftharpoons TiO^- + H_2O \quad (18)$$

vii. *presence of oxygen*: oxygen can produce superoxide ions ($O_2^{\bullet -}$) that initiates reactions leading to the formation of additional hydroxyl radicals, also via the formation of hydrogen peroxide.

$$O_2 + e^- \longrightarrow O_2^{\bullet -} \quad (19)$$

$$O_2^{\bullet -} + H+ \longrightarrow HO_2^{\bullet} \quad (20)$$

$$HO_2^{\bullet -} + e^- \longrightarrow HO_2^- \quad (21)$$

$$HO_2^- + H^+ \longrightarrow H_2O_2 \quad (22)$$

$$H_2O_2 + e^- \longrightarrow OH^{\bullet} + OH^- \quad (23)$$

Another oxidant specie which influences positively the photocatalytic reaction is H_2O_2 due to the formation of hydroxyl radicals. However, an excess of H_2O_2 can induce a detrimental effect because it acts as scavenger of valence band holes and $^{\bullet}OH$, producing hydroperoxyl radicals which has a less oxidizing power than $^{\bullet}OH$:

$$H_2O_2 + 2h^+ \longrightarrow O_2 + 2H^+ \quad (24)$$

$$H_2O_2 + {}^{\bullet}OH \longrightarrow H_2O + HO^{\bullet} \quad (25)$$

I.5 Photocatalytic activity of semiconductor materials

A photocatalyst is a semiconductor material that must be able to convert the light energy of the radiation into the chemical energy of the electron-hole pairs. Therefore, an adequate bandgap energy together with chemical and physical stability, non-toxic nature, availability and low cost are important requirements that allow it to operate in photocatalytic reactions. Several semiconductor materials used as photocatalysts are reported in the literature; the most popular are oxides (TiO_2, Fe_2O_3, SnO_2, ZnO, ZrO_2, CeO_2, WO_3, V_2O_5, etc.) or sulphides (CdS, ZnS, WS_2, etc.). Figure I.3 shows the redox potentials of semiconductor materials which are between +4.0 and -1.1 volts relative to the normal hydrogen electrode (NHE) for valence and conduction, thus allowing for the conversion of a wide range of molecules through photocatalytic reactions. A photocatalytic reaction can only take place if the electrochemical potential value of the electron acceptor is more positive (bottom in the graph) than the conduction band potential of the semiconductor and furthermore if the electron donor potential is more negative (top in the graph) than that of the semiconductor valence band.

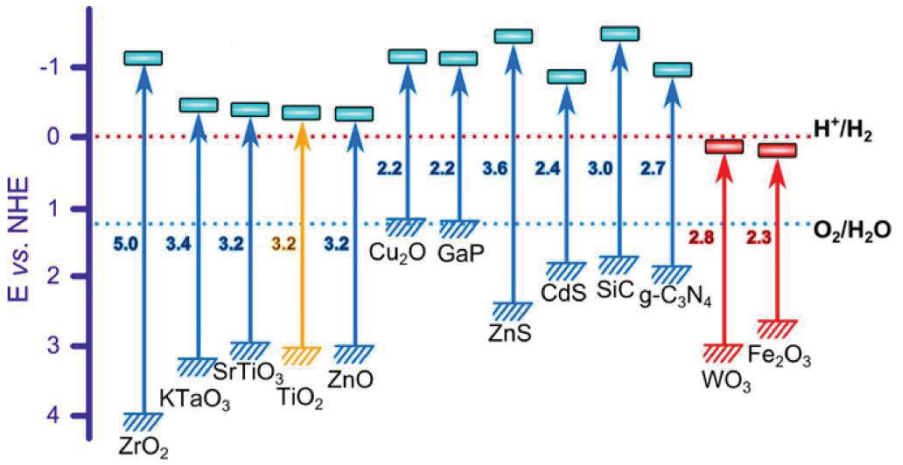

Figure I.3 *Bandgap energies, conduction, and valence band positions (referred to the Normal Hydrogen Electrode (NHE) potential at pH 0) of different semiconductors (Luciani et al., 2020).*

Among all the semiconductor oxides tested as photocatalysts, the most used material is titanium dioxide (TiO_2) for its properties, such as strong oxidizing power, high thermal stability, photostability, hydrophilicity, efficiency, chemical inertness, non-toxicity, high reactivity and environmentally safety (Nakata and Fujishima, 2012).
Photocatalytic activity of TiO_2 depends on its morphology, crystalline structure, size distribution and porosity. TiO_2 is a polymorphic material, whose crystalline forms are anatase, brookite and rutile. Among all, anatase is the most active because it has a greater affinity towards organic molecules (Nakata and Fujishima, 2012). TiO_2 presents a wide band gap (3.2 eV for anatase) and therefore, it can be excited only by ultraviolet light irradiation (k = 315–400 nm), which represents 3–5% of solar radiation (Nakata and Fujishima, 2012).
Recombination of electron-hole pairs can occur, in competition with charge transfer to adsorbed species, in the volume of the semiconductor particle or in its surface with the release of heat. This phenomenon represents the major deactivation path which could significantly decrease the overall photocatalytic efficiency. Therefore, the goal of scientific research has been to find the means to improve the efficiency of the sunlight use and the photocatalytic quantum efficiency in order to ensure a wider exploitation and application of the TiO_2 photocatalyst. In recent years, the modifications of TiO_2 by varying the electrical properties and inducing the bato-chromic shift of the band gap have been extensively investigated (Zangeneh et al., 2015). Modifications can be realized through TiO_2 doping. It has been considered

one of the most promising techniques to reduce the recombination of electrons and photogenerated holes and to extend the light absorption of TiO_2 in the visible region which, involves the introduction of metallic or non-metallic ions into the TiO_2 lattice (Yuan et al., 2011). Different dopants do not have the same effect on interaction with electrons and/or holes, due to the different position of the dopants in the host lattice. The coordination environments of dopants are influenced not only by the nature of the dopants, for example by the different ionic radii and concentration, but also by the synthesis method (Xu and Yu, 2011, Zangeneh et al., 2015). The doping of transition metal species such as Fe, V, Cr, and Mo in TiO_2 improves the photocatalytic activity under visible irradiation due to the enhancement of the adsorption of pollutants and the photogenerated electron-hole pairs. The shift of the light absorption region from UV to visible light is the result of the doping of the transition metal caused by the charge transfer between the d electrons of the transition metals and the conduction band (CB) or valance band (VB) of TiO_2. The possible expected action of TiO_2 doped with metals like Fe, is that metal ions can play as hole and electron traps enhancing the generation of species at high oxidizing power, such as hydroxyl radicals and super oxides (Cheng et al., 2018b). Thus, the generated highly oxidizing species further oxidize contaminants and intermediates up to the complete mineralization of the target pollutants. Although the addition of transition metals in the lattice represents a convenient and economical solution, especially for the degradation of organic substances, the need for expensive ion implantation systems during their preparation and their thermal instability producing poor photocatalytic activity makes them disadvantageous in applications (Deng et al., 2009, Xu and Yu, 2011, Tieng et al., 2011). Lanthanide ions (La^{3+} Ce^{3+} Nd^{3+}, Er^{3+}, Pr^{3+}, Gd^{3+} or Sm^{3+}) are used to enhance photocatalytic activity as they can form complexes with various Lewis bases in the interaction of functional groups of different organic molecules with their orbital f. It has been shown that the doping of lanthanide ions in a TiO_2 matrix allows to concentrate more easily the organic pollutants on the semiconductor surface and thus improve the photoreactivity. Furthermore, lanthanide ions can improve the separation efficiency of electron-hole pairs by trapping photogenerated electrons (Avram et al., 2021, Ndabankulu et al., 2019).

Noble metals such as Pt (Dong et al., 2011, Ioannides and Verykios, 1996), Pd (Ou and Lo, 2007, Seifvand and Kowsari, 2016) Au (Selvam and Swaminathan, 2010) and Ag (Fan et al., 2015, Baran and Yazici, 2016) have high Schottky barriers among the metal dopants and thus act as electron traps, facilitating electron–hole separation and thus, promoting the interfacial electron transfer process. There are different mechanisms for noble metal doping and/or deposition on TiO_2 depending on the photoreaction conditions. Noble metals are able to enhance the electron–hole separation by acting as electron traps, extend the light absorption into the visible range and

modify the surface properties of photocatalysts (Etacheri et al., 2015, Bumajdad and Madkour, 2014).

In addition to lanthanides, transition metals and noble metals the use of the other metals including aluminum (Al), gallium (Ga), indium (In) (Hinojosa-Reyes et al., 2013) tin (Sn), thallium (Tl), lead (Pb), and bismuth (Bi) (Hu et al., 2012) as doping agent were studied. These metallic elements are sometimes known as poor metals or post-transition metals, situated between the metalloids and the transition metals. Generally, these metals have higher electronegativity than the transition metals. In some cases, potassium (K) (Shin et al., 2016) magnesium (Giahi et al., 2019) and barium (Ba) (Mugundan et al., 2022) were also examined and shown to be effective in photoactivity of TiO_2 under visible light. However, the bad thermal stability related to metal doping of TiO_2 can impaire the photocatalytic activity of semiconductor (Pattanaik and Sahoo, 2014) and increase the recombination phenomena of charges due to probably a unappropriate amount of metal dopants into TiO_2 crystalline structure (Ghuman and Singh, 2013).

Therefore, doping TiO_2 with nonmetal atoms has recently received much attention (Patil et al., 2019). For example, the doping with nitrogen (N) (Ansari et al., 2016, Du et al., 2021) iodine (I) (Hou et al., 2011) boron (B) (Hosseini-Sarvari and Valikhani, 2021) chlorine (Cl) (Filippatos et al., 2019, Moitzheim et al., 2017) fluoride (F) (Czoska et al., 2008) sulfur (S) (Devi and Kavitha, 2014) phosphorous (P) (Gopal et al., 2012)
and carbon (C) (Irie et al., 2003), assures the activation of TiO_2 under visible light. Non-metal dopants, such as N may substitute semiconductor lattice atoms or enter into the lattice interstices of TiO_2 (Di Valentin and Pacchioni, 2013, Di Valentin et al., 2005). The introduction of a dopant in the lattice may allow the activation of TiO_2 in the visible range (Di Valentin et al., 2004). Metallic or non-metallic elements in TiO_2 structure can result in impurities promoting the recombination of photogenerated holes and electrons (Sharotri and Sud, 2017). Photocatalytic activity of N-doped TiO_2 was widely investigated (Kim et al., 2018, Sacco et al., 2015, Vaiano et al., 2019, Cheng et al., 2016, Wojtaszek et al., 2019).

In fact, it is reported that the incorporation of N in the TiO_2 structure induces the formation of an N 2p band above the original O 2p valance band leading to the band gap decrease and enhancing the photocatalytic activity under visible light (Kim et al., 2018). On the other hand, the presence of an optimal N content into structure can be explained considering that the oxygen sites of TiO_2 can be partially replaced with nitrogen ions (Shin et al., 1991) inducing oxygen vacancies and, as a consequence, the amount of Ti^{3+} increases with the increase of N content (Haoli et al., 2007, Qin et al., 2008) Both oxygen vacancies and Ti^{3+} species acted as hole traps, inhibiting the recombination of electron-hole pairs and, therefore, improving the photocatalytic activity under visible light (Linsebigler et al., 1995a). However, considering the practical applications, a higher reaction rate is still required since the

quantum efficiency of such non-metals and anion doped TiO_2 under visible light is much lower than that under UV light (Etacheri et al., 2015).
Moreover, the research interest has been recently focused on the co-doping of TiO_2 with two different ions (metal and non-metal, metal and metal, non-metal and non-metal), allowing a better separation of the photogenerated electrons and holes, assuring an effective enhancement of the visible light adsorption together with higher photocatalytic activity of TiO_2 (Su et al., 2011, Mancuso et al., 2020a).

I.6 Photocatalysis as water purification technique

In recent years, the development of industrialization and the constant growth of the population have led to an increase in the need of water which is a primary resource for human health and for the aquatic ecosystem. However, it is increasingly difficult to have clean water because many organic compounds are widespread in industrial effluents, such as dyes, aromatic hydrocarbons, pharmaceutical compounds, pesticides, heavy metal ions. The latest advances in sensing and monitoring technologies made it possible to classificate some pollutants as emerging contaminants (EC) that can be divided in persistent organic pollutants (POPs), pharmaceuticals and personal care products (PPCPs), endocrine disrupting chemicals (EDCs), according to their use and origin, in order to facilitate their removal (Gopinath et al., 2020, Zhu and Zhou, 2019). In particular, POPs, such as polychlorinated benzenes and hexachlorobenzene which are widely used in paint industries,are very stable organic pollutants in nature and difficult to biodegrade (Nguyen et al., 2020, Massima Mouele et al., 2020), while the prolonged use of PPCP (including antibiotics) can lead to an involuntary immunity without producing the necessary effects due to an intake greater than the permitted daily dose (Zhou et al., 2020, Chaker et al., 2020). EDCs are emerging water pollutants that alter the endocrine system by affecting the regular circulation of hormones in the body and, therefore, the proper functioning of various organs. These endocrine gland interfering compounds are able to mimic hormone molecules in receptor areas of the human body, in order to be recognized by the human body as hormones (Ribeiro et al., 2017).
They are also able to interact with binding proteins by altering hormonal metabolism (Gopinath et al., 2020). Among the EDCs, thiacloprid (THI) is an insecticide, belonging to the second-generation neonicotinoid pesticides, introduced by Bayer Crop Science with the name Calipsol. Like all neonicotinoid insecticides, THI selectively acts on the insect nervous system as an agonist of the nicotinic acetylcholine receptors.
Moreover, synthetic dyes can be considered emerging contaminants because they have potential toxic and genotoxic properties. The most widely used

dyes belong to the class of azo compounds derived from certain aromatic amines and are imployed in different products such as textiles, foodstuffs, cosmetics, house products, paints, and inks. The use of azo dyes to colour the textiles can causes serious environmental issue because of the high volume of water involved in the dyeing process. Consequently, high volumes of wastewaters containing dyes and pigments are produced and may be released into the environment (Ribeiro and Umbuzeiro, 2014). Among all azo-dyes, acid Orange 7 (AO7) is present in the effluents coming from the textile industry. It is a coloring agent consisting of an azo group bonded to aromatic rings. This azo dye can react with other chemical substances producing aromatic amines which cause toxic and carcinogenic effects in the environment. For this reason, it is necessary to eliminate this compound from aqueous discharges.

Conventional physical, chemical and biological methods have been used for wastewater treatment. However, many organic compounds are resistant to such treatments which are therefore limited by low removal efficiency, high operating costs, process complexity and slow operation. (Gutierrez-Urbano et al., 2021, Cherniak et al., 2022).

Among physical processes, sedimentation alone is not an effective treatment process. Membrane filtration is an effective process, but continual clogging of the membrane due to particles in the wastewater carries additional costs. Adsorption is another effective treatment process but, it does not indicate a real treatment process and is slightly more expensive than other processes depending on the properties and the preparation technique of the adsorbent. Some natural adsorbents including clays and soils are often used for low cost and, some of these adsorbent obtained from agricultural residues are employed to reduce the concentrations of pigments from industrial wastewater. Therefore, the filtration and adsorption techniques are non-destructive due to the transfer of contaminants from the liquid phase to a solid surface that requires further treatment. Chemical coagulation produces huge amount of sludge causing secondary pollution if the produced sludge is not handled properly. The biological treatment process is considered as the most economical and green treatment technology but, it not able to guarantee the degradation of the some organic compounds such as azo dyes for their biopersistency nature. However, some oxidation processes such as chlorination and ozonation are effective in a destruction of some classes of dyes (Ulson et al., 2010, Shriram and Kanmani, 2014, Ghernaout, 2017). Nowadays, Advanced Oxidation Processes (AOPs) appear as promising technologies for the degradation of non-biodegradable pollutants (Dong et al., 2022). AOPs are oxidation processes carried out under ambient conditions. AOPs involve the generation of highly reactive species, such as hydroxyl radicals (•OH) in order to remove organic or even some inorganic compounds that cannot be oxidized by conventional oxidants (gaseous oxygen, ozone, and chlorine) until to assure their complete mineralization

obtaining CO_2 and H_2O (Andreozzi et al., 1999, Dewil et al., 2017). Among different AOPs, heterogenous photocatalysis is low cost and environmentally benign technology widely used in water and air purification field.

TiO_2 material is widely used as a photocatalyst for its low cost, good optical activity, high chemical stability, and non-toxic nature. It can lead the breaking down of contaminant molecules present in wastewater through the presence of light source without the sludge production and, thus, further steps of the residues disposal. The main drawbacks of bare TiO_2 are due to its large bandgap equal to 3.0 eV for rutile crytalline phase and 3.2 eV for anatase phase and the high rate recombination of photogenerated electrone-hole (e^-/h^+) pairs, which limite the photocatalytic efficiency. In order to activate the degradation process of water pollutants, TiO_2 is normally excited by UV light with wavelength <387 nm. However, UV light represents only 5–8% of the solar spectrum at sea level. Therefore, the aim of researchers is to activate the catalysts by natural sunlight and prevent the photogenerated electron-hole pairs recombination. A possible strategy to reduce the band gap by extending the photoresponse of the catalyst to the visible light region is the chemical modification through the doping of the crystal structure of TiO_2 with metals or with non-metals. The addition of the dopant elements can inhibit the recombination of photo-induced holes and electrons by increasing the charge separation in order to achieve the complete degradation in a very short time also in presence of small amount of photocatalyst. TiO_2 lattice can be modified by introduction of transition metals, noble metals, and rare earth (RE) elements. Doping TiO_2 with transition metal ions (for example, Fe, Zn, V, Cr, Co Mn, and Ni) and with Ag, Au and Ru, generates a red shift in the absorption band of semiconductor from the UV to the visible region, resulting in an improvement of photocatalytic efficiency (Cheng et al., 2018a). Modifying TiO_2 materials with metal ions, especially d block metal ions such as Fe^{3+} and Cr^{3+} results in the insertion of impurity energy levels between the CB and VB. The inserted energy levels provide sub-bandgap irradiation from which electrons can be excited by lower energy photons than are required by undoped photocatalyst, and thus transferred from dopant d-band to CB or from VB to dopant d-band. In some cases the presence of metal dopants enhances charge separation as well as interfacial charge transfer while in many other cases, the metal dopants actually generate the rapid charge recombination and thereby reducing the electron diffusion length and lifetime (Kamat, 2012, Ibhadon and Fitzpatrick, 2013). In literature the TiO_2 doping with Fe ions was widely investigated (Marami et al., 2018, Jonidi Jafari and Moslemzadeh, 2020, Ellouzi et al., 2020).

Sood et al described the application of Fe-doped TiO_2 photocatalyst in the field of environmental remediation for visible light driven degradation of highly stable and toxic molecules such as para-nitrophenol and methylene blue dye (Sood et al., 2015). Likewise, the photocatalytic activity of Fe-

doped TiO_2 and Ni-doped TiO_2 was tested for the wastewater treatment to remove methylene blue from water under visible light (Ali et al., 2017a, Guan et al., 2020). Furthermore, the researchers studied visible light induced degradation of the acid orange 7 azo dye present in texile wastewater, the removal of the 2,4-Dichlorophenoxyacetic toxic herbicide and nitrobenzene from water and soil using Fe-doped TiO_2 photocatalyst, (Shen et al., 2020, Ebrahimi et al., 2021, Crişan et al., 2015) On the other hand, various literature studies have demonstrated that TiO_2 doping process with RE elements prevents the photogenerated electron–hole pairs recombination confirming a better visible light degradation of organic compounds present in water and in air (Mazierski et al., 2018, Li et al., 2005, Hewer et al., 2011, Ramya et al., 2019). For example, Pr-doped TiO_2 was used for the mineralization of phenol (Reszczynska et al., 2014). Among different EDCs, bisphenol A was treated in presence of visible light using Pr-doped TiO_2 photocatalyst (Cordeiro et al., 2021).

Sm, Er, Gd and Ce-doped TiO_2 photocatalysts reported an interesting visible light driven activity in the degradation of dyes and water soluble phenolic compounds (Singh et al., 2018, Xu et al., 2009, Silva et al., 2009). The photocatalytic activity of non-metal doped photocatalysts under visible light irradiation is commonly investigated for the removal of several dyes. (Zhang et al., 2020, Piątkowska et al., 2021). Among all the non-metal dopants, nitrogen is the most usually used (Di Valentin and Pacchioni, 2013) due to its small ionization energy and its atomic size comparable with that of oxygen (Vaiano et al., 2015a). The introduction of nitrogen as an impurity in TiO_2 is an efficient way of improving the solar light harvesting ability and photocatalytic activity of N-doped TiO_2 compared to bare TiO_2. N-doped TiO_2 photocatalysts can be used for a wide range of applications such as the degradation of organic pollutants (i.e. dyes and drugs) (Sacco et al., 2018b, Vaiano et al., 2015a, Monteiro et al., 2015) and air purification, sensors, solar energy conversion, and photovoltaics owing to its nontoxicity, ease of synthesis, low cost, and high chemical stability (Sun et al., 2018, Kamaei et al., 2018). In addition to the degradation of industrial textile effluents, N-doped TiO_2 is utilized as a self-cleaning material, for air purification and teeth whitening (Padmanabhan and John, 2020, Bersezio et al., 2021).

The incorporation of N in the TiO_2 structure induces the generation of an N 2p band above the original O 2p valance band leading to the band gap reduction with an increase of the photocatalytic activity under visible light (Kim et al., 2018, Vaiano et al., 2015a). In particular, the oxygen sites of TiO_2 can be partially replaced with nitrogen ions with formation of oxygen vacancies and an increase of Ti amount as the content of N increases. Both oxygen vacancies and Ti species acted as hole traps, inhibiting the recombination of electron-hole pairs and, therefore, improving the photocatalytic activity under visible light (Herrmann, 1999). However, an optimal amount of dopant element is required to ensure an improvement in

photocatalytic performance because the presence of an excessive amount of dopant ions in TiO_2 could favor the recombination phenomena of the electron-hole pairs causing a worsening of the photocatalytic activity (Qin et al., 2008). Bakre et al evidenced the effectivity of N-doped TiO_2 catalysts in the degradation of cationic dye, methylene blue and rhodamina B, under sunlight in comparison with commercial TiO_2 (Bakre et al., 2020). Other non-metals, such as C, S, P, used less than N have been considered by several researchers to improve the optical response of TiO_2 in the visible light spectrum. In general, the doping of TiO_2 with S element can be via cationic or anionic S routes. It was reported that cationic doping takes place by substitution of titanium ions with S^{4+} or S^{6+}, while anionic doping occurs by oxygen ions substitution with S^{2-}

Additionally, being the ionic radius of S^{2-} (1.7 Å) higher than that of O^{2-} (1.22 Å), the incorporation of sulfur by substitution of Ti4+ with S^{6+} is energetically more favorable than the replacement of O^{2-} by S^{2-}. (Bu et al., 2015). Both cationic and anionic S-doped photocatalysts revealed the enhanced visible light photocatalytic activity. However, S^{6+} was found to be responsible for reducing the TiO_2 crystallite size and in the cationic S-doped TiO_2 the photoinduced holes and hydroxyls played a major role during photocatalysis. On the other hand, the S^{2-} doping resulted in an increased TiO_2 crystallite size, and in anionic S-doped TiO_2, the photoinduced holes and electrons played approximately the same role in the photocatalytic activity. In the case of the cationic and anionic S-doped TiO_2, the enhancement of the photoactivity was justified by the formation of Ti-O-S and O-Ti-S bands in the crystal lattice under the cationic and anionic S-doping, respectively, which introduce new impurity levels between the VB and CB. The photocatalytic activity of S-doped TiO_2 under visible light is usually investigated on mineralization of different organic pollutants. In fact, Sharotri et al examined the photocatalytic response of S-doped TiO_2 for various model compounds such as rhodamine 6G (synthetic dye), quinalphos (an organophosphate pesticide), and diclofenac (a pharmaceutical waste) confirming the improved performance of doped nanoparticles with respect to bare TiO_2 (Sharotri et al., 2022). Boningari et al. investigated the photodegradation of acetaldehyde with a cationic S-doped TiO_2 in the presence of visible light and reaveled a higher efficient total organic carbon (TOC) removal of approximately 60% (Boningari et al., 2018). Bakar et al examined the decomposition of methylene orange and phenol using both anionic and cationic S-doped TiO_2 in presence of visible light by underling that the efficiency of phenol photodegradation was similar to that observed for methylene orange (Bakar and Ribeiro, 2016). The photodegradation of atrazine was also investigated. The studies revealed higher effectiveness of atrazine oxidation by the solar/Sdoped TiO_2 system in comparison with the solar/TiO_2 system. The authors also emphasized that lower water pH favored the photodegradation of herbicide, while the presence of humic acids (HA)

decreased the decomposition rate due to the competition with the atrazine molecules for hydroxyl radicals and partial absorption of sunlight before it reached TiO_2 (Liu et al., 2009). Lin et al. examined the synthesized S-doped TiO_2 in terms of degradation of gaseous 1,2-dichloroethane (Lin et al., 2014). S-doped TiO_2 photocatalysts exhibited superior photocatalytic activity under visible light compared to that of pure TiO_2. The conversion rate of 1,2-dichloroethane was 55.3 nmol/ min· g , whereas in the case of the undoped TiO_2 it was 2.16 nmol /min·g after 60 min of irradiation. The S-doped TiO_2 synthesized by Baeissa et al. was applied for photooxidation of cyanide in water reaching, the efficiency of photocatalytic oxidation of cyanide equal to 100% after 30 min of irradiation with a blue fluorescent lamp (Baeissa, 2015). Furthermore, the S-doped TiO_2 showed potential for application in antimicrobial field. Dunnill et al. investigated the inhibition of E. coli growth in the presence of the S-doped TiO_2 films recording the complete inihibition efficiency of bacterial growth after 24 hours of irradiation (Dunnill et al., 2009). Recently, Zhang et al. studied the activity of P-doped TiO_2 photocatalysts for oxidative coupling of benzylamines and photodegradation of phenol under visible light irradiation. The enhanced performance of photocatalyst was attribuited by TiO_2 doping with P element which can exist as a pentavalent oxidation state and can replace Ti^{4+} ions in the crystal lattice of anatase, by trapping photogenerated electrons in order to greatly reduce the recombination rate of electron/hole pairs (Zhang et al., 2020). In the last decade, for the treatment of wastewater containing biorecalcitrant organic pollutants, the research interest has focused on the TiO_2 co-doping with two different ions, allowing a better separation of photogenerated electrons and holes and thus ensuring an effective enhancement of visible light adsorption together with increased photocatalytic activity of TiO_2 (Mancuso et al., 2020a, Su et al., 2011). The codoping process of TiO_2 semiconductor can take place with metal/metal, metal/non-metal and non-metal/non-metal.

I.7 Photocatalysis as organic synthesis technique

Heterogeneous photocatalysis is universally recognized as a “green” and inexpensive technology because it can be carried out under mild experimental conditions (ambient temperature and pressure in the presence of cheap and non-toxic semiconductors as photocatalysts), often by using water as the solvent, O_2 as the oxidizing agent and solar light or artificial light with low-energy consumption as the irradiation sources. Visible light photocatalysis has become a powerful organic synthesis tool that exploits light to activate photocatalytic systems to be used for obtaining valuable chemical compounds. Using light to induce chemical reactions is attractive

because photons are traceless reagents that provide energy to activate substrates, reagents, or catalytic intermediates under mild conditions. Traditionally, photochemical reactions were carried out using UV light to excite substrates or reagents (Hoffmann, 2008). The high energy of these light sources requires special equipment and often causes unselective reactions, which are difficult to predict and control. This has changed with the development of photocatalysts that can be activated with low-energy photons, paving the way for sustainable chemical synthesis that is driven by a non-hazardous and environment-friendly reagent: visible light (Crisenza and Melchiorre, 2020). Most organic synthesis activities focus on the development of novel photoredox reactions, but a number of interesting new concepts have recently been considered (Reischauer and Pieber, 2021). Nevertheless, photocatalysis also presents some drawbacks as the low selectivity towards the partial oxidation products (especially by using water as the solvent and photocatalyst in powder form). The efficiency of photocatalytic organic syntheses can be improved by operating different strategies, both on the typical parameters of the photocatalysts (crystallinity degree, type of polymorph, surface acid-base properties, exposure of particular crystalline facets, coupling of different semiconductors, position of the valence and conduction band edge, addition of doping agents) and on parameters related to the reaction system (setup configuration and reactor geometry, type of solvent, type and amount of photocatalyst, initial pH, presence of gases, temperature). Selective photocatalytic formation of high value organic compounds can occur either through oxidation reactions or reduction of the starting substrate, therefore parameters that influence the oxidizing or reducing power, respectively, are to be taken into account.

Moreover, strictly speaking, a chemical reaction can be defined a “synthesis reaction” when the target product is separated from the reaction mixture and purified. This step of the main product separation and isolation is generally very difficult in the photocatalytic processes and not widely discussed in literature (Parrino et al., 2018). For example, a possible research interest in the field of chemical reactions is to find some remedies to perform organic synthesis in a single step unlike industrial processes and to discover new promising strategies to control the path of reactions in order to improve the selectivity towards the desired product assuring its separation and recover.

For this regard, a great interest is devoted to processes in which the direct photocatalytic oxidation of benzene to phenol is achieved, thanks to the use of suitable catalysts and oxidant species. including homogeneous and heterogeneous photocatalysts in order to obtain the selective conversion of benzene to phenol.

I.7.1 Synthesis of phenol

Phenol is a valuable chemical raw material widely used as a precursor for the production of resin plastics and drugs and as the main reactant in chemical synthesis. It was discovered in coal tar and, under ambient conditions, appears as a white crystalline solid with a characteristic odor. It is an important industrial commodity, typically obtained from benzene. The use of phenol has been increasing due to its importance as a raw material to obtain other products. The conversion of benzene to phenol covers great relevance since phenol is a solvent and an intermediate of other industrial productions being a precursor to many materials and useful compounds. Some examples of the usage of phenol are reported in the following:
1) PHENOLIC RESINS: by the reaction of phenol or substituted phenol with formaldehyde, phenol formaldehyde resins or phenolic resins can be obtained. The first example was Bakelite as commercial synthetic resins.
2) POLYCARBONATES (a very pure phenol feed is required): polycarbonates are thermoplastic polymers containing carbonate groups in their chains. They are strong, tough materials, and some grades are optically transparent. Products made from polycarbonate can contain the precursor monomer bisphenol A.
3) EPOXY RESINS: epoxy phenolic resins are resins modified at the phenolic hydroxyl group to include an epoxide functional group. This addition increases the ability for the resin to crosslink, creating a stronger polymer.
4) INTERMEDIATE FOR CAPROLACTAM (nylon production):caprolactam is a monomer for the nylon production. Among the routes for its manufacture, one is via cyclohexanone and cyclohexanone oxime. Cyclohexanone can be prepared either from phenol or from cyclohexane. The phenol route is a two-stage process, in which the first stage foresees the reaction among phenol and hydrogen in the presence of a nickel catalyst at about 180°C to form cyclohexanol, subsequentely dehydrogenated at about 400°C in the presence of a copper catalyst to yield the cyclohexanone (Brydson, 1999)
In 2014 the production of phenol in the world was 8.9 million tonnes, in Asia 3.7 million tonnes, in Europe 2.7 million tonnes and US 2.3 million tonnes. Current worldwide capacity for phenol production is nearly 7 million metric tonnes per year (Weber and Weber, 2010). The cumene process (cumene to phenol process, Hock process) is the most important industrial process for synthesizing phenol and acetone from benzene and propylene (Schmidt, 2005).This process converts two relatively cheap starting materials, benzene and propylene, into two more valuable ones, phenol and acetone. Other reactants required are oxygen from air and small amounts of a radical initiator. The process is very complex, as it consists of several stages,

passing through the formation of hydroperoxide (very reactive substance that can give runaway phenomena), which allows the indirect production of phenol and acetone.The process has three main reaction steps plus furthermore a step of concentration of cumene hydroperoxide and they are: i) production of cumene; ii) conversion of cumene to cumene hydroperoxide; iii) concentration of cumene hydroperoxide; iv) hydrolysis of cumene hydroperoxide.
The scheme of the reactions is reported in Figure I.IV

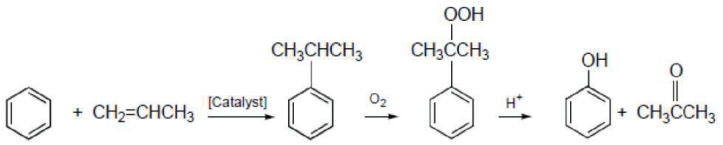

Figure I.4 Reaction steps for phenol production via cumene process (Mancuso et al., 2020b).

The production of cumene (isopropylbenzene) is a Friedel-Crafts reaction and occurs by the reaction between benzene and propene, using an acid catalyst.The first used heterogeneous catalyst was H_3PO_4/Pumice then a zeolite, such as ZSM-5, at about 330 °C and under pressure (about 10 atm) in a fixed bed reactor was applied (Zakoshansky, 2007).
In one process, benzene and propene (3:1mole ratio) are passed over an acid catalyst. The excess of benzene acts to limits the polyalkylations and the by-reactions of oligomerization of propene. The zeolite is more environmentally friendly than traditional acid catalysts. The problems are related to selectivity because isomers can be produced with respect to cumene.
The second step, the conversion of cumene to cumene hydroperoxide involves the use of air to give the hydroperoxide in the presence of small quantities of radical initiator (benzoil peroxide, for example) in slightly basic conditions.
The reaction is autocatalyzed by cumene hydroperoxide. The reaction takes place at temperatures between 77-117 °C and 1-7 atm pressure, to hold the system in the liquid phase.
After the concentration of the cumene hydroperoxide, performed usually with an evaporator at descendent film, the third and final reaction is the decomposition of cumene hydroperoxide by mixing with sulfuric acid at 40-100 °C to give, after neutralisation, phenol and propanone (acetone). Then the products are separated through distillation columns.
The economicity and effectiveness of this process is related to the market of acetone, apart from phenol. Often, much more phenol is needed than the propanone that is produced at the same time. Moreover this multistage

process has a low overall yield (less than 5%), requires high energy, and formation of by-products such as acetophenone, 2-phenylpropan-2-ol, and α-methylstyrene is encountered (Park and Choi, 2005).

Today, almost 95% of the worldwide phenol production is based on the 'cumene process' although the previously mentioned drawbacks, which are poor ecology, the formation of an explosive intermediate (cumene hydroperoxide), high capital investment, a high acetone production as a co-product which results in an oversupply in the market, and a multistep character which sorts difficult to achieve high phenol yields with respect to benzene feed (Molinari and Poerio, 2010), yield in highly desirable development of alternative synthetic processes of phenol more efficient and environmentally benign. Actually, in this regards a great interest is devoted to the process in which direct oxidation of benzene to phenol is achieved, thanks to the use of suitable catalysts and oxidant species with the aim to overcome the disadvantages of the industrial process.

To this purpose, the selective hydroxylation of benzene to phenol by means of photocatalysis using different oxidizing agent including O_2 (Bal et al., 2006), N_2O (Xia et al., 2008), or H_2O_2 (Borah et al., 2012) was the object of several research papers.

For this purpose, both homogeneous and heterogeneous photocatalysts were studied although the latter evidenced some drawbacks. More specifically, in a homogeneous system it is difficult to separate the catalyst from the reaction products (Chen et al., 2018). In the case of homogeneous systems, Fenton's reaction is one of the well-known homogeneous oxidation process in which Fe^{2+} is used as a catalyst and hydrogen peroxide as oxidant (Chen et al., 2009). However, this process requires acidic conditions that lead to corrosion phenomena (Sannino et al., 2011), and also more than 40% of the used hydrogen peroxide is consumed by side reactions (Zhang et al., 2013).

Moreover the literature reported the selective oxygenation of benzene to phenol with an oxygen-saturated acetonitrile solution containing benzene water and at ambient conditions using of 3-cyano-1-methylquinolinium ion ($QuCN^+$) as homogeneous photocatalyst, showing a strong oxidizing ability towards benzene (Ohkubo et al., 2011).

As alternative to homogeneous photocatalysis, the heterogeneous photocatalytic process could represent a possible green alternative for selective oxidation reactions (Sannino et al., 2013, Sannino et al., 2012, Vaiano et al., 2017c, Fessi et al., 2020, Žerjav et al., 2020). Among the semiconductor photocatalysts, TiO_2 is the most used material because of its chemical stability and its high oxidizing ability. It has been reported that crystalline anatase phase of TiO_2 has the higher photocatalytic activity, if compared to rutile TiO_2, because anatase phase has higher levels of hydroxyl groups on its surface (Sclafani and Herrmann, 1996). The anatase TiO_2 presents a wide band gap of 3.2 eV and it is normally activated under ultraviolet (UV) light (Vaiano et al., 2016, Devaraji and Jo, 2018). When

TiO_2 photocatalyst is irradiated with energy greater than the TiO_2 band gap energy, positive charge-holes are genertaed in the valence band while the electrons are promoted in the conduction band. Both positive holes and electrons take part in oxidation–reduction reactions. In particular, the photogenerated positive hole is able to react with adsorbed water to produce hydroxyl radicals whereas the electron can reduce O_2, generating strongly oxidizing superoxide ions. These highly reactive species, such as hydroxyl radicals, are employed for phenol production from benzene under mild conditions through photocatalytic process (Gupta et al., 2015, Mancuso et al., 2020b).

Moreover, photocatalytic oxidation of benzene to phenol in liquid phase is generally studied using H_2O_2 as oxidant and titanium dioxide (TiO_2) modified with noble metals (Devaraji et al., 2014, Yuzawa et al., 2012). However, such photocatalytic formulations do not allow to achieve an adequate phenol yield (<15%) even if a high selectivity is observed (80-100%). It was shown that, due to its higher reactivity compared to benzene, phenol can be further converted to quinone compounds (such as hydroquinone, 1,4-benzoquinone) or even oxidized to carbon dioxide (Su et al., 2014, Xiong and Tang, 2021).

Therefore, the development of new and efficient photocatalysts able to suppress to a certain extent the phenol overoxidation reactions is highly anticipated, thus also guaranteeing a suitable selectivity to the desired product (phenol).

For this reason, in order to assure an improvement in selectivity to phenol together with high benzene conversion, several studies have suggested the formulation of different types of photocatalyst.

Some research groups synthetized photocatalytic systems based on metal noble nanoparticles (such as Au, Pd, Ag) dispersed on carbon nitride surface (C_3N_4) to produce directly phenol from benzene under visible light irradiation in presence of H_2O_2. The authors evidenced that the presence of C_3N_4 support suppress the mineralisation of benzene, favouring the evolution of phenolic compounds (Hosseini et al., 2018, Verma et al., 2017). Moreover, others literature papers proposed nanostructured composite photocatalysts, such as carbon nanotubes (CNT) as support for TiO_2 powder, nano-metal-organic frameworks (MOFs) or iron (II) phthalocyanine (FePc), showing a significant enhancement of selectivity to phenol under visible light irradiation (Dasireddy and Likozar, 2018, Xu et al., 2017, Asghari et al., 2020). However, also such photocatalytic systems did not assure a high selectivity to phenol combined to an acceptable benzene conversion. In this perspective, promising results under UV light were reported by Zhang et al. which entrapped undoped TiO_2 nanoparticles in hydrophobic silica foam, obtaining almost 36% of benzene conversion and approximately 35% of selectivity to phenol (Zhang et al., 2011a).

I.8 Potentials and limits of the photocatalytic processes

Photocatalytic processes include a great variety of reactions, such as partial or total oxidation, degradation of organic compounds, reduction reactions, fuel synthesis (e.g. H_2 production through water splitting), metal corrosion prevention, disinfection, etc.

The application fields of photocatalysis can be divided in two main groups:

i. Purification process: Photocatalytic techniques are mainly used to remove organic pollutants both in water and air. This application has been extensively studied in literature generating great interest because it represents a promising alternative capable of degrading organic bio-recalcitrant compounds that cannot be eliminated through traditional treatments. In this context, In this context, photocatalysis represents an useful "green" purification technique, because, as result of a chain of oxidation reactions, a wide range of organic molecules also containing in their structure heteroatoms, can be mineralised to inorganic species: carbon to CO_2, hydrogen to H_2O, nitrogen to nitrate, sulphur to sulphates and phosphorus to phosphate. Many studies have been led to overcome the growing problem of wastewater contamination by different pollutants (dyes, pesticides, herbicides, pharmaceutical compounds ...) by means of photocatalytic reactions (Lair et al., 2008, Karunakaran and Dhanalakshmi, 2008, Lhomme et al., 2008). Photocatalytic treatments of the air have also been reported to solve the environmental problem of gaseous emissions from industries and other human activities. Several volatil organic compounds (VOCs) such as methyl-t-butyl ether (MTBE)(Šihor et al., 2019), toluene (Demeestere et al., 2007, Marcı et al., 2003), bromomethane, (Huang and Wan, 2009) benzene (Hu et al., 2011, Yan et al., 2008), formaldehyde (Huang and Zhu, 2007), etc., have been successfully degraded by photocatalytic processes. In recent years, the purifying property of TiO_2 has been exploited in construction materials not only at the laboratory level but also in concrete structures to maintain their aesthetic characteristics. Moreover, the photocatalytic materials are able, thanks to their strong hydrophilicity, to keep their aesthetic appearance unchanged over time; they can remove dust and dirt from the external surfaces of buildings with a simple rain. The combination of engineering and chemistry has therefore created photocatalytic materials containing TiO_2 particles, which, applied not only to urban and building environments but also in hospitals, clinics, schools and laboratories, can generate positive effects in terms of both anti-pollution and antibacterial. TiO_2 predominantly in the nanometric form has gained great interest from the construction industry, where it is mainly used for coatings, paints, antiseptic tiles and self-cleaning glass. Despite the enormous potential recognized for TiO_2 in the construction field, there are still many open questions regarding its effectiveness in real applications by varying the support material, its long-term effectiveness, the real self-

cleaning effect in the real environment (the ability to self-clean is often tested with laboratory tests that necessarily simplify the conditions of exposure) and in its impact on the environment and human health, all aspects that are still under study. Photocatalytic reduction processes are also applied to remove toxic and non-degradable metal ions with dangerous ionic states, such as Cr (VI) Pd (II) Hg (II), dissolved in waste water (Anand et al., 2019, Cappelletti et al., 2008, Singh et al., 2021).

The reduction of these metals results not only in the prevention of pollution but also in the recovery and reuse of precious metal products with respectively environmental and economic issues. Photocatalytic reactions have also been investigated to obtain the synergistic effect of the reduction of metal ions with the simultaneous degradation of organic contaminants.For example, redox reactions have been used in the literature for the purification of aqueous systems containing contaminants such as Cr (VI) and bisphenol A (Ali et al., 2020), Fe (VI) and ammonia (Sharma and Chenay, 2005) Cr (VI) and azo dyes (Papadam et al., 2007), Ag (I) and dyes (Siddiqui and Jaiswal, 2021). Photocatalytic processes have also been exploited for the conversion of other potentially toxic inorganic ions and molecules into their corresponding harmless forms. In this context, photocatalytic reactions are reported in the literature to reduce bromate ions to Br- (Noguchi et al., 2002), nitrite and nitrate to ammonia and nitrogen (Ranjit and Viswanathan, 1997), or to oxidize sulphite, thiosulfate and sulphide ions into harmless SO_4^{2-}, PO_3^{3-} in PO_4^{3-} or CN^- in NO^{3-} ions (Herrmann et al., 2007). In recent years, the researchers focused their study on the possibility of using the photogeneration of active oxygenated radicals to attack the cell membrane of microorganisms and cause their inactivation. The antimicrobial activity of the UV light activated photocatalyst was tested against different types of bacteria, yeasts, algae and viruses (Coronado et al., 2005, Guillard et al., 2008). Furthermore, the cytotoxicity of photocatalysis for cancer treatment was also tested, proving the possible application of photocatalytic reaction in medical field. In particular, Fujishima et al. (Fujishima et al., 2000) examined the antineoplastic photocatalytic effect using in vitro experiments which confirmed tumor growth inhibition.

ii. *Synthetic pathways:* Due to the highly non-selective reactions involved in photocatalytic processes, the application of this technology has been mainly aimed at the treatment of hazardous compounds in the liquid and gaseous phase. However, it has been widely demonstrated that by selecting or modifying some photocatalytic parameters, such as the surface of the semiconductor or the wavelength, it is possible to control the reaction by obtaining a better selectivity towards some desired products. In this regard, photocatalysis could represent an alternative synthetic path able to satisfy some of the principles of Green Chemistry. Several studies have reported the selective oxidation of hydrocarbons in water and

in the organic phase (Almquist and Biswas, 2001, Pomilla et al., 2021, Shimizu et al., 2004). In particular, Park and Choi studying the photocatalytic conversion of benzene into phenol, showed the possibility of increasing the phenol yield and selectivity by adding Fe^{3+} or/and H_2O_2 to the TiO_2 suspension or by modifying the surface of the catalyst by deposition of Pt nanoparticles (Park and Choi, 2005).

Gondal et al. studied the photocatalytic activity of several semiconductor catalysts for the conversion of methane to methanol at room temperature in the aqueous solution achieving a conversion of 29%, 21% and 20% using WO_3, TiO_2 and NiO respectively (Gondal et al., 2004). In addition, selective photooxidation reactions to convert alcohols carbonyls have been studied (Shiraishi and Hirai, 2008, Palmisano et al., 2007)

The synthesized photocatalysts were found to be more selective than the samples from two commercial TiO_2 Degussa P25 and Merck.

Colmenares et al. reported the use of different metal-doped TiO_2 systems for selective gas phase photooxidation from 2-propanol to acetone. They observed that doping the catalyst with Pd, Pt or Ag caused an increase in molar conversion compared to bare-TiO_2, while the presence of Fe and Zr had a detrimental effect (Colmenares et al., 2006). Numerous studies on the photocatalytic reduction of chemicals are reported in literature to convert nitrobenzene compounds to the corresponding amino-derivates (Ahn et al., 2007, Zhang et al., 2006, Maldotti et al., 2000) carbonate to methane and methanol (Ku et al., 2004, Sasirekha et al., 2006).

Based on the above considerations, photocatalysis is an attractive green process not only as a purification method, but also as a synthetic route. Several advantages can be summarized for the photocatalytic process:

- it can be applied to a wide range of compounds in aqueous, gaseous and solid forms phase;
- the reactions are carried out quickly and under mild experimental conditions, usually at ambient temperature and pressure;
- generally no additives are required, only oxygen from the air;
- it is also applicable to solutions with low concentrations;
- is capable of destroying a variety of dangerous molecules with the formation of harmless products, solving the problem of disposing of pollutants associated with conventional methods of wastewater treatment;
- it can be exploited to convert toxic metal ions into their non-toxic forms they can be recovered and reused;
- a synergistic effect can be obtained when coupled with other technologies;
- the ability to use sunlight makes it an interesting and economical process.

However, the application of the photocatalytic process at an industrial level is limited from various drawbacks related to the reactions involved and the configuration of the reactor.

The development of photocatalytic systems requires knowledge of kinetic models which include all the parameters that influence the process and make it possible to design a reactor useful for industrial applications. As previously described, the radical reactions that occur in a photocatalytic process are highly non-selective and very fast. When the goal is to use photocatalysis as a synthetic route, therefore, it is important to control the reaction kinetics to avoid secondary reactions that lead to unwanted products. In this regard, a lot of efforts have been made to obtain more selective reactions by modifying the semiconductor materials in powder form. Regarding the reactor configuration, few studies have been conducted for the design of efficient photoreactors for commercial exploitation. In particular, one of the main drawbacks concerns the recovery of the catalyst which is suspended into reactive environment and the separation of the products from the reactive environment. Practical engineering applications require that photocatalytic particles must be immobilized on bulky support materials in order to simplify their recovery from the treated water or to avoid damages to the recirculation pumps. In the immobilized system the catalyst can be coated on the reactor walls, supported on a solid substrate or deposited around the case of the light source, using alumina, zeolite as support materials (Shimizu et al., 2004, Zama et al., 2000) activated carbon (AC) (Sobana et al., 2008, Zhang and Lei, 2008), silica support (Coronado et al., 2005, Huang et al., 2008) polymer membranes (Bonchio et al., 2006). Several advantages are reported in literature on the use of immobilized systems. In particular, the immobilization of photocatalysts on macroscopic supports could lead to the development of structured catalysts with great stability and high recyclablity which allow to avoid the separation of catalyst powders from the liquid phase and, therefore to design the efficient and low-cost systems in order to easily recover the target product from reactive environment. For example, in a study on the photodegradation of 4-acetylphenol, Sobana et al., observed that catalysts based on zinc oxide immobilized on activated carbon showed a much more higher adsorption and photodegradation rate than bare ZnO due to a higher adsorption of the substrate on the activated carbon (Sobana et al., 2008). Moreover, Sacco et al. have tested the increse of phenol photocatalytic removal from water using N-doped TiO_2 powder dispersed in polymeric matrix, in comparison with a slurry system in which the N-doped TiO_2 particles were suspended in the aqueous solution under continuous stirring (Sacco et al., 2018a). Similarly, for the application of photocatalysis in the synthesis process, the researchers also focused their attention on composite photocatalysts to achieve an enhancement of the photocatalytic activity and obtain a higher production of the main product. For example, for the phenol synthesis, Zhang and Park

studied CuPd bimetallic alloy nanoparticle-coated holey carbon nitride materials (g-C_3N_4/CuPd) as photocatalyst (Zhang and Park, 2019); Wang et al. studied the benzene hydroxylation reaction over two different metal−organic framework (MOF)-based photocatalysts (Wang et al., 2015). Another studied material was a Zn_2Ti-layered double hydroxide (ZnTi-LDH) photocatalyst, which showed an enhancement of photoinduced charge carrier separation due to the presence of oxygen vacancies on the LDH surface and an increase in superoxide radicals which assure the realization of an advanced activity in terms of phenol production under UV-Vis light irradiation (Li et al., 2020a). Thus, the possibility to exploit the synergic effects obtained with particular support, to recover the catalyst without additional separation steps and to design continuous flow photoreactors, makes the immobilized systems interesting for industrial application. Nevertheless, the immobilized catalysts have several disadvantages such as:

- low light utilization efficiencies due to light scattering by immobilized photocatalyst. This aspect can be explained considering that heterogeneous catalysis is a surface phenomenon, therefore the overall kinetic parameters are dependent from the real exposed catalyst surface area. In the supported systems only a part of the photocatalyst is accessible to light and to substrate.
- restricted processing capacities due to possible mass transfer limitations;
- possible deactivation of immobilized catalyst surface since the support could enhance the recombination of photo generated electron/hole pairs and a limitation of oxygen diffusion in the deeper layers is observed.

On this basis, greater efforts are needed in photocatalytic engineering to overcome these drawbacks and to realize more efficient photocatalytic reactors. A promising idea to improve the photocatalytic activity in terms of productivity of the desired product and to facilitate its recovery and separation from the reactive environment, could be to devise a photoreactive polymer composite system in which to embedd the catalyst. This photocatalytic hybrid system represents the reactor itself which exploits the low affinity of catalyst hydrophobic polymeric support towards desired product (a hydrophilic compound) to favor desorption of this main product from the catalyst surface, preventing further oxidation reactions and increasing reaction yield and selectivity (Zhang et al., 2011a).

I.9 Polymeric structure for overcoming the limits of photocatalytic process

As discussed in the previuos section, suspended photocatalysts show some advantages, such as a higher surface area and a higher reaction kinetic, which lead to higher photocatalytic efficiency of contaminant removal
However, the separation and recovery of the photocatalyst may require expensive and time-consuming processes. Heterogeneous photocatalysis with the immobilization of the catalyst on different substrates or with the dispersion of catalyst in powder form into polymeric matrix eliminates the need for recovery and separation processes, thus minimizing the catalyst loss (Zakria et al., 2021, Singh et al., 2013, Bagheri et al., 2014).
Additionally, the support can offer a high dispersion of the nanoparticle catalyst and simplify electron transfer, both of which contribute to better catalytic activities. Therefore it seems essential to develop suitable supports for photocatalyst particles capable of overcome these limits. Among the various supports, polymeric materials are promising for the good features, such as flexible nature, low cost, chemical resistance, mechanical stability, low density, high durability and availability (Silva et al., 2022).
The use of some polymers as supports allows to preserve the photocatalytic properties of powder photocatalysts and to minimize the aggregation phenomena between the photocatalyst particles that typically occur when they are used in traditional suspension photocatalytic reactors (Sacco et al., 2018a). Furthermore, great attention of research was focused on organic synthesis for the formulation of catalytic systems able to realize the direct conversion of organic molecules to selectively obtain interest compounds (Mancuso et al., 2022b, Zhang et al., 2011a). However, as can be observed in literature, the use of photocatalytic powder in suspension does not allow to obtain adequate conversions with high selectivities of the main product which unfortunately is further converted to give secondary products (Su et al., 2014). The product selectivity is low since OH radicals, photogenerated by light source, are highly reactive and non-selective towards the main product which is further oxidized.
This result justify the necessity to select a suitable polymeric support in which the photocatalyst is dispersed in order to avoid further oxidation reactions of desired product and, therefore increasing its productivity (Mancuso et al., 2022b).

I.9.1 Cyclodextrins

Many studies on the photocatalytic properties of TiO_2 have been performed, frequently with the aim of improving the catalytic efficiency (Borgarello et al., 1986). In this regard, surface adsorption of cyclodextrin

(CD) to semiconductor colloids has been found to improve the kinetics for charge transfer from the photoexcited semiconductor to electron acceptors retained in the CD cavity (Dimitrijevic et al., 2004). In detail, TiO_2 modified with cyclodextrin has sparked renewed interest since Willner et al. observed that CD could stabilize TiO_2 colloids against aggregation and facilitate interfacial electron transfer processes (Willner and Eichen, 1987, Du et al., 2007). Different articles have reported the stimulating effect of cyclodextrin on the photocatalytic degradation of organic pollutants in TiO_2 suspensions (Anandan and Yoon, 2004, Zhang et al., 2011c, Zhang et al., 2010)
CD plays electron-donating and hole-capturing roles when attached to TiO_2 colloids, leading to restriction of charge hole recombination and improvement of photocatalytic efficiency. However, it is difficult the recover of cyclodextrin after the reaction and, moreover, the synthesis of CD-modified TiO_2 colloids is complicated and time-consuming; the colloids are stable only under acidic conditions (Zhang et al., 2010). Therefore, it is worth finding a new synthesis for the formulation of the hybrid system in TiO_2 powder grafted on CD to study its photocatalytic performance in the field of degradation of organic compounds contained in water and organic synthesis for the production of valuable compounds.

I.9.1.1 Definition and classification

CDs are non-reducing cyclic oligosaccharides composed of 6, 7 and 8 D-glucopyranose rings (glucose units) labelled α-, β- and γ-CD, respectively. CDs are produced from starch by cyclodextrin glycosyltransferase and shaped like truncated cones, with a hydrophobic inner cavity and a hydrophilic outer surface (Velusamy et al., 2014). The specific number of hydroxyl groups according to the number of glucose units makes it possible to establish strong interactions with other molecules and can form inclusion complexes with guest molecules (Serra-Gómez et al., 2012, Xin et al., 2012, Rajalakshmi et al., 2017).
Since they can generate non-covalent inclusion complexes with a great number of the organic contaminants in soil (petroleum hydrocarbons, polycyclic aromatic hydrocarbons, etc.) and microcontaminants occurring in water (pharmaceutical and cosmetic active agents, pesticides, etc.), are primarily used in the pharmaceutical, cosmetic and household chemical industry to reduce the environmental impact of the chemical pollutants. The CD derivatives, which are well soluble in water, such as hydroxypropyl and methylated CDs, can enhance desorption of the contaminants from the soil and are useful in soil remediation technologies (e.g., in situ/ex situ microbial degradation and chemical oxidation of contaminants in soil) (Villaverde and Morillo, 2011). CD-based absorbents in form of microspheres, nanosponges, microfibers, etc. able to remove micro-contaminants from purified wastewater can be obtained by immobilization of CDs either by crosslinking or by coupling to the surface of natural or synthetic polymers (Agócs et al.,

2016). As reported in literature (Wang et al., 2006, Kamiya et al., 1994) the photodegradation of bisphenol A was enhanced in aqueous solutions containing β-CD, while the photodecomposition of parathion and paraoxon which are pesticides with similar structure was inhibited or catalyzed respectively by β-CD. It is widely documented that TiO_2 and ZnO can only absorb a small fraction of sunlight (ultraviolet and near ultraviolet) due to their broad band gap (3.0–3.2 eV) and therefore, it is necessary to modify photocatalysts which can effectively be utilized the solar energy to a greater extent. In the same way, in literature the possible effect of coupling of CDs with TiO_2 was investigated. Therefore, it was demonstrated that the presence of CD caused a delay in the photocatalytic degradation of toluene (Lannoy et al., 2016) and showed a protective effect for ibuprofen degradation(Agócs et al., 2016) while, on the other hand the CD existence on TiO_2 surface (Attarchi et al., 2013) and on ZnO surface (Rajalakshmi et al., 2017) both evidenced a synergistic photocatalytic effect for photodecomposition of the methylene blue.

These results indicate that CD can catalyse or inhibit the photodecomposition of a compound depending on the position of the light-sensitive bonds of the included compound. Therefore, the complex that arises between polluting compound and CD can either protect the compound from the effect of light or speed up the decomposition (Glass et al., 2001, Sortino et al., 2001)

CD can be adsorbed on surface of TiO_2 nanoparticles to increase the stability of TiO_2 surface (Figure I.4). The adsorption of CD on TiO_2 surface leads to an enhancement of photocatalytic performance. CD plays electron-donating and hole-capturing roles when linked to nanoTiO_2 colloids inhibiting the charge–hole recombination phenomenon (Willner et al., 1994). The efficiency is further improved by keeping the ligands close to the surface of TiO_2 nanoparticles via inclusion complexation.

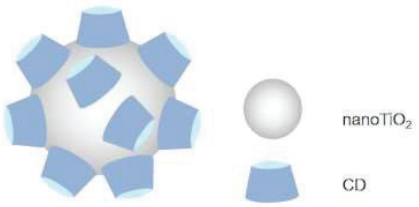

Figure I.5 *Adsorption of β-CD on the surface of nanoTiO_2(Agócs et al., 2016).*

I.9.2 Polymeric Aerogel

An important drawback of the photodegradation process is the post-treatment recovery of phototocatalyst nanoparticles from the treated water which is both time and money consuming. To overcome this limit together with the possible aggregation phenomena related to the catalyst in powder form, a large variety of possible inorganic and organic supports in particular polymeric ones, have been tried for embedding photocatalyst nanoparticles.
To obtain an easy recovery of photocatalytic nanoparticles, the supports must assure the permanent immobilization of nanoparticles on or within the support, good chemical and mechanical stability and no decrease of the photocatalyst efficiency. Different classes of materials such as activated carbon, zeolites, clays, and natural organic substances were used as supports/adsorbents (Park et al., 2019, Wang and Peng, 2010). However, despite their excellent adsorption performances, they bear some drawbacks including limited working capacity and/or selective removal of target molecules (Nevskaia et al., 2004). In recent years, polymeric aerogels have been developed as an alternative to common sorption substrates (Long et al., 2018, Guo et al., 2012, Deze et al., 2012, Salam et al., 2011).
Thermoplastic polymers are considered economic, recyclable, and easy-to-handle materials which can act very effectively in the absorption of organic molecules from aqueous solutions. In this perspective, monolithic aerogels based on thermoplastic polymers such as syndiotactic polystyrene (sPS) (Daniel et al., 2008) being hydrophobic in nature, are able to concentrate the non-polar organic molecules, making easy their recovery (Sacco et al., 2019) sPS aerogels have the perculiarity that, both the amorphous phase, which has disordered cavities typical of aerogels, and the crystalline phase, when it is one of the sPS porous forms, contribute to aerogel porosity. sPS aerogels, based on a porous crystalline form of this polymer (nanoporous sPS aerogels), allow to trap non-polar compounds both in the perfectly identical and ordered nanocavities of crystal lattice, and in those of random shape and randomly distributed of the amorphous phase (Daniel et al., 2013). Therefore, sPS aerogels seem to be promising materials to selectively recover some useful aromatic molecules from aqueous solutions or moreover, they can be also used in environmental remediation for the degradation of water pollutants. On the other hand, the polymeric photoreactive composites could allow a significant leap forward in the development of innovative green processes for the selective oxidation of aromatic hydrocarbons under mild conditions, assuring to production of valuable chemical raw materials. For this purpose, since the sPS aerogel has hydrophobic nature, it presents low affinity towards hydrophilic compounds (i.e phenol) and, therefore, favours its desorption from the catalyst surface and preventing thus further oxidation reactions in order to increase reaction yield and selectivity.

I.9.2.1 Definition and classification

A class of porous materials, which has received in the last decade attention by the scientific community, is constituted by semicrystalline thermoplastic polymers whose crystalline phase is nano porous (micro by IUPAC definition). The existence of nanoporous polymeric crystalline phases has been described so far only for two commercial polymers: syndiotactic polystyrene (sPS) and poly(2,6-dimethyl-1,4- phenylene)oxide (PPO) (Guerra et al., 2012). These nanoporous crystalline polymers are able to absorb low molecular mass molecules also when present in traces and have been proposed for applications in chemical separations and in air/water purification It has been shown that CO_2 extraction of sPS thermoreversible gels leads to a special class of monolithic physically crosslinked aerogels, where the crystallites that constitute the physical knots of the aerogel exhibit a nanoporous crystalline phase (Daniel et al., 2005). These nanoporous crystalline aerogels present, beside disordered amorphous meso and macropores (typical of all aerogels), also all identical nanopores of the crystalline phases. (Daniel et al., 2008, Daniel et al., 2009, Daniel et al., 2012)

The formation of crystalline nanopores after solvent extraction from PPO thermoreversible gels has been also observed but in this case the extraction method, lead to powders rather than to monolothic aerogels. This result is due to the formation of a spherulic morphology in PPO gels rather than a fibrillar morphology as observed in sPS gels. However it has been shown that monolithic PPO based aerogels with nanoporous crystalline phases can easily be obtained starting from mixed PPO/sPS gels thanks to fibrillar morphology ensured by sPS (Daniel et al., 2012, Daniel et al., 2009). The association of amorphous meso- and macropores and crystalline nanopores confers unique properties to this type of material, specially in the VOC sorption from aqueous diluted solutions or from air at low vapor pressures. In fact, these PPO/sPS aerogels showed a fast sorption kinetics typical for aerogels (due to the high porosity and the large pore size) and a high sorption capacity characteristic (due to the sorption of the organic molecules in the host nanopores of the crystalline phase). These sorption properties as well as their good handling characteristics makes these new materials particularly suitable as a sorption medium to remove traces of pollutants from water and air (Daniel and Guerra, 2015).

Regarding syndiotactic polystyrene (sPS), it presents a complex polymorphic behavior mainly based on different crystalline forms (named α, β, γ, δ and ε). The polymer chains adopt the all-trans planar zig-zag structure in the α- and β- form while s(2/1)2 helical trans-trans-gauche-gauche conformation is present in the γ- and δ- forms.

In addition to these crystalline forms, semicrystalline clathrate structures characterized by the helical chain conformation can be obtained by sorption of suitable compounds (mainly halogenated or aromatic) in amorphous sPS

samples as well as in sPS samples being in the α-, γ-, or δ form(Daniel and Guerra, 2005). Therefore, sPS is able to cocrystallize with several low-molecular-mass compounds leading to cocrystals (clathrate and intercalate), which by using suitable guests have been proposed as advanced optical materials. The δ-form can be obtained by complete guest removal from cocrystals, by suitable extraction procedures. The δ-form is characterized by the presence of two cavities per unit cell and is able to rapidly absorb volatile organic compounds (VOCs) (mainly halogenated or aromatic hydrocarbons) from water and air, also when present at very low concentrations. Two different modifications have been described for the δ-form: a monoclinic one characterized by two cavities per unit cell (Daniel et al., 2016) (Figure I.6A,A') and a triclinic one with only one bigger cavity per unit cell (Figure I.6B,B')(Daniel et al., 2018).
The volume of the isolated cavities of the nanoporous monoclinic δ-form is close to 0.12 (Milano et al., 2001), whereas the volume of the triclinic δ-form cavities is evaluated to be c.30% larger. The ε form is characterized by an orthorhombic unit cell where the empty space is present as channels rather than as isolated cavities (Figure I.6C,C') (Petraccone et al., 2008).

Therefore, these materials for their hydrophobic nature seem particularly suitable for applications in chemical separation, in water and moist air purification, and in sensors (Daniel et al., 2008).

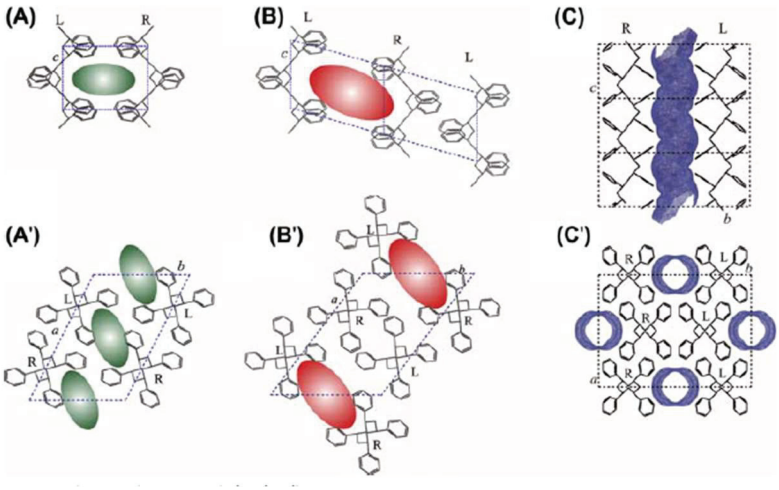

Figure I.6 *Lateral (A, B, C) and top (A', B', C') views of the structure of the syndiotactic polystyrene nanoporous crystalline forms: monoclinic δ(A, A'), triclinic δ(B, B'), and orthorhombic ε (C, C') (Daniel et al., 2020).*

I.9.2.2 Materials

sPS aerogels can form by thermoreversible gels using a large variety of solvents for polymer concentrations in the typical range 0.02 g/g-0.5 g/g. Solvent extraction from sPS gels can be achieved in supercritical conditions without the shrinkage of the gel and monolithic aerogels with apparent density in the range 0.004-0.5 g/cm^3 and apparent porosity as high as 99.5% to can be easily prepared (Figure I.7).

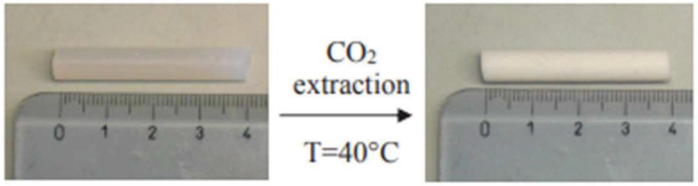

Figure I.7 *Illustration of sPS gel prepared in chloroform at C_{pol} = 0.10 g/g, before and after total solvent extraction with supercritical CO_2 at 40°C.*

For sPS gels having co-crystalline phases, the corresponding aerogels are formed by semicrystalline nanofibrils presenting the nanoporous crystalline δ-form (as schematically shown in Figure I.7) while disordered macropores are located between the fibers. It is worth adding that solvent extraction in supercritical conditions at temperature above 120°C leads to monolithic aerogels being characterized by the non-porous γ and β crystalline forms of sPS.

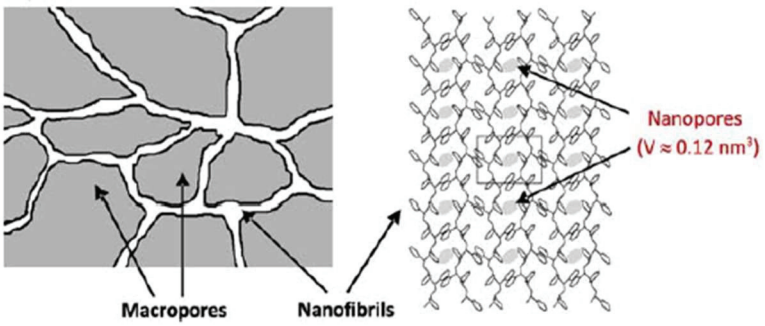

Figure I.8 *Schematic presentation of the texture (left) and the crystalline structure (right) of the sPS aerogel.*

If the size of the crystalline nanopores only depends on the crystalline form and thus is independent on both the gel polymer concentration and

the solvent type, it is possible to tune the meso- and macroporosity volume of the aerogels, by adjusting the polymer to solvent ratio used for gel preparation. For aerogels obtained from sPS/chloroform gels where the percentage of porosity P was calculated from the aerogel mass/volume ratio using the equation:

$$P = 100 * (1 - \frac{\rho_{app}}{\rho_{pol}}) \quad (26)$$

where ρ_{app} is the aerogel apparent density determined from the mass/volume ratio of the monolithic aerogels and ρ_{pol} is the density of the polymer matrix (e.g., equal to 1.02 g cm^{-3}, for δ-form sPS samples with a crystallinity of nearly 40% (Daniel et al., 2008).

I.7.2.3 Transport through aerogel

The fluid flow through aerogel can be viscous, diffusional or a combination of viscous and diffusional flows. Knudsen number (Kn) determines the flow regime. It is defined by the following equation:

$$Kn = \lambda / d_p \quad (27)$$

λ is the mean free path of gases and d_p is the mean size of the pores. The mean free path of gases should be determined for characterizing the fluid flows in a monolithic aerogel.

If Kn << 1, the fluid flow is purely viscous. The viscous flow is driven by the pressure gradient and the viscosity of the fluid as per Darcy's law, as in equation (14).

$$j = - k \mu \nabla P \quad (28)$$

In equation (14), j is the flux with unit m/s, k is permeability, μ is viscosity and P is pressure. If Kn≈1, the fluid flow becomes the combination of viscous and diffusional flows.

If Kn >> 1, the fluid flow is diffusional. Diffusional flow is driven by concentration gradient as Fick's law describes, as in equation (15).

$$j_D = -D \nabla \psi \quad (29)$$

Where, j_D is the diffusion flux (mol/m^2 s), D is diffusivity (cm^2 /s) and ψ is the concentration (mol/m^3) (Gui et al., 2020).

I.10 Future perspectives for polymeric aerogels application

Aerogels are an exceptional class of materials that are of interest for several high performance applications thanks to their extraordinary physical properties such as very high porosity, high specificity, extremely low surface and density combined with very versatile synthesis approaches. Various aerogels have been explored for catalytic and photocatalytic applications, even if in the last decades numerous discoveries have been made on different aspects ranging from the most efficient catalysis in organic synthesis, to energy-related processes and environmental catalytic remediation using airgel. For both catalytic and photocatalytic performance, aerogel monoliths prepared with sol-gel approaches accompanied by an appropriate drying technique, in particular supercritical point drying, have become surprising alternative catalysts or catalytic supports with respect to those currently used prepared with traditional wet synthesis approaches. In the light of growing concerns regarding the ever-rising air pollution and subsequent global warming, different catalysts were explored to convert the various hazardous atmospheric organic and inorganic pollutants into less harmful compounds. In this respect, the contribution of monolithic aerogel from different molecular resources has been notable to protect and improve the environment from various hazardous pollutants. Nowadays, aerogels are mainly studied in environmental remediation processes as a heterogeneous catalyst and photocatalyst for air and water cleaning applications (Cheng and Bi, 2014, Guan et al., 2014, Sacco et al., 2018a) but, recently they are also used in other application fields, such as organic synthesis to selectively produce valuable organic compounds (Pekala, 1989, Mancuso et al., 2022b). A drastic enhancement in catalytic activity, selectivity, and stability can be due to the combination of aerogels exclusive physical properties, like high specific surface areas accessible to reactant molecules, high dispersion of active species, and to the high and uniform dispersion of photocatalytic active phases into aerogel, preventing aggregation phenomenon of nanoparticles to assure therefore a better photocatalytic performance. Although aerogel catalysts are widely used in environmental cleaning applications, this promoting class of materials has also shown fruitful performances in steam reforming processes for producing hydrogen as a clean energy source for onboard, on-demand applications as well as chemical product synthesis. However, despite the fact that the catalytic applications of aerogels are potentially numerous and huge in impact, they are not currently commercially available due to the rather expensive processing as well as the presence of inconvienents like low thermal resistance and delicate mechanical strength. In order to pave the way for large-scale productions and applications, today, these issues are being mitigated to some extent by using, for example, cheap inorganic salts instead

of their expensive alkoxide or using sustainable and safe sources as precursors.
Particular emphasis is given to the nanoporous-crystalline aerogels where two kinds of interconnected cavities (disordered spaces between crystallites and all identical spatially ordered crystalline cavities in the crystallites) are present. For the morphology of these materials, applications in many different fields are expected, like for instance:

- stationary phases in chromatography;
- hosting of catalysts between fibrils, with the nanoporous crystalline cavities acting as reservoir of reactants or products;
- sensing elements of gravimetric sensors where the aerogel structure is expected to improve the kinetic of response;
- dielectric materials (as for other aerogels) (Pierre and Pajonk, 2002) which could benefit of the advantage of including highly polar low-molecular-mass molecules in the crystalline cavity, (Daniel et al., 2007, Daniel et al., 2011) thus allowing to control the dielectric constant;
- hosting of biomolecules between fibrils and profiting of the nanoporous-crystalline cavities or encapsulating bioactive low-molecular-mass molecules for the controlled release of active principles or for the release of growth factors in biomedical applications (tissue engineering) (Daniel et al., 2013).

I.11 Aim of the Ph.D thesis

This Ph.D project is aimed to formulate innovative visible light active photocatalysts to be used both for degradation of water pollutants and for the selective photo-oxidation of benzene to phenol. The experimental activity was focused on:

- Preparation and characterization of codoped photocatalysts active under visible light and their coupling with β-cyclodextrins;
- Photocatalytic tests using organic dyes and pesticides under visible and solar light in order to identify an optimal formulation;
- Direct selective oxidation of benzene to phenol on optimized photocatalysts in powder form;
- Direct selective oxidation of benzene to phenol using visible active photocatalysts in powder form embedded in monolithic polymeric aerogels;
- Formulation of transition metal oxides (V_2O_5, Fe_2O_3 and CuO) supported on visible active photocatalyst and their dispersion in polymeric aerogels to enhance both the benzene consumption rate and phenol production rate, maximizing, simultaneously, the selectivity and yield to the desired product under visible light;

- Selective photocatalytic oxidation of benzene to phenol using metal oxides supported on visible active photocatalyst embedded in sPS: optimizing of operating conditions (photocatalyst dosage, pH of solution);

II. Experimental results: photocatalytic degradation of water pollutants under visible light

II.1 Photocatalysts preparation

II.1.1 Preparation of codoped TiO_2 photocatalysts

N-doped TiO_2 photocatalysts with different nitrogen content were synthetized through sol-gel method using urea as nitrogen precursor and titanium tetraisopropoxide as TiO_2 precursor. In the same way, praseodymium-doped TiO_2 (Pr-TiO_2) photocatalyst was synthetized using praseodymium nitrate hexahydrate as praseodymium precursor and titanium tetraisopropoxide as TiO_2 precursor. Fe-doped TiO_2 (Fe-TiO_2) photocatalyst was prepared by reaction between titanium tetraisopropoxide and an aqueous solution containing iron(II) acetylacetonate. In order to prepare photocatalysts doped with Fe and N, distilled water containing a certain amount of urea were mixed with a solution of titanium tetraisopropoxide and iron(II) acetylacetonate. Fe-Pr codoped TiO_2 at different Pr content, was prepared employing distilled water containing a defined amount of praseodymium nitrate that was mixed with a solution of titanium tetraisopropoxide and iron acetylacetonate.The system was maintained at room temperature under continuous stirring for 10 minutes. The obtained suspension was centrifuged for the separation of a precipitates, which were was washed with distilled water three times and finally placed in a furnace at 450 °C for 30 minutes in static air. The obtained samples were named (N-TiO_2_x or Fe-N-TiO_2_x) where x indicates the amount of urea (in grams) used for synthesis. Pr doped photocatalysts were called Pr(x)-TiO_2 or Fe-

Pr(x)-TiO_2, where x, in this case, indicates the amount of praseodymium nitrate hexahydrate (in milligrams) used in the preparation of the samples. The Fe/Ti molar ratio used for the preparation of Fe-TiO_2 was equal to 0.0017 and corresponds to an optimized catalyst formulation as reported in a previous work (Zuorro et al., 2019) Table II.1 reports the solution volume, the amount of N and Fe precursor, the amount of Pr and Fe precursor used for the photocatalysts synthesis with together N/Ti, Fe/Ti and Pr/Ti molar ratio for all the prepared photocatalysts using 12.5 mL of TTIP.

Table II.1 *List of prepared photocatalyst, amount of chemicals used in the synthesis, Fe/Ti, N/Ti and Pr/Ti molar ratio.*

Catalyst	Urea (g)	Distilled water (mL)	Iron acetylacetonate (mg)	Praseodymium nitrate (mg)	Fe/Ti	N/Ti	Pr/Ti
TiO_2	0	50	0	0	0	0	0
N-TiO_2_0.3	0.3	50	0	0	0	0.24	0
N-TiO_2_0.6	0.6	50	0	0	0	0.48	0
N-TiO_2_1.2	1.2	50	0	0	0	0.97	0
N-TiO_2_2.4	2.4	50	0	0	0	1.94	0
Fe-TiO_2	0	50	25	0	0.0017	0	0
Fe-N-TiO_2_1.2	1.2	50	25	0	0.0017	0.97	0
Pr(8.5)-TiO_2	0	50	0	8.5	0	0	0.0069
Fe-Pr(4)-TiO_2	0	50	25	4	0.0017	0	0.0032
Fe-Pr(8.5)-TiO_2	0	50	25	8.5	0.0017	0	0.0069
Fe-Pr(12.5)-TiO_2	0	50	25	12.5	0.0017	0	0.0101
Fe-Pr(17)-TiO_2	0	50	25	17	0.0017	0	0.0137

II.1.2 Preparation of tri-doped TiO_2 photocatalysts

Fe-N-x and y-N-S/TiO_2 (where x is S, Pr or P and y is P or Pr) tri-doped photocatalysts were synthetized through sol-gel method. Fe-N-x photocatalysts were prepared starting from 50 ml of distilled water containing 1.2 g of urea and 17 ml of phosphoric acid or 0.025 g of sodium sulfate or 0.0085 g of praseodymium nitrate hexahydrate. Then the obtained solution was mixed with a solution obtained dissolving 0.025 g of iron(II)

acetylacetonate in 12.5 ml of titanium tetraisopropoxide The obtained photocatalysts were called Fe-N-P/TiO_2 or Fe-N-S/TiO_2 or Fe-N-Pr/TiO_2. y-N-S/TiO_2 photocatalysts were prepared starting from a 50 ml of distilled water and 1.2 g of urea and 17 ml of phosphoric acid or with 0.025 g of sodium sulfate or 0.0085 g of praseodymium nitrate hexahydrate. The obtained aqueous solution was finally added into 12.5 ml of titanium tetraisopropoxide. The prepared photocatalysts were named P-N-S/TiO_2 or P-N-Pr/TiO_2. The obtained suspensions were centrifuged for the separation of precipitates and were washed with distilled water three times. Finally the precipitates were placed in a furnace at 450 °C for 30 minutes in static air. Table II.2 summarized the solution volume, the amount of metal or non-metal precursors used for the synthesis with together molar ratio values for all the prepared photocatalysts.

Table II.2 *List of all prepared photocatalysts, amount of urea, iron acetylacetonate (F), phosphoric acid (Pac), sodium sulfate (Ss) and praseodymium nitrate hexahydrate (PrN) used for the synthesis and N/Ti, Fe/Ti , P/Ti, S/Ti and Pr/Ti molar ratio.*

Sample	Urea (g)	F (mg)	Pac (µl)	Ss (mg)	PrN (µl)	N/Ti	Fe/Ti	P/Ti	S/Ti	Pr/Ti
TiO_2	0	0	0	0	0	0	0	0	0	0
Fe-N-P/TiO_2	1.2	25	17	0	0	0.97	0.0017	0.01	0	0
Fe-N-S/TiO_2	1.2	25	0	25	0	0.97	0.0017	0	0.005	0
Fe-N-Pr/TiO_2	1.2	0	0	0	8.5	0.97	0.0017	0	0	0.0069
P-N-S/TiO_2	1.2	0	17	25	0	0.97	0	0.01	0.005	0
Pr-N-S/TiO_2	1.2	0	17	0	8.5	0.97	0	0.01	0	0.0069

II.2 Characterization techniques of prepared photocatalysts

Different characterization techniques were used to examine the physical and chemical properties of all prepared materials:

- Wide-angle-X-ray diffraction (WAXD)
- UV-vis reflectance spectra (UV-vis);
- Micro Raman spectroscopy;
- Fourier Transform Infrared (FTIR) spectroscopy;
- N_2 adsorption at -196 °C to obtain specific surface area and porosity characteristics
- Point of zero charge (ZPC).

II.2.1 Wide Angle X-ray Diffraction (WAXD) powder diffraction

To date, most of our knowledge about the spatial arrangements of atoms in materials has been gained from diffraction experiments. In a diffraction experiment, an incident wave is directed into a material and a detector is typically moved about to record the directions and intensities of the outgoing diffracted waves "Coherent scattering" preserves the precision of wave periodicity. Constructive or destructive interference then occurs along different directions as scattered waves are emitted by atoms of different types and positions. There is a profound geometrical relationship between the directions of waves that interfere constructively, which comprise the "diffraction pattern," and the crystal structure of the material. The diffraction pattern is a spectrum of real space periodicities in a material. Atomic periodicities with long repeat distances cause diffraction at small angles, while short repeat distances (as from small interplanar spacings) cause diffraction at high angles.

It is not hard to appreciate that diffraction experiments are useful for determining the crystal structures of materials. Crystals with precise periodicities over long distances have sharp and clear diffraction peaks. Crystals with defects (such as impurities, dislocations, planar faults, internal strains, or small precipitates) are less precisely periodic in their atomic arrangements, but they still have distinct diffraction peaks. Their diffraction peaks are broadened, distorted, and weakened, however, and "diffraction lineshape analysis" is an important method for studying crystal defects. In a diffraction experiment, the incident waves must have wavelengths comparable to the spacings between atoms.

Wide-angle X-ray diffraction (WAXD) patterns were performed with an automatic Bruker D8 Advance diffractometer (VANTEC-1 detector) using reflection geometry and nickel filtered Cu-Kα radiation

II.2.2 UV-vis Diffuse Reflectance Spectroscopy

Diffuse Reflectance Spectroscopy is based on the interaction between a UV or visible beam and a powdered sample, from which the beam can be reflected in all directions.

Only the fraction of beam which is scattered within a sample and returned to the surface is considered to be a diffuse reflection. All the reflected radiation can thus be collected within an integrating sphere, enhancing the signal-to noise ratio.

The internal walls of the sphere are usually covered with barium sulfide, a compound that ensures a reflectivity greater than 0.98 in the UV-vis light region. Moreover the reflectance spectrum of a reference standard ($BaSO_4$) should always be recorded prior to that of any other sample. A Perkin Elmer

spectrometer Lambda 35 spectrophotometer (Waltham, MA, USA) sing the ultraviolet-visible diffuse reflectance spectra (UV-Vis DRS) of the samples were recorded with an RSA-PE-20 reflectance spectroscopy accessory (Labsphere Inc., North Sutton, NH, USA). The reflectance data were reported as the $F(R_\infty)$ values, from Kubelka-Munk theory, vs wavelength. The band gap values were determined through the corresponding Kubelka-Munk function (KM) and by plotting $[F(R_\infty)\cdot h\upsilon]^{0.5}$ against $h\upsilon$(eV) since TiO_2 in the anatase phase is typically considered as an indirect band gap semiconductor.

II.2.3 Surface area and pore structure evaluation

The Brunauer, Emmett, and Teller (BET) surface area of the samples was evaluated from dynamic N_2 adsorption measurement at low-temperature (-196 °C) using a Costech Sorptometer 1042 (Costech International S.p.A., Milan, Italy). The measurement was performed by continuous-flow method after sample pre-treatment at 150 °C for 30 min in He flow, in order to measure total specific surface area (via single and multi-point methods) and micropore volume (via micropore method).

II.2.4 Point of zero charge (PZC)

Mass titration method was used to estimate the acidity of sample powders. The PZC, which describes the acidity of oxide materials, may be measured using potentiometric titration, mass titration, or measurement of the wetting angles. The mass titration method of PZC characterization was initially proposed by Noh and Schwarz (Noh and Schwarz, 1989). In this work, the mass titration studies were performed using procedures described elsewhere (Noh and Schwarz, 1989). Shorter stabilization times after each powder addition (2 hours in this study) were used to minimize possible dissolution of sample powders.

II.2.5 Raman spectroscopy

Raman spectroscopy is a technique for the identification and quantification of the chemical components of specimens.
When light is scattered by any form of matter, the energies of the majority of the photons are unchanged by the process, which is elastic or *Rayleigh* scattering. However, about one in one million photons or less, lose or gain energy that corresponds to the vibrational frequencies of the scattering

molecules. This can be observed as additional peaks in the scattered light spectrum. The process is known as *Raman* scattering and the spectral peaks with lower and higher energy than the incident light are known as *Stokes* and *anti-Stokes* peaks respectively. Raman spectroscopy uses a single frequency of radiation to irradiate the sample and it is the radiation scattered from the molecule, one vibrational unit of energy different from the incident beam, which is detected. Thus, unlike infrared absorption, Raman scattering does not require matching of the incident radiation to the energy difference between the ground and excited states. In Raman scattering, the light interacts with the molecule and distorts (polarizes) the cloud of electrons round the nuclei to form a short-lived called a 'virtual state'.
Laser Raman spectra were obtained at room temperature with a Dispersive MicroRaman (Invia, Renishaw, Wotton-under-Edge, United Kingdom), equipped with 514 nm laser, in the range of 100–900 cm^{-1} Raman shift.

II.2.6 Fourier Transform Infrared (FT-IR) spectroscopy

Infrared spectroscopy is certainly one of the most important analytical techniques available to today's scientists. This technique is based on the analysis of the absorption or of laser light by specific chemical bonds. Fourier transform infrared (FT-IR) spectra were obtained via M2000 FT-IR (MIDAC Co, Costa Mesa, CA, USA) at a resolution of 0.5 cm^{-1}. The scan wavenumber range was 4000–1000 cm^{-1}, and 16 scan signals were averaged to reduce the noise. All samples were well mixed with potassium bromide (KBr), which was used as the infrared transparent matrix. The discs, containing about 1 mg of sample and 100 mg of KBr, were prepared by compressing the powders through a hydraulic press.

II.3 Photocatalytic activity test: codoped TiO_2 photocatalysts

Photocatalytic tests are performed in a cylindrical pyrex photoreactor (ID = 2.6 cm, L_{TOT} = 41 cm and V_{TOT} = 200 mL). Visible-LEDs strip (nominal power: 10 W; provided by LED lighting hut; emission in the range 400-800 nm; light intensity: 13 mW/cm^2) is positioned in contact to the external surface of the photoreactor. The configuration of the reactor and the position of the LEDs strip have been designed and arranged in such a way as to guarantee a uniform distribution of the photons inside the reactor body. The total volume of solution was 100 mL with 10 mg/L AO7 initial concentration (pH=5.95). The photocatalyst dosage was equal to 3 g/L. The suspension was left in dark conditions for 60 minutes to achieve the adsorption/desorption equilibrium of AO7 dye on the photocatalyst surface.

After the dark phase, the LEDs were switched on and the photocatalytic test started. During the light irradiation, the reaction suspension was continuously mixed using a magnetic stirrer to avoid the sedimentation of the catalyst at the bottom of the photoreactor (Figure II.2). An air distributor device (Q_{air}=150 cm^3/min (STP)) was also used to assure the presence of oxygen in the reaction medium and therefore to favor the oxidation reactions of the organic compound.
At regular time intervals, about 3 mL of the suspension was withdrawn from the photoreactor and centrifuged to remove the catalyst particle. The aqueous solution was then analyzed by UV-Vis spectrophotometer (Thermo Scientific Evolution 201) to monitor the reaction progress. In details, the color removal of the chosen dye was monitored by measuring the maximum absorbance value at 485 nm (Rodríguez et al., 2019). The mineralization of the target pollutant was assessed by the measure of the total organic carbon (TOC) content of the solutions during the irradiation time. The TOC of solution was measured from CO_2 obtained by the high temperature (680 °C) catalytic combustion (Franco et al., 2019)The discoloration efficiency and mineralization (by TOC removal) were evaluated using the following relationships:

$$\text{Discoloration efficiency} = \left(1 - \frac{C}{C_0}\right) \cdot 100 \tag{30}$$

$$\text{TOC removal (mineralization)} = \left(1 - \frac{TOC}{TOC_0}\right) \cdot 100 \tag{31}$$

Where:
C=pollutant concentration at the generic irradiation time (mg/L);
C_0=initial AO7 concentration (mg/L);
TOC=total organic carbon at the generic irradiation time (mg/L);
TOC_0=initial total organic carbon (mg/L).

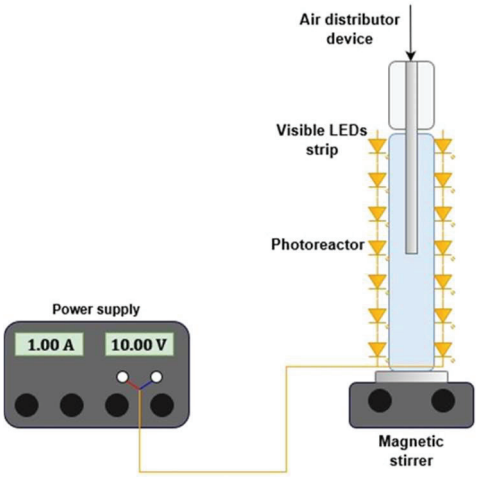

Figure II.1 *Experimental apparatus for photocatalytic tests.*

II.4 Photocatalytic activity tests: tri-doped TiO_2 photocatalysts

Photocatalytic tests were carried out using a volume of 75 mL of thiachloprid (THI) aqueous solution (initial concentration: 0.5 mg/L) and 300 mg of catalyst. The batch photoreactor used for the all the tests was a pyrex cylinder. The suspension was continuously mixed using an external recirculation system assured by a peristaltic pump. The reactor was irradiated by an UV-A (emission: 365 nm; irradiance 13 W/m^2) and visible (emission range: 400–800 nm; irradiance: 16 W/m^2) LEDs strip wrapped around and in contact with external surface of the reactor body. Moreover, additional tests were carried out under the direct solar light (latitude 40°N, longitude 14°E), the average solar UV-A irradiance for all the tests was about 2.2 W/m^2. The total exposure time for each experiment was 180 min. Experiments under the direct solar light were performed on May and typically started at 10.00–11.00 am till 01.00 - 02.00 pm. Sunlight irradiance spectra were measured by radiometer BLACK-Comet Stellar Net UV-VIS (StellarNet, Florida, 130 USA). During each test, the system was left in the dark for 60 min to reach the adsorption equilibrium of THI on the photocatalysts surface and then irradiated for 180 min. At different times, about 1.5 mL of the suspension was withdrawn from the photoreactor and filtered to remove the catalyst particles. The aqueous solution was then

analyzed by HPLC UltiMate 3000 Thermo Scientific system (equipped with DAD detector, quaternary pump, column thermostat and automatic sample injector with 100μL loop) and using a reversed-phase Luna 5u C18 column (150mm×4.6mm i.d., pore size 5μm) (Phenomenex) at 25 °C. The mobile phase consisted of an acetonitrile/water mixture (70/30 v/v). The flow rate, injection volume and detection wavelength were 1 mL/min, 40 μL and 242 nm, respectively.

II.5 Experimental results

II.5.1 Characterization results of codoped TiO_2 photocatalysts

Table II.3 reports the specific surface area (S_{BET}) of all samples evaluated by BET method. The undoped titania sample showed the lowest value of 107 m^2/g. All doped titania samples presented values of specific surface area higher than those of the undoped titania. Moreover, it seems that the S_{BET} values are not influenced by urea amount used as precursor for the preparation of N-TiO_2_x samples. On the other hand, the specific surface area of Fe-N codoped TiO_2 sample was found to be 117 m^2/g, very similar to the value observed for the N-doped TiO_2 sample prepared with the same amount of urea (N-TiO_2_1.2). Instead, regarding Pr doped TiO_2 samples it appears that the amount Pr precursor used for the synthesis of Fe-Pr(x)-TiO_2 samples did not significantly affect the S_{BET} results. However, the specific surface area of Fe-Pr(8.5)-TiO_2 was found to be 120 m^2/g, which is a value higher than that one observed for Pr(8.5)-TiO_2, Fe-Pr(4)-TiO_2 and Fe-Pr(17)-TiO_2, but slightly lower than Fe-TiO_2 and Fe-Pr(12.5)-TiO_2. The reflectance spectra of TiO_2 and N-TiO_2_x samples are reported in Figure II.2

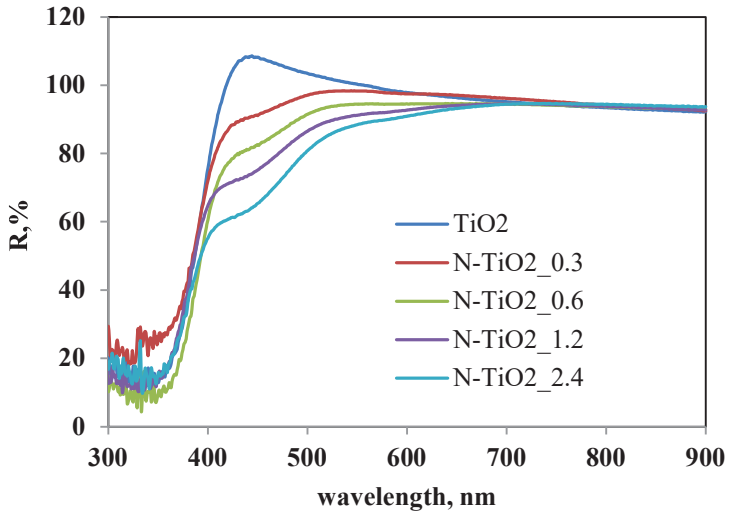

Figure II.2 *Reflectance spectra vs wavelength for TiO_2 and N-TiO_2_x samples.*

As expected, the main absorption edge of undoped titania lies in the range 390-400 nm (UV region). On the other hand, a marked shift toward the visible region for N-TiO_2_x samples was achieved since the presence of a weak shoulder in the range 400-500 nm was observed and its intensity progressively enhanced with the increase of the urea content used for samples synthesis (Shao et al., 2008, Chainarong et al., 2011). Possibly, this result indicates that the doping with N led to new electron state above VB, shifting the absorption edge towards the visible light region, as already reported in literature (Chainarong et al., 2011, Cheng et al., 2012b) Figure II.3 displays the optical properties of undoped TiO_2, N-TiO_2_1.2, Fe-TiO_2 and Fe-N-TiO_2_1.2 photocatalysts.

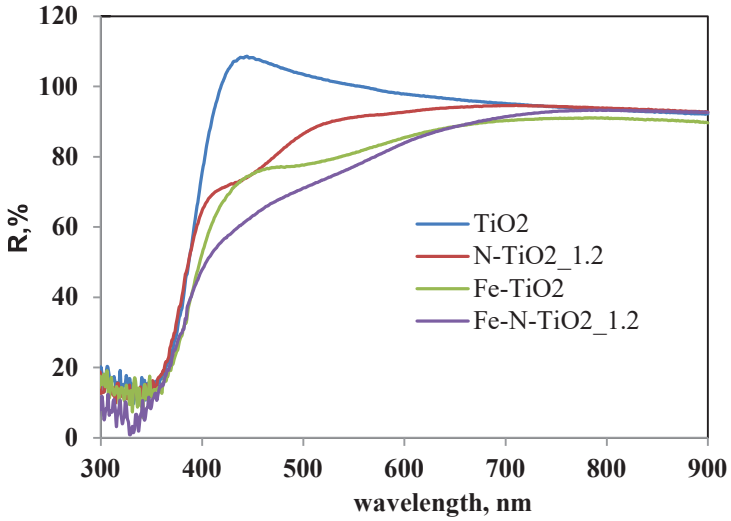

Figure II.3 *Reflectance spectra vs wavelenght for TiO_2, N-TiO_2_1.2, Fe-TiO_2 and Fe-N-TiO_2_1.2 samples*.

The reflectance spectra indicate that the doping of Fe into TiO_2 lattice shifts its optical absorption edge from UV into visible range (i.e. red shift) (Wu and Chen, 2004). This red shift is due to the charge transfer transitions between the metal ion d electrons and the CB of TiO_2 (Ganesh et al., 2012, Ali et al., 2017a). It is worthwhile to note that Fe-N-TiO_2_1.2 sample gives rise visible-light absorptions contributions higher than those of undoped TiO_2, N-TiO_2_1.2 and Fe-TiO_2 photocatalysts, similarly to the results reported in a previous paper (Yen et al., 2011). Additionally, the Fe-N-TiO_2_1.2 showed a noticeable absorbance at less than 500 nm and a marked increase of absorption properties in the range 400-500 nm compared to N-TiO_2_1.2 or Fe-TiO_2 (Yen et al., 2011).
UV-Vis DRS spectra of TiO_2, Fe-TiO_2, Pr(8.5)-TiO_2 and Fe-Pr(x)-TiO_2 samples in the range of 300 – 800 nm are shown in Figure II.4

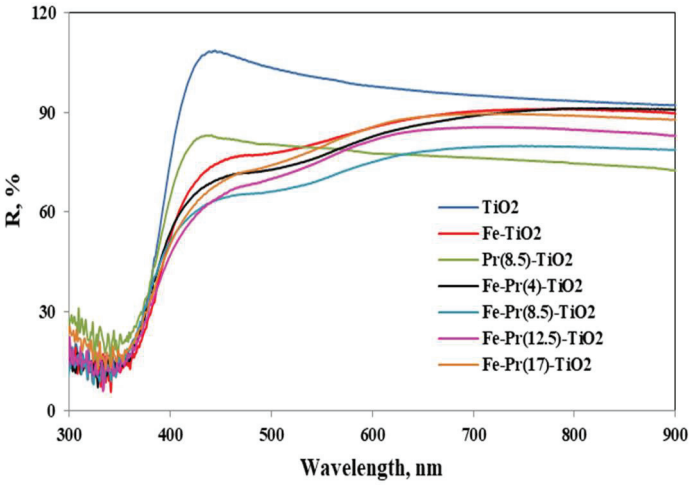

Figure II.4 *Reflectance spectra as function of wavelength for TiO_2, Fe-TiO_2, Pr(8.5)-TiO_2, Fe-Pr(4)-TiO_2, Fe-Pr(8.5)-TiO_2, Fe-Pr(12.5)-TiO_2 and Fe-Pr(17)-TiO_2 samples.*

Considering that the minimum of reflectance corresponds almost to the absorption maximum,the main absorption of the undoped TiO_2 is located in the range 390-400 nm (UV region) and no absorption is detected above 400 nm. Indeed, a slightly absorption in the visible region is observed for Pr(8.5)-TiO_2 while a more marked absorption in the range 450- 600 nm is observed for all Fe-Pr(x)-TiO_2 samples and for Fe-TiO_2.

In detail, the Fe-Pr(8.5)-TiO_2 photocatalyst showed light absorption performances in visible region higher than TiO_2 and Pr-(8.5)-TiO_2 photocatalysts and an increase of optical absorption properties in the range 450–600 nm compared to Fe-TiO_2 (Yen et al., 2011) Fe-Pr(4)-TiO_2, Fe-Pr(12.5)-TiO_2 or Fe-Pr(17)-TiO_2 photocatalysts (Figure II.4).

As reported in literature, the doping of TiO_2 with praseodymium significantly influences the optical properties of the photocatalyst. (Spadavecchia et al., 2012) The presence of Pr for the Pr(8.5)-TiO_2 sample generated a slight red shift of the absorption band edge, probably determined by the introduction of Pr^{3+} ions at the first excited state which could interact with the electrons of the TiO_2 conduction band, allowing a higher energy transfer from TiO_2 to Pr^{3+} ions (Song et al., 2015, Reszczyńska et al., 2016). The introduction of Fe^{3+} into TiO_2 lattice leads to a shift of the absorption edge in the visible light region possibly due to the charge transfer between the d level of Fe^{3+} ion and the conduction band of TiO_2 (Ibram et al., 2013, Ali et al., 2017b). On the other hand, as pointed above, Fe-Pr codoped TiO_2

photocatalysts showed a more marked absorption into visible region. The presence of some weak shoulders in the range 450-600 nm may be ascribed to the metal d electron transitions related to the substitution of Ti^{4+} by Fe^{3+} incorporated into the TiO_2 lattice and the electron transfer between Pr^{3+} and TiO_2 linked to the introduction of an internal electronic level (4f), as already reported in the literature (Spadavecchia et al., 2012, Parnicka et al., 2018).
The presence of these impurities in the semiconductor lattice reduces the energy required for the electron transition and causes a red shift of the optical absorption edge. Additionally, Fe^{3+} and Pr^{3+} ions inserted into TiO_2 structure produced some surface defect sites, which act as electron traps, allowing a more effectively separation of electron-hole pairs (Li et al., 2020b). Band gap values (E_{bg}) were obtained by UV-Vis DRS measurements are included in Table II.3.

Table II.3 *Crystallite size, lattice parameter, specific surface area (S_{BET}), band gap (E_{bg}) and zero point charge (ZPC) of all prepared samples.*

Catalyst	Cristallite size (nm)	Lattice parameter (Å)		S_{BET}	E_{bg}	ZPC
		a=b	*c*	(m^2/g)	(eV)	(pH unit)
TiO_2	9	3.74	8.68	107	3.20	6.02
N-TiO_2_0.3	6	3.79	9.20	139	3.00	5.14
N-TiO_2_0.6	7	3.78	9.33	112	3.00	5.10
N-TiO_2_1.2	7	3.77	8.81	115	2.90	5.12
N-TiO_2_2.4	6	3.78	9.06	126	2.90	5.14
Fe-TiO_2	6	3.77	9.21	122	2.80	5.15
Fe-N-TiO_2_1.2	7	3.75	8.58	117	2.70	5.02

According to the E_{bg} values and the trend of the reflectance curves, undoped TiO_2 revealed to be active only under UV irradiation.
E_{bg} value was 3.2 eV for undoped titania and 2.9-3 eV for N-TiO_2_x samples. This change in E_{bg} values can be attributed to the presence of nitrogen in the TiO_2 lattice (Cheng et al., 2012b). Moreover, from the E_{bg} values and the trend of the reflectance curves, undoped TiO_2 is expected to be active under UV irradiation, while Fe-TiO_2 under visible light. E_{bg} was about 2.8 eV for Fe-TiO_2 sample while it was possible to obtain a further decrease in E_{bg} up to the value of 2.7 eV with Fe-N-TiO_2_1.2 photocatalyst. The narrow band gap of Fe-N-TiO_2_1.2 may be therefore an indication of the possible enhancement of the photocatalytic activity in the visible light region with respect to both Fe-TiO_2 and N-TiO_2_1.2 samples (Cong et al., 2007).

E_{bg} value of Pr(8.5)-TiO_2 sample was equal to 3.0 eV while it was 3.2 for undoped TiO_2. This variation in E_{bg} value can be associated to the defect states due to presence of the oxygen vacancies obtained by Pr^{3+} substitution with Ti^{4+} (Spadavecchia et al., 2012, Nithyaa and Jaya, 2018, Li et al., 2020b). A further decrease in E_{bg} from about 2.85 to 2.7 eV for all Fe-Pr(x)-TiO_2 samples was obtained. The narrow band gap values of Fe-Pr(x)-TiO_2, probably related to the greater presence of oxygen vacancies deriving from the introduction of Fe and Pr metals into crystal structure of TiO_2 (Li et al., 2015), could be a possible indication of the enhanced photocatalytic activity in the visible light region with respect to both Fe-TiO_2 and Pr(8.5)-TiO_2 samples. It is worthwhile to note that the lowest E_{bg} value of about 2.7 eV, the same value obtained for Fe-N-TiO_2_1.2, it was also reached with Fe-Pr(8.5)-TiO_2 photocatalyst confirming that the optimal amount of praseodymium nitrate as precursor was 8.5 mg.
Figure II.5 reports the WAXD patterns of TiO_2, N-TiO_2_x, Fe-TiO_2 and Fe-N-TiO_2_1.2 samples.

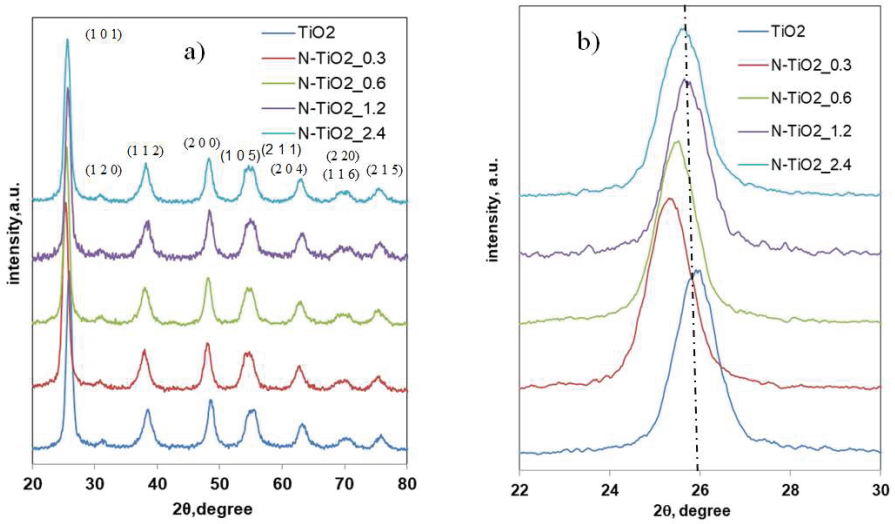

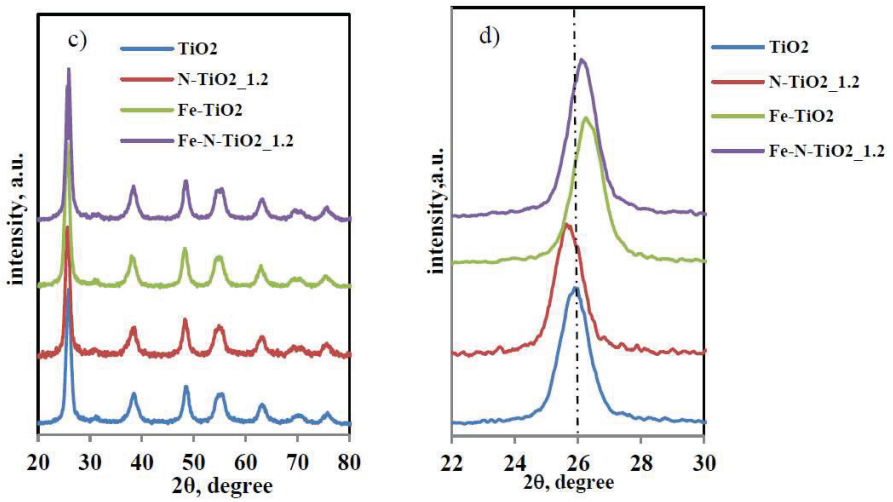

Figure II.5 *WAXD patterns for TiO_2 and N-TiO_2_0.3, N-TiO_2_0.6, N-TiO_2_1.2 and N-TiO_2_2.4 samples in the range 2Θ=20-80° (a) and in the range 2Θ = 22-30° (b). WAXD patterns for TiO_2 and N-TiO_2_1.2, Fe-TiO_2 and Fe-N-TiO_2_1.2 samples in the range 2Θ =20-80° (c) and in the range 2Θ =22-30° (d).*

In particular, the sharp peaks of anatase phase at 2θ = 25.91° (1 0 1) and 2θ=48.62° (2 0 0) for undoped titania are evident (JCPDS Card No. 21-1272). Similarly the WAXD patterns all doped samples exhibited the characteristic peaks of TiO_2 anatase phase. The peak corresponding to the (1 0 1) crystalline plane was the most intense (Ramalingam et al., 2017). No peaks of rutile phase was observed in all the N-TiO_2_x samples prepared with different urea loadings (Figure II.5a) and in Fe-TiO_2 (Figure II.5c) (Cheng et al., 2008, Zuorro et al., 2019). This result indicates that the phase transformation from anatase to rutile does not take place when nitrogen doped titania powders are calcined at temperature of 450°C. In fact, as reported in literature, the use of urea as a nitrogen precursor inhibits the transformation from anatase to rutile phase (Cheng et al., 2008). Furthermore, traces of brookite phase were observed in the WAXD pattern at about 2θ=31° (1 2 0) (Figure II.5a and Figure II.5c) (Lee and Yang, 2006b, Bhave, 2007, Yanqing et al., 2000) The diffraction patterns of all N-TiO_2_x samples were analyzed more in detail in the 2θ range between 22 and 30° (Figure II.5b). It is possible to observe a shift to lower values of 2θ, from 2θ=25.91° (undoped TiO_2) to 2θ=25.30° (N-TiO_2_0.3). This shift is consistent with literature and it can be associated to distortion and strain phenomena in the TiO_2 crystal lattice induced by the incorporation of the nitrogen ions (Smirniotis et al., 2018, Sun et al., 2008). In particular, this

phenomenon may occur because nitrogen ions replace oxygen in the TiO_2 structure due to differences in binding properties (Vaiano et al., 2015a, Batzill et al., 2006) indicating that the crystalline structure of TiO_2 was doped with nitrogen.The ***a*** and ***c*** lattice parameters calculated for the N-TiO_2_x samples are reported in Table II.3. The values of ***a*** and ***c*** parameters for the N-TiO_2 samples are both higher than those observed for the undoped titania. It has also been possible to consider that the increase of N/Ti ratio does not influence both the value of ***a*** parameter (3.79Å to 3.78Å) and ***c*** parameter (9.20Å to 9.06Å). As shown in the Figure II.5d, the presence of Fe led to a slight shift of the peak related to the anatase phase for Fe-TiO_2 at higher value (2θ=26.31°) with respect to undoped TiO_2 (2θ=25.91°)(Morales et al., 2017). Generally, the Fe doping does not change the crystalline structure of TiO_2, while a small change in the lattice parameters can be observed as reported in Table II.3. The ***a*** and ***c*** lattice constant values for undoped TiO_2 are 3.74 Å and 8.68 Å, respectively, whereas with the addition of Fe ions, the value of ***a*** parameter was 3.77 Å, while the ***c*** parameter changed to 9.21 Å. These lattice parameter values suggest that the iron doping caused the decrease of TiO_2 crystallite size along **c**-axis because the ionic radius of Fe (0.64 Å) is relatively smaller compared to the ionic radius of Ti (0.68 Å) (Ganesh et al., 2012). Probably, due to the almost similar ionic radius, some portion of Ti ions in TiO_2 lattice was replaced with Fe ions (Ganesh et al., 2012). When Fe ions substitute Ti ions, defective sites are formed which act as a long-lasting space charge region. Consequently, the electrical energy of these defects improves the efficiency of the carriers separation and the charge transfer (Prajapati et al., 2017). Thus, the WAXD results indicate that the crystallinity of the iron and nitrogen doped materials is not affected by the presence of the dopant element. The WAXD patterns of Fe-N-TiO_2_1.2 sample (Figura II.5c) showed the presence of all diffraction peaks related to the anatase phase and a small signal associated to brookite, similarly to the other analyzed samples. The peak corresponding to anatase (1 0 1) plane evidenced a shift up to 2θ = 26.11°, as also observed for Fe-TiO_2 sample (Figure II.5d) (Ramalingam, 2017). Finally, ***a*** and ***c*** lattice parameters for Fe-N-TiO_2_1.2 are 3.75 Å and 8.58 Å, respectively (Table II.3). The ***a*** lattice parameter for this sample seems to be similar to undoped TiO_2 (3.74 Å) and lower than N-TiO_2_1.2 and Fe-TiO_2 (3.77 Å), whereas the ***c*** lattice parameter for Fe-N-TiO_2_1.2 (8.58 Å) is lower with respect to undoped TiO_2 (8.68 Å), N-TiO_2_1.2 (8.81 Å) and Fe-TiO_2 (9.21 Å).

The average crystallite size is in the range 6-9 nm (Table II.3). Photocatalysts exhibiting the lowest values of crystallite size, showed the highest values of S_{BET}, as expected.

Figure II.6 reports the WAXD patterns of undoped TiO_2, Pr(8.5)-TiO_2 and Fe-Pr(x)-TiO_2 samples

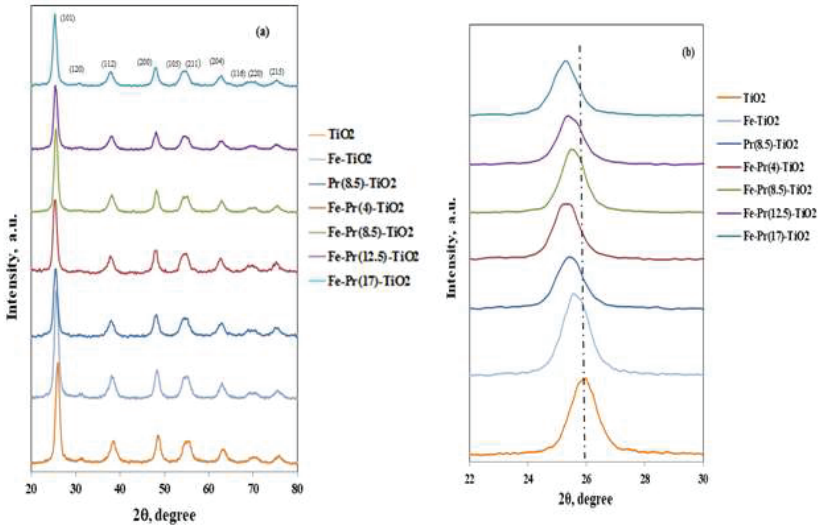

Figure II.6 *WAXD patterns for TiO_2, Fe-TiO_2, Pr(8.5)TiO_2, Fe-Pr(4)-TiO_2, Fe-Pr(8.5)-TiO_2, Fe-Pr(12.5)-TiO_2 and Fe-Pr(17)-TiO_2 samples in the range 2θ=20–80° (a) and in the range 2θ=22–30° (b).*

Specifically, the undoped TiO_2, Pr(8.5)-TiO_2 and Fe-Pr(x)-TiO_2 samples present the sharp and well-defined peaks which are typical of anatase phase (Figure II.6) (Parnicka et al., 2018, Ramalingam, 2017, Chiou and Juang, 2007). Furthermore, traces of brookite phase were only evident in the XRD pattern of TiO_2 and Fe-TiO_2 at about 2θ=31° (1 2 0) (Figure II.6a) (Lee and Yang, 2006a, Zheng et al., 2000). On the contrary, Pr(8.5)TiO_2 and Fe-Pr(x)-TiO_2 photocatalysts did not evidence peaks of brookite phase, according to the available literature (Singh et al., 2018, Liang et al., 2007). No diffraction peaks associated to praseodymium oxide or iron oxide are detectable after the doping with Fe and Pr probably because these dopant elements are present in very small amount and/or located inside the TiO_2 lattice (Li et al., 2020b, Adyani and Ghorbani, 2017). The XRD patterns of all photocatalysts were examined more closely in the 2θ range between 22 and 30° (Figure II.6b). It is possible to observe a shift to lower values of 2θ, from 2θ=25.91° (undoped TiO_2) to 2θ=25.41° (Pr(8.5)-TiO_2), due to distortion phenomena caused by the incorporation of the Pr^{3+} ions in the TiO_2 crystal lattice and it is indicative of the effective doping process of TiO_2 with Pr (Vaiano et al., 2017a, Khan and Swati, 2016). The introduction of praseodymium could induce a strain and distortion phenomena of TiO_2 crystal lattice because the Pr^{3+} ions (1.01 Å) present a higher ion radius than the Ti^{4+} ions (0.68 Å) leading also a little reduction of crystallite size with respect to undoped TiO_2, as evidenced in Table 6 (Nithyaa and Jaya, 2018, Li et al., 2020b).

Table II.4 *Crystallite size, lattice parameter, specific surface area (S_{BET}) and band gap (E_{bg}) of all prepared samples.*

Catalyst	Crystallite size (nm)	Lattice parameter (Å)		S_{BET}	E_{bg}
		a*=*b	***c***	(m^2/g)	(eV)
TiO_2	9	3.74	8.68	107	3.20
Fe-TiO_2	6	3.77	9.21	122	2.80
Pr(8.5)-TiO_2	8	3.77	9.33	113	3.00
Fe-Pr(4)-TiO_2	8	3.79	8.94	113	2.80
Fe-Pr(8.5)-TiO_2	7	3.77	9.15	120	2.70
Fe-Pr(12.5)-TiO_2	7	3.78	9.45	123	2.80
Fe-Pr(17)-TiO_2	7	3.78	9.59	117	2.85

The **a** and **c** lattice parameters calculated for the TiO_2, Fe-TiO_2, Pr(8.5)-TiO_2 and all Fe-Pr(x)-TiO_2 samples are reported in Table II.4. The values of the **a** and **c** parameters for Fe-TiO_2, Pr(8.5)-TiO_2 and all Fe-Pr(x)-TiO_2 samples are higher than those observed for the undoped TiO_2. As shown in Figure II.6b, the presence of Fe produced a shift of the peak correlated to anatase phase for Fe-TiO_2 at higher value (2θ=26.31°) compared to that of undoped TiO_2 (2θ=25.91°) (Morales et al., 2017). Generally, the Fe doping does not affect the crystalline structure of TiO_2, while small changes in the lattice parameters can be observed. In fact, as reported in Table II.4, the **a** and **c** lattice constant for undoped TiO_2 are 3.74Å and 8.68Å, respectively, whereas for Fe-TiO_2 sample the value of **a** parameter was 3.77 Å and **c** parameter value was measured equal to the 7.71 Å. These lattice parameter values suggest that the iron doping caused the decrease of TiO_2 crystallite size (6 nm) along c-axis because the ionic radius of Fe^{3+} ions (0.64 Å) is quite smaller with respect to the ionic radius of Ti^{4+} ions (0.68 Å) (Ibram et al., 2013). It has been possible to value that the increase of Pr/Ti ratio for Fe-Pr(x)-TiO_2 photocatalysts does not lead to a substantial change in the value of a parameter (3.78Å to 3.77Å); nevertheless a small variation in c parameter value (9.59Å to 9.15Å) was observed. Thus, the results indicate that the presence of the Fe and Pr elements produced an expansion of TiO_2 lattice but did not influence the crystallinity of the codoped samples. The diffraction patterns of Fe-Pr(8.5)-TiO_2 sample (Figure II.6a) evidenced the presence of all diffraction peaks corresponding to the anatase phase and a shift of the anatase peak at (1 0 1) plane up to 2θ=25.50°(Figure II.6b). Finally, the **a** and **c** lattice parameters for Fe-Pr(8.5)-TiO_2 are 3.77 Å and

9.15 Å, respectively (Table II.4). The **a** lattice parameter for this sample seems to be higher than undoped TiO_2 (3.74 Å) and similar to Pr(8.5)-TiO_2 (3.77 Å), Fe-TiO_2 (3.77 Å) and Fe-Pr(x)-TiO_2 (3.77-3.78 Å), whereas the **c** lattice parameter for Fe-Pr(8.5)-TiO_2 (9.15 Å) is rather higher both compared to undoped TiO_2 (8.68 Å) and Fe-TiO_2 (7.71 Å), but lower than Pr(8.5)-TiO_2 (9.33 Å) and Fe-Pr(x)-TiO_2 (9.40-9.59Å). Moreover, it was noted that, increasing the Pr/Ti ratio, the average crystallite size slightly decreased (Table II.4). In particular, the values of the average crystallite size for Fe-Pr(x)-TiO_2 samples are in the range 7-8 nm. It is worth noting that the photocatalysts with low crystallite size values showed a higher specific surface area.

Photoluminescence (PL) spectra of TiO_2, Fe-TiO_2, Pr(8.5)-TiO_2 and all Fe-Pr(x)-TiO_2 samples in the range 420-500 nm are reported in Figure II.7.

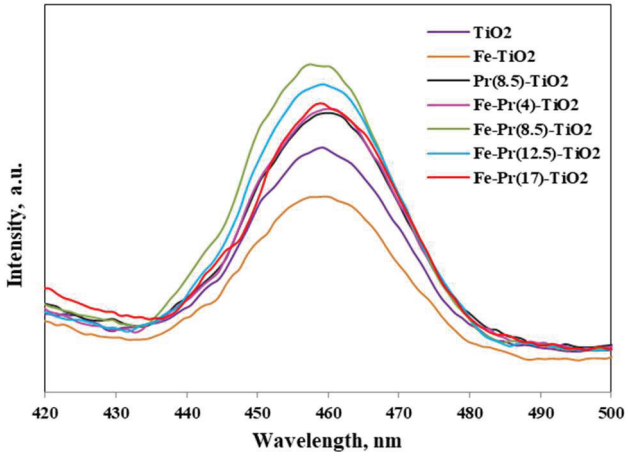

Figure II.7 *Photoluminescence spectra for TiO_2, Fe-TiO_2, Pr(8.5)-TiO_2, Fe-Pr(4)-TiO_2 Fe-Pr(8.5)-TiO_2 Fe-Pr(12.5)-TiO_2 and Fe-Pr(17)-TiO_2 samples.*

A significant photoluminescence emission occurred from 435 to about 480 nm, with the presence of a marked signal at about 460 nm (Pallotti et al., 2017). These results are typical of TiO_2 materials doped with RE elements and the observed maximum signal at about 460 nm could be associated to oxygen vacancies generated by the introduction of the Pr^{3+} ions in the TiO_2 lattice (Narayanan and Deepak, 2018, Nithyaa and Jaya, 2018, Qi and Wang, 2020). Moreover, the shape of PL spectra for TiO_2, Pr-TiO_2 and all Fe-Pr(x)-TiO_2 samples was relatively similar but with different intensity. The presence of Pr dopant initially leads to an enhancement of the PL intensity, nevertheless, when the amount of praseodymium nitrate was increased above 8.5 mg, a decrease in PL emission is appreciated. This result can be justified by the presence of an optimal amount of praseodymium nitrate used as a precursor of Pr that could disadvantage the recombination process of

positive holes and electrons (Xiao et al., 2007). In detail, Fe-Pr(8.5)TiO_2 photocatalyst exhibits a visible peak with the highest intensity.
Instead, the entire PL spectrum of Fe-TiO_2 is lower than that of undoped TiO_2 because Fe doping causes a significant effect on TiO_2 electronic structure. Thus, the lower PL intensity of Fe-doped TiO_2 could be attributed to the lower recombination rate of photogenerated charge carriers (Khan and Swati, 2016). Raman spectra in the range of 100–900 cm^{-1} for undoped and N-doped TiO_2. Raman bands were observed at 144, 397, 516 and 638 cm^{-1} together with a weak shoulder at 195 cm^{-1} in the spectra of all samples, indicating that anatase was the predominant crystalline structure (Mancuso et al., 2020a). No Raman signals associated to TiN bonds were detectable in the N-TiO_2_x samples (Gurkan et al., 2012) This result may be an indication that N anions did not react with TiO_2 surface, meaning that the dopant element is placed in the interstitial or the substitutional sites of the titania structure (Gurkan et al., 2012), as also evidenced by XRD and UV-Vis DRS results. TiO_2 common signals related to the anatase phase were also evident for Fe-TiO_2 sample.
No bands due to iron oxides were detected (Zuorro et al., 2019). Fe-doped TiO_2 maintained the TiO_2 structure indicating that the Fe^{3+} ions are present into the TiO_2 framework, replacing Ti^{4+} cations (Ali et al., 2017a). Additionally, the intensity of the Raman bands for Fe-TiO_2 sample was lower than those observed for undoped TiO_2, indicating the possible incorporation of Fe^{3+} into the substitutional sites of the TiO_2 lattice (Prajapati et al., 2017), in agreement with XRD results. Fe-N-TiO_2_1.2 photocatalyst also showed the typical Raman signals related to anatase TiO_2 and the intensity of these bands is lower than that of undoped TiO_2, Fe-TiO_2 and N-TiO_2_1.2 photocatalysts.
Raman spectra are investigated in the range of 100–900 cm^{-1} of the TiO_2 and Fe-TiO_2, Pr(8.5)-TiO_2 and Fe-Pr(x)-TiO_2 samples.
In the spectra for all samples, Raman bands were observed at 144, 195, 397, 516 and 638 cm^{-1} in the spectra for all samples, indicating that the predominant crystalline phase was anatase. Fe-doped TiO_2 has no bands due to iron oxides because Fe^{3+} ions replace Ti^{4+} cations into the substitutional sites of the TiO_2 preserving the semiconductor structure (Ali et al., 2017a, Prajapati et al., 2017). Ordinary Raman signal associated to crystalline phase are evidenced in the spectrum of Pr(8.5)TiO_2 and Fe-Pr(x)-TiO_2. These samples doped with Pr^{3+} ions did not show bands linked to praseodymium oxides (Singh et al., 2018) as also confirmed by WAXD (Figure II.6) and UV-Vis DRS results (Figure II.4).
The surface acidity of the TiO_2, Fe-TiO_2, N-TiO_2_x and Fe-N-TiO_2_1.2 samples was estimated using the mass titration method. The pH values (representative of PZC) are reported in Table II.3. In particular, the PZC value of undoped TiO_2 is 6.02, very close to those reported in literature for TiO_2 in anatase phase(Ciambelli et al., 2005) .

On the other hand, N-TiO_2_x, Fe-TiO_2 and Fe-N-TiO_2_1.2 photocatalysts showed an acidic character, being the ZPC values equal to 5.10, 5.15 and 5.02 pH unit, respectively (Ganesh et al., 2012). It is worth to underline that the result obtained for the N-TiO_2_x samples could be an indication about the absence of surface nitrogen groups, which typically induce a basic character to the surface of TiO_2 samples modified with nitrogen (Sorrentino et al., 2001). Figure II.8 shows the FESEM images of TiO_2, Fe-TiO_2, N-TiO_2_1.2 and Fe-N-TiO_2_1.2 photocatalysts. In particular, from the images it is possible to observe that all the samples are characterized by a non-uniform structure of macro aggregates indicating that the doping process does not influence the photocatalysts morphology.

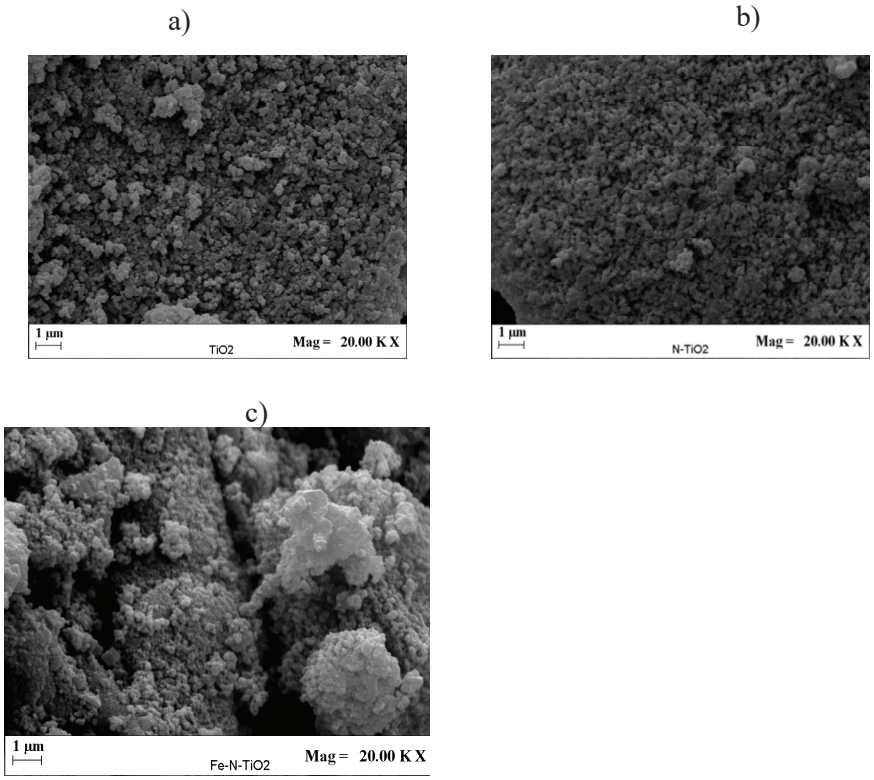

Figure II.8 *FESEM images of TiO_2(a), N-TiO_2_1.2(b), and Fe-N-TiO_2_1.2 (c) photocatalysts*

.

II.5.2 Characterization results of tri-doped TiO_2 photocatalysts

Specific surface area (S_{BET}) of synthesized tri-doped TiO_2 samples, calculated by BET method, are reported in Table II.5 and also compared with S_{BET} of an undoped TiO_2 sample. The undoped TiO_2 sample shows S_{BET}

value of 107 m^2/ g, which is comparable with S_{BET} value of P-N-S/TiO_2 and Fe-N-P/TiO_2 samples, while all the other tri-doped TiO_2 samples have lower S_{BET} values. Lower values of Fe-N-S/TiO_2, Fe-N-P /TiO_2, Fe-Pr-N/TiO_2 and Pr-N-S/TiO_2 S_{BET} compared to undoped TiO_2 may be associated with the formation of metal oxide clusters which could obstruct structural pores (Khlyustova et al., 2020) UV-Vis DRS spectra of TiO_2, Fe-N-P/TiO_2, Fe-N-S/TiO_2, Fe-Pr-N/TiO_2, Pr-N-S/TiO_2 and P-N-S/TiO_2 samples were reported in the range 300 – 900 nm (Mancuso et al., 2021a).

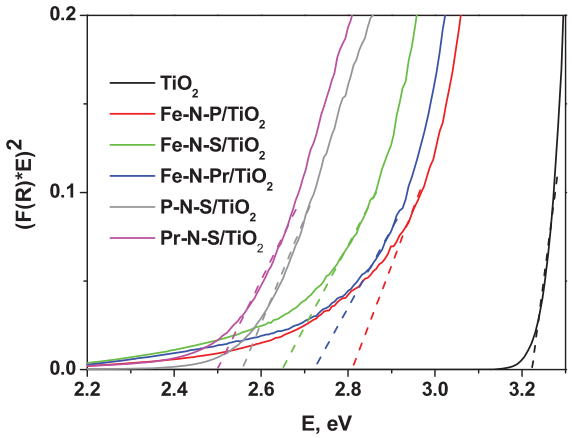

Figure II.9 *Band gap energies (E_{bg}) evaluation of all prepared samples.*

The main absorption of the undoped TiO_2 is located in the UV-A region and no absorption is detected in the visible region. The Fe-N-P/TiO_2, Fe-N-S-TiO_2 and Fe-Pr-N-TiO_2 samples exhibit similar absorption performances in the range 450-600 nm, probably due to the presence of dopant elements into TiO_2 lattice (Cheng et al., 2012a, Xing et al., 2010). Both Pr-N-S/TiO_2 and P-N-S/TiO_2 sample absorption spectra present a shoulder in the visible region. Band gap energies (E_{bg}) are calculated by Kubelka–Munk function (Figure II.9) (Alcaraz de la Osa et al., 2020) and the values are shown in Table II.5. In detail, the band gap value decreases from 3.2 eV for undoped TiO_2 to 2.5-2.8 eV for the tri-doped TiO_2 samples. These results demonstrate that the introduction of metallic and non metallic elements in the TiO_2 crystal structure can induce the absorbtion of visible light, due to the decrease of band gap value. WAXD patterns of the undoped TiO_2 and tri-doped samples in the 2Θ range 20-80° are reported in Figure II.10.

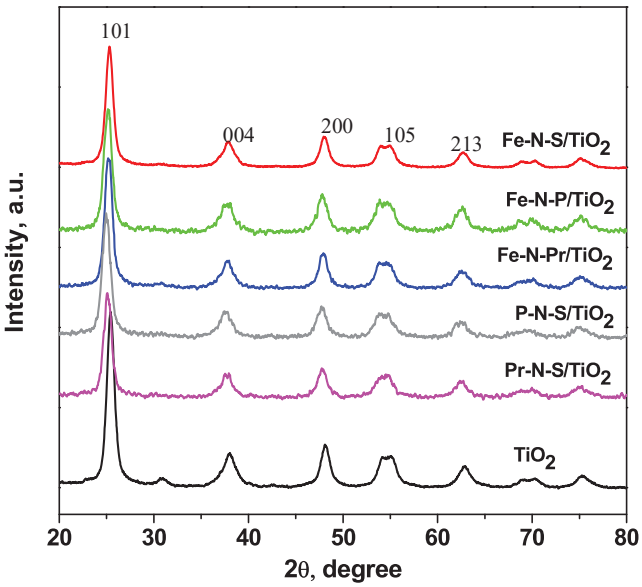

Figure II.10 *WAXD patterns of all prepared samples.*

Pure TiO_2 and all tri-doped samples present only the characteristic WAXD peaks of TiO_2 anatase phase (Ricci et al., 2013). None of characteristic peaks of dopant element oxides have been detected in WAXD patterns of all tri-doped samples, despite this, small quantity of oxides, lower than that detectable by the WAXD, could be also present. Moreover, a remarkable shift of (101) reflection to lower 2θ angles, with respect to the TiO_2 WAXD peak position, was observed in the WAXD pattern of Pr-N-S/TiO_2 and P-N-S/TiO_2 samples. This shift can be explained by the insertion of dopant elements into semiconductor TiO_2 crystalline structure resulting to an increasing of TiO_2 lattice parameters. It is in fact well known that, the lattice parameters data (determined by using Scherrer's equation and the (101) reflections of WAXD patterns) of undoped and tri-doped TiO_2 samples are reported in Table II.5. The crystallite sizes of most of tri-doped samples are lower than that of TiO_2. This result is in agreement with literature results (Xing et al., 2010, Giannakas et al., 2016, Adyani and Ghorbani, 2017), which show that the tri-doping process commonly hinders the crystallite growth. In detail, P-N-S/TiO_2 and Fe-N-P/TiO_2 samples exhibit crystallite size values lower to that of undoped TiO_2 (9 nm). The lattice parameters (Table II.5) of all tri-doped samples undergo an increase with respect to the value of undoped titania (**a**=**b**=3.74 Å, **c**=8.68 Å), which could be attributed to the difference between the radius of dopant elements and those of the host semiconductor atoms (Akshay et al., 2018).

Table II. 5 *Crystallite size, lattice parameters, specific surface area and band gap data of all prepared photocatalysts*.

Sample	Crystallite size (nm)	Lattice parameter (Å) *a=b*	*c*	S_{BET} (m^2/g)	E_{bg} (eV)
TiO_2	9	3.74	8.68	107	3.2
Fe-N-P/TiO_2	8	3.80	10.00	105	2.8
Fe-N-S/TiO_2	9	3.79	9.40	81	2.65
Fe-N-Pr/TiO_2	10	3.81	9.92	91	2.73
P-N-S/TiO_2	8	3.80	10.09	109	2.55
Pr-N-S /TiO_2	9	3.81	9.86	85	2.5

The Raman bands at 144, 197, 399, 516, and 639 cm^{-1} were observed for undoped TiO_2 and tri-doped TiO_2 samples confirming the presence of anatase crystalline phase in all the prepared samples (Mancuso et al., 2021a). It is worth noting that the most intense Raman band at 144 cm^{-1} of undoped TiO_2 was slightly shifted (blue shift) after the doping process. This experimental evidence could be related to the disorder in the TiO_2 lattice due to the incorporation of dopant elements that generate defects (such as oxygen vacancies in anatase structure) (Akshay et al., 2018).

Figure II.11 shows the FTIR absorbance spectra of all tri-doped TiO_2 samples.

The IR band-at about 3400 cm^{-1} is due to the O−H stretching vibration, and the band at 1630 cm^{-1} corresponds to the H−O−H bending vibration of adsorbed water on the photocatalysts surface (Ramandi et al., 2017, Wang et al., 2001) The low-frequency broad band in the range 400–900 cm^{-1} corresponds to the Ti-O-Ti vibrational mode (Wang et al., 2001). It is worth to observe that all tri-doped TiO_2 samples show different shape of low frequency band together with a little shift of the position to lower wavenumbers that could be an indication of structure defects (Gaur et al., 2019). Consistent with WAXD results and according to studies already reported in the literature (Gaur et al., 2019, Ramandi et al., 2017, Wang et al., 2001), the observed band shift should be related to the introduction of dopant species into the TiO_2 framework. Figure II.12 reports photoluminescence spectra (PL), acquired at room temperature in the emission range 325-500 nm, of all the samples, by using an excitation wavelength of 280 nm. All samples evidence a strong emission peak at ca 380 nm, due to the electron–hole pairs recombination. The intensity of this band, together with intensity of the entire emission spectrum, is instead reduced in all tri-doped TiO_2 samples. Indetail, the intensity of the 380 nm PL peak decreases in the following order: TiO_2>Fe-N-S/TiO_2>Fe-N-Pr/TiO_2>P-N-Pr/TiO_2> Pr-N-S/TiO_2>Fe-N-P/TiO_2. As it is generally accepted that a low PL intensity indicates a lower electrons-holes recombination rate and longer duration of photogenerated carries (Jiang et al., 2012) the result of Figure II.12 suggests that for tri-doped TiO_2 a photogenerated gap separation higher than in undoped TiO_2 is expected. Taking in mind that generally PL intensity is directly related with the

recombination of electrons and holes and lower PL intensity indicates a lower recombination rate as well as higher lifespan of photogenerated carries, this result is expected. The observed lower PL band intensity in tri-doped TiO_2 with respect to undoped TiO_2 should be related to a better separation of photogenerated electron-hole in the doped samples.

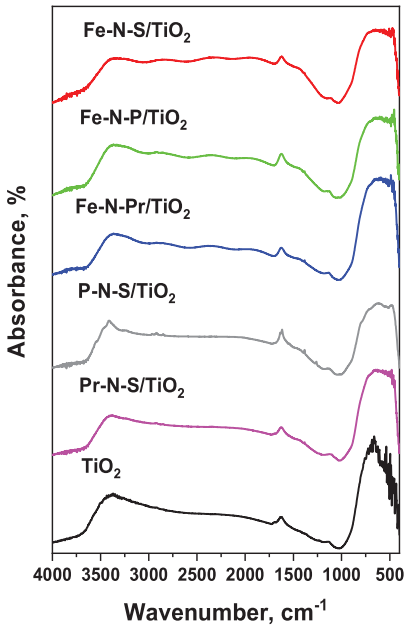

Figure II.11 *Fourier-transform infrared (FTIR) spectra of all prepared samples*

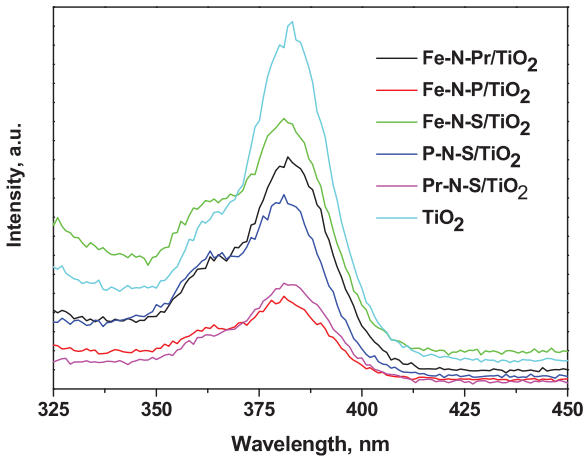

Figure II.12 *Photoluminescence (PL) spectra of all the prepared samples.*

II.6 Photocatalytic activity results

II.6.1 Photodegradation of Acid Orange 7 with codoped TiO_2 photocatalysts

II.6.1.1 Fe-N codoped TiO_2: formulation effect

The visible light driven degradation of AO7 was investigated for all prepared photocatalysts. Figure II.13 reports the AO7 relative concentration as a function of irradiation time showing the influence of the amount of urea in N-TiO_2_x in the photocatalytic discoloration efficiency.

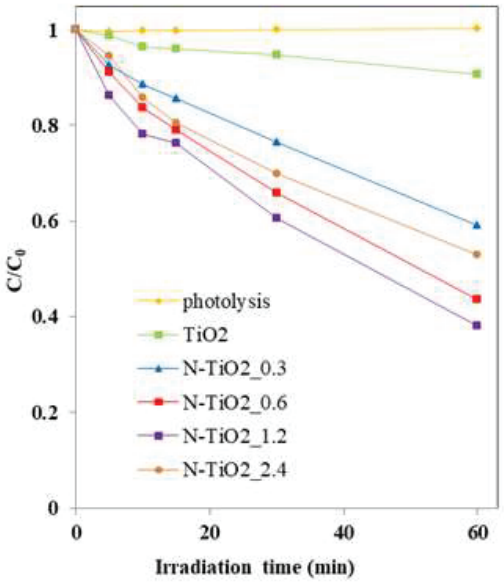

Figure II.13 *Photocatalytic discoloration of TiO_2, N-TiO_2_0.3, N-TiO_2_0.6, N-TiO_2_1.2, N-TiO_2_2.4 photocatalysts under visible light irradiation*

The AO7 relative concentration did not change under visible irradiation for 60 minutes in the absence of photocatalyst, indicating that the photolysis effect is negligible. In the presence of the photocatalysts, the AO7 relative concentration progressively decreased. In detail, after 60 minutes AO7 discoloration efficiency was equal to about 10% with undoped TiO_2. All N-TiO_2_x samples were more active than undoped TiO_2 under visible light

irradiation: the increase in the amount of urea from 0.3 to 1.2 g in the preparation causes an increase of photocatalytic activity. A further increase in the urea content shows a worsening of the photocatalytic performance. The optimal colour removal efficiency (about 62%) was obtained using the photocatalyst prepared with a urea amount equal to 1.2 g (N-TiO_2_1.2). The influence of N presence and its content on photocatalytic activity of N-doped TiO_2 is widely reported in literature (Kim et al., 2018, Qin et al., 2008, Sacco et al., 2018a, Sacco et al., 2015, Vaiano et al., 2015b, Cheng et al., 2016, Reda et al., 2017, Wojtaszek et al., 2019). It is reported that the incorporation of N in the TiO_2 structure induces the formation of an N 2p band above the original O 2p valance band leading to the band gap decrease and enhancing the photocatalytic activity under visible light (Kim et al., 2018, Vaiano et al., 2015a). On the other hand, the existence of an optimal N content can be explained considering that the oxygen sites of TiO_2 can be partially replaced with nitrogen ions (Shin et al., 1991) inducing oxygen vacancies and, as a consequence, the amount of Ti^{3+} increases with the increase of N content (Haoli et al., 2007, Qin et al., 2008). Both oxygen vacancies and Ti^{3+} species acted as hole traps, inhibiting the recombination of electron-hole pairs and, therefore, improving the photocatalytic activity under visible light (Linsebiger et al., 1995). However, when the concentration of N in N-doped TiO_2 is excessively high, the recombination of the photogenerated electron-hole pairs became easier (Li et al., 2004) since the excessive amount of oxygen vacancies and Ti^{3+} species act as recombination centres for electron-hole pairs (Haoli et al., 2007, Qin et al., 2008). The previous observations can explain why the AO7 discoloration efficiency becomes lower when the N content was higher than the optimal amount (1.2 g).

Fe-TiO_2 sample was much more active than undoped TiO_2 under visible light. From Figure II.14, it is also possible to notice a substantial enhancement of the photocatalytic performances for Fe-TiO_2 sample with a discoloration efficiency of about 80%, compared to 62 % achieved using N-TiO_2_1.2 photocatalyst.

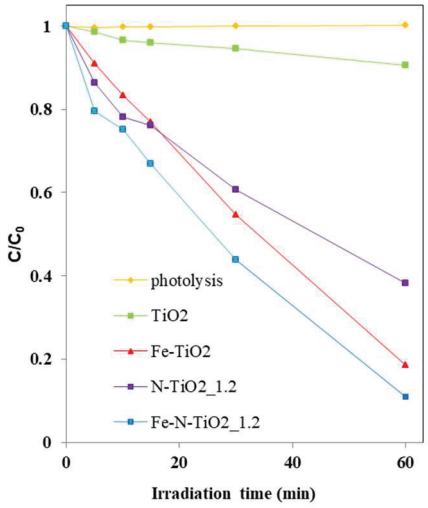

Figure II.14 *Photocatalytic discoloration of TiO_2, N-TiO_2_1.2, Fe-TiO_2 and Fe-N-TiO_2_1.2 photocatalysts under visible light irradiation.*

A further increase in visible light driven AO7 discoloration was obtained using Fe-N codoped TiO_2 prepared with the optimal amount of urea, as assessed from the photocatalytic tests carried out on N-TiO_2_x photocatalysts. In particular, after 60 minutes of irradiation time, the relative AO7 concentration for Fe-N-TiO_2_1.2 photocatalyst was lower than Fe-TiO_2 and N-TiO_2_1.2 photocatalysts, reaching a discoloration efficiency of about 90%. The higher photocatalytic activity of Fe-TiO_2 with respect to undoped TiO_2 should be due to the substitution of Ti^{4+} ions with Fe^{3+}, which acts as electron acceptors promoting the charge separation of photo-generated electrons and holes and yielding more hydroxyl radicals on the surface of the oxide lattice, as reported in literature (Delekar et al., 2012, Zhang et al., 2011b). Additionally, Fe-TiO_2 showed a higher S_{BET} and a lower E_{bg} with respect to N-TiO_2_1.2 (Table II.3), justifying the better performances of Fe-TiO_2 photocatalyst under visible light. On the other hand, the enhanced photocatalytic activity by modification of the TiO_2 structure with N and Fe may be associated with the simultaneous action of Fe^{3+} (previously underlined) and N anions, which are able to replace the oxygen sites of TiO_2 lattice, generating Ti^{3+} sites and oxygen vacancies (Ramalingam et al., 2017). At the same time, despite Fe-N-TiO_2_1.2 sample presented a S_{BET} slightly lower than Fe-TiO_2, the codoped photocatalyst displayed a lower Ebg value (Table II.3). Therefore, it is not surprising that Fe-N-TiO_2_1.2 showed the best photocatalytic activity under visible light irradiation. It is worthwhile to note that, with Fe-N-TiO_2_1.2 sample, about 90 % of AO7

discoloration was achieved in a very short time (60 minutes), if compared to the treatment time reported in several papers, about the AO7 degradation under visible light using also different photocatalyst formulations (,Wu et al., 2010b, Wu et al., 2010a, Ji et al., 2012).
The TOC of solutions was measured after 60 minutes of visible light irradiation to assess the mineralization performances of the photocatalysts (Mancuso et al., 2020a).
The highest mineralization efficiency (55 %) was observed for the N-TiO_2_1.2 sample, confirming that 1.2 g of urea was the optimal value also for the mineralization of the target pollutant.
TOC removal of Fe-N-TiO_2_1.2 photocatalyst was found to be equal to 83 %. The codoped sample (Fe-N-TiO_2_1.2) was certainly more efficient than the undoped titania (5 %), but it also showed a better efficiency in the AO7 mineralization compared to N-TiO_2_1.2 (55 %) and Fe-TiO_2 (73 %) samples. So, it is worthwhile to note that discoloration and mineralization occurs simultaneously under visible light irradiation of N-doped and Fe-N codoped photocatalysts.

II.6.1.2 Kinetics evaluation of AO7 discoloration and mineralization using Fe-N codoped TiO_2

The apparent kinetic constant for AO7 discoloration and mineralization was evaluated in order to better evidence the influence of co-doping on photocatalytic performances. It was considered that AO7 photodegradation reaction follows a pseudo first-order kinetic, as reported in literature (Li et al., 2016, Wu et al., 2010a, Omrania et al., 2019). The photocatalytic degradation rate (r) depends on AO7 concentration or TOC in aqueous solution according to the following relationship:

$$r = k \cdot s \tag{32}$$

Where:
s = concentration of AO7 (mg L^{-1}) or TOC (mg_c L^{-1});
k = apparent kinetic constant (min^{-1}).
Integrating the mass balance (eq. 32) equation between the initial time (t=0) and a generic irradiation time t, it is possible to obtain the equation eq.33

$$\frac{ds}{dt} = -k \cdot s \tag{33}$$

$$-\ln\left(\frac{s}{s_0}\right) = k \cdot t \tag{34}$$

The values of the apparent kinetic constant k are calculated by plotting $-\ln\left(\frac{S}{S_0}\right)$ as a function of the irradiation time (t).

The obtained values (k_{dec} for discoloration and k_{min} for mineralization) are reported in Figure II.15 for the TiO_2, N-TiO_2_1.2, Fe-TiO_2 and Fe-N-TiO_2_1.2 samples.

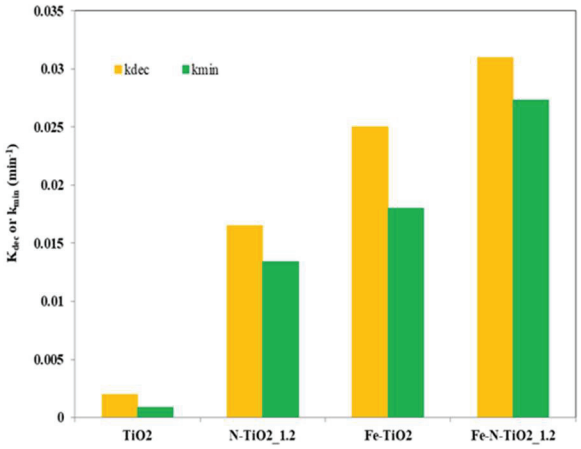

Figure II.15 *Apparent kinetics constant for AO7 discoloration (k_{dec}) and mineralization (k_{min}) using TiO_2, N-TiO_2_1.2, Fe-TiO_2 and Fe-N-TiO_2_1.2 photocatalysts.*

The overall rate constants for AO7 discoloration were given in the following order:

$k_{dec\ Fe\text{-}N\text{-}TiO2\_1.2} > k_{dec\ Fe\text{-}TiO2} > k_{dec\ N\text{-}TiO2\_1.2} > k_{dec\ N\text{-}TiO2\_x} > k_{dec\ TiO2}$, indicating the faster AO7 discoloration and therefore the higher photocatalytic activity for Fe-N-TiO_2_1.2 photocatalyst.

The mineralization rate constants also increased in the following order:

$k_{min\ Fe\text{-}N\text{-}TiO2\_1.2} > k_{min\ Fe\text{-}TiO2} > k_{min\ N\text{-}TiO2\_1.2} > k_{dec\ N\text{-}TiO2\_x} > k_{minTiO2}$, thus proving that also the AO7 mineralization with Fe-N-TiO_2_1.2 photocatalyst is faster than that with undoped TiO_2, N-TiO_2_1.2 and Fe-TiO_2 photocatalysts. In order to compare the system under investigation (Fe-N-TiO_2_1.2) with the literature dealing with the Fe-N doped TiO_2 formulation, the electric energy consumption ($E_{E/O}$) was estimated. It is recognized that $E_{E/O}$ (given in kWh in European Countries) represents a scale-up parameter required to remove a pollutant by one order of magnitude (90%) in 1 m^3 of polluted water (YASAR and YOUSAF, 2012). The $E_{E/O}$ values were calculated using the following proposed equation eq.35 (Azbar et al., 2004, Vaiano et al., 2019):

$$E_{E/O} = \frac{P \cdot t \cdot 1000}{V \cdot 60 \cdot \ln\left(\frac{C_0}{C_f}\right)} \quad (35)$$

Where:

P = nominal power of the light source (kW);
t =irradiation time (minutes);
V =solution volume (L);
C_o =AO7 initial concentration (mg L^{-1});
C_f =AO7 final concentration (mg L^{-1}).

The $E_{E/O}$ values confirm that the electric energy consumption for the AO7 degradation by Fe-N-TiO_2_1.2 photocatalyst under investigation is drastically less than $E_{E/O}$ data related to the removal of water pollutants under visible light with similar photocatalysts (Mancuso et al., 2020a)

II.6.1.3 Fe-Pr codoped TiO_2: formulation effect

All prepared photocatalysts were tested in the photocatalytic degradation of AO7 solution under visible light irradiation. Figure II.16 shows the behavior of dye relative concentration as function of irradiation time, proving the influence of the praseodymium nitrate amount in Fe-Pr(x)-TiO_2 samples on the photocatalytic discoloration efficiency.

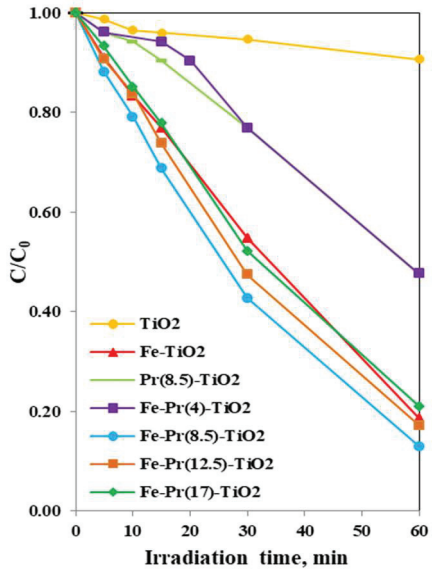

Figure II.16 *Photocatalytic AO7 discoloration using TiO_2, Fe-TiO_2, Pr(8.5)-TiO_2, Fe-Pr(4)-TiO_2 Fe-Pr(8.5)-TiO_2 Fe-Pr(12.5)-TiO_2 and Fe-Pr(17)-TiO_2 photocatalysts under visible light irradiation.*

It was possible to observe a progressive decrease of the AO7 relative concentration for all the tested photocatalysts. In detail, after 60 min the AO7 discoloration efficiency was equal to about 10% with undoped TiO_2. Pr(8.5)-TiO_2 sample was more efficient in the color removal compared to undoped TiO_2 and, moreover, it showed a discoloration efficiency (about 53%) similar to Fe-Pr(4)-TiO_2 photocatalyst. Fe-TiO_2 sample was much more active than undoped TiO_2 under visible light. In particular, a considerable enhancement of the photocatalytic performances for Fe-TiO_2 sample with a discoloration efficiency of about 80% was achieved. The higher photocatalytic activity of Fe-TiO_2 with respect to undoped TiO_2 can be explained according to the fact that the TiO_2 doping with the iron allows a better use of visible light (as evidenced by its E_{bg} value reported in Table II.3) ensuring the separation of produced positive holes and electrons and then limiting their recombination rate (Delekar et al., 2012, Zhang et al., 2011b), as also confirmed by PL spectrum. All Fe-Pr(x)-TiO_2 photocatalysts were largely more active than undoped TiO_2 under visible light irradiation and, in particular, during the overall irradiation time, the relative AO7 concentration for Fe-Pr-(8.5)-TiO_2 photocatalyst was lower than that one observed for Fe-TiO_2, Pr-(8.5)-TiO_2, Fe-Pr-(4)-TiO_2, Fe-Pr-(12.5)-TiO_2 and Fe-Pr-(17)-TiO_2. Therefore, the optimal colour removal efficiency (about 87%) was reached using Fe-Pr(8.5)-TiO_2 photocatalyst. The increase in

visible light driven AO7 discoloration obtained using Fe-Pr codoped TiO_2 prepared with the optimal amount of praseodymium nitrate (8.5 mg) can be justified by a possible synergistic action when both Fe and Pr ions are both into the TiO_2 crystal lattice. In particular, the introduction of Fe^{3+} ions in interstitial or more probably in substitional sites of the TiO_2 lattice can produce defect states which allow the addition the new donor levels in the electronic structure of TiO_2, also leading an enhanced visible light absorption, as observed from UV-vis DRS results (Figure II.4). In addition, as pointed above, Fe dopant elements can also trap charge carriers and inhibit the electron-positive hole recombination (Khan and Swati, 2016). On the other hand, Pr^{3+} ions can replace Ti^{4+} ions causing localized charge perturbation and the formation of oxygen vacancies (as evidenced by PL spectra reported in Figure II.7) that work as electron scavengers and may react with the superoxide species to prevent the positive holes-electrons recombination, thus increasing photo-oxidation efficiency (Burns et al., 2001). In addition, Fe-Pr(8.5)-TiO_2 photocatalyst showed the lowest E_{bg} value (2.7 eV). These observations can justify the enhanced photocatalytic activity of Fe-Pr(8.5)-TiO_2 compared to Fe-TiO_2 and Pr(8.5)-TiO_2 under visible light. However, an increase in the praseodymium nitrate content above 8.5 mg induced a lower AO7 photocatalytic discoloration efficiency because the charge carriers recombination is favored due to the excessive amount of oxygen vacancies (Reszczynska et al., 2014, Shi et al., 2012), as it was observed by photoluminescence spectra for the Fe-Pr(12.5)-TiO_2 and Fe-Pr(17)-TiO_2 in which their PL intensity decreased (Figure II.7) and also by their lower optical absorption noted by UV-Vis DRS measurements (Figure II.4). In addition, the decrease of TOC solutions was measured in order to characterize the mineralization performance of the tested photocatalysts. TOC removal efficiency after 60 min of treatment time for Pr(8.5)-TiO_2 sample was about 45% which is higher than that of undoped titania (5%) and similar to that achieved with Fe-Pr(4)-TiO_2. Instead, Fe-Pr(8.5)-TiO_2 photocatalyst showed the highest TOC removal (80%). Moreover, for Fe-Pr(12.5)-TiO_2 and Fe-Pr(17)-TiO_2, a little decrease in the mineralization efficiency was noted up to 72 % and 70%, respectively. These results confirm that Fe-Pr(8.5)-TiO_2 was the optimal codoped phtotocatalyst for the mineralization of the target pollutant (Mancuso et al., 2021b). The value of the kinetic constant k is found by the slope of the straight line obtained by plotting vs the irradiation time (t). The obtained k values (kdec for discoloration and kmin for mineralization) are reported in Figure II.17 for the TiO_2, Fe-TiO_2, Pr(8.5)-TiO_2 and Fe-Pr(x)-TiO_2 samples.

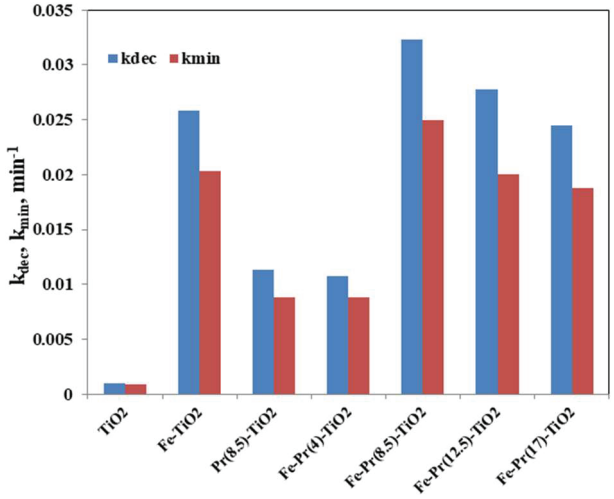

Figure II.17 *Apparent kinetics constant for AO7 discoloration (k_{dec}) and mineralization (k_{min}) using TiO_2, Fe-TiO_2 and Pr(8.5)-TiO_2, Fe-Pr(4)-TiO_2 Fe-Pr(8.5)-TiO_2 Fe-Pr(12.5)-TiO_2 and Fe-Pr(17)-TiO_2 photocatalysts.*

The overall rate constants for AO7 discoloration were given in the following order:

$k_{decFe\text{-}Pr(8.5)\text{-}TiO2} > k_{decFe\text{-}Pr(12.5)\text{-}TiO2} > k_{decFe\text{-}TiO2} > k_{decFe\text{-}Pr(17)\text{-}TiO2} > k_{decPr(8.5)\text{-}TiO2} > k_{decFe\text{-}Pr(4)\text{-}TiO2} > k_{decTiO2}$, indicating the faster AO7 discoloration and therefore the higher photocatalytic activity for Fe-Pr(8.5)-TiO_2 photocatalyst.

The mineralization rate constants also increased in the following order:

$k_{minFe\text{-}Pr(8.5)\text{-}TiO2} > k_{minFe\text{-}TiO2} \cong k_{minFe\text{-}Pr(12.5)\text{-}TiO2} > k_{minFe\text{-}Pr(17)\text{-}TiO2} > k_{minFe\text{-}Pr(4)\text{-}TiO2} \cong k_{minPr(8.5)\text{-}TiO2} > k_{minTiO2}$, thus demonstrating that also the AO7 mineralization with Fe-Pr(8.5)-TiO_2 photocatalyst is faster compared to the other tested photocatalysts.

Furthermore, the photocatalytic performances of Fe-Pr(8.5)-TiO_2 were compared with several data of literature literature papers dealing with different TiO_2 materials codoped with iron and RE elements and with TiO_2 formulations tri-doped with iron, RE elements and non-metal elements available in the literature and studied for the degradation of several organic dyes (Mancuso et al., 2021b). The data reported by Mancuso et al. (Mancuso et al., 2021b) confirm the superior performances of the Fe-Pr-TiO_2 optimized in this work with respect to Fe-Ce-TiO_2 (Shi et al., 2012) Fe-Er-TiO_2 (Hou et al., 2012) and Fe-La-TiO_2 (Wang et al., 2011) Photocatalytic degradation efficiency similar to Fe-Pr(8.5)-TiO_2 was observed for Fe-Ce-TiO_2 (Jaimy et al., 2012) and Fe-Ce-N-TiO_2 (Wang et al., 2013). However, for these photocatalyst formulations, an irradiation time significantly higher than 60

min is necessary. Finally, only Fe-Gd-N-TiO_2 exhibited a degradation efficiency of about 97% (Li et al., 2020b), but only after 180 min of visible light irradiation.

II.6.1.4 Possible role of reactive oxygen species towards the AO7 discoloration under visible light

The possible role of reactive oxygen species (ROS), such as hydroxyl radicals, superoxide and positive holes has been investigated during the AO7 photocatalytic discoloration process using Fe-N-TiO_2_1.2. Fe-Pr(8.5)-TiO_2 photocatalyst was also used to understand the possible photocatalytic mechanism of AO7 discoloration. The scavenger probe molecules were: isopropanol (IPA, 10 mmol L^{-1}) for hydroxyl radicals (Zhang et al., 2018a), benzoquinone (BQ, 1 µmol L^{-1}) for superoxide (Zhang et al., 2017) and disodium ethylenediamine tetra-acetate (EDTA, 10 mmol L^{-1}) for positive holes. Figure II.18 shows the effects of the scavengers presence on photocatalytic performances.

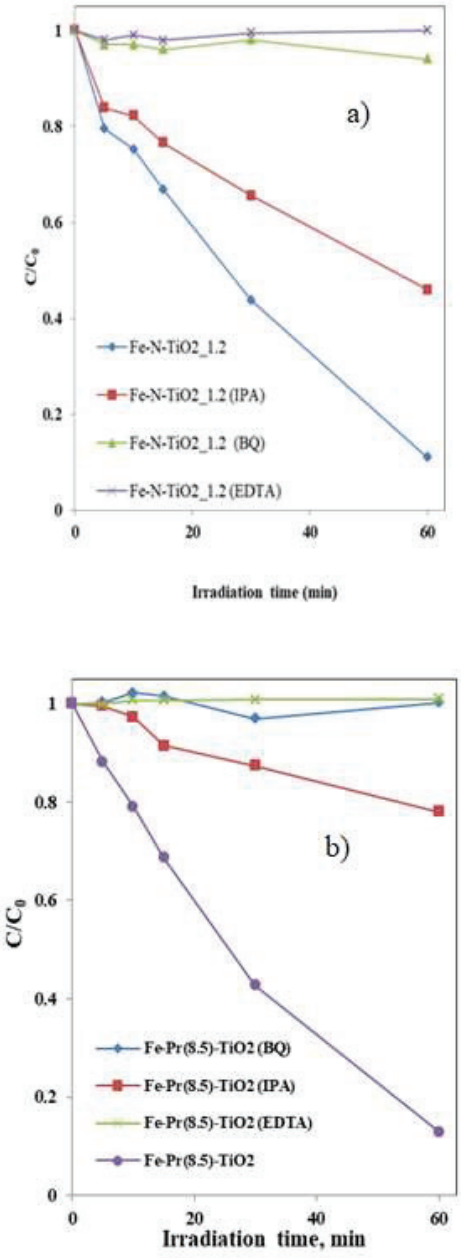

Figure II.18 *Effects of different scavengers on AO7 photodegradation using Fe-N-TiO_2_1.2 photocatalyst under visible light irradiation a) using Fe-Pr(8.5)-TiO_2 b).*

In general, it can be seen as the addition of IPA, BQ and EDTA influenced the AO7 discoloration rate. In particular, it was found that the IPA presence slightly decreased the AO7 discoloration efficiency while, the addition of BQ and EDTA completely inhibited the photocatalytic process either with Fe-N-TiO_2_1.2 or Fe-Pr(8.5)-TiO_2. These results demonstrate that the main reactive oxygen species involved in the AO7 discoloration mechanism were represented by superoxide and positive holes. They are consistent with the literature reporting the role of ROS on visible light driven photodegradation of AO7 (Stylidi et al., 2004).

II.6.2 Photodegradation of Thiacloprid with tri-doped TiO_2 photocatalysts

The photocatalytic degradation of THI in aqueous solution under UV and visible light irradiation was evaluated for all the doped photocatalysts and compared with bare TiO_2. Figure II.19 reports the THI relative concentration as a function of irradiation time for all the tested photocatalysts in presence of UV-A, visible and direct solar light.

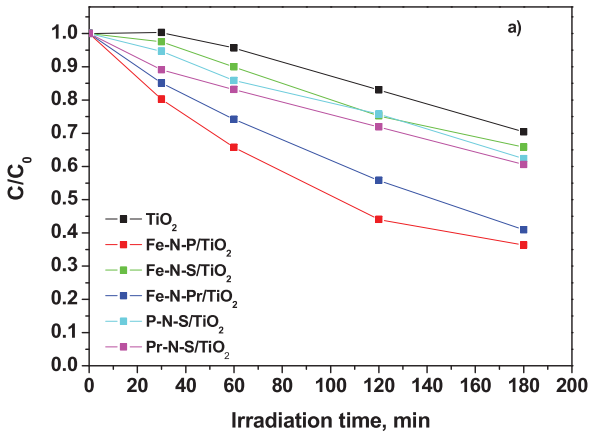

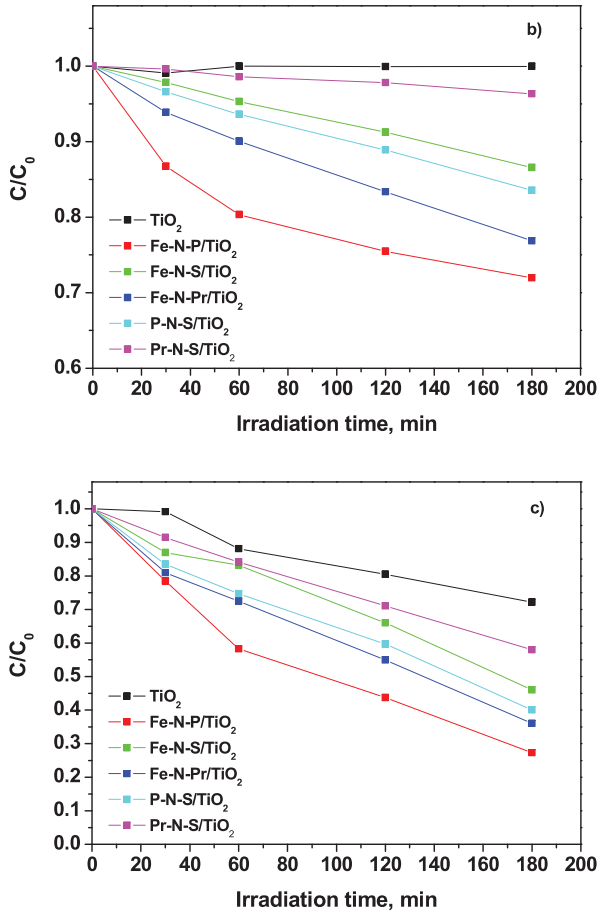

Figure II.19 *Photocatalytic degradation of THI under UV-A a), visible b) and direct solar light irradiation c).*

A progressive decrease of the THI concentration was observed in the presence of all the doped photocatalysts under UV, visible light and direct solar light irradiation, evidencing that the doping of TiO_2 is able to increase the photocatalytic activity. The Fe-N-P tri-doped TiO_2 sample exhibits the highest photodegradation degree (64% under UV-A light, 29% under visible light and 73% under solar light) among all the samples, indicating that Fe, N and P tri-doping comes possibly into a synergistic effect, resulting in a catalyst with superior performances than other doped one.

Considering that P-N-S/TiO_2 and Fe-N-P/TiO_2 samples showed a comparable S_{BET} value and despite P-N-S/TiO_2 photocatalyst have an E_{bg} lower than that of Fe-N-P/TiO_2 (Table II.5), the highest photoactivity of such sample is possibly linked to a recombination rate of photogenerated electron-hole lower than the other tested samples (as shown by PL results). Keeping

in mind that, to our knowledge, no articles have been reported in the literature so far dealing with the use of the TiO_2 tri-doped sample for THI removal under direct sunlight, these results are quite exciting. It is worth underling that the optimized Fe-N-P/TiO_2 catalyst showed a superior photocatalytic activity, especially under UV irradiation and sunlight using a pollutant concentration and catalyst dosage very low if compared with data reported in the literature (Mancuso et al., 2021a). Moreover, Fe-N-P/TiO_2 sample evidenced a visible light activity very similar to a catalyst based on a noble metal (e.g. Ag_3PO_4) (Lee et al., 2020). The degradation mechanism of THI is mainly driven by •OH radicals and holes. Indeed, it is reported by Berberidou et al. and Zhong et al. (Berberidou et al., 2019, Zhong et al., 2020) that THI photodegradation mechanism proceeds via three different decomposition pathways because of non-selective attach by •OH radicals. During the photocatalytic reaction, the main by-products are formed by hydroxylation/oxidation reactions of the THI molecules and of the portions of the molecule resulting from the detachment of the (thiazolidin-2-ylidene) cyanamide group and/or the 2-chloro-5-methylpyridine group.

II.6.2.1 Kinetics evaluation of THI degradation

The apparent kinetic constant for THI degradation was calculated to underline the influence of doping elements on photocatalytic activity. It was assumed that the photocatalytic degradation rate depends on THI concentration in aqueous solution according to the pseudo first order kinetics.

The values of the apparent kinetic constant k are calculated by plotting $-\ln\left(\frac{C}{C_0}\right)$ as a function of the irradiation time (t). The obtained values (k_{UV}, k_{Vis} and k_{solar} for THI degradation) are reported in Table II.6 for the TiO_2, Fe-N-P/TiO_2, Fe-N-S/TiO_2, Fe-Pr-N/TiO_2, P-N-S/TiO_2 and Pr-N-S/TiO_2 samples.

Table II. 6 *Apparent kinetic constant for TiO_2, Fe-N-P/TiO_2, Fe-N-S/TiO_2, Fe-N-Pr/TiO_2, P-N-S/TiO_2 and Pr-N-S /TiO_2 samples*.

Sample	k_{UV} (min^{-1})	k_{Vis} (min^{-1})	k_{solar} (min^{-1})
TiO_2	$1.7\cdot10^{-3}$	$7.58\cdot10^{-6}$	$1.8\cdot10^{-3}$
Fe-N-P/TiO_2	$6.0\cdot10^{-3}$	$2.1\cdot10^{-3}$	$7.2\cdot10^{-3}$
Fe-N-S/TiO_2	$2.2\cdot10^{-3}$	$7.88\cdot10^{-4}$	$3.9\cdot10^{-3}$
Fe-N-Pr/TiO_2	$4.9\cdot10^{-3}$	$1.5\cdot10^{-3}$	$5.5\cdot10^{-3}$
P-N-S/TiO_2	$2.5\cdot10^{-3}$	$1.0\cdot10^{-3}$	$4.8\cdot10^{-3}$
Pr-N-S /TiO_2	$2.8\cdot10^{-3}$	$2.02\cdot10^{-4}$	$2.9\cdot10^{-3}$

As it is possible to note, the Fe-N-P/TiO_2 photocatalyst showed the highest apparent kinetic constant values (k_{UV} = $6.0 \cdot 10^{-3}$ min^{-1}, $k_{Vis=}$ $2.1 \cdot 10^{-3}$ min^{-1} $k_{Solar=}$ $7.2 \cdot 10^{-3}$ min^{-1}) among all the analyzed samples.

III. Experimental results: photocatalytic degradation of water pollutants using photocatalysts coupled with β-CD

Cyclodextrins can be used to support the photocatalysis reaction with TiO_2 semiconductor to remove pollutants (dyes, active ingredients of drugs, etc.) from wastewater. The photocatalytic efficiency of the TiO_2 semiconductor can also be limited by large electron-hole recombination rates, which would hinder the transfer of photogenerated charges to the catalyst surface (Qian et al., 2019, Dong et al., 2015). β-CD can stabilize TiO_2 colloids and facilitate the interfacial electron transfer process. It plays a role as an electron donor and can fill the "holes" when connected to TiO_2 colloids, creating a restricted recombination of the "charge-holes" with a consequent improvement in photocatalytic efficiency. For this purpose, the four chapter reports the production of photocatalytic TiO_2/β-CD hybrid systems by supercritical technique to be used in the removal of water pollutants. The goal was to micronize the cyclodextrins, thus increasing their dissolution rate and improving contact between cyclodextrin and photocatalyst, in order to degrade the pollutant more efficiently.

III.1 Synthesis of hybrid photocatalyst particles

β-CD particles were produced through the SAS process. The core of the process is the precipitation chamber (PC), a cylindrical vessel with an internal volume equal to 500 cm^3. Two high-pressure pumps, P1 and P2,

allow feeding the CO_2 (antisolvent) from tank V1 and the liquid solution (DMSO + β-CD) contained in a burette (V2). In particular, the liquid solution is injected into the precipitation chamber through a stainless-steel nozzle. The CO_2 is pre-cooled through a refrigerating bath (RB) and then delivered to the chamber. The pressure in the PC is regulated by a micrometering valve (MV) and measured by a test gauge manometer (M). The operating temperature inside the chamber is ensured by a proportional integral derivative (PID) controller connected with heating bands. A steel filter, characterized by pores with a diameter of 0.1 μm, is located at the bottom of the PC to collect the precipitated powders and permit the CO_2-solvent mixture to pass through. Then, the liquid solvent is recovered in a second collection vessel (LS), whose pressure (approximately 24 bar) is regulated by a back-pressure valve (BPV). The flow rate of CO_2 and its total quantity delivered are measured by a rotameter (R). The laboratory plant is sketched in Figure III.1.

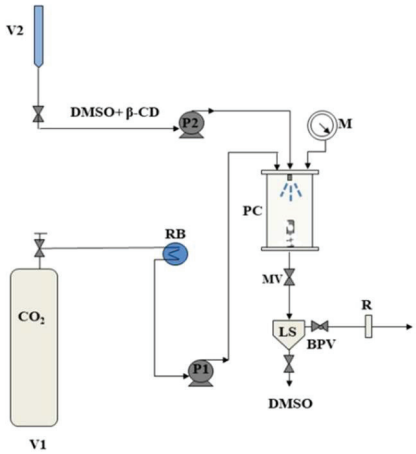

Figure III.1 *Schematic representation of SAS apparatus; V1: CO_2 vessel, V2: liquid solution vessel, P1, P2: pumps, RB: refrigerating bath; PC: precipitation chamber, M: manometer, MV: micrometric valve, LS: liquid separator, BPV: back pressure valve, R: rotameter*

A typical SAS experiment begins by sending the CO_2 to the precipitation chamber until the desired pressure and temperature are reached. After, the pure solvent is injected through the nozzle up until a quasi-steady state composition of solvent and antisolvent is achieved within the chamber. Finally, the liquid solution containing the solute to be micronized is fed through the nozzle, leading to the precipitation of the solute. At the end of the solution injection, CO_2 continues to flow to remove the solvent residues completely. After this washing step, the CO_2 pumping is stopped, and the precipitation chamber is slowly depressurized up to the atmospheric pressure. In detail, selecting dimethylsulfoxide (DMSO) as the liquid solvent, SAS experiments were performed using a flow rate of the liquid solution and CO_2 equal to 1 mL/ min and 30 g/ min, respectively (Yadav et al., 2021).
In addition, all SAS experiments were performed under the following operating conditions: injector diameter equal to 100 μm, a temperature of 40 °C, a pressure of 150 bar, and a variable solute concentration: 30 mg/mL, 50 mg/mL, 70 mg/mL and 100 mg/mL. In general, the first step is preparing the solution to be injected: a fixed amount of commercial cyclodextrins was dissolved in 40 mL of DMSO, to have the desired concentration every time. At the end of a SAS experiment, the powder is recovered in the precipitator, whereas DMSO is extracted by $scCO_2$. The samples are named β-CD SASx, where x is the solute concentration. Thus, the precipitated powders are collected and characterized. After the micronization of β-CD SASx, a suspension containing 4 g/ L of PC500 and 3.4 g/ Lof β-CD was mixed for 3 hours to obtain the hybrid photocatalysts. The adsorption of β-CD on titania is dependent on the pH value of the suspension, and there is a higher adsorption efficiency at pH values between 5 and 7; consequently, a solution with a known concentration of NaOH has been added inside the suspension to obtain the desired pH (Lu et al., 2004). After the agitation period, the suspension was centrifuged and the solid phase was thoroughly washed twice with distilled water. The collected final samples were dried at room temperature for 24 hours and named PC500/unprocessed β-CD, PC500/β-CD SAS30, PC500/β-CD SAS50, PC500/β-CD SAS70, PC500/β-CD SAS100.

III.2 Experimental Results

III.2.1 Characterization of β-CD

To characterize the samples studied in this section the following techniques were used:

- A field emission scanning electron microscopy (FESEM)
- UV-vis reflectance spectroscopy (UV-vis DRS);
- Raman spectroscopy;
- Fourier Transform Infrared (FTIR) spectroscopy;
- N_2 adsorption at -196 °C to obtain specific surface area and porosity characteristics.

III.2.1.1 A field emission scanning electron microscopy (FESEM)

The β-CD precipitated with the SAS technique were analyzed with the field emission scanning electron microscope (FESEM mod. LEO 1525, Carl Zeiss SMT AG, Oberkochen, Germany) that was used to observe the morphology of powders previously dispersed on a carbon tab (Agar Scientific, Stansted, United Kingdom) and then coated with gold-palladium (layer thickness 250 Å) using a sputter coater (mod. 108 A, Agar Scientific). The mean diameters and the particle size distributions (PSDs) of the micronized β-CDs were measured using the Sigma Scan Pro image analysis software (v5.0, Aspire Software International, Ashburn, VA, USA), considering approximately 1000 particles. Instead, PSDs of the photocatalysts were measured by dynamic light scattering (DLS, mod. Mastersizer S, Malvern Instruments Ltd., Worcestershire, UK). Analyses were performed using several milligrams of each sample (corresponding to more than one million particles). Size evaluation analyses were performed in triplicate. From the FESEM images reported in Figure III.2, it is possible to observe the morphological aspect of the samples and compare it with the unprocessed β-CD (Figure III.2a). The images of the micronized powders reported in Figures III.2a have been taken at the same enlargement, and are representative of the different morphologies among the unprocessed β-CD and the β-CD SAS50. In particular, it is possible to observe how the particle morphology changes considerably following the micronization tests and how the morphology changes with the amount of solute concentration equal to 50 mg/mL.

(a) (b)

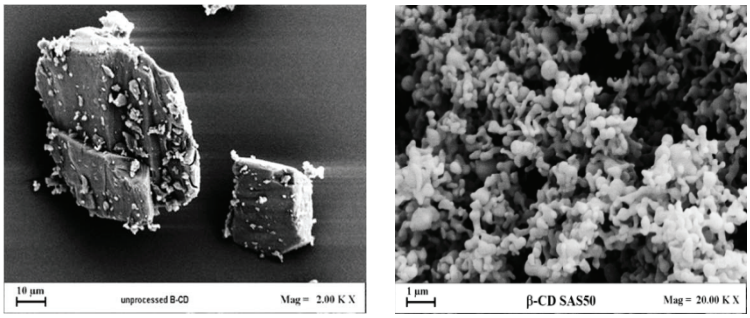

Figure III.2 *FESEM of unprocessed β-CD (a), β-CD SAS50(**b**).*

The diameters of the particles obtained were calculated through the image analysis software Sigma Scan Pro. Table III.1 shows, for all the investigated concentrations, the morphology of the obtained particles, the mean diameter (md), and the standard deviation (sd) of the particles. In particular, it was evaluated the effect of the concentration of the liquid solution on particle morphology, fixing the pressure at 150 bar and the temperature at 40 °C and varying the concentration of the liquid solution from 30 to 100 mg/mL in DMSO (as it is possible to see in Table III.1). β-CD precipitated in the form of sub-microparticles for a solute concentration of up to 50 mg/mL. In contrast, microparticles ranging from 0.2 to 0.4 µm were obtained at 70 and 100 mg/mL. Therefore, increasing the concentration of the liquid solution, an increase in the average particle size was obtained.

Table III.1 *Summary of micronization experiments (SMP: sub-microparticles; MP: microparticles; md: mean diameter; sd: standard deviation).*

Sample	Concentration of β-CDx [mg/ mL]	Morphology	md± sd [µm]
β-CD SAS30	30	SMP	0.27±0.27
β-CD SAS50	50	SMP	0.25±0.35
β-CD SAS70	70	MP	0.41±0.36
β-CD SAS100	100	MP	0.39±0.41

Unprocessed β-CD and SAS micronized powders were used to prepare the photocatalytic particles. A summary of the prepared samples is reported in Table III.2 with the indication of the morphology, mean diameter (md),

standard deviation (sd) of particles (obtained by dynamic light scattering analysis), specific surface area S_{BET} and band-gap energy values.

Table III. 2 *Summary of the experimental results (MP: microparticles; md: mean diameter; sd: standard deviation).*

Sample	Morphology	md± sd [μm]	S_{BET} [m^2/g]	E_{bg} [eV]
PC500	MP	1.75±0.09	226	3.2
PC500/unprocessed β-CD	MP	3.52±0.17	215	3.2
PC500/β-CD SAS30	MP	1.94±0.13	196	3.22
PC500/β-CD SAS50	MP	1.59±0.16	195	3.22
PC500/β-CD SAS70	MP	2.06±0.17	200	3.22
PC500/β-CD SAS100	MP	2.11±0.18	210	3.25

DLS analysis showed that the presence of micronized β-CD SASx allows a lower aggregation of PC500/β-CD SASx particles. FESEM images of the different samples are reported in Figure III.3. It is possible to observe that, when mixed with unprocessed β-CD, TiO_2 particles are present as agglomerates on the surface of large-sized crystals, while in the case of PC500/β-CD SAS50, TiO_2 particles are more uniformly distributed according to the size of SAS micronized samples. A similar result was obtained for the other PC500/β-CD SASx samples.

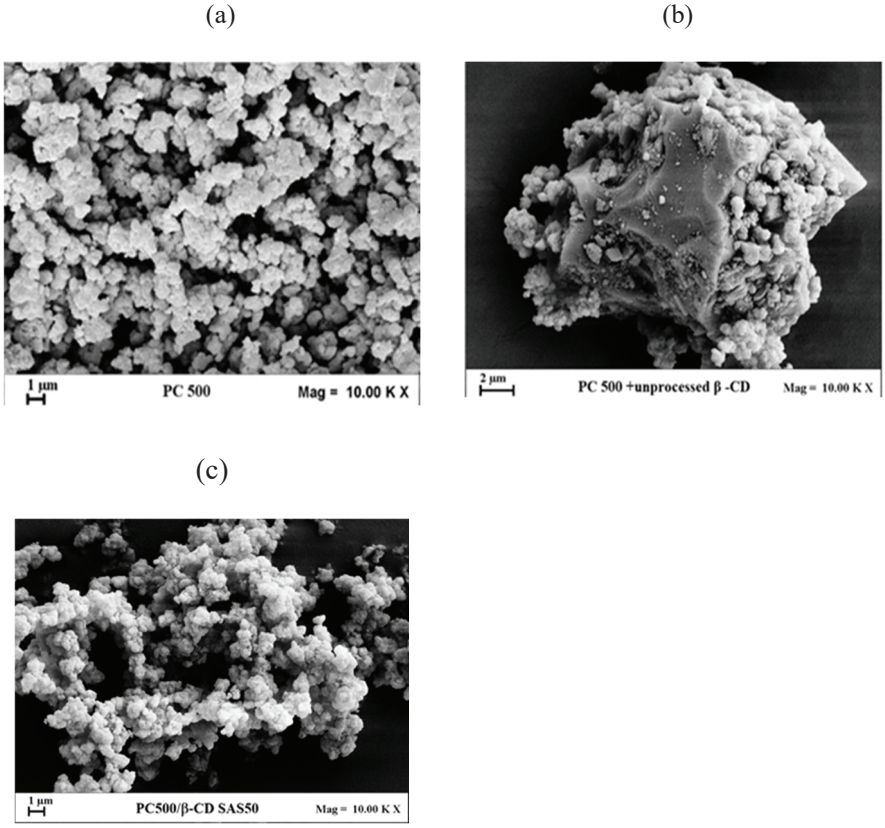

Figure III. 3 *FESEM images of TiO_2 PC500 (a), hybrid PC500/unprocessed β-CD (b) PC500/β-CD SAS50(c).*

III.2.1.2 Fourier transform infrared (FT-IR) spectroscopy

FT-IR results of the synthesized photocatalysts were obtained via M2000 FT-IR (MIDAC Co, Costa Mesa, CA, USA) at a resolution of 0.5 cm^{-1} with the scan wavenumber range was 4000–1000 cm^{-1} (Figure III.4). The FT-IR spectra of the hybrid PC500/β-CD SASx particles were studied using the spectra of commercial titania PC500 and unprocessed β-CD as references (Figure III.4a). For the spectrum of PC500, the signals at around 1380 cm^{-1} and 1630 cm^{-1} can be attributed, respectively, to Ti-O modes and bending

modes of Ti-OH (León et al., 2017). The broad band at about 3500 cm^{-1} can be attributed to the stretching vibration of the hydroxyl group O-H due to

water molecules adsorbed on TiO_2 surface (León et al., 2017). For the spectrum of unprocessed β-CD, the signal at 1030 cm^{-1} is related to the vibrational modes of the –C–O–C– groups, while the peak at 1160 cm^{-1} is associated with C-O stretching vibration. The bands at about 2927 cm^{-1} and 3420 cm^{-1} can be attributed, respectively, to the C–H stretching vibration and O–H group (Iacovino et al., 2013, Lopes Colpani et al., 2018). Figure 44b shows that, for all the hybrid photocatalysts, the band's intensity at around 1380 cm^{-1} disappeared and new signals appeared after the combination between PC500 with both unprocessed β-CD and β-CD SASx, indicating a possible interaction between β-CD molecules and the hydroxyl of Ti-OH functional group. Indeed, on the spectra of hybrid photocatalysts (Figure III.4b), new signals at 1030, 1078, and about 1153 cm^{-1} appear. In detail, the band at 1153 cm^{-1} is assigned to C–O–C (glycosidic) stretch while the signals at around 1030 and 1078 cm^{-1} are both linked to coupled C–C stretch/C–O stretch vibrations (Zhang et al., 2011c) .

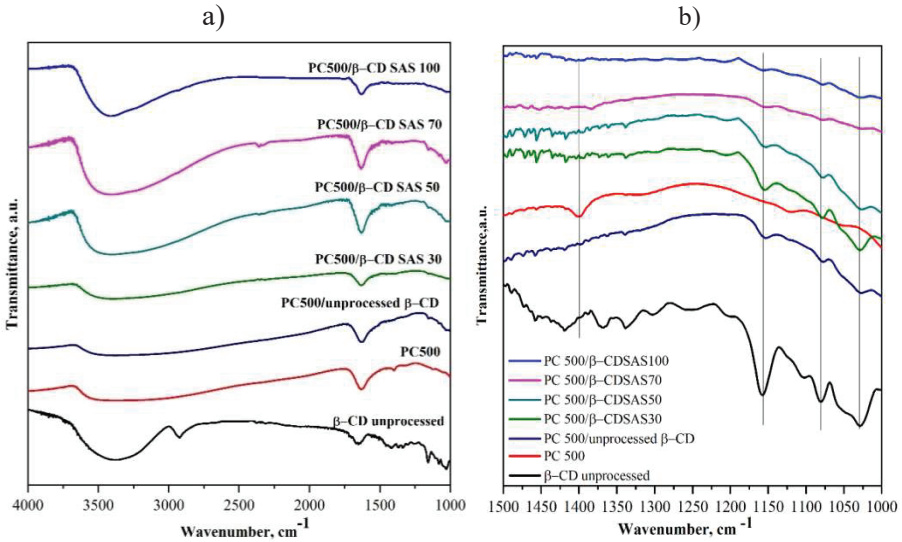

Figure III.4 *Comparison between FT-IR spectra of the examined photocatalysts (a) and between FT-IR spectra of the examined photocatalysts in the range 1000-1500 cm^{-1} (b).*

III.2.1.3 UV-vis diffuse reflectance (UV-Vis DRS)

UV–Vis reflectance spectra (UV-Vis DRS) of catalysts were recorded by a Perkin-Elmer spectrometer Lambda 35 using a RSA-PE-20 reflectance spectroscopy accessory (Labsphere Inc., North Sutton, NH). All spectra were

obtained using an 88 sample positioning holder, giving total reflectance relative to a calibrated standard SRS-010-99 (Labsphere Inc., North Sutton, NH). The reflectance data were reported as the $F(R_\infty)$ value from Kubelka-Munk theory vs the wavelength. Band gap determinations were made by plotting $[F(R_\infty)\cdot h\nu]^2$ vs hν (eV) and calculating the x intercept of a line passing through $0.5 < F(R_\infty) < 0.8$.

The main absorption edge of commercial titania PC500 lies in the range of 390–400 nm (UV region) (Mottola et al., 2022). All PC500/β-CD samples did not show substantial differences in the absorption properties, also confirmed by the calculation of band gap values using UV-vis DRS measurements and reported in Table III.2.

III.2.1.4 Wide-angle ray diffraction (WAXD) spectra

Wide-angle X-ray diffraction (WAXD) patterns were performed with an automatic Bruker D8 Advance diffractometer (VANTEC-1 detector) using reflection geometry and nickel filtered Cu-Kα radiation. Figure III.5 reports WAXD patterns for PC500, PC500/ unprocessed β-CD and all PC-500/β-CD SAS x. In particular, commercial PC500 shows the diffraction signals at 2Θ equal to 25.2° (1 0 1), 37.8 °(0 0 4), 47.7°(2 0 0) and 54.3°(1 0 5) associated to the anatase tetragonal crystal structure (Zhang et al., 2009, Kansal et al., 2013). No peaks of the other crystalline phases (rutile and brookite) were observed. Therefore, all hybrid PC-500/β-CD systems exhibit diffraction peaks similar to the PC500 sample, confirming that anatase is the predominant crystalline phase (Velusamy et al., 2014). This result has also been confirmed by calculating crystallite size using the Debye–Scherrer formula (Yadav et al., 2021). The obtained crystallite size for the hybrid PC-500/β-CD SASx systems (10 nm) is quite similar to the estimated values for PC500 and PC500-β-CD unprocessed samples (9 nm).

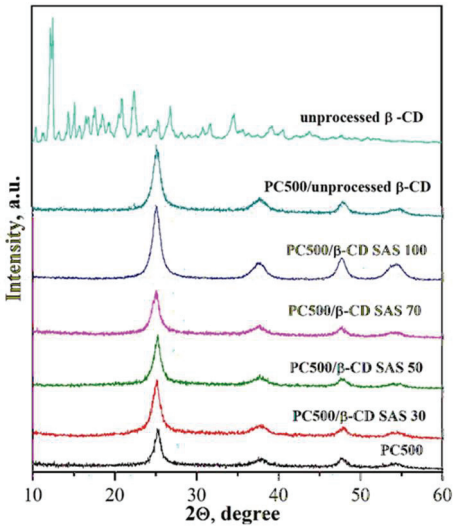

Figure III.5 *Wide angle X-ray diffraction (WAXD) patterns in the range 2θ = 10–60°.*

III.2.1.5 Raman spectroscopy

Laser Raman spectra are displayed for all the samples in the range of 100–900 cm^{-1} at room temperature with a Dispersive MicroRaman (Invia, Renishaw, Wotton-under-Edge, United Kingdom), equipped with 514 nm laser. All PC500/β-CD systems show only the main bands of the uncomplexed commercial PC500 (in anatase crystalline form) at 148, 516 and 638 cm^{-1} (Zhang et al., 2000), without the presence of additional bands associated with β-CD (Guo et al., 2010, Wang et al., 2021) since the Raman spectrum of unprocessed β-CD did not show signals in the selected Raman shift range (Mottola et al., 2022).

III.3 Photocatalytic activity test

The photocatalytic tests were always performed in a cylindrical pyrex reactor (ID = 3 cm and VTOT = 200 mL, Microglass Heim Srl, Naples, Italy). UV-LEDs strip emitting at 365 nm (nominal power: 10 W, provided by LED lightinghut, Shenzhen, China) was positioned around the external body of the reactor to irradiate the solution volume uniformly. The reactor was also equipped with an air distributor device (Qair = 150 cm3/min). During the light irradiation, the reaction suspension was continuously stirred to avoid the sedimentation of the catalyst at the bottom of the photoreactor. The initial AO7 concentration was 20 mg/L, the solution volume was 100

mL, and the photocatalyst dosage was 1 g/L. The suspension was left in dark conditions for 30 min to reach the adsorption/desorption equilibrium of AO7 on the photocatalyst surface. After this step, the photocatalytic reaction was begun by switching on the LEDs, with an overall irradiation time of 60 min. The analysis of withdrawn liquid samples was conducted through the UV-Vis spectrophotometer evaluating AO7 mineralization by the total organic carbon (TOC) content of the solutions during the irradiation time,.

The discoloration efficiency and mineralization (by TOC removal) were calculated with the same formulas used previously.

III.4 Photocatalytic activity results

III.4.1 Effect of the combination between PC500 and β-CD on AO7 degradation

All the photocatalysts were tested in the photocatalytic degradation of AO7 solution under UV irradiation. Figure III.6 shows the behavior of dye relative concentration as a function of irradiation time, proving the influence of SAS micronized β-CD combined with PC500 on the photocatalytic discoloration efficiency.

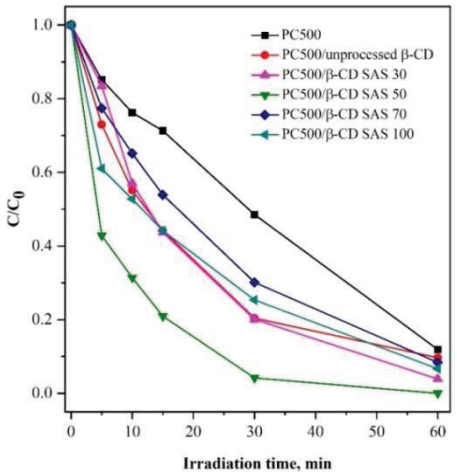

Figure III.6 *Photocatalytic discoloration of aqueous solutions containing AO7 using the various hybrid photocatalysts.*

It was possible to observe that the relative concentration of the AO7 gradually decreased for all the tested samples. In particular, all the hybrid

photocatalysts were more efficient in color removal than PC500. The higher photocatalytic activity of the PC500/ unprocessed β-CD sample with respect to PC500 was related to the role of β-CD. Indeed, according to the available literature, the attached β-CD played a role as a "channel" or "bridge" between AO7 and PC500, facilitating the electron injection from the excited dye to the conduction band of PC500 and, therefore, leading to a faster photodegradation of AO7 (Zhang et al., 2012, Sangari, 2018).

On the other hand, it is worthwhile to note that the samples obtained from the combination with SAS micronized β-CD were even more active than PC500 combined with the unprocessed β-CD. In detail, PC500/β-CD SAS 50 exhibited almost complete color removal after 30 min of UV light. The better activity of this hybrid sample can be related to its smaller agglomerate size (1.59 μm) in aqueous suspension (Table III.2). The TOC of solutions was measured to evaluate the prepared photocatalysts' mineralization performance (Mottola et al., 2022). TOC removal achieved with PC500/β-CD SAS50 is approximately 96% after 60 min of Uv light irradiation, higher than the mineralization efficiency obtained using PC500 and the other tested hybrid systems. These results confirm that PC500/β-CD SAS50 was the optimal hybrid photocatalyst both in terms of discoloration and mineralization of AO7 under UV light. To establish the effect of SAS micronized β-CD on photocatalytic performances, the apparent kinetic constant for AO7 discoloration was calculated, considering that the photodegradation mechanism follows pseudo-first-order kinetics, as described in the literature (Li et al., 2016, Wu et al., 2010b). The value of the discoloration kinetic constant (K_{dec}) is found by the slope of the straight line obtained by plotting $-\ln(C/C_0)$ vs the irradiation time (t). It was found that the PC500/β-CD SAS50 sample guaranteed a higher discoloration rate characterized by constant kinetics equal to 0.226 min^{-1}, higher than the PC500 alone and PC500/unprocessed β-CD, which showed constant values equal to 0.0326 min^{-1} and 0.055 min^{-1}, respectively. The discoloration kinetic constant decreased almost linearly with the increase of microparticles' mean size. From this result, it could be argued that the tendency for the agglomeration, and consequently the size of agglomerates, influence the ability of the different PC500/β-CD SASx samples in the AO7 photocatalytic discoloration. More in detail, when β-CD SAS50 is complexed with PC500, the organic phase spread on the TiO_2 surface allows achieving the smallest agglomerate size, leaving exposed to the UV light irradiation a PC500 photoactive surface higher than the other PC500/β-CD SASx hybrid photocatalysts and inducing, as a consequence, the best

photocatalytic activity of PC500/β-CD SAS50. Such a result is consistent with the literature about the influence of aggregate size on the photoactivity of TiO_2-based photocatalysts in aqueous suspensions (Vaiano et al., 2017b). Therefore, based on such results, the PC500/β-CD SAS50 sample is the optimal photocatalyst for the AO7 photodegradation.

III.4.2 Possible photocatalytic mechanism of PC500/β-CD SAS50 hybrid photocatalyst

The PC500/β-CD SAS50 hybrid photocatalyst was used to understand the possible role of reactive oxygen species (ROS), such as hydroxyl radicals and superoxide, during the AO7 photocatalytic discoloration process. The used scavenger probe molecules were: isopropanol (IPA, 10 mmol/L) for hydroxyl radicals (Zhang et al., 2018b) and benzoquinone (BQ, 1 μmol/L) for superoxide (Zhang et al., 2017). The effects of the scavengers on photocatalytic performances are shown in Figure III.7a.

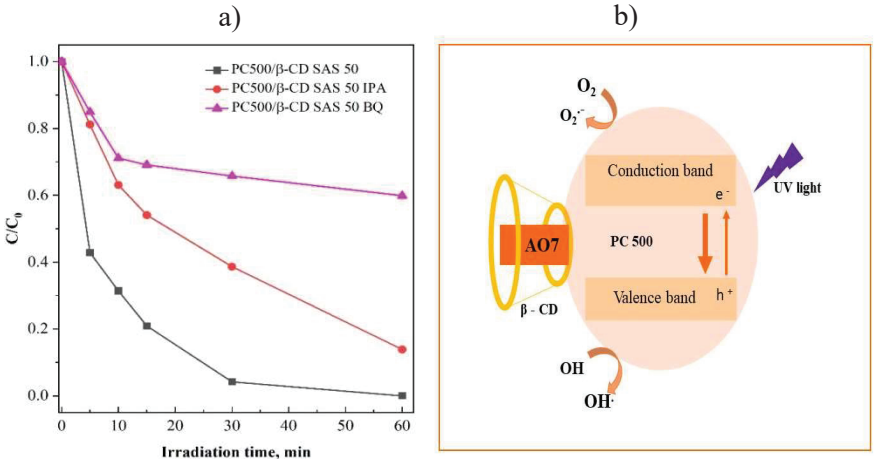

Figure III.7 *Effect of different scavengers on AO7 discoloration under UV light irradiation(a); schematic diagram on the charge separation and transfer in the presence of PC500/β-CD SAS 50 hybrid photocatalyst under UV light(b).*

It was observed that the AO7 discoloration rate is changed after the addition of both IPA and BQ in the aqueous solution. In detail, the BQ presence led

to AO7 discoloration efficiency of about 30%, whereas the addition of IPA decreased the photocatalytic activity to a lower extent since the obtained discoloration efficiency was 80 %. These results prove that both superoxide anions and hydroxyl radicals participate in the AO7 discoloration mechanism, and, in particular, the superoxide is more involved in the photocatalytic process. The mechanism of enhancing photocatalytic efficiency in the presence of β-CD for the discoloration of AO7 is schematically explained in Figure III.7b.
β-CD has a high affinity toward the PC500 surface; for this reason, β-CD is adsorbed on the surface and occupies the reaction sites of PC500, achieving the formation of a stable complex (Sangari, 2018). The presence of β-CD allows capturing the AO7 inside its hydrophobic cavity by generating the inclusion complexes, so increasing the density of azo dye on the catalyst surface and putting it in contact with the ROS generated during the UV light irradiation. Then, the photogenerated ROS reacts with AO7 molecules, enhancing the photocatalytic degradation performance (Zhang et al., 2009).

III.4.3 Stability test of PC500/β-CD SAS50 hybrid photocatalyst

Additional photocatalytic tests were performed to assess the stability of the PC500/β-CD SAS 50 photocatalyst that showed the best photocatalytic activity. In particular, the experiments were performed using a catalyst dosage of 1g/ L, with an initial AO7 concentration of 20 ppm and a solution volume equal to 100 mL. At the end of each test, the photocatalyst present in suspension was recovered and washed with distilled water in order to reuse it in a subsequent test carried out under the same operating conditions. After the fifth reuse cycle, the discoloration efficiency is only reduced of approximately 1%. These results confirm the stability of the optimized PC500/β-CD SAS 50 hybrid photocatalyst.

III.5 Photocatalytic activity tests using the optimized Fe-N-P/TiO_2 coupled with β-CD for enhancing thiacloprid degradation

In a typical activity test 1 g/L of photocatalyst powder was suspended in 100 mL of THI solution (initial concentration: 0.5 mg/L). The suspension was left in dark condition for 30 min to reach the adsorption equilibrium, and then photocatalytic reaction was initiated up to 2 hours. The experiments were performed with a pyrex cylindrical photoreactor (ID = 2.5 cm) equipped with an air distributor device (Qair = 150 cm^3/min (STP)), a

magnetic stirrer to maintain the photocatalyst suspended in the aqueous solution. The reactor was irradiated by an UV-A (emission: 365 nm; irradiance 13 W/m^2) and visible (emission range: 400–800 nm; irradiance: 16 W/m^2) LEDs strip wrapped around and in contact with external surface of the reactor body. Moreover, additional tests were carried out under the direct solar light (latitude 40°N, longitude 14°E), the average solar UV-A irradiance for all the tests was about 2.2 W/m^2. Experiments under the direct solar light were performed on May and typically started at 10.00–11.00 am till 01.00 - 02.00 pm. Sunlight irradiance spectra were measured by radiometer BLACK-Comet Stellar Net UV-VIS (StellarNet, Florida, 130 USA). Slurry samples were collected at fixed time intervals, and filtered for to remove the catalyst particles. The aqueous solution was then analyzed by HPLC UltiMate 3000 Thermo Scientific system (equipped with DAD detector, quaternary pump, column thermostat and automatic sample injector with 100μL loop) and using a reversed-phase Luna 5u C18 column (150mm×4.6mm i.d., pore size 5μm) (Phenomenex) at 25 °C. The mobile phase consisted of an acetonitrile/water mixture (70/30 v/v). The flow rate, injection volume and detection wavelength were 1 mL/min, 40 μL and 242 nm, respectively.

III.6 Effect of the combination between the optimized Fe-N-P/TiO_2 and β-CD on photocatalytic THI degradation

Fe-N-P/TiO_2 photocatalyst was tested in the photocatalytic degradation of THI solution under UV light. Figure III.8 shows the relative concentration of THI pesticide as a function of irradiation time, to compare the photodegradation activity exhibited by Fe-N-P/TiO_2 photocatalyst and Fe-N-P-TiO_2 combined with unprocessed β-CD and the influence of SAS micronization on the photocatalytic THI degradation using Fe-N-P-TiO_2/ β-CD.

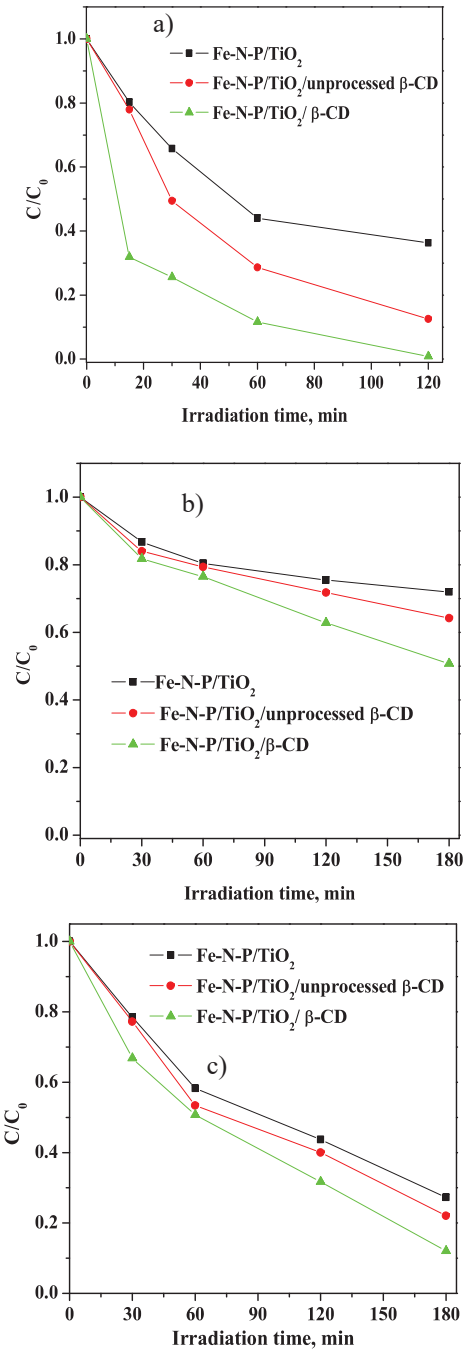

Figure III. 8 *Photocatalytic degradation of THI using the Fe-N-P/TiO₂, Fe-N-P/TiO₂ unprocessed β-CD and Fe-N-P/TiO₂/ β-CD micronized by SAS under UV light (a); under visible light (b) under sunlight (c).*

It is possible to observe from Figure III.8a that Fe-N-P/TiO_2 exhibits the lowest THI photodegradation activity under UV light, whereas the THI relative concentration quickly decreases under UV light using Fe-N-P/TiO_2 combined with unprocessed β-CD photocatalyst, especially in 30 min of UV irradiation, reaching a degradation efficiency of about 50%. The THI relative concentration using Fe-N-P/TiO_2/β-CD micronized by SAS technique decreases more quickly during 30 min of UV light than observed with Fe-N-P/TiO_2 photocatalyst and this micronized hybrid sample achieves a THI degradation efficiency of approximately 75% after 30 min of UV light.
Figure III.8b) shows the behaviour of THI relative concentration as a function of visible light irradiation revealing the most effective decrease of THI relative concentration with Fe-N-P/TiO_2/β-CD processed by SAS confirming the favorable effect of supercritical micronization and the combination of tridoped TiO_2 photocatalyst with β-CD on photocatalytic degradation performance in presence of visible light. Indeed, Fe-N-P/TiO_2/β-CD shows a THI degradation efficiency of approximately 50% after 180 min of visible light, higher than those observed with Fe-N-P/TiO_2/unprocessed β-CD and Fe-N-P/TiO_2, which are 36% and 29%, respectively.
The photocatalytic degradation of THI was also performed under sunlight. As reported in Figure III.8c, the Fe-N-P/TiO_2/β-CD hybrid sample micronized by SAS evidences the best photocatalytic THI degradation activity with an efficiency of about 88 % after 180 min of sunlight. On the other hand, Fe-N-P/TiO_2 sample degrades THI with an efficiency of 73% after 180 min of sunlight, a value higher than that obtained with Fe/N-P/TiO_2/unprocessed β-CD (78%). The results on photocatalytic degradation of THI confirm that the micronization of β-CD and their combination with catalytic particles led to charge-hole recombination restriction and photocatalytic efficiency enhancement since β-CD play electron-donating and hole-capturing roles when linked to TiO_2 colloids. β-CD is hypothesized to play a role as a "channel" or "bridge" between the contaminant and TiO_2 powders, which facilitates the electron injection from excited contaminant to the conduction band of TiO_2 (Zhang et al., 2011c). Therefore, the inhibition of the electron-hole recombination with consequent enhancement of the quantum efficiency due to the coupling of catalytic particles with β-CD micronized by SAS is particularly evidenced under visible light and sunlight where, Fe-N-P/TiO_2/β-CD shows the best photodegradation performance toward THI degradatrion.

IV. Experimental results: direct synthesis of phenol from benzene using photocatalysts in powder form

IV.1 Experimental apparatus for direct synthesis of phenol from benzene

The photocatalytic oxidation reactions were performed in 35 mL aqueous solution containing benzene (initial concentration: 25.6 mmol/L) and acetonitrile (2.3 mL) as a co-solvent with 0.1 g/L of photocatalyst in powder form or 3 g/L of nanostructured aerogel (corresponding to a powder dosage of 0.1 g/L) under continuous stirring. The system was first kept in dark at room temperature for 60 min to obtain sorption equilibrium of benzene on photocatalysts in powder form. Before irradiating the reactor, 2.8 mL of H_2O_2 (30 wt% in H_2O) was added to the reaction mixture. Then, the reactor was irradiated for 600 min by an UV-A (emission: 365 nm; irradiance 13 W/m^2) or visible (emission range: 400–800 nm; irradiance: 16 W/m^2) LEDs strip placed around and in contact to the external surface of the pyrex reactor. The reactor was cooled down by a fan during photoirradiation time. Solution aliquots were withdrawn from the reactor at different times by a 1mL syringe, filtered through a 0.22 µ CA filter (SIMPLEPURE) to remove solid particles for the tests with N-TiO_2 photocatalyst and immediately analyzed quantitatively by an Agilent gas cromatograph (model 7820 A) equipped with a flame ionization detector (FID) to evaluate the benzene and phenol concentration.
GC separation was achieved with a DB Heavy Wax fused-silica capillary column (30m x 0,35mm i.d. x 0,25µm) under the following conditions:

column temperature 40-300°C (40 °C held 2 min, rate 5 °C/min to 90 °C, rate 20 °C/min to 250 °C, held 10 min); helium at a constant flow rate of 1 mL/min; injection port operated at 10:1 split mode; temperature of injector and detector at 180 °C and 300 °C respectively.
Hydroquinone, resorcinol, p-benzoquinone and catechol were determined quantitatively by HPLC using a Dionex UltiMate 3000 Thermo Scientific system equipped with DAD detector, column thermostat and automatic sample injector with 100µL loop. Separations were carried out on a Phenomenex Luna C-18 column (150 x 4.6 mm i.d.; 5µm) eluted with mixture of water (solvent A) and acetonitrile (solvent B) according to the program: 0-14 min, 15% B (isocratic); 14-23 min, 60-100% B (linear gradient); 23-30 min, 15% B (isocratic). The chromatographic conditions were: oven temperature 35°C; flow rate 0.8mL min^{-1}; injection volume 50 µL and UV detector at 270 nm.
Benzene conversion, phenol yield, selectivity to phenol and selectivities to by-products were calculated using the following relationships:

$$Benzene\ conversion = \left(1 - \frac{C}{C_0}\right) x\ 100 \quad (36)$$

$$Phenol\ yield = \left(\frac{Q}{Q_0}\right) x\ 100 \quad (37)$$

$$selectivity\ to\ P\ (S_P)\ = \left(\frac{S\ (or\ Deg)}{S_{TOT}\ + De}\right) x\ 100 \quad (38)$$

where,

C_0 = benzene concentration after the dark period (mmol/L);
C = benzene concentration at the generic irradiation time (mmol/L);
Q_0 = moles of benzene in solution after the dark period (mmol);
Q = moles of produced phenol at the generic irradiation time (mmol);
P = reaction product (phenol or hydroquinone or catechol or resorcinol or p-benzoquinone);
S_{TOT} = total moles of the reaction products in liquid phase (mmol);
S= moles of phenol or hydroquinone or catechol or resorcinol or p-benzoquinone in liquid phase (mmol).

Deg= ring-opened products and CO_2 = (benzene reacted−S_{TOT}) (Zhang et al., 2011a)

IV.2. Results

IV.2.1 Direct oxidation of benzene to phenol using doped or codoped TiO_2 samples in powder form

It was considered appropriate to use for the direct oxidation of benzene to phenol under UV light and/or visible light irradiation the photocatalysts in powder form based on undoped TiO_2 and metallic and/or non-metallic elements doped TiO_2 (Fe-TiO_2, N-TiO_2, Fe-N-TiO_2, Fe-Pr-TiO_2 and Fe-N-P/TiO_2) previously optimized for the removal of contaminants from aqueous solution. Table IV.1 indicates benzene conversion, phenol yield and selectivity to phenol for all TiO_2-based photocatalyst in powder form under UV light.

Table IV. 1 *Benzene conversion, phenol yield and selectivity to phenol for all the optimized TiO_2-based photocatalyst in powder form under UV and visible light. [n.d.= not detectable]*

Catalyst	light	Benzene conversion, %	Phenol yield, %	Selectivity to phenol, %	light	Benzene conversion, %	Phenol yield, %	Selectivity to phenol, %
TiO_2	UV	72	2.7	3.8	visible	3	n.d.	n.d
N-TiO_2	UV	66	3.6	5.5	visible	62	n.d.	n.d.
Fe-TiO_2	UV	27	3.7	13.5	visible	23	n.d.	n.d.
Fe-N-TiO_2	UV	69	3.9	5.6	visible	30	n.d.	n.d.
Fe-Pr-TiO_2	UV	30	6.4	3.5	visible	27	n.d.	n.d.
Fe-N-P/TiO_2	UV	45	3.1	4.5	visible	39	n.d.	n.d.
Fe-N-P/TiO_2/β-CD	UV	55	1.5	1	visible	45	n.d.	n.d.

Table IV.1 shows benzene conversion, phenol yield and selectivity to phenol for all TiO_2-based photocatalyst in powder form under UV and visible light.
It is worth noting the high oxidative capacity of undoped TiO_2 under UV radiation. All TiO_2-based photocatalysts showed a high benzene conversion but very low selectivity to phenol under UV light. However, N-TiO_2 exhibits a high conversion of benzene under visible light without phenol production. Therefore, since N-TiO_2 was the only photocatalyst to exhibit the highest benzene conversion under visible light, the idea was to disperse N-TiO_2 in powder form into a polymeric medium in order to guarantee the phenol production and improve the selectivity to phenol also allowing, at the same time, a high conversion of benzene. Based on these results, it seems that the ideal support should have a high affinity with benzene (hydrophobic compound) and a very low affinity with phenol (hydrophilic compound),

favoring its desorption from the surface of the photocatalyst and preventing further reactions of oxidation of the desired product.
On the other hand, it is widely reported that nitrogen-doped TiO_2 (N-doped TiO_2) can be activated by both UV rays and visible light, essentially favoring the degradation of different organic compounds in aqueous solution and, therefore, the introduction of N in The TiO_2 lattice is only capable of modifying the light-absorbing properties of TiO_2 without giving it the ability to adjust the selectivity of the reactions involved towards the desired products. Therefore, the strategy was to disperse active N-doped TiO_2 particles with visible light in hydrophobic syndiotactic polystyrene (sPS) aerogel (Sacco et al., 2018a, Daniel et al., 2008, Daniel et al., 2005) and consequently, the resulting composite system was employed for the direct oxidation of benzene to phenol in liquid phase under UV irradiation and visible light with the aim of increasing both the selectivity of phenol and the conversion of benzene. It is worth noting that photocatalytic studies on the selective oxidation of benzene to phenol in the liquid phase are not reported in the literature using polymeric aerogels functionalized with photocatalytic particles.

V. Experimental results: direct oxidation of benzene to phenol using N-TiO_2/sPS

V.1 Synthesis and characterization of N-TiO_2/ sPS aerogel

The sPS polymer was dispersed in chloroform inside a hermetically sealed test tube at 100°C until complete polymer dissolution. The obtained mixture was sonicated at room temperature until complete gelation of the polymer and then cooled to produce a gel. The monolithic aerogels (D=0.5 cm and h= 5 cm) were obtained by treating the gels with supercritical carbon dioxide (by using an ISCO SFX 220 extractor), for 4 hours at T=40 °C and P= 20 MPa, to extract the solvent. The obtained aerogel was deeply characterized from physical-chemical point of view in our previous papers (Daniel and Guerra, 2015, Venditto et al., 2015). In summary, X-ray diffraction pattern shows typical signals of sPS delta crystal form (δ) in the 2θ range 8-25° with a degree of crystallinity of c.a. 40% and BET analysis evidences a high specific surface area equal to 260 m^2/g. For the preparation of N-TiO_2/sPS aerogel, sPS and N-TiO_2 were dispersed in chloroform inside hermetically sealed test tube at 100°C until complete polymer dissolution. The obtained mixture was sonicated at room temperature until complete gelation of the polymer and then cooled to produce a gel. The monolithic composite aerogels (D.I.=5.6 mm and a h= 3 cm) were obtained by treating the gels with supercritical carbon dioxide (by using an ISCO SFX 220 extractor), for 4 hours at T=40 °C and P= 20 MPa, to extract the solvent. In the final sample, the content of N-TiO_2 embedded into the aerogel structure was 10 wt%. This amount was optimized dealing with the photocatalytic degradation of phenol under visible light (Sacco et al., 2018a).

V.2 Experimental setup for absorption tests in dark conditions

The absorption tests were performed in 35 mL aqueous solution containing benzene (initial concentration: 50 mg/L), toluene (initial concentration: 50 mg/L) and phenol (initial concentration: 50 mg/L) using 3 g/L of sPS aerogel under continuous stirring for 1440 min to obtain absorption equilibrium of aromatic compounds. All the absorption tests were performed using a closed pyrex flask filled with the aqueous solutions maintained under continuous stirring. During each test, liquid samples were withdrawn from the pyrex flask at different times and analyzed quantitatively by an Agilent gas cromatograph (model 7820 A) equipped with a flame ionization detector (FID) to evaluate the benzene, toluene and phenol concentration.
GC separation was achieved with a DB Heavy Wax fused-silica capillary column (30 m x 0.35 mm i.d. x 0.25 μm) under the following conditions: column temperature 40-300 °C (40 °C held 2 min, rate 5 °C/min to 90 °C, rate 20 °C/min to 250 °C, held 10 min); helium at a constant flow rate of 1 mL/min; injection port operated at 10:1 split mode; temperature of injector and detector at 180 °C and 300 °C respectively. The chromatographic conditions were: oven temperature 35 °C; flow rate 0.8 mL/min; injection volume 50 μL and UV detector at 270 nm.

V.3 Experimental setup for photocatalytic activity tests

The photocatalytic oxidation reactions were performed in 35 mL aqueous solution containing benzene (initial concentration: 25.6 mmol/L) and acetonitrile (2.3 mL) as a co-solvent with 0.1 g/L of N-TiO_2 photocatalyst in powder form or 3 g/L of N-TiO_2/sPS aerogel (corresponding to an N-TiO_2 dosage of 0.1 g/L) under continuous stirring.
The system was first kept in dark (without any light irradiation) at room temperature for 60 min or for 1280 min to obtain sorption equilibrium of benzene on photocatalyst powder or on N-TiO_2/sPS aerogel, respectively. Before irradiating the reactor, 2.8 mL of H_2O_2 (30 wt% in H_2O) was added to the reaction mixture. Then, the reactor was irradiated for 600 min by an UV-A (emission: 365 nm; irradiance 13 W/m^2) or visible (emission range: 400–800 nm; irradiance: 16 W/m^2) LEDs strip placed around and in contact to the external surface of the pyrex reactor. The reactor was cooled down by a fan during photoirradiation time. Solution aliquots were withdrawn from the reactor at different times by a 1mL syringe, filtered through a 0.22 μ CA filter (SIMPLEPURE) to remove solid particles for the tests with N-TiO_2 photocatalyst and immediately analyzed quantitatively by an Agilent gas cromatograph (model 7820 A) equipped with a flame ionization detector (FID) to evaluate the benzene and phenol concentration.

GC separation was achieved with a DB Heavy Wax fused-silica capillary column (30m x 0,35mm i.d. x 0,25μm) under the following conditions: column temperature 40-300°C (40 °C held 2 min, rate 5 °C/min to 90 °C, rate 20 °C/min to 250 °C, held 10 min); helium at a constant flow rate of 1 mL/min; injection port operated at 10:1 split mode; temperature of injector and detector at 180 °C and 300 °C respectively.
Hydroquinone, resorcinol, p-benzoquinone and catechol were determined quantitatively by HPLC using a Dionex UltiMate 3000 Thermo Scientific system equipped with DAD detector, column thermostat and automatic sample injector with 100μL loop. Separations were carried out on a Phenomenex Luna C-18 column (150 x 4.6 mm i.d.; 5μm) eluted with mixture of water (solvent A) and acetonitrile (solvent B) according to the program: 0-14 min, 15% B (isocratic); 14-23 min, 60-100% B (linear gradient); 23-30 min, 15% B (isocratic). The chromatographic conditions were: oven temperature 35°C; flow rate 0.8mL/min; injection volume 50 μL and UV detector at 270 nm.
The mathematical formulas for the determination of benzene conversion, phenol yield, selectivity to phenol and selectivity to by-products are reported in IV.1.

V.4 Experimental Results

V.4.1 Characterization of N-TiO_2/sPS

The physico-chemical properties of the samples were investigated through the following characterization techniques:

- Wide angle X-ray diffraction (WAXD)
- N_2 adsorption at -196 °C to obtain specific surface area and porosity characteristics
- Field emission scanning electron microscopy (FESEM).

V.4.1.1 Wide angle X-ray diffraction (WAXD)

WAXD patterns with nickel filtered Cu-Kα radiation were obtained, with an automatic Bruker D8 Advance diffractometer, in reflection. As observed in Figure V.1, N-TiO_2 showed the presence of typical signals of titanium dioxide in anatase form. N-TiO_2/sPS showed the typical signals of the sPS structure and an additional one (at about 25.3 degrees) due to the titanium dioxide in anatase form. The mean crystallite size of N-TiO_2 remains substantially unchanged after inclusion in the sPS aerogel. The N-TiO_2/sPS

pattern also shows the diffraction peaks of the nanoporous delta crystalline form of sPS, whose degree of crystallinity (≈45%) is not substantially altered by the presence of the filler in the aerogel.

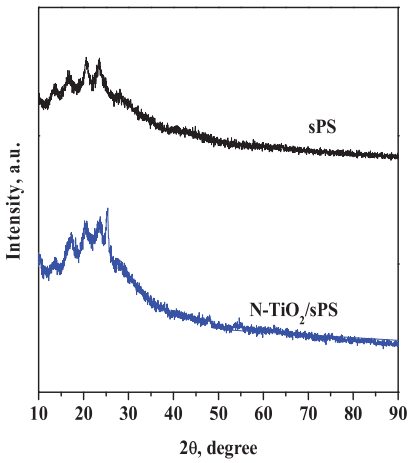

Figure V.1 *Wide angle X-ray diffraction (WAXD) patterns of sPS and N-TiO_2/sPS.*

V.4.1.2 Surface area and pore structure evaluation by N_2 adsorption at -196 °C.

The specific surface areas (S_{BET}) for N-TiO_2 sample, S_{BET} is equal to 115 m^2/g and for sPS is equal to 260 m^2/g. The presence of N-TiO_2 in the sPS aerogels determines a decrease of the specific surface area up to 222 m^2/g (Sacco et al., 2018a, Vaiano et al., 2014).

The high surface areas of the sPS aerogels is strictly depending on the nature of the polymer crystalline phase, varying from 20-40 m^2/g for the dense α, β and γ forms to 240-320 m^2/g for the nanoporous delta and epsilon forms (Daniel et al., 2009). Because the delta crystalline phase and its crystallinity remain essentially unaltered as a consequence of composite aerogel preparation, the insertion of the N-TiO_2 catalysts is to be found in the pores of highest dimension and the reduction of S_{BET} can be mainly attributed to the observed reduction of the overall porosity from 95% down to 80%. Moreover, a further confirmation that the reduction of the overall porosity is likely responsible of the decrease of S_{BET} with respect to that one of sPS aerogels in delta form, can be drawn from the proportional evaluation of the percentage of specific surface area exposed by the N-TiO_2/sPS aerogel, subtracted of the contribution of N-TiO_2, with respect to the sPS aerogel alone. This calculated percentage is close to the value of 80%, so almost coincident to the value of the overall porosity found. So, the micro- and meso-pores structure remains unaltered, and the slight decrease of the

specific surface area of composite N-TiO_2/sPS can be ascribed to the matrix shrinkage of the polymeric aerogel.

V.4.1.3 Field emission scanning electron microscopy (FESEM)

The morphology of N-TiO_2/sPS aerogels was revealed by FESEM analysis (Figure V.2). The N-TiO_2/sPS aerogels exhibited highly porous structure. However, N-TiO_2 particles (indicated as Nt in the Figure) could not be easily differentiated from the fibrillar morphology of the polymer (Figure V.2). Few small aggregates of N-TiO_2 particles are observable in the same figure and the overall network appears homogeneous.

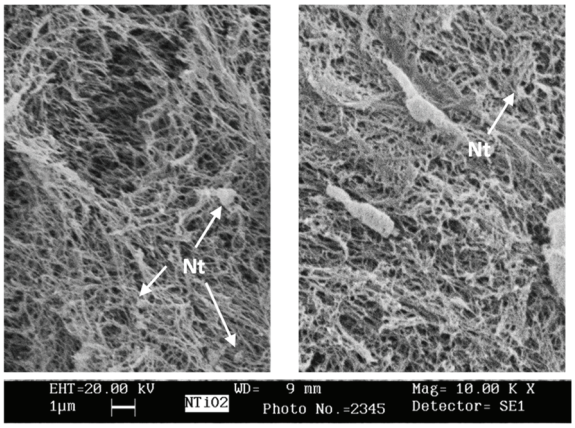

Figure V.2 *FESEM image of N-TiO_2-sPS aerogel*

V.4.2 Benzene, toluene and phenol absorption in sPS aerogels in dark conditions

Absorption tests by sPS aerogels were first performed on aqueous solution of a single aromatic compound: benzene (initial concentration: 50 mg/L), toluene (initial concentration: 50 mg/L) or phenol (initial concentration: 50 mg/L) and, subsequently, on binary and ternary mixtures of these organic compounds. Under these experimental conditions, the solute molecules are absorbed only in the nanoporous crystalline lattice of sPS δ-form (Mensitieri et al., 2008)] .
The relative concentration in liquid phase of these organic compounds as a function of run time is displayed in Figure V.3.

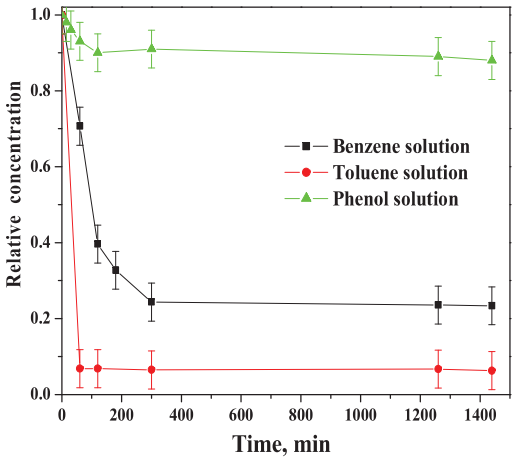

Figure V.3 *Benzene, toluene and phenol relative concentration (C/C_0) in aqueous solution as a function of run time using sPS aerogel ($C_{0\ benzene}$ = 50 mg/L, $C_{0\ toluene}$ = 50 mg/L, $C_{0\ phenol}$ = 50 mg/L).*

A very high absorption efficiency of toluene (~94%) and benzene (~77%) by sPS aerogels after 1440 min of run time were found, whereas phenol was poorly absorbed in the same conditions with an efficiency of about 12%.
In agreement to the literature, this result can be explained by the ability of the sPS, due to its hydrophobic nature, to absorb non-polar aromatic compounds (benzene and toluene), compared to polar compounds (phenol), in the cavities of its nanoporous lattice (Devaraji et al., 2014, Ide et al., 2011, Zhang et al., 2011a).
The affinity of sPS aerogel towards non-polar compounds was more emphasized in presence of a binary aqueous solutions containing benzene and phenol. Indeed, benzene was selectively retained into the cavities of sPS nanoporous lattice with an efficiency equal to 80% while the phenol was absorbed by the aerogel for only 2%. This behavior was further demonstrated with a toluene-phenol binary aqueous solution where the decrease of toluene relative concentration was very fast and, therefore, the toluene was largely absorbed by polymer with an efficiency equal to 88% after 60 min of run time, whereas the phenol absorption efficiency was very low and equal to 2.5% (Table V.1).
Furthermore, the absorption capacity of non-polar compounds by sPS polymer was investigated considering benzene-toluene binary aqueous solution Table V.1.
Both non-polar aromatic compounds were remarkably entrapped into crystalline nanoporous cavities of sPS. However, toluene was absorbed by n-sPS aerogel more rapidly than benzene obtaining a high absorption

efficiency of toluene equal to 84% after 60 min of run time compared to that of benzene (47%). In detail, toluene reached the absorption equilibrium with an efficiency of approximately 92%, whereas the benzene was uptaken by n-sPS aerogel for about 75% after 1440 min. This result further confirms the very high affinity of sPS aerogel towards the absorption of non-polar aromatic compounds.

Moreover, it was examined as the sPS polymer selectively absorbs benzene and toluene with respect to phenol considering benzene-toluene-phenol ternary mixture (Table V.1).

Table V.1 underlines as toluene and benzene were absorbed strongly into sPS aerogel with sorption efficiency of about 87% and 76% after 1440 min of treatment time, respectively, while phenol was hardly absorbed in the same conditions, achieving a sorption efficiency of approximately 2%. In particular, it was possible to notice as the relative concentration of toluene decreases more rapidly than that of benzene already after 60 min, showing a preferential absorption of toluene by sPS aerogel also in the case of benzene-toluene-phenol ternary mixture.

All the achieved experimantal results are summarized and reported in Table V.1.

Table V.1 *Equilibrium absorption efficiency of aromatic compound by sPS aerogel*

Aromatic compound aqueous solution	Equilibrium absorption efficiency
Benzene	77%
Toluene	94%
Phenol	12%
Binary aqueous mixture	
Benzene in benzene-phenol	80%
Phenol in benzene-phenol	2%
Toluene in toluene-phenol	88%
Phenol in toluene-phenol	2.5%
Benzene in benzene-toluene	75%
Toluene in benzene-toluene	92%
Ternary aqueous mixture	
Benzene in benzene-toluene-phenol	76%
Toluene in benzene-toluene-phenol	87%
Phenol in benzene-toluene-phenol	2%

V.4.3 Evaluation of diffusivity constant in sPS aerogel

To calculate the diffusivity coefficient of guest aromatic molecules inside the sPS aerogel structure for the tested operating conditions, it was first simulated the concentration profile of each compound as a function of run time, using a pseudo-first-order kinetics model for the absorption process, in agreement with the literature concerning the removal of aromatic compounds from the liquid phase by means of PS nanofibers (Sun et al., 2011). In detail, the mathematical model was developed considering that, in the closed pyrex flask, sPS aerogel absorbs aromatic compounds from aqueos solution, causing a decrease of their concentration during the run time until to reach the equilibrium conditions.

Therefore, the concentratration of benzene, toluene and phenol in liquid phase was calculated by the following mass balance (eq.39):

$$V\frac{dC}{dt} = -k(C(t) - C_\infty) \cdot m \qquad (39)$$

Where,

C_∞ is equilibrium concentration of benzene, toluene and phenol (ppm); k is absorption kinetics constant (L/g·min); m is sPS aerogel mass (g); V is aqueous solution volume (L).

The initial condition is: t=0 $C=C_0$.

Eq.39, together with the initial condition, was solved by the Eulero iterative method.

The simulation goal by mathematical model was to identify the absorption constant k by fitting the achieved experimental data. The fitting procedure was done by using the least squares approach. Figure V.4a compares the model calculations and the experimental data for the aqueous solutions containing a single aromatic compound. It was important to underline that the concentration values predicted by the model are in agreement with the experimental data in all cases, validating the use of the pseudo-first order type kinetic model for the absorption process. The obtained k values are reported in Table V.2.

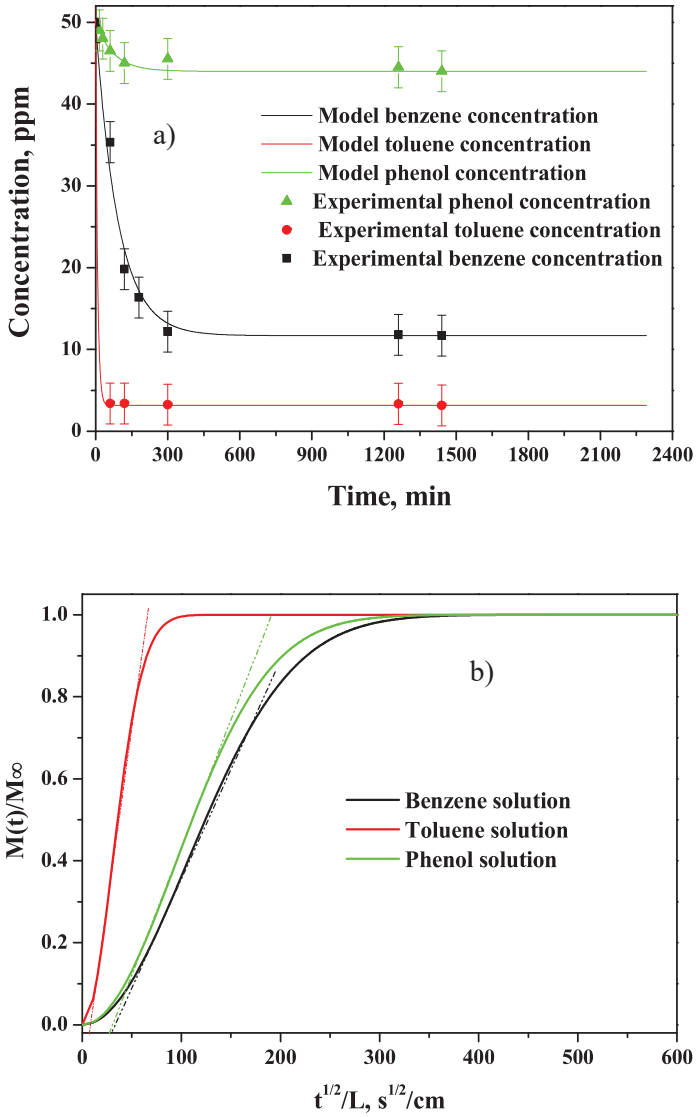

Figure V.4 *Comparison between model calculation and experimental data to find the model absorption constant k for the aqueous solutions containing a single aromatic compound ($C_{0benzene}$ = 50 mg/L, $C_{0toluene}$ = 50 mg/L, $C_{0phenol}$ = 50 mg/L)* a*) and estimation of diffusivity constants for aqueous solution of aromatic compound b).*

The obtained concentration profiles allow to calculate the amount of aromatic compounds absorbed by the aerogel at any given time t (eq.40) and when the equilibrium condition is achieved (eq.41).

$$M(t) = \frac{(C_0 - C(t))}{m} \cdot V \tag{40}$$

$$M_\infty = \frac{(C_0 - C_\infty)}{m} \cdot V \tag{41}$$

The apparent diffusivity constants (D) take into account the diffusion both in the amorphous phase and in the crystalline phase. D values (Table V.2) were calculated from the slopes of linear region of the curves reporting the behaviour of $M(t)/M_\infty$ as a function of time square root divided by the macroscopic thickness ($t^{1/2}/L$) of sPS aerogel (Figure V.4b) to evidence the Fick diffusion phenomena into sPS, as described in literature (Daniel et al., 2008, Kuipers and Beenackers, 1993)

Table V.2 *Absorption kinetics and apparent diffusivity constants for aromatic compounds aqueous solution in sPS aerogel. ($C_{0\ benzene}$ = 50 mg/L, $C_{0\ toluene}$= 50 mg/L $C_{0phenol}$= 50 mg/L)*

Aromatic compound aqueous solution	Absorption kinetics constant (k), L/(g·min)	Diffusion constant (D), cm^2/s
Benzene	$3.4 \cdot 10^{-3}$	$5.5 \cdot 10^{-3}$
Toluene	$4 \cdot 10^{-2}$	$1.9 \cdot 10^{-2}$
Phenol	$4.2 \cdot 10^{-3}$	$6.2 \cdot 10^{-3}$

for toluene ($k=4 \cdot 10^{-2}$ L/(g·min)). However, the aerogel exhibits a phenol absorption kinetic ($k=4.2 \cdot 10^{-3}$ L/(g·min)) slightly higher than that obtained for benzene ($k=3.4 \cdot 10^{-3}$ L/(g·min)). Similarly, the diffusivity constant found for phenol ($D=6.2 \cdot 10^{-3}$ cm^2/s) is a little higher than the diffusivity value obtained for benzene ($D=5.5 \cdot 10^{-3}$ cm^2/s). This result evidences that, despite it is absorbed in lower extent with respect to benzene and toluene, phenol is able to diffuse into the crystalline phase of sPS aerogel when it is the only aromatic compound present in the aqueous medium.
The mathematical kinetic modeling was also performed on binary aqueous mixtures (benzene-phenol, toluene-phenol and benzene-toluene). Figure V.5 shows the kinetic modelling for the benzene-phenol mixture.

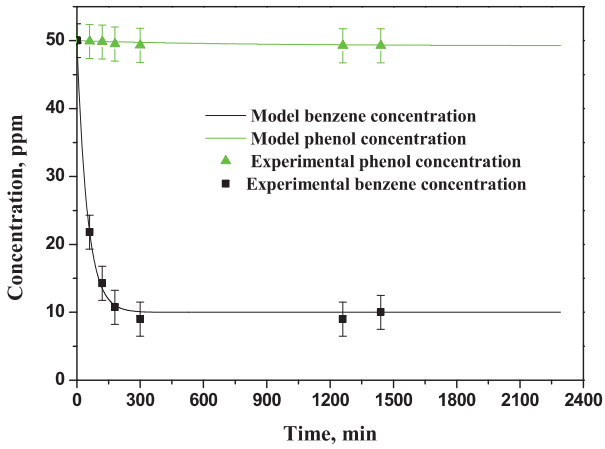

Figure V.5 *Comparison between model calculation and experimental data to find the model absorption constant k for benzene-phenol binary aqueous solution ($C_{0\ benzene}$ = 50 mg/L, $C_{0phenol}$= 50 mg/L).*

The trend of curves in Figure V.5 evidenced as the concentration of non-polar aromatic compounds decreased progressively over the time indicating that benzene and toluene were widely absorbed by sPS aerogel, whereas phenol, being a polar aromatic compound and, therefore, being not affine with the sPS hydrophobic nature (Daniel et al., 2008, Joseph et al., 2018, Sacco et al., 2019), poorly entered into the polymer crystal structure. This result was also confirmed by the curves related to the behaviour of $M(t)/M_\infty$ (Figure V.6) since for benzene and toluene, $M(t)/M_\infty$ achieved the equilibrium value at shorter times than that of phenol.

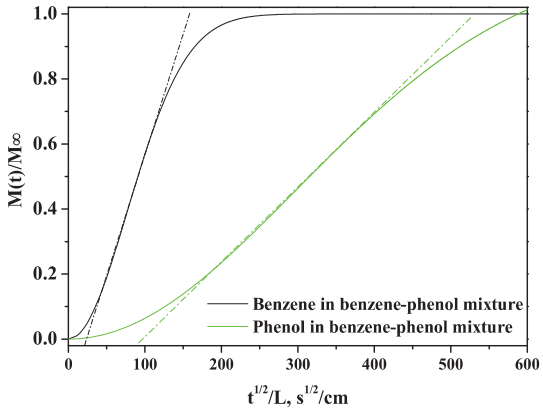

Figure V.6 *Estimation of diffusivity constants for the benzene-phenol binary aqueous solution.*

The values of k and D constants for binary aqueous solutions are reported in Table V.3

Table V.3 *Absorption kinetics and apparent diffusivity constants for binary aqueous mixture in sPS aerogel. ($C_{0\ benzene}$ = 50 mg/L, $C_{0\ toluene}$= 50 mg/L $C_{0phenol}$ = 50 mg/L).*

Binary aqueous mixture	Absorption kinetic constant (k), L/(g·min)	Diffusion constant (D), cm^2/s
Benzene in benzene-phenol	$6.4 \cdot 10^{-3}$	$7.0 \cdot 10^{-3}$
Phenol in benzene-phenol	$4.3 \cdot 10^{-4}$	$2.3 \cdot 10^{-3}$
Toluene in toluene-phenol	$4.5 \cdot 10^{-2}$	$1.9 \cdot 10^{-2}$
Phenol in toluene-phenol	$4.8 \cdot 10^{-4}$	$2.4 \cdot 10^{-3}$
Benzene in benzene-toluene	$5.4 \cdot 10^{-3}$	$6.5 \cdot 10^{-3}$
Toluene in benzene-toluene	$1.0 \cdot 10^{-2}$	$8.7 \cdot 10^{-3}$

The data collected in Table V.3 evidence sPS aerogel more rapidly absorbed benzene or toluene considering their binary mixture with phenol while, in presence of toluene and benzene aqueous mixture, toluene was preferentially uptaken by the aerogel with a superior kinetic ($k=1.0 \cdot 10^{-2}$ L/(g·min)) and higher diffusivity constant ($D=8.7 \cdot 10^{-3}$ cm^2/s) with respect to benzene.
Finally, the simulation through mathematical model was also performed for a benzene-toluene-phenol ternary mixture with the aim to estimate k and D values (Table V.4). The decrease of benzene and toluene concentration during the time indicating that sPS aerogel tends to preferentially absorb non-polar aromatic compounds and, in particular toluene with higher absorption rate ($k=1 \cdot 10^{-2}$ L/(g·min)) (Table V.4). The absorption of phenol by sPS is negligible proving again the low affinity of polymer towards polar compounds.
This behaviour was also confirmed by trend of $M(t)/M_\infty$ for toluene that achieves the equilibrium at slightly lower times than benzene with a diffusivity constant for toluene equal to about $9.0 \cdot 10^{-3}$ cm^2/s and for benzene of approximately $7.8 \cdot 10^{-3}$ cm^2/s (Table V.4).

Table V.4 *Absorption kinetics and apparent diffusivity constants for benzene-toluene-phenol ternary aqueous solution in sPS aerogel ($C_{0\ benzene}$ = 50 mg/L, $C_{0\ toluene}$ = 50 mg/L $C_{0phenol}$ = 50 mg/L)*

Ternary aqueous mixture	Absorption kinetics constant (k), L/(g·min)	Diffusivity constant (D), cm^2/s
Benzene in benzene-toluene-phenol	$7.6 \cdot 10^{-3}$	$7.9 \cdot 10^{-3}$
Toluene in benzene-toluene-phenol	$1 \cdot 10^{-2}$	$9.0 \cdot 10^{-3}$
Phenol in benzene-toluene-phenol	–	–

V.4.4 Photocatalytic oxidation of benzene to phenol with N-TiO_2/sPS aerogel

The UV light-driven benzene oxidation, using N-TiO_2/sPS as photoreactive solid phase, is shown in Figure V.7.

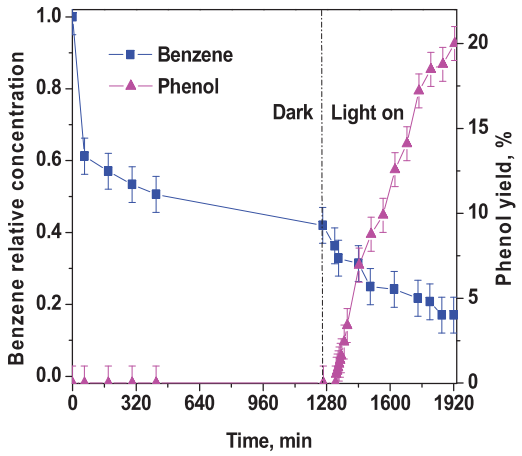

Figure V.7 *Benzene relative concentration and phenol yield as a function of run time, in dark and under UV light, using N-TiO_2/sPS as photocatalytic solid phase.*

In the absence of UV light (dark condition), N-TiO_2/sPS absorbs almost 60% of benzene after 1280 min. It is worthwhile to note that no phenol formation was observed in dark conditions despite the presence of H_2O_2, indicating that light is necessary to activate catalytically the desired reaction. This result is consistent with the literature dealing with the selective formation of phenol

from benzene photooxidation when H_2O_2 is used as oxidant molecule (Ye et al., 2014, Devaraji and Jo, 2018).
When UV-LEDs were switched on, benzene started to be converted and, consequently, its relative concentration decreased with run time (Figure V.7). Phenol yield progressively increased during irradiation time, reaching a value of 20%, after 600 min of irradiation, clearly indicating that the photoreactive solid phase is able to promote the formation of phenol via benzene hydroxylation in presence of UV light. Under irradiation, electrons are promoted from the valence band (VB) to the conduction band (CB) of N-TiO_2. Hydroxyl radicals are then generated from the reaction between H_2O_2 and the electrons promoted in the CB of N-TiO_2 (Chu et al., 2007, Mancuso et al., 2022a). The hydroxyl radical reacts with benzene to generate hydroxylated benzene radical and, finally, the photogenerated positive hole in the VB of N-TiO_2 oxidize hydroxylated benzene radical to phenol via a deprotonation process (Tomita et al., 2011, Devaraji and Jo, 2018). Furthermore, the holes in the VB can react with benzene to produce benzene radical ions, which react with hydroxyl radicals, forming phenol, probably via deprotonation of an unstable intermediate (Devaraji and Jo, 2018).
Photocatalytic activity using N-TiO_2 in powder form and N-TiO_2/sPS aerogel, under UV and visible light irradiation, was compared in Figure V.8.
In detail, after 600 min of UV light irradiation, benzene conversion was 66 and 52 % using N-TiO_2 and N-TiO_2/sPS, respectively (Figure V.8a), while the phenol yield was 4 and 20% with N-TiO_2 and N-TiO_2/sPS, respectively (Figure V.8b). It is worth pointing out that although benzene conversion is similar using N-TiO_2 powder and N-TiO_2/sPS aerogel, the phenol yield is five times greater when N-TiO_2/sPS is used.
After 600 min of visible light irradiation, benzene conversion was about 62 and 72% with N-TiO_2 powder and N-TiO_2/sPS aerogel, respectively (Figure V.8c), while phenol is not produced using N-TiO_2 and a phenol yield of only 6.5% is obtained using N-TiO_2/sPS (Figure V.8d). The observed mismatch between benzene conversion and phenol yield is obviously due to the formation of reaction products other than phenol.

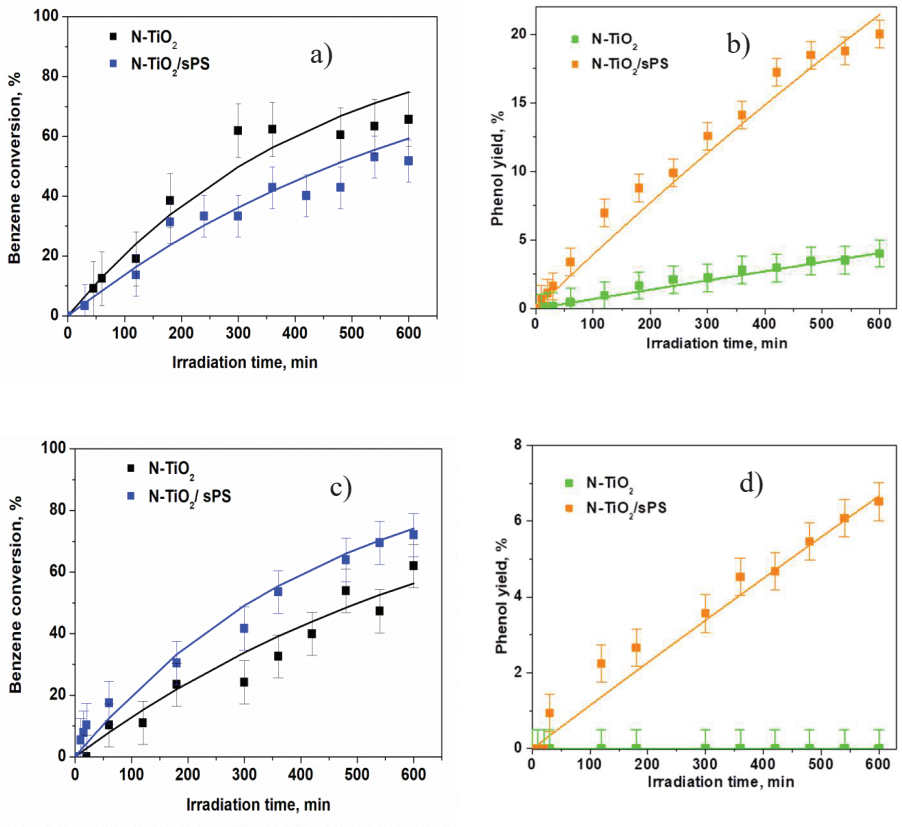

Figure V.8 *Benzene conversion and phenol yield as a function of irradiation time using N-TiO_2 in powder form and N-TiO_2/sPS photoreactive composite. Benzene conversion under UV light (a); phenol yield under UV light (b); benzene conversion under visible light (c); phenol yield under visible light (d).*

In Table V.5 phenol yield is compared with that of other reaction by-products (hydroquinone, catechol resorcinol and p-benzoquinone) detected by HPLC analysis. These reaction by-products are also shown in several literature papers (Schneider et al., 2014, Devaraji et al., 2014, Zhang et al., 2011a).

Table V.5 *Benzene conversion, phenol selectivity, CO_2 and other ring-opened compounds selectivity, phenol, yield to hydroquinone, catechol and resorcinol obtained using N-TiO_2 or N-TiO_2/sPS after 600 min of UV and visible light irradiation (Vis) (p-benzoquinone was also detected with a yield<1% in all cases).*

Catalyst	light	Bz_{conv}	Y_{phenol}	$Y_{hydroquinone}$	$Y_{catechol}$	$Y_{resorcinol}$	S_{phenol}	S_{Deg}
N-TiO_2	UV	66%	4%	<1%	n.d	<1%	5.5%	93%
N-TiO_2/sPS	UV	52%	20%	1.3%	1.8%	n.d	38%	54%
N-TiO_2	Vis	62%	n.d	<1%	n.d	n.d	n.d	>98%
N-TiO_2/sPS	Vis	72%	6.5%	<1%	<1%	n.d	9%	88%

According to the data in Table V.5, the phenol selectivity using N-TiO_2/sPS is remarkably higher than that obtained with N-TiO_2 in powder form under both UV and visible light. Indeed, the selectivity to ring-opened products and CO_2 (labeled as S_{Deg} in Table V.5) decreases in presence of N-TiO_2/sPS for both irradiation conditions.

Therefore, the phenol overoxidation reactions were inhibited to a certain extent thanks to the sPS aerogel polymeric matrix in which N-TiO_2 photocatalyst is embedded.

The results can be rationalized based on the different affinity of benzene (a non-polar compound) and phenol (a polar compound) with sPS aerogel (a non-polar polymer). As shown in Figure V.4, even in a binary benzene-phenol aqueous solution, the benzene solubility in the sPS polymer is six times more than the phenol one. Therefore, the phenol formed by benzene hydroxylation with N-TiO_2 photocatalyst dispersed in the sPS matrix, easily desorbs from the polymer considerably preventing the phenol overoxidation reactions (Figure V.9).

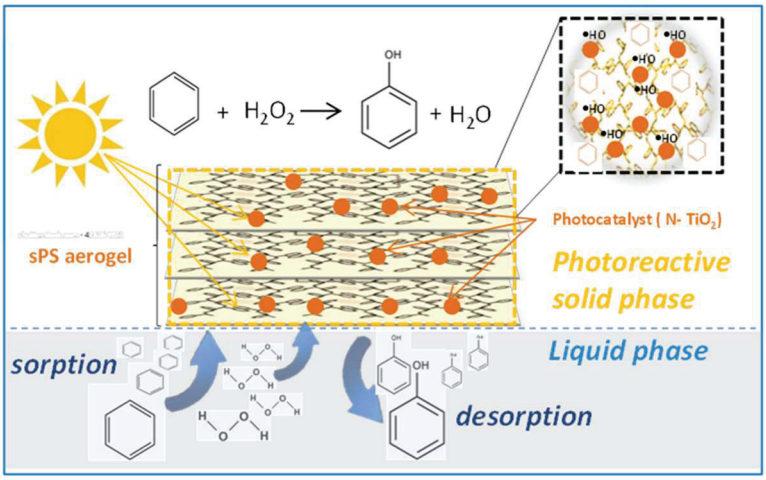

Figure V.9 *Reaction scheme of benzene to phenol using N-TiO_2/sPS as photoreactive solid phase under visible light.*

V.4.4.1 Influence of pH on selectivity to phenol

Based on previous obtained results, a possible route to increase the phenol selectivity is to further reduce the phenol affinity towards sPS polymer, increasing its affinity towards the aqueous phase surrounding the N-TiO_2/sPS solid phase. It has been recently reported that a decrease in the pH of the aqueous solution in which the sPS polymer is immersed drastically decreases the phenol sorption in the sPS aerogel (Sacco et al., 2019).
To confirm such behavior also for N-TiO_2/sPS composite, additional experiments in dark conditions were carried out to measure the amount of phenol absorbed from the aqueous phase at different pH values (Figure V.10).

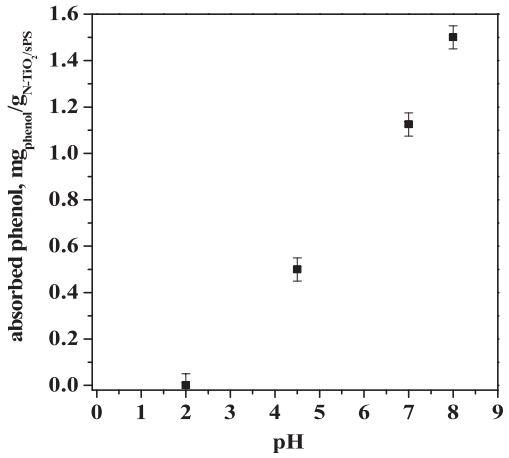

Figure V.10 *Effect of pH on phenol absorption by N-TiO_2/sPS composite in dark conditions ($C_{0\,phenol}$ = 0.5 mmol/L; N-TiO_2/sPS amount: 3g/L).*

As result, the pH of the solution influenced the phenol uptake. In detail, there was a progressive increase of phenol absorption into N-TiO_2/sPS with pH increase, while no phenol absorption was observed at pH=2. In strongly acidic conditions, phenol forms clusters with H_3O^+ (Parthasarathi et al., 2007), which give rise to an electrostatic repulsion with the sPS polymer, totally preventing the phenol absorption into the polymer itself (Sacco et al., 2019). According to literature findings (Sacco et al., 2019) and considering the results reported in Figure V.10, the pH of the aqueous phase surrounding the N-TiO_2/sPS photoreactive solid phase was changed from about 7 to 2 by adding hydrochloric acid.

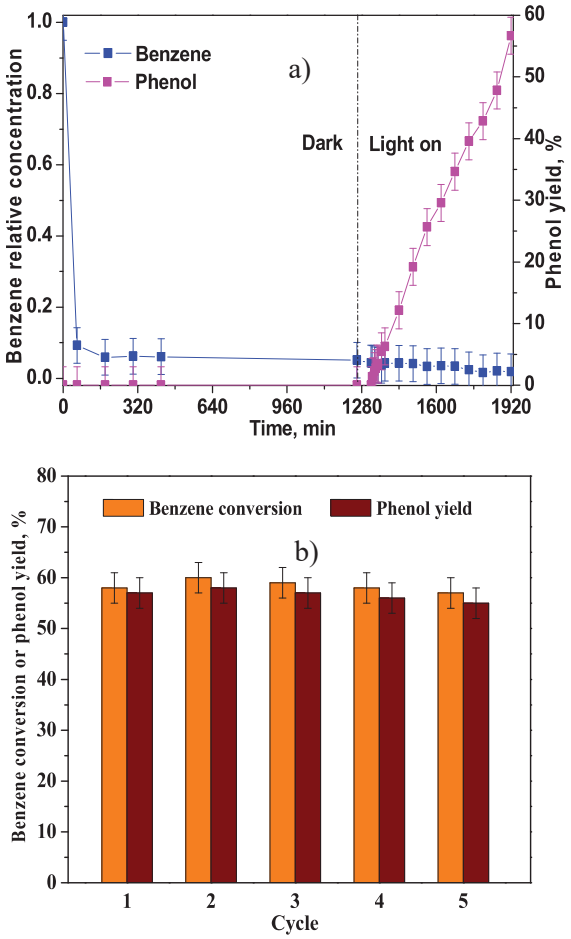

Figure V.11 *Benzene relative concentration and phenol yield as a function of run time under visible light at pH=2 using N-TiO_2/sPS photoreactive composite a); benzene conversion and phenol yield after 600 min of visible light irradiation at pH=2 for different reuse cycles b).*

The visible light-driven benzene oxidation, using N-TiO_2/sPS photoreactive solid phase surrounded by aqueous phase at pH = 2, is shown in Figure V.11. The reaction driven by visible light was preferred over the one driven by UV light since the former is the one showing a lower phenol yield and selectivity (see data in Table V.6).

Figure V.11a evidenced that benzene concentration drastically decreased in the dark period, achieving a sorption efficiency of approximately 91%. Under visible light irradiation, phenol was obtained as the main product and its yield was 57 % after 600 min of irradiation.

Photocatalytic performances obtained using N-TiO_2/sPS, under visible light irradiation, in neutral (pH=7) and acidic conditions (pH=2), are compared in Table V.6, to better evaluate the impressive contribution that acidic conditions give to the selectivity of benzene hydroxylation to phenol. At pH=2, phenol selectivity and phenol formation rate were, respectively, 98% and 0.63 mmol/($g_{N\text{-}TiO2}$·h), remarkably higher than those achieved at pH=7 (9% and 0.31 mmol/($g_{N\text{-}TiO2}$·h)). It is worth pointing out that the selectivity to ring-opened products and CO_2 is lower than 1% at pH=2.

Table V.6 *Benzene conversion, phenol formation rate (F_{phenol}), selectivity to phenol and selectivity to ring-opened products and CO_2 using N-TiO_2/sPS under visible light in neutral (pH=7) and acidic conditions (pH=2)*

Catalyst	pH	Bz_{conv}	F_{phenol}	S_{phenol}	S_{Deg}
N-TiO_2/sPS	7	72%	0.31 mmol/($_{gN\text{-}TiO2}$·h)	9%	88 %
N-TiO_2/sPS	2	58%	0.63 mmol/($_{gN\text{-}TiO2}$·h)	98%	<1%

To prove the stability of N-TiO_2/sPS, recycling experiments were performed under the reaction conditions that allowed to achieve the best results (under visible light and at pH=2). The N-TiO_2/sPS composite was removed from the liquid phase, dried at room temperature for 24 hours and reused up to five times. As shown in Figure V.11b, any significant decrease both in benzene conversion and phenol yield was observed, demonstrating the stability of the catalytic material.

V.4.5 Proposed reaction mechanism

Based on the concentration profiles of by-products detected by HPLC analysis during irradiation (Figure V.12 and Figure V.15) and the mechanism hypotheses reported in the literature (Zhang and Park, 2019, Devaraji and Jo, 2018), a possible reaction path was proposed.

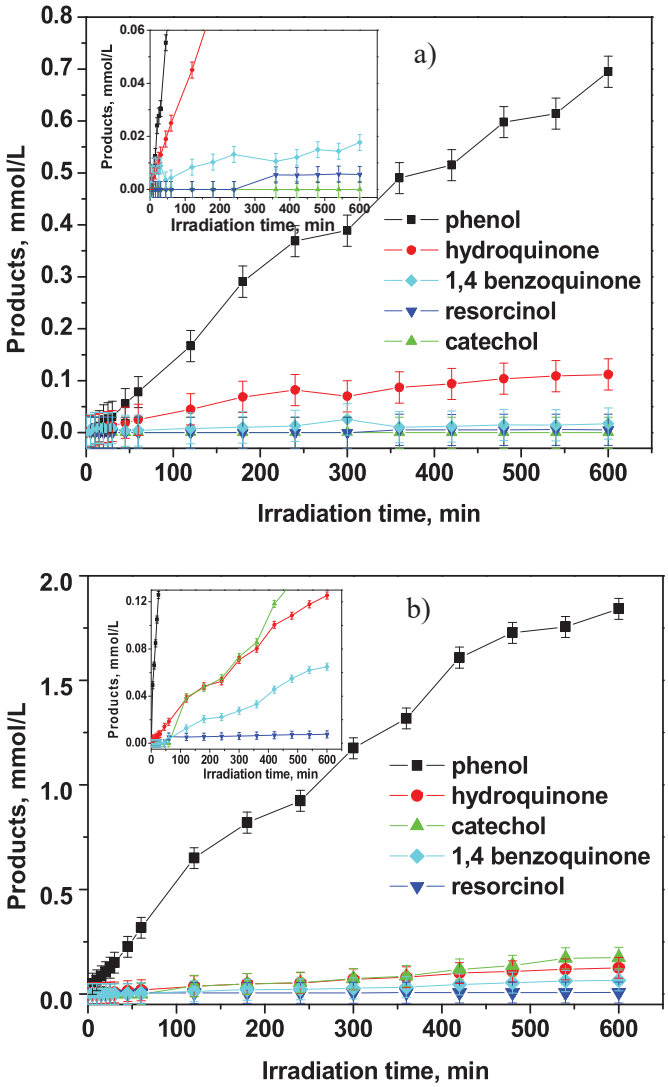

Figure V.12 *Reaction products concentration (mmol/L) as function of irradiation time (min) with N-TiO_2 photocatalyst in powder form under UV light irradiation (a); Reaction products concentration (mmol/L) as function of irradiation time (min) with N-TiO_2/sPS photoreacrive composite under UV light irradiation (b).*

Concentration variation of by-products, detected in the liquid phase, during the photocatalytic tests carried out by irradiating N-TiO_2 photocatalyst and N-TiO_2/sPS with UV light (Figure V.12a), showed that the first photoproduced compound is phenol. In detail, with N-TiO_2, hydroquinone is detected almost simultaneously with phenol, while all the other by-products

are detected at a longer time (Figure V.12a). Therefore it is reasonable to assume that, in the case of N-TiO_2, phenol and hydroquinone are formed directly from benzene. Using N-TiO_2/sPS, all reaction by-products are instead detected at much longer times than phenol (Figure V.12b). Therefore, it is reasonable to assume that they are produced from phenol rather than benzene.

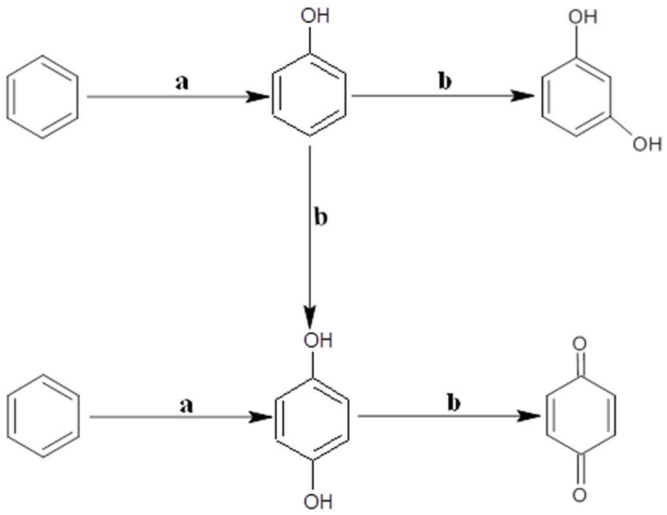

Figure V.13 *Scheme of possible reaction mechanism on benzene oxidation with N-TiO_2 photocatalyst under UV light.*

Based on these observations, two possible reaction paths (**a** and **b** in Figure V.13) were proposed for the mechanism of benzene oxidation using N-TiO_2 photocatalyst in powder form under UV light irradiation. In path **a** of Figure V.13, benzene is directly hydroxylated to phenol and hydroquinone. Hydroquinone oxidizes consequently producing benzoquinone (path **b** in Figure V.13) However, hydroquinone and resorcinol can be also produced by phenol hydroxylation (path **b** in Figure V.13). Based on the data reported in Table V.6, further oxidation of benzoquinone to CO_2 and other ring-opened compounds occurs (Schneider et al., 2014, Bui et al., 2011). On the other hand, a different reaction mechanism could be presumed with N-TiO_2/sPS (Figure V.14). Starting from the benzene, the primary reaction product is phenol which oxidizes to give catechol and hydroquinone (in this case resorcinol was not detected). Hydroquinone can further be oxidized to benzoquinone. Also in this case, further oxidation of benzoquinone to CO_2 and other ring-opened compounds is evidenced by data reported in Table V.6.

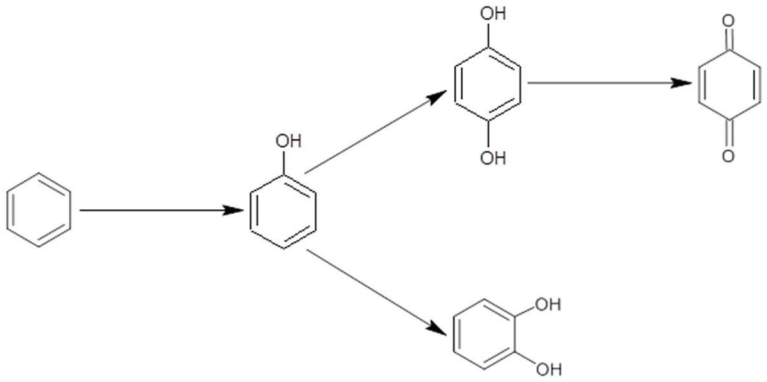

Figure V.14 Scheme of ossible reaction mechanism on benzene oxidation with N-TiO_2/sPS under UV light.

Variation of by-product concentrations, detected under visible light in the liquid phase at pH=7, showed that phenol is detected only when N-TiO_2/sPS is used (Figure V.15). Indeed, by using N-TiO_2, benzene is completely converted to CO_2 and other ring-opened compounds (S_{Deg}>98%).
By using N-TiO_2/sPS (Figure V.15), phenol is the main reaction product and only traces of hydroquinone, benzoquinone and catechol are evident. Therefore it is possible to argue that a reaction mechanism close to that observed under UV light occurs under visible light. However, also in this case, most of the benzene is converted to CO_2 and other ring-opened compounds (benzene conversion: 72%; S_{Deg}: 88 %).

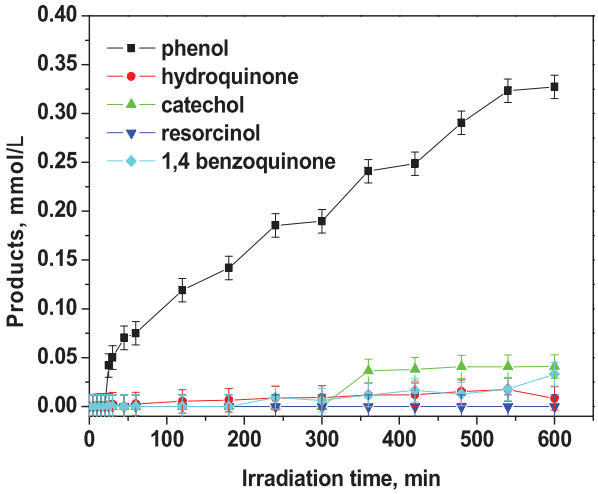

Figure V.15 *Reaction products concentration (mmol/L) as function of irradiation time (min) with N-TiO_2/sPS photoreactive composite under visible light irradiation.*

The reaction mechanism at pH=2 is identical to that at pH=7, but the phenol overoxidation is prevented by the high stability of phenol in the aqueous solution surrounding the photoreactive solid phase (S_{phenol} and S_{Deg} are 9 and 88% at pH=7 against 98 and <1 %, respectively, at pH=2).

VI. Experimental results: direct oxidation of benzene to phenol using N-TiO_2 powders loaded with transition metal oxides

As for the direct oxidation of benzene to phenol, N-TiO_2 powders showed a strong oxidizing power. Indeed, as observed from the experimental results in the previous chapter, the benzene oxidation in presence of N-TiO_2 photocatalyst showed a high conversion of benzene without phenol production under visible light. Therefore, a possible strategy to increase the phenol production is to formulate a photocatalyst which guarantees a high benzene conversion together with an appropriate phenol yield and selectivity under visible light.

VI.1 Synthesis of N-TiO_2 loaded with transition metal oxides

Cu, Fe and V oxides loaded on N-TiO_2 (Cu/N-TiO_2, Fe/N-TiO_2, and V/N-TiO_2) were prepared by an incipient wet impregnation (Papp et al., 1994). N-TiO_2 powder was suspended in a aqueous solution containing the appropriate amount of trihydrate copper nitrate as copper precursor, nonahydrate iron nitrate as iron precursor and ammonium metavanadate as vanadium precursor (Aldrich) in order to obtain catalysts with metal loading equal to 5wt%. The suspensions were dried at 120°C for 12 hours and finally calcined in a muffle oven at 450°C for 30 min, affording catalyst powders.

VI.2 Photocatalytic activity tests

The photocatalytic oxidation reactions were performed in 35 mL aqueous solution containing benzene (initial concentration: 25.6 mmol/L) and acetonitrile (2.3 mL) as a co-solvent with 0.1 g/L of Cu/N-TiO_2, Fe/N-TiO_2, and V/N-TiO_2 photocatalyst in powder form under continuous stirring.

The system was first kept in dark (without any light irradiation) at room temperature for 60 min to obtain sorption equilibrium of benzene on photocatalyst powder. Before irradiating the reactor, 2.8 mL of H_2O_2 (30 wt% in H_2O) was added to the reaction mixture. Then, the reactor was irradiated for 600 min by visible (emission range: 400–800 nm; irradiance: 16 W/m^2) LEDs strip placed around and in contact to the external surface of the pyrex reactor. The reactor was cooled down by a fan during photoirradiation time. Solution aliquots were withdrawn from the reactor at different times by a 1mL syringe, filtered through a 0.22 µ CA filter (SIMPLEPURE) to remove solid particles and immediately analyzed quantitatively by an Agilent gas cromatograph (model 7820 A) equipped with a flame ionization detector (FID) to evaluate the benzene and phenol concentration.

GC separation was achieved with a DB Heavy Wax fused-silica capillary column (30m x 0,35mm i.d. x 0,25µm) under the following conditions: column temperature 40-300°C (40 °C held 2 min, rate 5 °C/min to 90 °C, rate 20 °C/min to 250 °C, held 10 min); helium at a constant flow rate of 1 mL/min; injection port operated at 10:1 split mode; temperature of injector and detector at 180 °C and 300 °C respectively.

Hydroquinone, resorcinol, p-benzoquinone and catechol were determined quantitatively by HPLC using a Dionex UltiMate 3000 Thermo Scientific system equipped with DAD detector, column thermostat and automatic sample injector with 100µL loop. Separations were carried out on a Phenomenex Luna C-18 column (150 x 4.6 mm i.d.; 5µm) eluted with mixture of water (solvent A) and acetonitrile (solvent B) according to the program: 0-14 min, 15% B (isocratic); 14-23 min, 60-100% B (linear gradient); 23-30 min, 15% B (isocratic). The chromatographic conditions were: oven temperature 35°C; flow rate 0.8mL/min; injection volume 50 µL and UV detector at 270 nm.

VI.3 Experimental results

VI.3.1 Characterization of Cu/N-TiO_2, Fe/N-TiO_2 and V/N-TiO_2

The samples were analyzed with the following characterization techniques:

- Wide-angle X-Ray diffraction (WAXD);
- N_2 adsorption at -196 °C to obtain specific surface area (S_{BET}) UV-Vis reflectance;
- Raman spectroscopy.

VI.3.1.1 Wide-angle X-Ray diffraction (WAXD) patterns

The results from X-ray diffraction analysis for all the synthesized samples showed the presence of signals typical of the titanium dioxide in the anatase crystalline phase (Figure VI.1) (Theivasanthi and Alagar, 2013). No signals related to rutile phase have been observed. The peak at 38° related to Fe_2O_3 is not revealed for Fe/N-TiO_2 as reported in literature (Tanarungsun et al., 2007) probably because the loading of Fe (5% wt) is below the detection limit of the instrument.

On the other hand, the presence of CuO phase associated to the peaks at 2θ =36 ° and 38 ° (Lee et al., 2002, Magesan et al., 2016), is detected for Cu/N-TiO_2 sample. In the case of V/N-TiO_2, the absence of an additional peak around 20° belonging to the orthorhombic phase V_2O_5 is also absent, probably for the different synthesis conditions from those reported in the literature (Avansi Jr et al., 2019, Avansi Jr et al., 2009)

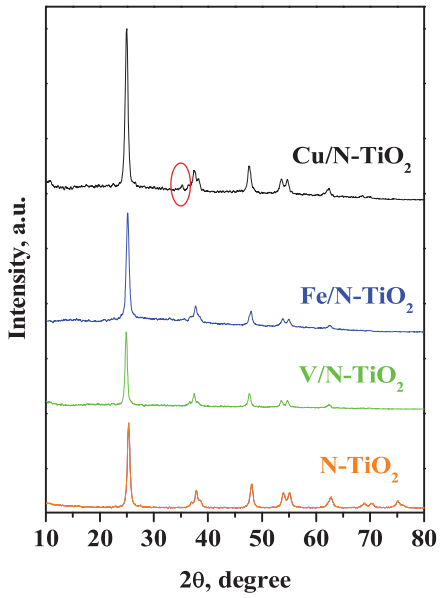

Figure VI.1 *Wide angle X-ray diffraction (WAXD) patterns of TiO_2, N-TiO_2, Cu/N-TiO_2, Fe/N-TiO_2 and V/N-TiO_2 samples.*

VI.3.1.2 Specific surface area (S_{BET}), crystalline size and band gap energy (E_{bg}) values

All samples prepared by impregnation have a lower S_{BET} value than that of the N-TiO_2 sample. This result is also related to a higher crystallite size calculated for the metal impregnated samples than for the N-TiO_2 sample. The average crystallite size of N-TiO_2, Cu/N-TiO_2, Fe/N-TiO_2, and V/N-TiO_2 samples was calculated using the Scherrer equation and the obtained values are reported in Table VI.1. Furthermore, the reflectance data were reported as the $F(R_\infty)$ value from Kubelka-Munk theory vs the wavelength. Band gap determinations were made by plotting $[F(R_\infty)\cdot h\nu]^2$ vs hν (eV).N-TiO_2 sample exhibits an increase of optical properties in the visible region with a reduction of band-gap values from 3.20 eV (the typical band-gap of undoped TiO_2) to 2.90 eV. This change in band-gap is therefore attributed to the presence of nitrogen in the crystal structure phase. All the metal loaded N-TiO_2 samples show a lower band gap value. In particular, Cu/N-TiO_2 has a band gap value equal to 2.40 eV confirming the increase of light absorption capacity in the visible region.

Table VI.1 *Crystallite size, specific surface area (S_{BET}) and band gap (E_{bg}) of all prepared samples.*

Catalyst	Crystallite size (nm)	E_{bg} (eV)	S_{BET}
N-TiO_2	7	2.90	115
Cu/N-TiO_2	9	2.40	34
Fe/N-TiO_2	10	2.43	42
V/N-TiO_2	10	2.55	30

VI.3.1.3 Raman spectra

The Raman spectra of N-TiO_2, Cu/N-TiO_2, Fe/N-TiO_2 and V/N-TiO_2

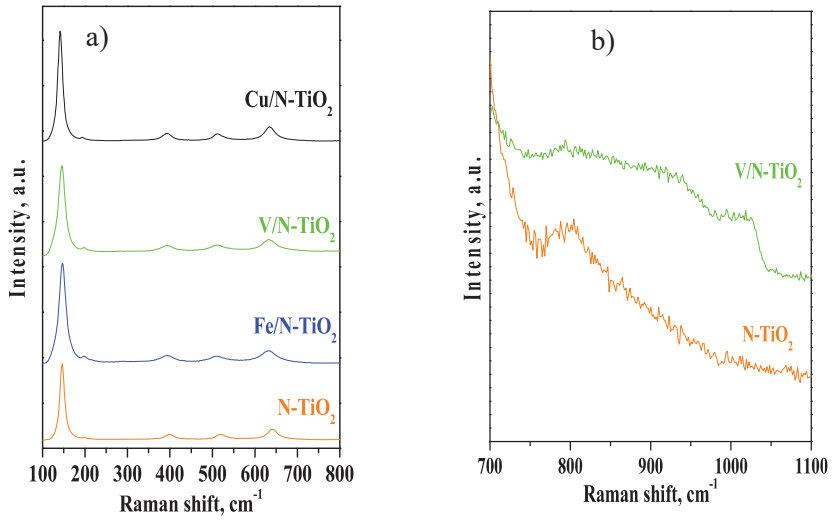

samples are shown in Figure VI.2a.

Figure VI. 2 *Raman spectra of N-TiO_2, Cu/N-TiO_2, Fe/N-TiO_2 and V/N-TiO_2 (a). Raman spectra of N-TiO_2 and V/N-TiO_2 in narrow Raman shift range 700-1100 cm^{-1} (b).*

N-TiO_2 sample showed bands at 144, 397, 516 and 638 cm^{-1} and a weak shoulder at 195 cm^{-1}, due to the Raman-active fundamental modes of anatase (Giarola et al., 2010). On the other hand, additional Raman bands at 279 cm^{-1}, and 216 cm^{-1} associated with CuO and Cu_2O, respectively, as discussed in literature, were not discovered (Vitiello et al., 2019, Lee et al., 2002). This result can be attributed either to the overlapping of the anatase TiO_2 Raman bands with the copper oxide bands or to the low amount of copper (Hu et al., 2022, Bahadori et al., 2020).

From the observation of the Raman spectrum for the Fe/N-TiO_2 sample, it was noted that the peak related to magnetite (Fe_3O_4) at 670 cm^{-1} observed with the 514 nm diode-laser, as reported in the literature, was not found (Panta and Bergmann, 2015). Contrariwise, Raman spectrum of V/N-TiO_2 displayed in the range 700-1100 cm^{-1} (Figure VI.2b) a wide band at about 940 cm^{-1}, assigned to the V-O-V functionality, indicating the presence of polyvanadate species. The photocatalyst also shows a contribution to about 1016 cm^{-1} which occurs in the stretch region V=O and it is attributed to the corresponding mode of the polyvanadates dispersed on the surface (Ciambelli et al., 2009).

VI.4 Photocatalytic benzene oxidation with Cu/N-TiO_2, Fe/N-TiO_2 and V/N-TiO_2 photocatalysts.

The visible light-driven benzene oxidation, using Cu/N-TiO_2, Fe/N-TiO_2 and V/N-TiO_2 samples is shown in Figure VI.3.

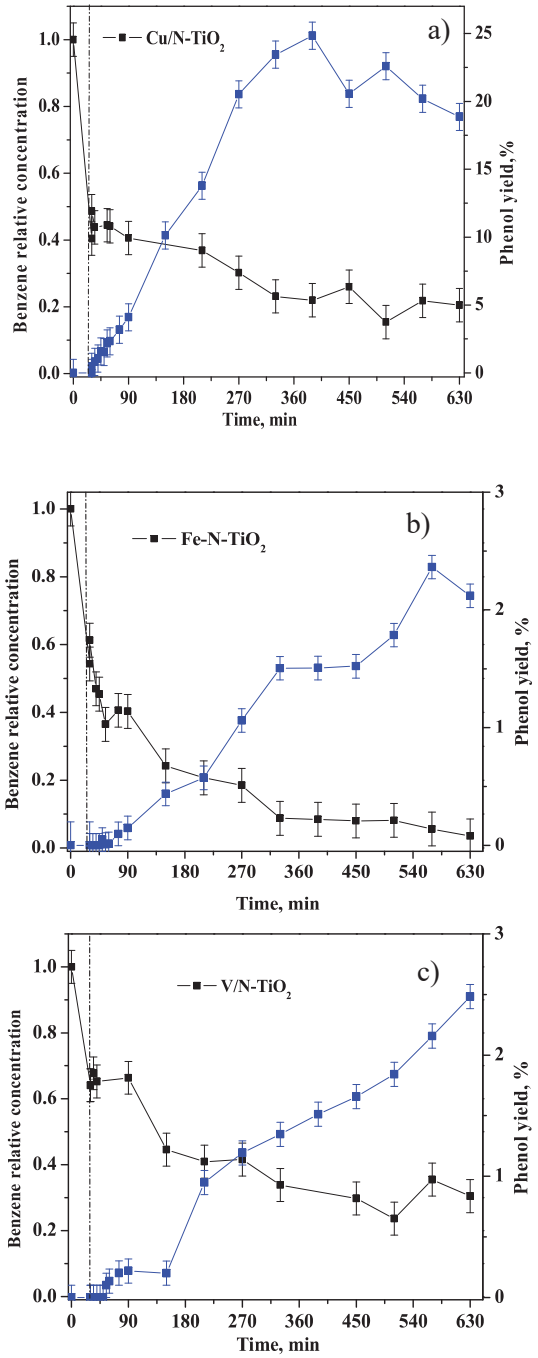

Figure VI.3 *Benzene relative concentration and phenol yield as a function of run time, in dark and under visible light, using Cu/N-TiO_2 (a), Fe/N-TiO_2 (b) and (c) V/N-TiO_2 photocatalysts.*

In the absence of visible light (dark condition), benzene is adsorbed on Cu/N-TiO_2 surface for almost 50% after 30 min. Despite the presence of H_2O_2 as oxidant, phenol was not produced during dark condition.
When visible LEDs were switched on, benzene is converted and, consequently, its relative concentration decreased with run time (Figure VI.3). Phenol yield gradually increased during irradiation time in presence of Cu/N-TiO_2, reaching a maximum value of 25% after 360 min of irradiation, and then it decreased recording a value of 19% at the end of the test (600 min of visible light). Fe/N-TiO_2 photocatalyst adsorbs benzene for about 46% after 30 min of dark condition. As the reactor is irradiated with visible LEDs, the reaction begins and the benzene is converted. The phenol is produced not immediately as in the case of the Cu/N-TiO_2 catalyst but after 20 min from the switching on of the visible LEDs reaching a phenol yield of 2% at the end of the test (600 min of visible irradiation). Similarly, V/N-TiO_2 adsorbs benzene in dark up to 36% and, when the reaction is initiated thanks to the irradiation of visible light and the presence of H_2O_2, a progressive decrease of benzene relative concentration can be observed.
Figure VI.4 shows the phenol yield as a function of irradiation time obtained with Cu/N-TiO_2, Fe/N-TiO_2 and V/N-TiO_2 samples.

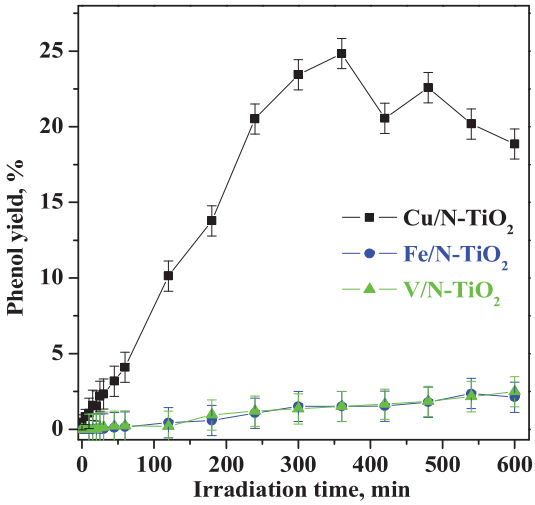

Figure VI.4 *Phenol yield as a function of visible irradiation using Cu/N-TiO_2, Fe/N-TiO_2 and V/N-TiO_2 photocatalysts.*

After 600 min of visible light, Cu/N-TiO_2 photocatalyst achieves a phenol yield equal to 19% significantly higher than that observed with Fe/N-TiO_2 (2%) and V/N-TiO_2 (2.5%).

Table VI.2 *Benzene conversion, selectivity to phenol and CO_2 and other ring-opened compounds, yield to phenol, hydroquinone, catechol and resorcinol obtained using Cu/N-TiO_2, Fe/N-TiO_2 V/N-TiO_2 powder after 600 min of visible light irradiation (Vis).*

Catalyst	*light*	*Bz_{conv}*	*Y_{phenol}*	*$Y_{hydroquinone}$*	*$Y_{catechol}$*	*$Y_{resorcinol}$*	*$Y_{p\text{-}benzoquinone}$*	*S_{phenol}*	*S_{Deg}*
Cu/N-TiO_2	Vis	82 %	19%	2%	11%	<1%	5%	23%	99.5 %
Fe/N-TiO_2	Vis	94 %	2%	<1%	n.d	n.d	<1%	2%	97.4 %
V/N-TiO_2	Vis	71 %	2.5%	<1%	<1%	n.d	<1%	3.5 %	99.9 %

According to the data in Table VI.2, the phenol selectivity and yield using Cu/N-TiO_2 are higher than those obtained with Fe/N-TiO_2 and V/N-TiO_2 under visible light.

VI.4.1 Kinetic modelling of the direct oxidation of benzene to phenol using Cu/N-TiO_2, Fe/N-TiO_2 and V/N-TiO_2 photocatalysts

The experimental data reported Figure VI.5 together with the concentration of by-products detected by HPLC analysis were used for the kinetic modelling of the three formulated photocatalysts in order to calculate the phenol production kinetic constant for each photocatalytic system.

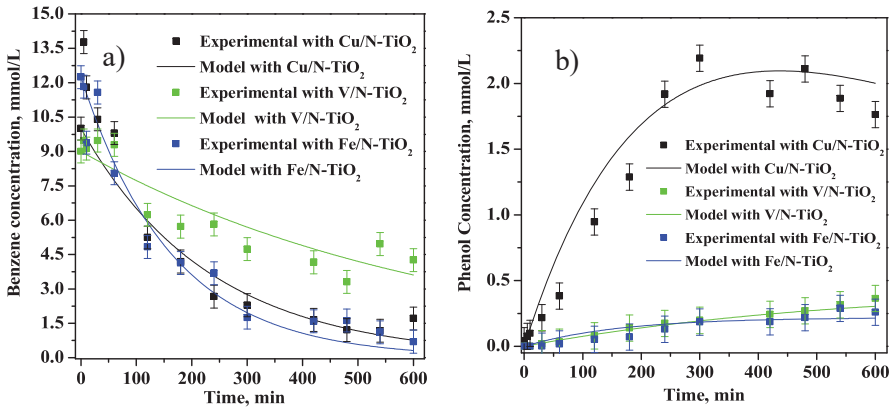

Figure VI.5 *Comparison between model calculation and experimental data to find the model oxidation constant k for benzene concentration (mmol/L) (a); phenol concentration (mmol/L) as a function of time obtained with Cu/N-TiO_2, Fe/N-TiO_2 and V/N-TiO_2 under visible light (b).*

The main problem of the benzene (BZ) hydroxylation to phenol (PhOH) is the consecutive reactions, which lead to by products (hydroquinone (HQ), benzoquinone (BQ), catechol (CT), resorcinol (RS) and other open rings and CO_2 production. The identified reaction paths are shown in Figure VI.6.. When the photocatalytic hydroxylation of benzene occurs using Cu/N-TiO_2 photocatalyst, the production of all by-products can be observed according to the reaction mechanism shown in Figure VI.6a. On the other hand, Fe/N-TiO_2 does not provide detectable production of catechol (CT) and resorcinol (RS), suggesting that the route of addition of hydroxyl groups to benzene takes place preferably in the para position (Figure VI.6b). Instead, V/N-TiO_2 photocatalyst leads to the production of phenol and the the other by-products, except resorcinol (Figure VI.6c).

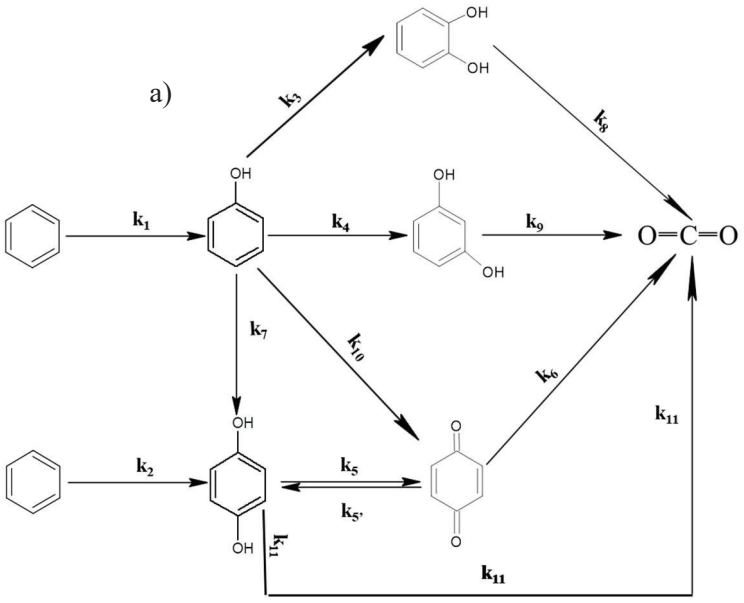

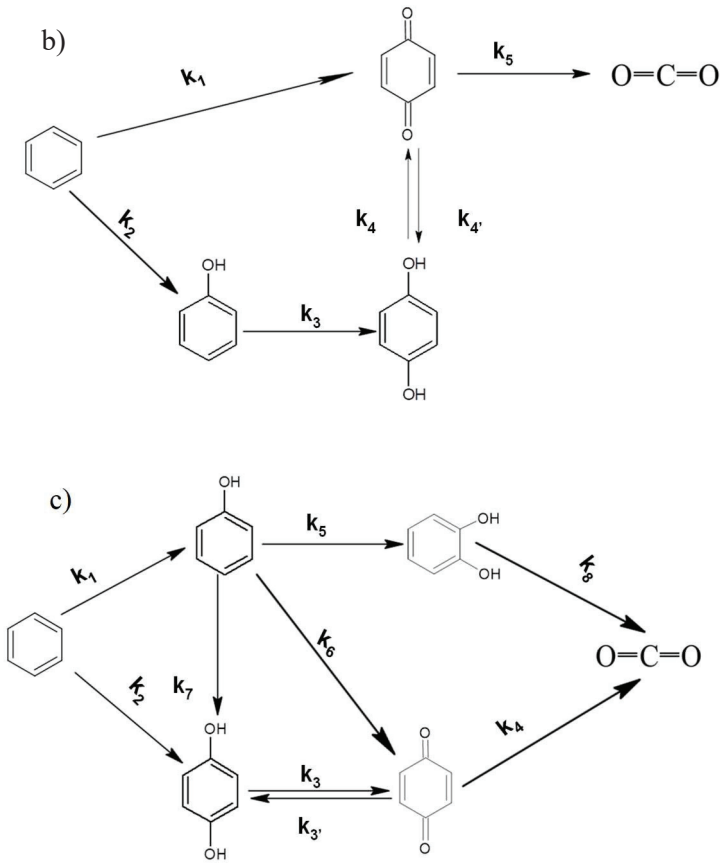

Figure VI.6 *Reaction paths for the photocatalytic conversion of benzene with Cu/N-TiO_2 (a), Fe/N-TiO_2 (b)and V/N-TiO_2 (c).*

More in detail, in presence of visible LEDs and Cu/N-TiO_2 as photocatalyst, benzene is directly hydroxylated to phenol and HQ. The oxidative conditions of the system leads to the conversion of HQ to BQ, but the equilibrium reaction between these two species in the aqueous system cannot be excluded. On the other hand, it is reasonable to accept that the production of BQ may occur from phenol, since the •OH radical is highly reactive. However, CA and RS can be produced by phenol hydroxylation (Figure VI.6 a). The concentration of BQ and CA reached appreciable values with respect to the HQ and RS concentration with Cu/N-TiO_2 photocatalyst.
Phenol and BQ can be produced by benzene with Fe/N-TiO_2 in presence of visible light and H_2O_2. HQ can be formed from phenol Then, HQ can give BQ. Also in this case, the equilibrium reaction between HQ and BQ can not be excluded (Figure VI.6b). In the same reaction conditions with V/N-TiO_2 photocatalyst, benzene is directly converted to phenol and HQ that can be

further oxidized to BQ. HQ can be produced from benzene and phenol. Consequently, phenol can give CA, HQ and can directly oxidized to BQ (Figure VI.6c).

Taking into account the reaction schemes proposed in Figure VI.6, a kinetic model for the photocatalytic hydroxylation of benzene is developed. . The mass balance equations for Cu/N-TiO_2 photocatalyst are given below::

$$\frac{dC_{Bz}}{dt} = -k_1 C_{Bz} - k_2 C_{Bz} \quad (42)$$

$$\frac{dC_{PhOH}}{dt} = k_1 C_{Bz} - k_4 C_{PhOH} - k_7 C_{PhOH} - k_3 C_{PhOH} - k_{10} C_{PhO} \quad (43)$$

$$\frac{dC_{HQ}}{dt} = -k_5 C_{HQ} + k_2 C_{Bz} + k_7 C_{PhOH} + k_5' C_{BQ} - k_{11} C_{HQ} \quad (44)$$

$$\frac{dC_{CT}}{dt} = k_3 C_{PhOH} - k_8 C_{CT} \quad (45)$$

$$\frac{dC_{RS}}{dt} = k_4 C_{PhOH} - k_9 C_{RS} \quad (46)$$

$$\frac{dC_{BQ}}{dt} = k_5 C_{HQ} - k_6 C_{Bz} - k_5' C_{Bz} + k_{10} C_{PhOH} \quad (47)$$

$$\frac{dC_{CO_2}}{dt} = 6 * k_6 C_{BQ} + 6 * k_8 C_{CT} + 6 * k_9 C_{RS} + 6 * k_{11} C_{HQ} \quad (48)$$

The mass balance equations for Fe/N-TiO_2 photocatalyst are reported below:

$$\frac{dC_{Bz}}{dt} = -k_1 C_{Bz} - k_2 C_{Bz} \quad (49)$$

$$\frac{dC_{PhOH}}{dt} = -k_1 C_{Bz} - k_3 C_{PhOH} \quad (50)$$

$$\frac{dC_{HQ}}{dt} = k_3 C_{PhOH} - k_4 C_{HQ} + k_4' C_{BQ} \quad (51)$$

$$\frac{dC_{BQ}}{dt} = k_2 C_{BZ} - k_5 C_{BQ} + k_4 C_{HQ} - k_4' C_{BQ} \quad (52)$$

$$\frac{dC_{CO_2}}{dt} = 6 * k_5 C_{BQ} \quad (53)$$

For V/N-TiO_2 photocatalyst, the mass balance equations are the following::

$$\frac{dC_{Bz}}{dt} = -k_1 C_{Bz} - k_2 C_{Bz} \quad (54)$$

$$\frac{dC_{PhOH}}{dt} = k_1 C_{Bz} - k_5 C_{PhO} \quad - k_7 C_{PhOH} - k_8 C_{PhOH} \quad (55)$$

$$\frac{dC_{HQ}}{dt} = -k_3 C_{HQ} + k_2 C_{Bz} + k_7 C_{PhOH} + k_3' C_{BQ} \quad (56)$$

$$\frac{dC_{CT}}{dt} = k_5 C_{PhOH} - k_6 C_{CT} \quad (57)$$

$$\frac{dC_{BQ}}{dt} = k_3 C_{HQ} - k_4 C_{BQ} - k_3' C_{Bz} + k_8 C_{PhOH} \quad (58)$$

$$\frac{dC_{CO_2}}{dt} = 6 * k_4 C_{BQ} + 6 * k_6 C_{CT} \quad (59)$$

The differential equations for each photocatalyst are solved considering the initial condition:

t=0 $C_{Bz}=C_{BZ_0}$.

t=0 $C_{phOH}=C_{HQ}=C_{BQ}=C_{CT}=C_{CO2}=0$

The system of differential equations was solved by a numerical procedure using the Euler method. It is the most basic explicit method for the numerical integration of ordinary differential equations (ODEs) with a given initial value. The values of the apparent kinetic constant for each reaction were attained by using the least-squares approach, minimizing the sum of squared residuals between the experimental data acquired at different irradiation times and the values provided by the model. The results of the optimization procedure were reported in Figure VI.5.

Table VI.3 shows the kinetic constants for phenol production (k_1).

Table VI. 3 *Phenol production kinetic constants (k_1) derived from the proposed mechanism for photocatalytic hydroxylation of benzene considering Cu/N-TiO_2, Fe/N-TiO_2 and V/N-TiO_2 samples.*

Photocatalyst	k_1, min^{-1}
Cu/N-TiO_2	$1.41 \cdot 10^{-3}$
Fe/N-TiO_2	$1.09 \cdot 10^{-4}$

V/N-TiO_2	$9.21 \cdot 10^{-5}$

The values of the phenol production kinetic constants evidence that the Cu/N-TiO_2 photocatalyst showed the highest rate of phenol formation with respect the other formulated photocatalysts.
Ultimately, Cu/N-TiO_2 photocatalyst is more effective as it produces phenol faster than the other formulated photocatalysts and it allows to achieve the highest phenol yield (19%) and selectivity to phenol (23%).
Therefore, to further increase the yield and selectivity of phenol and produce phenol in shorter times, Cu/N-TiO_2 photocatalyst in powder form was dispersed inside the sPS aerogel.

VII.Experimental results: direct oxidation of benzene to phenol using Cu/N-TiO_2/sPS

VII.1 Synthesis of Cu/N-TiO_2/sPS aerogel

sPS and Cu/N-TiO_2 were dispersed in chloroform inside hermetically sealed test tube at 100°C until complete polymer dissolution. The obtained mixture was sonicated at room temperature until complete gelation of the polymer and then cooled to produce a gel. The monolithic composite aerogels (D.I.=5.6 mm and a h= 3 cm) were obtained by treating the gels with supercritical carbon dioxide (by using an ISCO SFX 220 extractor), for 4 hours at T=40 °C and P= 20 MPa, to extract the solvent. In the final sample, the content of Cu/N-TiO_2 dispersed into the monolythic polymer was 10 wt%.

VII.2 Photocatalytic activity test with Cu/N-TiO_2/sPS aerogel

The photocatalytic reactions were performed in 35 mL aqueous solution containing benzene (initial concentration: 25.6 mmol/L) and acetonitrile (2.3 mL) as a co-solvent with 3 g/L of Cu/N-TiO_2/sPS aerogel (corresponding to an Cu/N-TiO_2 dosage of 0.1 g/ L) under continuous stirring. The Cu/N-TiO_2/sPS aerogel acted as a reactive solid phase and preserved the cylindrical shape during the overall test time.
The system was first kept in dark conditions at room temperature for 1280 min to obtain benzene sorption equilibrium on Cu/N-TiO_2/sPS aerogel.. Before irradiating the reactor, 2.8 mL of H_2O_2 (30 wt% in H_2O) was added to the reaction mixture. Then, the reactor was irradiated for 600 min by visible (emission range: 400–800 nm; irradiance: 16 W/m^2) LEDs strip placed around and in contact with the external surface of the pyrex reactor.

The reactor was cooled down by a fan during photoirradiation time. Solution aliquots were withdrawn from the reactor at different times by a 1mL syringe, filtered through a 0.22 μ CA filter (SIMPLEPURE) to remove solid particles for the tests with Cu/N-TiO_2 photocatalyst and immediately analyzed quantitatively by an Agilent gas chromatograph (model 7820 A) equipped with a flame ionization detector (FID) to evaluate the benzene and phenol concentration
Hydroquinone, resorcinol, p-benzoquinone and catechol were determined quantitatively by HPLC using a Dionex UltiMate 3000 Thermo Scientific system equipped with DAD detector, column thermostat and automatic sample injector with 100μL loop.

VII.3 Experimental results

VII.3.1 Characterization results of Cu/N-TiO_2/sPS aerogel

The aerogels were investigated through the following characterization techniques:

- N_2 adsorption at -196 °C to obtain specific surface area (S_{BET})
- Wide angle X-ray diffraction (WAXD)
- Fourier-transform infrared (FTIR) spectroscopy.

VII.3.1.1 Specific surface area (S_{BET}) results
Table VII.1 reports the specific surface area (S_{BET}) of the composite aerogels.

Table VII.1 *Specific surface area (S_{BET}) of the composite aerogels.*

Sample	S_{BET} [m^2/g]
CuO/sPS	267
N-TiO_2/sPS	222
Cu/N-TiO_2/sPS	286

The formulated samples show S_{BET} values t significantly higher than the values obtained for the CuO (1.6 m^2/g), N-TiO_2 (115 m^2/g) and Cu/N-TiO_2 (34 m^2/g).

However, it is interesting to underline that the addition of the catalytic powders led to a reduction of the specific surface compared to the value of the bare sPS, equal to 340 m^2/g.

VII.3.1.2 Wide angle X-ray diffraction (WAXD) patterns

Figure VII.1 displays the WADX patterns for CuO/sPS, N-TiO_2/sPS and Cu/N-TiO_2 /sPS aerogels in the 2ϑ =5-60° range.

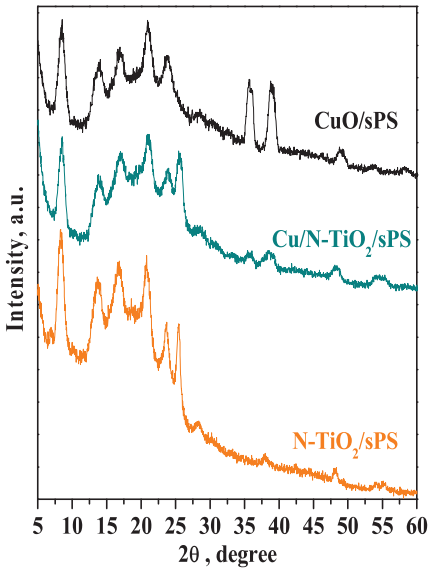

Figure VII.1 *Wide angle X-ray diffraction (WAXD) patterns of CuO/sPS, N-TiO_2/sPS and Cu/N-TiO_2/sPS composite aerogels*

The WAXD spectra of the polymeric composites (Figure VII.1) show signals at 2θ = 8.5°, 13.9°, 17.1°, 20.7° and 23.9° typical of the nanoporous crystalline form of sPS (Sacco et al., 2018a). While, the peak observed at 2θ = 25° for N-TiO_2/sPS and Cu/N-TiO_2 /sPS corresponds to the crystalline phase of TiO_2 in anatase phase (Sacco et al., 2018a). The diffraction peaks corresponding to the presence of copper oxide, on the other hand, are obtained for 2θ = 36° and 38° (Magesan et al., 2016) and are clearly detectable in the CuO/sPS sample; while they are less evident in the Cu/N-TiO_2/sPS sample.

VII.3.1.3 Fourier-transform infrared (FT-IR) spectra

Figure VII.2 shows the FT-IR spectra for CuO/sPS, N-TiO_2/sPS and Cu/N-TiO_2 /sPS aerogels in the range 500-3500 cm^{-1}.

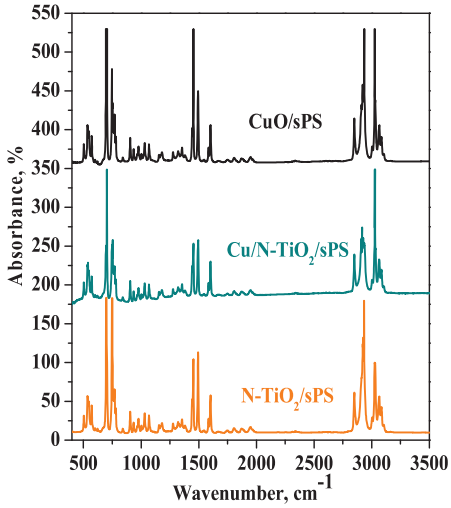

Figure VII.2 *FT-IR spectra of CuO/sPS, N-TiO_2/sPS and Cu/N-TiO_2/sPS composite aerogels*.

The FT-IR spectra of the CuO/sPS, N-TiO_2/sPS and Cu/N-TiO_2/sPS samples show the presence of the characteristic peaks of the sPS polymer in the range between 800 and 940 cm^{-1} (Wu et al., 2001).
On the other hand, the absorption bands observed in the range between 500 and 600 cm^{-1} are typical of the Cu-O vibrational motions (Chen et al., 2008). Furthermore, a band due to an elongation vibration of CuO at 1680 cm^{-1} is clearly evident in the CuO/sPS sample and in the Cu/N-TiO_2/sPS sample (Lopez et al., 1992). Finally, the absorption bands in the region between 3100 and 3150 cm^{-1} are attributable to the Ti-OH and OH hydroxyl groups present in TiO_2 (Lopez et al., 1992).

VII.4 Photocatalytic benzene oxidation with Cu/N-TiO_2/sPS aerogel

VII.4.1 Comparison of visible light driven benzene oxidation between N-TiO_2/sPS and Cu/N-TiO_2/sPS

Benzene conversion and phenol yield using Cu/N-TiO_2/sPS and N-TiO_2/sPS aerogel are displayed in Figure VII.3. Benzene conversion for Cu/N-TiO_2/sPS composite was remarkably higher than that observed for N-TiO_2/sPS. It is worth pointing out that benzene conversion was higher than that obtained with N-TiO_2/sPS at low irradiation times. In detail, benzene conversion was about 30% with Cu/N-TiO_2/sPS aerogel after 60 min of visible light, while it is less than 20% with N-TiO_2/sPS aerogel (Figure VII.3a).. Instead, benzene conversion with N-TiO_2/sPS continuously increased with respect to the irradiation time and reached a value of about 58% after 600 min of visible light whereas benzene conversion for Cu/N-TiO_2/sPS was was higher and equal to about 73%. Figure VII.3b shows phenol yield as a function of irradiation time with Cu/N-TiO_2/sPS and N-TiO_2/sPS. Phenol yield obtained with Cu/N-TiO_2/sPS aerogel reached a value of about 20 % whereas phenol yield observed using N-TiO_2/sPS was lower, approximately 6.5%, after 600 min of visible light.

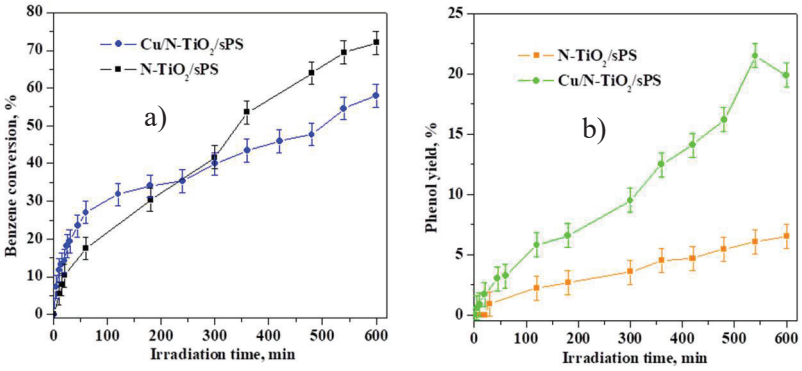

Figure VII.3 *Benzene conversion as a function of irradiation time using Cu/N-TiO_2/sPS and N-TiO_2/sPS photoreactive composite under visible light (a); phenol yield as a function of irradiation time using Cu/N-TiO_2/sPS and N-TiO_2/sPS photoreactive composite under visible light (b).*

According to the literature (Tomita et al., 2011) the oxidation of benzene to phenol on Cu/N-TiO_2 may be occurred through the following reactions (Dasireddy and Likozar, 2018, Devaraji and Jo, 2018, Janczarek and Kowalska, 2017):

$$N\text{-}TiO_2 + h\nu \longrightarrow e_{CB}^- + h^+ \quad (60)$$

$$Cu^{2+} + e_{CB}^- \longrightarrow Cu^+ \quad (61)$$

$$Cu^+ + H_2O_2 \longrightarrow Cu^{2+} + \bullet OH + OH^- \quad (62)$$

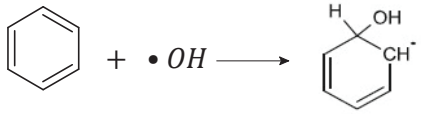

(63)

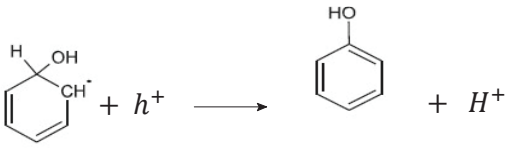

(64)

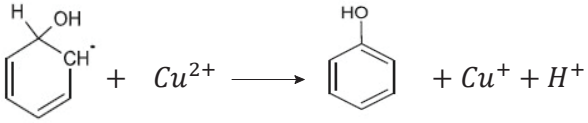

(65)

The hole-electron pairs are produced by following the activation of the N-TiO_2 under irradiation. Cupric ions could react with the photogenerated electrons, producing cuprous ions. Therefore, Cu^+ ions could be re-oxidized to Cu^{2+} by H_2O_2, generating •OH. The hydroxyl radical reacts with benzene to generate hydroxylated benzene radical, which is then oxidized by a positive hole or by Cu^{2+} on the photocatalyst surface and deprotonated, producing phenol.

VII.4.2 Effect of Cu/N-TiO_2/sPS dosage

Figure VII.4 shows the effect of Cu/N-TiO_2/sPS aerogel dosage on photocatalytic activity in terms of benzene conversion and phenol yield. In detail, the photocatalytic benzene oxidation was performed by using 3 g/L and 6 g/L of Cu/N-TiO_2/sPS aerogel under visible light irradiation. Benzene conversion was 58 and 81% using 3 g/L and 6 g/L of Cu/N-TiO_2/sPS

dosage, respectively (Figure VII.4a), after 600 min of visible light irradiation, while the phenol yield was 20 and 9.5% with 3 g/L and 6 g/L of Cu/N-TiO_2/sPS, respectively (Figure VII.4b). It is worth pointing out that, with 6 g/L of Cu/N-TiO_2/sPS aerogel, the conversion of benzene after 420 min of visible light irradiation was similar to that obtained with 3g/L of Cu/N-TiO_2/sPSafter 600 min of visible light irradiation, confirming that the increase of Cu/N-TiO_2/sPS amount causes a higher benzene conversion rate. Phenol yield was about 28% with 6 g/L of Cu/N-TiO_2/sPS aerogel after 420 min of visible light irradiation. The detected mismatch between benzene conversion and phenol yield, particularly notable after 600 min of visible light irradiation (Table VII.2) is due to the formation of reaction products other than phenol.

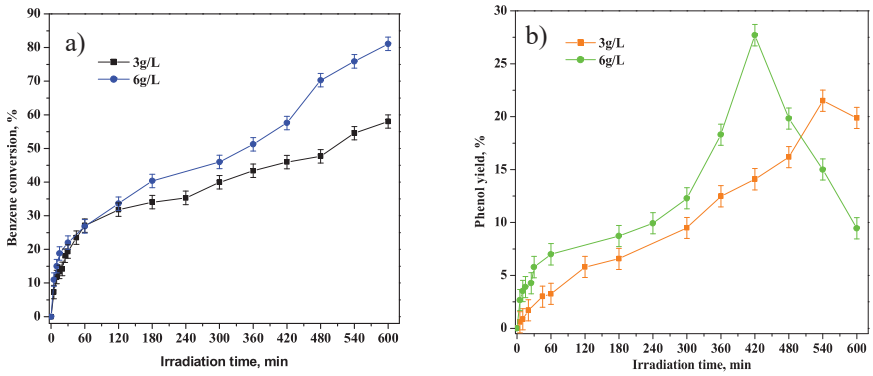

Figure VII.4 *Benzene conversion as a function of irradiation time using 3g/L and 6g/L of Cu/N-TiO_2/sPS photoreactive composite under visible light (a); phenol yield as a function of irradiation time using 3g/L and 6g/L of Cu/N-TiO_2/sPS photoreactive composite under visible light (b).*

In Table VII.2 phenol yield is compared with that of other reaction by-products (hydroquinone, catechol and resorcinol) detected by HPLC analysis. According to the data of table VII.2, the selectivity to phenol decreased by doubling the dosage of Cu/N-TiO_2/ sPS aerogel after 600 min of visible light irradiation because the selectivity to CO_2 and other ring-opened compounds increased.While the selectivity to phenol was about 48% after 420 min of visible light irradiation using 6g/L of Cu/N-TiO_2/sPS aerogel.

Table VII.2 *Benzene conversion, selectivity to phenol and CO_2 and other ring-opened compounds selectivity, yield to phenol hydroquinone, catechol*

and resorcinol obtained using 3 g/L and 6 g/L of Cu/N-TiO_2/sPS aerogel after 600 min of visible light irradiation (Vis).

Cu/N-TiO_2/sPS *dosage*	*light*	Bz_{conv}	Y_{phenol}	$Y_{hydroquinone}$	$Y_{catechol}$	$Y_{resorcinol}$	S_{phenol}	S_{Deg}
3g/L	Vis	58%	20	5%	8%	n.d	34%	33%
6g/L	Vis	81%	9.5%	3%	7%	n.d	12%	63%
6g/L*	Vis*	58%*	28%*	2%*	4%*	n.d*	48%*	26%*

*Experimental data obtained using 6 g/L of Cu/N-TiO_2/sPS aerogel after 420 min of visible light irradiation.

VII.4.3 Effect of pH

To further improve the phenol yield and, thus, reduce the phenol affinity towards the sPS polymer (by increasing the affinity of phenol towards the aqueous phase surrounding the Cu/N-TiO_2/sPS solid phase), the pH was modified from about 7 to 2 by adding the hydrochloric acid. Figure VII.5 shows the effect of pH on photocatalytic hydroxylation of benzene using 6g/L of Cu/N-TiO_2/sPS aerogel under visible light irradiation.

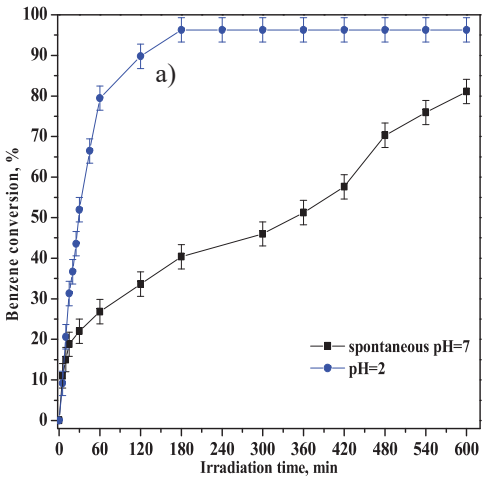

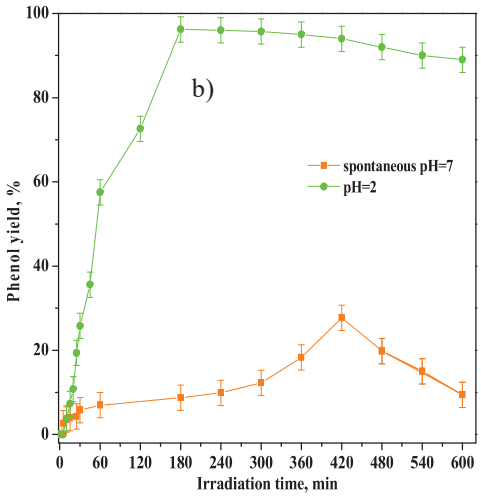

Figure VII.5 *Benzene conversion as a function of irradiation time using 6g/L of Cu/N-TiO_2/sPS photoreactive composite under visible light in neutral (pH=7) and acidic conditions (pH=2) (a); phenol yield as a function of irradiation time using 6g/L of Cu/N-TiO_2/sPS photoreactive composite under visible light in neutral (pH=7) and acidic conditions (pH=2) (b).*

Figure VII.5a shows that benzene conversion was always higher than that observed in neutral condition. In particular, the benzene conversion already reached the value of 96% after 180 min of visible light, then remaining almost constant for the overall reaction time. On the other hand, the benzene conversion in neutral condition with 6g/L of Cu/N-TiO_2/sPS under visible light increased as a function of the irradiation time, achieving a benzene conversion value of about 81 % after 600 min of visible light. Furthermore, the phenol yield increased up to 28% after 420 minutes of visible light in neutral conditions using 6 g/L of Cu/N-TiO_2/sPS and then decreased at longer irradiation times (Figure VII.5b). While the phenol yield was about 96% in acidic condition after 180 min of visible light irradiation.
Photocatalytic performances achieved with Cu/N-TiO_2/sPS, under visible light irradiation, in neutral (pH=7) and acidic conditions (pH=2), were compared in Table VII.3. At pH=2, the selectivity to phenol and the phenol formation rate were over 99% and equal to 5.4 mmol/($g_{Cu/N\text{-}TiO2}$·h), respectively, much higher values than those achieved at pH=7 (9.5% and 0.58 mmol/($g_{Cu/N\text{-}TiO2}$·h)). It is worth noting that the selectivity to ring-opened products and CO_2 was lower than 1% at pH=2.

Table VII.3 *Benzene conversion, phenol formation rate (F_{phenol}), selectivity to phenol and selectivity to ring-opened products and CO_2 using Cu/N-TiO_2/sPS under visible light in neutral (pH=7) and acidic conditions (pH=2)*

Catalyst	pH	Bz_{conv}	F_{phenol}	S_{phenol}	S_{Deg}
Cu/N-TiO_2/sPS	7	81%	0.58mmol/($_{gCu/N-TiO2}$·h)*	9.5%	26 %
Cu/N-TiO_2/sPS	2	96%	12.7mmol/($_{gCu/N-TiO2}$·h)**	>99%	<1%

*formation rate of phenol after 7h of visiblelight irradiation

** formation rate of phenol after 3 h of visible light irradiation

Reuse cycles were executed under the reaction conditions that allowed to achieve the best results (under visible light and at pH=2). Therefore, Cu/N-TiO_2/sPS composite was removed from the liquid phase, dried at room temperature for 24 hours and reused up to five times. Both benzene conversion and phenol yield were similar in all the reuse cycles (Figure VII.6), proving the stability of the Cu/N-TiO_2/sPS.

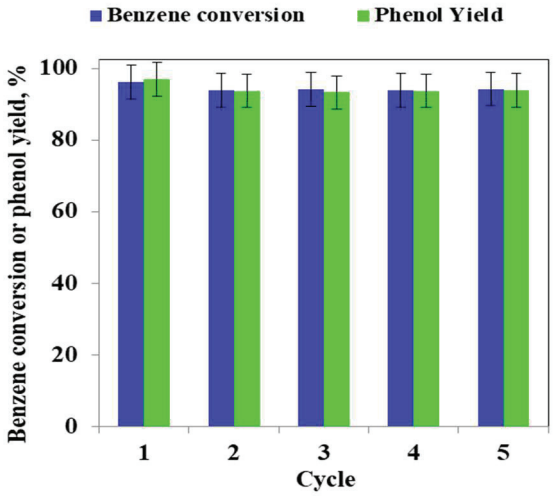

Figure VII.6 *Benzene conversion and phenol yield after 180 min of visible light irradiation at pH=2 for different reuse cycles using Cu/N-TiO_2/sPS photoreactive composite*

VII.5 Evaluation of effectiveness factor

To measure how much the reaction rate is lowered due to the diffusion resistance of the polymeric aerogel cavities and establish the limitant step of

the benzene oxidation process, effectiveness factor was calculated according to the following relationship:

$$Effectiveness\ factor,\ \ \eta = \frac{actual\ mean\ reaction\ rate\ within\ cavity}{rate\ if\ not\ slowed\ by\ cavity\ diffusion} = \frac{\dot{r}_{A,\ with\ diffusion}}{r_{A,with\quad diffusion\ resistance}} \tag{66}$$

For the cylindrical geometry, the Thiele module (ϕ) can be defined by the relashionship:

$$\phi = L \times \sqrt{\frac{k}{D}} = \frac{R}{2} \times \sqrt{\frac{k}{D}} \tag{67}$$

As shown in Figure VII.7: for large ϕ, or $\phi > 4$, it was found that $\eta = 1/\phi$, the reagent concentration quickly drops to zero as it moves into the cavity, so

diffusion strongly affects the reaction rate. Therefore the limiting regime in this case is the diffusion in the aerogel cavity. For small ϕ, or $\phi < 0.4$ related to cylindrical geometry, $\eta=1$, the concentration of reactant does not drop appreciably within the cavity; thus cavity diffusion offers negligible resistance. Therefore, the limitant step is the oxidation reaction into the cavities (Levenspiel, 1998).

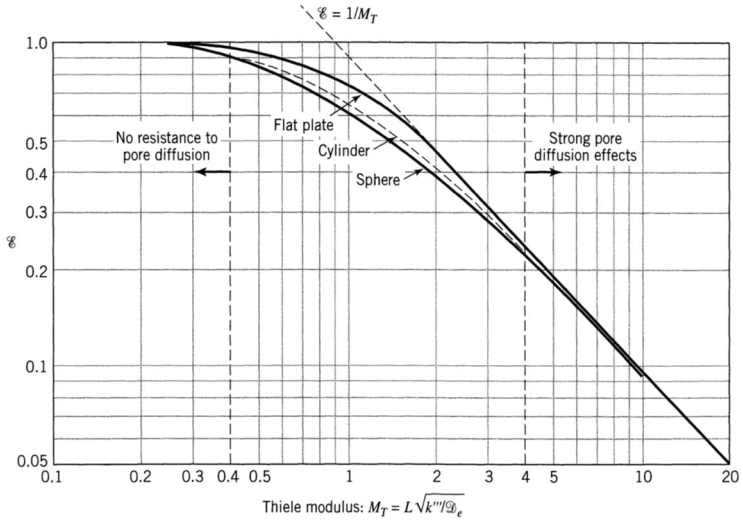

Figure VII.7 *Effectiveness factor versus* $\boldsymbol{\phi}$ *for porous particles of various shapes* (Levenspiel, 1998).

In the case of the binary benzene-phenol solution, the diffusion constant of benzene is 0.42 cm^2/min (evaluated from the mathematical modelling of benzene absorption in sPS), the kinetic constant for benzene consumption is $4.28 \cdot 10^{-3}$ min^{-1} (evaluated from the mathematical modelling on Cu/N-TiO_2) and the inner radius corresponds to 0.28 cm, then ϕ is equal to 0.0141. In such conditions η =1, evidencing that the benzene diffusion phenomena within Cu/N-TiO_2/sPS is not the limiting factor for benzene conversion and that the limiting step is the photoreaction occurring on Cu/N-TiO_2 embedded in the aerogel structure.

VIII. Conclusions

In this Ph.D. work, heterogeneous photocatalytic oxidation has been widely used as an innovative technology for water purification processes aimed at the removal of organic substances at room temperature and has also been extended to the synthesis of organic compounds under mild conditions. Firstly, visible light active photocatalysts in powder form have been formulated and used in the degradation of water pollutants (AO7 and THI). The photocatalytic performances under visible light irradiation of Fe-N codoped TiO_2 photocatalysts were investigated in the treatment of aqueous solutions containing AO7. The photocatalysts were prepared by sol-gel method and analyzed by different characterization techniques. UV–vis DRS spectra showed that Fe-N-TiO_2_1.2 sample gives visible-light absorption contributions higher than those of undoped TiO_2, N-TiO_2_1.2 and Fe-TiO_2 photocatalysts. It was observed a decrease in E_{bg} up to the value of 2.9 eV for N-TiO_2_1.2 and 2.8 eV for Fe-TiO_2, with respect to undoped TiO_2 (3.2 eV). It was observed an enhancement of photocatalytic AO7 discoloration and mineralization under visible light irradiation using Fe-N-TiO_2_1.2 photocatalyst, also confirmed by the kinetic constants values for AO7 degradation. In particular, Fe-N-TiO_2_1.2 was able to achieve 90% of discoloration efficiency and 83 % of TOC removal in 60 minutes of LEDs light irradiation. This enhancement of photocatalytic activity should be due to the modification of the TiO_2 structure with N and Fe associated with the simultaneous action of Fe^{3+} ions that inhibit the hole and electron recombination and nitrogen ions, which are able to replace the oxygen sites of TiO_2 lattice, generating Ti^{3+} sites and oxygen vacancies. The main reactive oxygen species responsible of AO7 photocatalytic degradation are superoxide and positive holes generated under visible light irradiation. Finally, the optimized Fe-N-TiO_2_1.2 evidenced photocatalytic performances better than other Fe-N codoped TiO_2 formulations investigated in literature, both in terms of treatment time and electrical energy consumption. The photocatalytic performance of Fe-Pr codoped TiO_2 photocatalysts in terms of color removal and mineralization efficiency was also studied for the treatment of aqueous solutions containing AO7 dye under visible light irradiation. UV–vis DRS spectra showed that Fe-Pr(8.5)-

TiO_2 sample evidenced visible-light absorption contributions higher than those of undoped TiO_2, Pr(8.5)-TiO_2 Fe-TiO_2 and the other Fe-Pr(x)-TiO_2 photocatalysts. It was observed a decrease in E_{bg} up to the value of 3.0 eV for Pr(8.5)-TiO_2 and 2.8 eV for Fe-TiO_2, with respect to undoped TiO_2 (3.2 eV). The further narrowing of Fe-Pr(8.5)-TiO_2 E_{bg} to value of 2.7 eV is an indication of the enhancement of the photocatalytic activity in the visible light region with respect to both Fe-TiO_2 and Pr(8.5)-TiO_2, but also with respect to Fe-Pr(4)-TiO_2, Fe-Pr(12.5)-TiO_2, Fe-Pr(17)-TiO_2 samples. Furthermore, XRD results showed that the main crystalline phase was anatase and revealed a slight expansion in the TiO_2 crystal lattice due to the incorporation of Fe^{3+} and Pr^{3+} ions. It was observed an enhancement of photocatalytic AO7 discoloration and mineralization under visible light irradiation using Fe-Pr(8.5)-TiO_2. Such sample allowed to achieve 87% of discoloration efficiency and 80% of TOC removal in 60 min of LEDs light irradiation. This improvement in the photocatalytic activity should be associated with the simultaneous doping of TiO_2 with Pr^{3+} and Fe^{3+} ions that induces a marked E_{bg} decrease together with an enhanced generation of oxygen vacancies (as evidenced by PL spectra), which can trap electrons, and therefore reducing their recombination with photogenerated positive holes. The photocatalytic performance of Fe-Pr(8.5)-TiO_2 in the visible light degradation of phenol demonstrated the absence of possible sensitization phenomena of photocatalyst surface by AO7 dye. The main reactive oxygen species which induce the AO7 photodegradation mechanism are superoxides and positive holes generated under visible light irradiation. In conclusion, Fe-Pr(8.5)-TiO_2 showed photocatalytic performances superior than other Fe-rare earth element codoped TiO_2 and Fe-RE element-nonmetal tri-doped TiO_2 formulations considered in literature, particularly in terms of treatment time.

It was assessed the effect of different doping elements towards the photocatalytic degradation of thiacloprid under UV, visible and solar light irradiation. XRD results of tri-doped TiO_2 samples showed the characteristic peaks of TiO_2 in anatase phase, while no signals of dopant species oxide can be detected. The shifting of the most intense mode in the Raman spectra of tri-doped TiO_2 powder indicate the incorporation of doped elements in TiO_2 lattice. The increase of absorption in the visible region and the shifting of the absorption edge of tri-doped TiO_2 samples evidence a narrowing of the band gap due to dopants elements incorporation in TiO_2 lattice, which is useful for visible light photocatalysis in practical applications. In addition, the reduction of PL intensity indicates a lower recombination rate and higher life span of photogenerated carriers for all the doped samples in comparison with the undoped TiO_2. Photocatalytic activity results showed that Fe-N-P tri-doped TiO_2 exhibited the highest THI degradation degree (64% under UV light, 29% under visible light and 73% under the direct solar light). To further improve the photocatalytic performances towards THI degradation,

Fe-N-P tri-doped TiO_2 was coupled with β-CD sub-microparticles precipitated by SAS technique, allowing to achieve a THI degradation efficiency equal to 75% after 30 min of UV light. Fe-N-P/TiO_2/β-CD showed a THI degradation efficiency of approximately 50% after 180 min of visible light.

The photocatalytic degradation of THI was also performed under sunlight. Fe-N-P/TiO_2/β-CD evidenced the best photocatalytic THI degradation activity with an efficiency of about 88% after 180 min of sunlight. On the other hand, Fe-N-P/TiO_2 sample degrades THI with an efficiency of 73% after 180 min of sunlight, a value lower than that obtained with Fe/N-P/TiO_2 coupled with unprocessed β-CD (78%). The results on photocatalytic degradation of THI confirm that the micronization of β-CD and their combination with photocatalytic particles lead to electron-hole recombination restriction and photocatalytic efficiency enhancement. Therefore the coupling among β-CD and Fe/N-P/TiO_2 could represent a significant step forward in the development of innovative photocatalytic systems for the removal of water pollutants under sunlight.

Subsequently, it was considered appropriate to use for the direct oxidation of benzene to phenol under UV light and visible light irradiation the photocatalysts in powder form (Fe-TiO_2, N-TiO_2, Fe-N-TiO_2, Fe-Pr-TiO_2 Fe-N-P/TiO_2 and Fe-N-P/TiO_2/β-CD) optimized for water pollutants degradation with the aim of exploring their potential application in a photocatalytic process for organic synthesis under mild conditions and therefore to overcome the limits associated to the industrial process of phenol production.

All TiO_2-based photocatalysts showed a high benzene conversion but very low selectivity to phenol under UV light. However, N-TiO_2 exhibits a high conversion of benzene under visible light without phenol production. Therefore, since N-TiO_2 was the only photocatalyst to exhibit the highest benzene conversion than the other photocatalytic formulations under visible light, the idea was to disperse N-TiO_2 in powder form into a polymeric medium in order to guarantee the phenol production and improve the selectivity to phenol. To this purpose, sPS monolithic aerogels were employed as support for photocatalytic particles. The sPS aerogels were prepared starting from syndiotactic polystyrene gels, obtained by dissolving the polymer in chloroform. After this step, the aerogels are obtained by supercritical carbon dioxide treatment, which extracts the solvent avoiding the gel collapsing. Absorption results in dark conditions showed that sPS aerogel absorbed phenol in very low extent, whereas higher benzene absorption efficiency was observed in the same conditions. These results can be explained considering the high affinity of sPS aerogels towards non-polar compounds (benzene) and its very low affinity with polar compounds (phenol).

Kinetic studies showed that the absorption process with sPS aerogels followed pseudo first-order model for all the tested guest molecules and for all the investigated operating conditions. The obtained values of kinetic constants evidenced as sPS aerogels absorbed benzene more rapidly than phenol because of the lower solubility of benzene in water with respect to phenol. Moreover, diffusivity constants of the tested aromatic compounds into sPS crystalline structure were evaluated. Photoreactive polymer composite based on N-doped TiO_2 embedded into syndiotactic polystyrene monolithic aerogel (sPS) was employed to improve the yield and selectivity to phenol from benzene hydroxylation in presence of UV and visible light. Under UV light, a very high benzene conversion (66%) was achieved with N-TiO_2 but with a low phenol selectivity (5.5%), while the use of N-TiO_2/sPS composite promoted an unexpected improved selectivity to phenol (38%), achieving simultaneously a high benzene conversion (52%). Under visible light, N-TiO_2 showed a high benzene conversion (62%) without phenol formation proving that the same photocatalyst, if used in powder form, is not selective to phenol. On the contrary, N-TiO_2/sPS under visible light led to increased phenol selectivity (9%) with a considerable benzene conversion (72%). In order to further improve the phenol selectivity under visible light, the pH of the aqueous solution was changed from about 7 to 2. The obtained results showed a remarkable enhancement of both selectivity (98%) and phenol yield (57%), preserving a high benzene conversion (58%). Therefore the polymeric matrix is able to make N-TiO_2, embedded in it, selective towards phenol, assuring a high benzene conversion. Since the benzene oxidation in presence of N-TiO_2 photocatalyst in powder form showed a high conversion of benzene without phenol production under visible light, it was chosen to modify the surface of N-TiO_2 by deposition of Cu, Fe and V oxides by wet impregnation to increase the phenol production.. After 600 min of visible light irradiation, Cu/N-TiO_2 photocatalyst achieves a phenol yield equal to 19% significantly higher than that observed with Fe/N-TiO_2 (2%) and V/N-TiO_2 (2.5%). Moreover, kinetic modeling of the direct oxidation of benzene to phenol using Cu/N-TiO_2, Fe/N-TiO_2 and V/N-TiO_2 photocatalysts was performed, allowing to obtain the values of kinetic constants for phenol production. The results evidenced that the Cu/N-TiO_2 photocatalyst showed the highest phenol formation rate with respect to Fe/N-TiO_2 and V/N-TiO_2. Therefore, Cu/N-TiO_2 photocatalyst was chosen for the dispersion inside the sPS aerogel. Cu/N-TiO_2/sPS aerogel under visible light irradiation showed photocatalytic performances better than N-TiO_2/sPS. Indeed, phenol yield obtained with Cu/N-TiO_2/sPS aerogel reached a value of about 20 % whereas phenol yield observed using N-TiO_2/sPS was lower, approximately 6.5%, after 600 min of visible light. Moreover, the calculation of effectiveness factor evidenced evidencing that the benzene diffusion phenomena within Cu/N-TiO_2/sPS is not the limiting factor for benzene conversion and that the limiting step is the photoreaction occurring on Cu/N-

TiO_2 embedded in the aerogel structure. The effect of Cu/N-TiO_2/sPS aerogel dosage was also evaluated. Benzene conversion was 58 and 81%, while the phenol yield was 20 and 9.5% with 3 g/L and 6 g/L of Cu/N-TiO_2/sPS, respectively, after 600 min of visible light irradiation. To increase the selectivity to phenol and reduce the phenol affinity towards the sPS polymer, the pH was modified from about 7 to 2. Benzene conversion obtained in acidic condition using 6g/L of Cu/N-TiO_2/sPS under visible light, is always higher than that observed in neutral condition. In particular, the benzene conversion was 96% after 180 min of visible light and remianinedconstant for the overall irradiation time (600 min). Simultaneously, phenol yield increased to about 96% in acidic condition after 180 min of visible light, and phenol selectivity was over 99% with aphenol formation rate equal to 5.4 mmol/($g_{Cu/N\text{-}TiO2}$·h), remarkably higher than those achieved at pH=7 (9.5% and 0.58 mmol/($g_{Cu/N\text{-}TiO2}$·h)). In addition, Cu/N-TiO_2/sPS was recovered from the aqueous solution and reused several times without significant loss of photoreactivity and reduction of phenol yield. As concluding remark, the achieved photoreactive solid phase (Cu/N-TiO_2/sPS) could allow a significant leap forward in the development of green processes capable of facing the challenge of selective oxidation reactions of aromatic hydrocarbons in mild conditions.

References

Adyani, S. M. & Ghorbani, m. 2017. A comparative study of physicochemical and photocatalytic properties of visible light responsive Fe, Gd and P single and tri-doped TiO 2 nanomaterials. *Journal of Rare Earths*.

Agócs, T. Z., Puskás, I., Varga, E., Molnár, M. & Fenyvesi, É. 2016. Stabilization of nanosized titanium dioxide by cyclodextrin polymers and its photocatalytic effect on the degradation of wastewater pollutants. *Beilstein Journal of Organic Chemistry,* 12**,** 2873-2882.

Ahn, W.-Y., Sheeley, S. A., Rajh, T. & Cropek, D. M. 2007. Photocatalytic reduction of 4-nitrophenol with arginine-modified titanium dioxide nanoparticles. *Applied Catalysis B: Environmental,* 74**,** 103-110.

Akshay, V., Arun, B., Mandal, G., Mutta, G. R., Chanda, A. & Vasundhara, M. 2018. Observation of optical band-gap narrowing and enhanced magnetic moment in co-doped sol–gel-derived anatase TiO2 nanocrystals. *The Journal of Physical Chemistry C,* 122**,** 26592-26604.

Alcaraz de la Osa, R., Iparragirre, I., Ortiz, D. & Saiz, J. 2020. The extended Kubelka–Munk theory and its application to spectroscopy. *ChemTexts,* 6**,** 1-14.

Ali, M. Y., Alam, A. U. & Howlader, M. M. 2020. Fabrication of highly sensitive Bisphenol A electrochemical sensor amplified with chemically modified multiwall carbon nanotubes and β-cyclodextrin. *Sensors and Actuators B: Chemical,* 320**,** 128319.

Ali, T., Tripathi, P., Azam, A., Raza, W., Ahmed, A. S., Ahmed, A. & Muneer, M. 2017a. Photocatalytic performance of Fe-doped TiO2 nanoparticles under visible-light irradiation. *Materials Research Express,* 4**,** 015022.

Ali, T., Tripathi, P., Azam, A., Raza, W., Shareef Ahmed, A., Ahmed, A. & Muneer, M. 2017b. Photocatalytic performance of Fe-doped TiO 2 nanoparticles under visible-light irradiation. *Materials Research Express,* 4**,** 015022.

Almquist, C. B. & Biswas, P. 2001. The photo-oxidation of cyclohexane on titanium dioxide: an investigation of competitive adsorption and its effects on product formation and selectivity. *Applied Catalysis A: General,* 214**,** 259-271.

Anand, S. R., Aggarwal, R., Saini, D., Sonker, A. K., Chauhan, N. & Sonkar, S. K. 2019. Removal of toxic chromium (VI) from the wastewater under the sunlight-illumination by functionalized carbon nano-rods. *Solar Energy,* 193**,** 774-781.

Anandan, S. & Yoon, M. 2004. Photocatalytic degradation of Nile red using TiO2-β cyclodextrin colloids. *Catalysis Communications,* 5**,** 271-275.

Andreozzi, R., Caprio, V., Insola, A. & Marotta, R. 1999. Advanced oxidation processes (AOP) for water purification and recovery. *Catalysis today,* 53**,** 51-59.

Ansari, S. A., Khan, M. M., Ansari, M. O. & Cho, M. H. 2016. Nitrogen-doped titanium dioxide (N-doped TiO 2) for visible light photocatalysis. *New Journal of Chemistry,* 40**,** 3000-3009.

Asghari, S., Farahmand, S., Razavizadeh, J. S. & Ghiaci, M. 2020. One-step photocatalytic benzene hydroxylation over iron (II) phthalocyanine: A new application for an old catalyst. *Journal of Photochemistry and Photobiology A: Chemistry,* 392**,** 112412.

Attarchi, N., Montazer, M. & Toliyat, T. 2013. Ag/TiO2/β-CD nano composite: preparation and photo catalytic properties for methylene blue degradation. *Applied Catalysis A: General,* 467**,** 107-116.

Avansi Jr, W., Catto, A. C., da Silva, L. F., Fiorido, T., Bernardini, S., Mastelaro, V. R., Aguir, K. & Arenal, R. 2019. One-dimensional V2O5/TiO2 heterostructures for chemiresistive ozone sensors. *ACS Applied Nano Materials,* 2**,** 4756-4764.

Avansi Jr, W., Ribeiro, C., Leite, E. R. & Mastelaro, V. R. 2009. Vanadium pentoxide nanostructures: an effective control of morphology and crystal structure in hydrothermal conditions. *Crystal Growth and Design,* 9**,** 3626-3631.

Avram, D., Patrascu, A. A., Istrate, M. C., Cojocaru, B. & Tiseanu, C. 2021. Lanthanide doped TiO2: Coexistence of discrete and

continuous dopant distribution in anatase phase. *Journal of Alloys and Compounds,* 851**,** 156849.

Azbar, N., Yonar, T. & Kestioglu, K. 2004. Comparison of various advanced oxidation processes and chemical treatment methods for COD and color removal from a polyester and acetate fiber dyeing effluent. *Chemosphere,* 55**,** 35-43.

Baeissa, E. 2015. Synthesis and characterization of sulfur-titanium dioxide nanocomposites for photocatalytic oxidation of cyanide using visible light irradiation. *Chinese Journal of Catalysis,* 36**,** 698-704.

Bagheri, S., Muhd Julkapli, N. & Bee Abd Hamid, S. 2014. Titanium dioxide as a catalyst support in heterogeneous catalysis. *The scientific world journal,* 2014.

Bahadori, E., Ramis, G., Zanardo, D., Menegazzo, F., Signoretto, M., Gazzoli, D., Pietrogiacomi, D., Michele, A. D. & Rossetti, I. 2020. Photoreforming of glucose over CuO/TiO2. *Catalysts,* 10**,** 477.

Bakar, S. A. & Ribeiro, C. 2016. A comparative run for visible-light-driven photocatalytic activity of anionic and cationic S-doped TiO2 photocatalysts: A case study of possible sulfur doping through chemical protocol. *Journal of Molecular Catalysis A: Chemical,* 421**,** 1-15.

Bakre, P. V., Tilve, S. & Shirsat, R. 2020. Influence of N sources on the photocatalytic activity of N-doped TiO2. *Arabian Journal of Chemistry,* 13**,** 7637-7651.

Bal, R., Tada, M., Sasaki, T. & Iwasawa, Y. 2006. Direct phenol synthesis by selective oxidation of benzene with molecular oxygen on an interstitial-N/Re cluster/zeolite catalyst. *Angewandte Chemie,* 118**,** 462-466.

Baran, E. & Yazici, B. 2016. Effect of different nano-structured Ag doped TiO2-NTs fabricated by electrodeposition on the electrocatalytic hydrogen production. *International Journal of Hydrogen Energy,* 41**,** 2498-2511.

Batzill, M., Morales, E. H. & Diebold, U. 2006. Influence of nitrogen doping on the defect formation and surface properties of TiO 2 rutile and anatase. *Physical review letters,* 96**,** 026103.

Bekkouche, S., Bouhelassa, M., Salah, N. H. & Meghlaoui, F. 2004. Study of adsorption of phenol on titanium oxide (TiO2). *Desalination,* 166**,** 355-362.

Berberidou, C., Kitsiou, V., Lambropoulou, D. A., Michailidou, D., Kouras, A. & Poulios, I. 2019. Decomposition and

detoxification of the insecticide thiacloprid by TiO2-mediated photocatalysis: kinetics, intermediate products and transformation pathways. *Journal of Chemical Technology & Biotechnology,* 94**,** 2475-2486.

Bersezio, C., Pardo, C., Miranda, S., Maran, B. M., Jorquera, G., da Silva Jr, A. R., Rodrigues, M. T. & Fernández, E. 2021. Evaluation of the effectiveness in teeth whitening of a single session with 6% hydrogen peroxide Laser/LED system. *Photodiagnosis and Photodynamic Therapy,* 36**,** 102532.

Bhave, R. 2007. Synthesis and photocatalysis study of Brookite phase titanium dioxide nanoparticles.

Blaser, H.-U. & Studer, M. 1999. The role of catalysis for the clean production of fine chemicals. *Applied Catalysis A: General,* 189**,** 191-204.

Bonchio, M., Carraro, M., Gardan, M., Scorrano, G., Drioli, E. & Fontananova, E. 2006. Hybrid photocatalytic membranes embedding decatungstate for heterogeneous photooxygenation. *Topics in catalysis,* 40**,** 133-140.

Boningari, T., Inturi, S. N. R., Suidan, M. & Smirniotis, P. G. 2018. Novel one-step synthesis of sulfur doped-TiO2 by flame spray pyrolysis for visible light photocatalytic degradation of acetaldehyde. *Chemical Engineering Journal,* 339**,** 249-258.

Borah, P., Ma, X., Nguyen, K. T. & Zhao, Y. 2012. A vanadyl complex grafted to periodic mesoporous organosilica: a green catalyst for selective hydroxylation of benzene to phenol. *Angewandte Chemie,* 124**,** 7876-7881.

Borgarello, E., Serpone, N., Barbeni, M., Minero, C., Pelizzetti, E. & Pramauro, E. 1986. Putting photocatalysis to work. *Homogeneous and Heterogeneous Photocatalysis.* Springer.

Brydson, J. A. 1999. *Plastics materials*, Elsevier.

Bu, X., Wang, Y., Li, J. & Zhang, C. 2015. Improving the visible light photocatalytic activity of TiO2 by combining sulfur doping and rectorite carrier. *Journal of Alloys and Compounds,* 628**,** 20-26.

Bui, T. D., Kimura, A., Higashida, S., Ikeda, S. & Matsumura, M. 2011. Two routes for mineralizing benzene by TiO2-photocatalyzed reaction. *Applied Catalysis B: Environmental,* 107**,** 119-127.

Bumajdad, A. & Madkour, M. 2014. Understanding the superior photocatalytic activity of noble metals modified titania under

UV and visible light irradiation. *Physical Chemistry Chemical Physics,* 16**,** 7146-7158.

Burns, A., Li, W., Baker, C. & Shah, S. 2001. Sol-gel synthesis and characterization of neodymium-ion doped nanostructured titania thin films. *MRS Online Proceedings Library (OPL),* 703.

Cappelletti, G., Bianchi, C. & Ardizzone, S. 2008. Nano-titania assisted photoreduction of Cr (VI): the role of the different TiO2 polymorphs. *Applied Catalysis B: Environmental,* 78**,** 193-201.

Chainarong, S., Sikong, L., Niyomwas, S. & Pavasupree, S. Synthesis and characterization of nitrogen-doped TiO2 nanomaterials for photocatalytic activities under visible light. 2011. Rajamangala University of Technology Thanyaburi.

Chaker, H., Fourmentin, S. & Chérif-Aouali, L. 2020. Efficient Photocatalytic Degradation of Ibuprofen under Visible Light Irradiation Using Silver and Cerium Co-Doped Mesoporous TiO2. *ChemistrySelect,* 5**,** 11787-11796.

Chen, L., Li, L. & Li, G. 2008. Synthesis of CuO nanorods and their catalytic activity in the thermal decomposition of ammonium perchlorate. *Journal of Alloys and Compounds,* 464**,** 532-536.

Chen, P., Chen, L., Zeng, Y., Ding, F., Jiang, X., Liu, N., Au, C.-T. & Yin, S.-F. 2018. Three-dimension hierarchical heterostructure of CdWO4 microrods decorated with Bi2WO6 nanoplates for high-selectivity photocatalytic benzene hydroxylation to phenol. *Applied Catalysis B: Environmental,* 234**,** 311-317.

Chen, X., Zhang, J., Fu, X., Antonietti, M. & Wang, X. 2009. Fe-g-C3N4-catalyzed oxidation of benzene to phenol using hydrogen peroxide and visible light. *Journal of the American Chemical Society,* 131**,** 11658-11659.

Cheng, H.-H., Chen, S.-S., Yang, S.-Y., Liu, H.-M. & Lin, K.-S. 2018a. Sol-Gel hydrothermal synthesis and visible light photocatalytic degradation performance of Fe/N codoped TiO2 catalysts. *Materials,* 11**,** 939.

Cheng, P., Deng, C., Gu, M. & Dai, X. 2008. Effect of urea on the photoactivity of titania powder prepared by sol–gel method. *Materials Chemistry and Physics,* 107**,** 77-81.

Cheng, S.-W., Li, Y.-H., Yuan, C.-S., Tsai, P.-Y., Shen, H.-Z. & Hung, C.-H. 2018b. An innovative advanced oxidation technology for effective decomposition of formaldehyde by combining iron modified nano-TiO2 (Fe/TiO2) photocatalytic

degradation with ozone oxidation. *Aerosol and Air Quality Research,* 18**,** 3220-3233.

Cheng, X. & Bi, X. T. 2014. A review of recent advances in selective catalytic NOx reduction reactor technologies. *Particuology,* 16**,** 1-18.

Cheng, X., Yu, X. & Xing, Z. 2012a. One-step synthesis of Fe–N–S-tri-doped TiO2 catalyst and its enhanced visible light photocatalytic activity. *Materials Research Bulletin,* 47**,** 3804-3809.

Cheng, X., Yu, X., Xing, Z. & Wan, J. 2012b. Enhanced photocatalytic activity of nitrogen doped TiO2 anatase nano-particle under simulated sunlight irradiation. *Energy Procedia,* 16**,** 598-605.

Cheng, X., Yu, X., Xing, Z. & Yang, L. 2016. Synthesis and characterization of N-doped TiO2 and its enhanced visible-light photocatalytic activity. *Arabian Journal of Chemistry,* 9**,** S1706-S1711.

Cherniak, S. L., Almuhtaram, H., McKie, M. J., Hermabessiere, L., Yuan, C., Rochman, C. M. & Andrews, R. C. 2022. Conventional and biological treatment for the removal of microplastics from drinking water. *Chemosphere,* 288**,** 132587.

Chiou, C.-H. & Juang, R.-S. 2007. Photocatalytic degradation of phenol in aqueous solutions by Pr-doped TiO2 nanoparticles. *Journal of Hazardous Materials,* 149**,** 1-7.

Chu, W., Choy, W. & So, T. 2007. The effect of solution pH and peroxide in the TiO2-induced photocatalysis of chlorinated aniline. *Journal of hazardous materials,* 141**,** 86-91.

Ciambelli, P., Sannino, D., Palma, V. & Vaiano, V. 2005. Cyclohexane photocatalytic oxidative dehydrogenation to benzene on sulphated titania supported MoOx. *Studies in Surface Science and Catalysis.* Elsevier.

Ciambelli, P., Sannino, D., Palma, V., Vaiano, V. & Mazzei, R. 2009. A step forwards in ethanol selective photo-oxidation. *Photochemical & Photobiological Sciences,* 8**,** 699-704.

Colmenares, J., Aramendia, M., Marinas, A., Marinas, J. & Urbano, F. 2006. Synthesis, characterization and photocatalytic activity of different metal-doped titania systems. *Applied Catalysis A: General,* 306**,** 120-127.

Cong, Y., Zhang, J., Chen, F., Anpo, M. & He, D. 2007. Preparation, photocatalytic activity, and mechanism of nano-TiO2 co-

doped with nitrogen and iron (III). *The Journal of Physical Chemistry C,* 111**,** 10618-10623.

Cordeiro, D. S., Cassio, F. L., Ciccotti, L., Hewer, T. L., Corio, P. & Freire, R. S. 2021. Photocatalytic activity of Pr-modified TiO2 for the degradation of bisphenol A. *SN Applied Sciences,* 3**,** 1-8.

Coronado, J. M., Soria, J., Conesa, J. C., Bellod, R., Adán, C., Yamaoka, H., Loddo, V. & Augugliaro, V. 2005. Photocatalytic inactivation of Legionella pneumophila and an aerobic bacteria consortium in water over TiO2/SiO2 fibres in a continuous reactor. *Topics in Catalysis,* 35**,** 279-286.

Crişan, M., Răileanu, M., Drăgan, N., Crişan, D., Ianculescu, A., Niţoi, I., Oancea, P., Şomăcescu, S., Stănică, N. & Vasile, B. 2015. Sol–gel iron-doped TiO2 nanopowders with photocatalytic activity. *Applied Catalysis A: General,* 504**,** 130-142.

Crisenza, G. E. & Melchiorre, P. 2020. Chemistry glows green with photoredox catalysis. *Nature communications,* 11**,** 1-4.

Cundall, R. B., Rudham, R. & Salim, M. S. 1976. Photocatalytic oxidation of propan-2-ol in the liquid phase by rutile. *Journal of the Chemical Society, Faraday Transactions 1: Physical Chemistry in Condensed Phases,* 72**,** 1642-1651.

Czoska, A., Livraghi, S., Chiesa, M., Giamello, E., Agnoli, S., Granozzi, G., Finazzi, E., Valentin, C. D. & Pacchioni, G. 2008. The nature of defects in fluorine-doped TiO2. *The Journal of Physical Chemistry C,* 112**,** 8951-8956.

Daniel, C., Alfano, D., Venditto, V., Cardea, S., Reverchon, E., Larobina, D., Mensitieri, G. & Guerra, G. 2005. Aerogels with a microporous crystalline host phase. *Advanced materials,* 17**,** 1515-1518.

Daniel, C., Antico, P. & Guerra, G. 2018. Etched fibers of syndiotactic polystyrene with nanoporous-crystalline phases. *Macromolecules,* 51**,** 6138-6148.

Daniel, C., Antico, P., Yamaguchi, H., Kogure, M. & Guerra, G. 2016. Microporous-crystalline microfibers by eco-friendly guests: An efficient tool for sorption of volatile organic pollutants. *Microporous and Mesoporous Materials,* 232**,** 205-210.

Daniel, C., Galdi, N., Montefusco, T. & Guerra, G. 2007. Syndiotactic polystyrene clathrates with polar guest molecules. *Chemistry of materials,* 19**,** 3302-3308.

Daniel, C., Giudice, S. & Guerra, G. 2009. Syndiotatic polystyrene aerogels with β,γ, and ε crystalline phases. *Chemistry of Materials,* 21**,** 1028-1034.

Daniel, C. & Guerra, G. Crystalline organization in syndiotactic polystyrene gels and aerogels. Macromolecular Symposia, 2005. Wiley Online Library, 247-252.

Daniel, C. & Guerra, G. Monolithic aerogels with nanoporous crystalline phases. AIP Conference Proceedings, 2015. AIP Publishing LLC, 130001.

Daniel, C., Longo, S., Cardea, S., Vitillo, J. G. & Guerra, G. 2012. Monolithic nanoporous–crystalline aerogels based on PPO. *RSC advances,* 2**,** 12011-12018.

Daniel, C., Longo, S., Ricciardi, R., Reverchon, E. & Guerra, G. 2013. Monolithic nanoporous crystalline aerogels. *Macromolecular rapid communications,* 34**,** 1194-1207.

Daniel, C., Navarra, W., Venditto, V., Sacco, O. & Vaiano, V. 2020. Nanoporous polymeric aerogels–based structured photocatalysts for the removal of organic pollutant from water under visible or solar light. *Visible Light Active Structured Photocatalysts for the Removal of Emerging Contaminants.* Elsevier.

Daniel, C., Rufolo, C., Bobba, F., Scarfato, A., Cucolo, A. M. & Guerra, G. 2011. Ferroelectric co-crystalline polymers. *Journal of Materials Chemistry,* 21**,** 19074-19079.

Daniel, C., Sannino, D. & Guerra, G. 2008. Syndiotactic polystyrene aerogels: adsorption in amorphous pores and absorption in crystalline nanocavities. *Chemistry of Materials,* 20**,** 577-582.

Dasireddy, V. D. & Likozar, B. 2018. Selective photocatalytic oxidation of benzene to phenol using carbon nanotube (CNT)-supported Cu and TiO2 heterogeneous catalysts. *Journal of the Taiwan Institute of Chemical Engineers,* 82**,** 331-341.

Delekar, S., Yadav, H., Achary, S., Meena, S. & Pawar, S. 2012. Structural refinement and photocatalytic activity of Fe-doped anatase TiO2 nanoparticles. *Applied surface science,* 263**,** 536-545.

Demeestere, K., Dewulf, J. & Van Langenhove, H. 2007. Heterogeneous photocatalysis as an advanced oxidation process for the abatement of chlorinated, monocyclic aromatic and sulfurous volatile organic compounds in air: state of the art. *Critical Reviews in Environmental Science and Technology,* 37**,** 489-538.

Deng, L., Wang, S., Liu, D., Zhu, B., Huang, W., Wu, S. & Zhang, S. 2009. Synthesis, characterization of Fe-doped TiO2 nanotubes with high photocatalytic activity. *Catalysis Letters,* 129**,** 513-518.

Devaraji, P. & Jo, W.-K. 2018. Noble metal free Fe and Cr dual-doped nanocrystalline titania (Ti1− x− yMx+ yO2) for high selective photocatalytic conversion of benzene to phenol at ambient temperature. *Applied Catalysis A: General,* 565**,** 1-12.

Devaraji, P., Sathu, N. K. & Gopinath, C. S. 2014. Ambient oxidation of benzene to phenol by photocatalysis on Au/Ti0. 98V0. 02O2: role of holes. *Acs Catalysis,* 4**,** 2844-2853.

Devi, L. G. & Kavitha, R. 2014. Enhanced photocatalytic activity of sulfur doped TiO2 for the decomposition of phenol: a new insight into the bulk and surface modification. *Materials Chemistry and Physics,* 143**,** 1300-1308.

Dewil, R., Mantzavinos, D., Poulios, I. & Rodrigo, M. A. 2017. New perspectives for advanced oxidation processes. *Journal of environmental management,* 195**,** 93-99.

Deze, E. G., Papageorgiou, S. K., Favvas, E. P. & Katsaros, F. K. 2012. Porous alginate aerogel beads for effective and rapid heavy metal sorption from aqueous solutions: Effect of porosity in Cu2+ and Cd2+ ion sorption. *Chemical engineering journal,* 209**,** 537-546.

Di Valentin, C. & Pacchioni, G. 2013. Trends in non-metal doping of anatase TiO2: B, C, N and F. *Catalysis today,* 206**,** 12-18.

Di Valentin, C., Pacchioni, G. & Selloni, A. 2004. Origin of the different photoactivity of N-doped anatase and rutile TiO 2. *Physical review B,* 70**,** 085116.

Di Valentin, C., Pacchioni, G. & Selloni, A. 2005. Theory of carbon doping of titanium dioxide. *Chemistry of Materials,* 17**,** 6656-6665.

Dimitrijevic, N. M., Rajh, T., Saponjic, Z. V., De La Garza, L. & Tiede, D. M. 2004. Light-induced charge separation and redox chemistry at the surface of TiO2/host− guest hybrid nanoparticles. *The Journal of Physical Chemistry B,* 108**,** 9105-9110.

Dixit, R., Malaviya, D., Pandiyan, K., Singh, U. B., Sahu, A., Shukla, R., Singh, B. P., Rai, J. P., Sharma, P. K. & Lade, H. 2015. Bioremediation of heavy metals from soil and aquatic environment: an overview of principles and criteria of fundamental processes. *Sustainability,* 7**,** 2189-2212.

Dong, F., Wang, H., Sen, G., Wu, Z. & Lee, S. 2011. Enhanced visible light photocatalytic activity of novel Pt/C-doped TiO2/PtCl4 three-component nanojunction system for degradation of toluene in air. *Journal of Hazardous materials,* 187**,** 509-516.

Dong, G., Chen, B., Liu, B., Hounjet, L. J., Cao, Y., Stoyanov, S. R., Yang, M. & Zhang, B. 2022. Advanced oxidation processes in microreactors for water and wastewater treatment: Development, challenges, and opportunities. *Water Research***,** 118047.

Dong, H., Zeng, G., Tang, L., Fan, C., Zhang, C., He, X. & He, Y. 2015. An overview on limitations of TiO2-based particles for photocatalytic degradation of organic pollutants and the corresponding countermeasures. *Water Research,* 79**,** 128-146.

Du, M.-H., Feng, J. & Zhang, S. 2007. Photo-oxidation of polyhydroxyl molecules on TiO 2 surfaces: from hole scavenging to light-induced self-assembly of TiO 2-cyclodextrin wires. *Physical review letters,* 98**,** 066102.

Du, S., Lian, J. & Zhang, F. 2021. Visible light-responsive N-doped TiO2 photocatalysis: synthesis, characterizations, and applications. *Transactions of Tianjin University***,** 1-20.

Dunnill, C. W., Aiken, Z. A., Kafizas, A., Pratten, J., Wilson, M., Morgan, D. J. & Parkin, I. P. 2009. White light induced photocatalytic activity of sulfur-doped TiO 2 thin films and their potential for antibacterial application. *Journal of Materials Chemistry,* 19**,** 8747-8754.

Ebrahimi, R., Maleki, A., Rezaee, R., Daraei, H., Safari, M., McKay, G., Lee, S.-M. & Jafari, A. 2021. Synthesis and application of Fe-doped TiO2 nanoparticles for photodegradation of 2, 4-D from aqueous solution. *Arabian Journal for Science and Engineering,* 46**,** 6409-6422.

Ellouzi, I., Harir, M., Schmitt-Kopplin, P. & Laânab, L. 2020. Coprecipitation Synthesis of Fe-Doped TiO2 from Various Commercial TiO2 for Photocatalytic Reaction. *International Journal of Environmental Research,* 14**,** 605-613.

Etacheri, V., Di Valentin, C., Schneider, J., Bahnemann, D. & Pillai, S. C. 2015. Visible-light activation of TiO2 photocatalysts: Advances in theory and experiments. *Journal of Photochemistry and Photobiology C: Photochemistry Reviews,* 25**,** 1-29.

Fan, X., Wan, J., Liu, E., Sun, L., Hu, Y., Li, H., Hu, X. & Fan, J. 2015. High-efficiency photoelectrocatalytic hydrogen generation enabled by Ag deposited and Ce doped TiO2 nanotube arrays. *Ceramics International,* 41**,** 5107-5116.

Fessi, N., Nsib, M. F., Cardenas, L., Guillard, C., Dappozze, F., Houas, A., Parrino, F., Palmisano, L., Ledoux, G., Amans, D. & Chevalier, Y. 2020. Surface and Electronic Features of Fluorinated TiO2and Their Influence on the Photocatalytic Degradation of 1-Methylnaphthalene. *Journal of Physical Chemistry C,* 124**,** 11456-11468.

Filippatos, P.-P., Kelaidis, N., Vasilopoulou, M., Davazoglou, D., Lathiotakis, N. N. & Chroneos, A. 2019. Defect processes in F and Cl doped anatase TiO2. *Scientific Reports,* 9**,** 1-10.

Fox, M. A. & Dulay, M. T. 1993. Heterogeneous photocatalysis. *Chemical Reviews,* 93**,** 341-357.

Franco, P., Sacco, O., De Marco, I. & Vaiano, V. 2019. Zinc oxide nanoparticles obtained by supercritical antisolvent precipitation for the photocatalytic degradation of crystal violet dye. *Catalysts,* 9**,** 346.

Friedmann, D., Hakki, A., Kim, H., Choi, W. & Bahnemann, D. 2016. Heterogeneous photocatalytic organic synthesis: state-of-the-art and future perspectives. *Green Chemistry,* 18**,** 5391-5411.

Fujishima, A. 1972. Electrochemical photocatalysis of water at a semiconductor electrode. *Nature,* 238**,** 5358.

Fujishima, A. & Honda, K. 1972. Electrochemical photolysis of water at a semiconductor electrode. *nature,* 238**,** 37-38.

Fujishima, A., Rao, T. N. & Tryk, D. A. 2000. Titanium dioxide photocatalysis. *Journal of photochemistry and photobiology C: Photochemistry reviews,* 1**,** 1-21.

Ganesh, I., Kumar, P. P., Gupta, A. K., Sekhar, P. S., Radha, K., Padmanabham, G. & Sundararajan, G. 2012. Preparation and characterization of Fe-doped TiO2 powders for solar light response and photocatalytic applications. *Processing and application of ceramics,* 6**,** 21-36.

Gaur, L. K., Kumar, P., Kushavah, D., Khiangte, K. R., Mathpal, M. C., Agrahari, V., Gairola, S., Soler, M. A., Swart, H. & Agarwal, A. 2019. Laser induced phase transformation influenced by Co doping in TiO2 nanoparticles. *Journal of Alloys and Compounds,* 780**,** 25-34.

Ghernaout, D. 2017. Water treatment chlorination: An updated mechanistic insight review. *Chemistry Research Journal,* 2**,** 125-138.

Ghuman, K. K. & Singh, C. V. 2013. Effect of doping on electronic structure and photocatalytic behavior of amorphous TiO2. *Journal of Physics: Condensed Matter,* 25**,** 475501.

Giahi, M., Pathania, D., Agarwal, S., Ali, G. A., Chong, K. F. & Gupta, V. K. 2019. Preparation of Mg-doped TiO2 nanoparticles for photocatalytic degradation of some organic pollutants. *Stud Univ Babes-Bolyai, Chem,* 64**,** 7-18.

Giannakas, A., Antonopoulou, M., Daikopoulos, C., Deligiannakis, Y. & Konstantinou, I. 2016. Characterization and catalytic performance of B-doped, B–N co-doped and B–N–F tri-doped TiO2 towards simultaneous Cr (VI) reduction and benzoic acid oxidation. *Applied Catalysis B: Environmental,* 184**,** 44-54.

Giarola, M., Sanson, A., Monti, F., Mariotto, G., Bettinelli, M., Speghini, A. & Salviulo, G. 2010. Vibrational dynamics of anatase TiO 2: Polarized Raman spectroscopy and ab initio calculations. *Physical Review B,* 81**,** 174305.

Glass, B., Brown, M., Daya, S., Worthington, M., Drummond, P., Antunes, E., Lebete, M., Anoopkumar-Dukie, S. & Maharaj, D. 2001. Influence of cyclodextrins on the photostability of selected drug molecules in solution and the solid-state. *International Journal of photoenergy,* 3**,** 205-211.

Gondal, M., Hameed, A., Yamani, Z. & Arfaj, A. 2004. Photocatalytic transformation of methane into methanol under UV laser irradiation over WO3, TiO2 and NiO catalysts. *Chemical physics letters,* 392**,** 372-377.

Gopal, N. O., Lo, H.-H., Ke, T.-F., Lee, C.-H., Chou, C.-C., Wu, J.-D., Sheu, S.-C. & Ke, S.-C. 2012. Visible light active phosphorus-doped TiO2 nanoparticles: an EPR evidence for the enhanced charge separation. *The Journal of Physical Chemistry C,* 116**,** 16191-16197.

Gopinath, K. P., Madhav, N. V., Krishnan, A., Malolan, R. & Rangarajan, G. 2020. Present applications of titanium dioxide for the photocatalytic removal of pollutants from water: A review. *Journal of Environmental Management,* 270**,** 110906.

Guan, B., Yu, J., Guo, S., Yu, S. & Han, S. 2020. Porous nickel doped titanium dioxide nanoparticles with improved visible light photocatalytic activity. *Nanoscale Advances,* 2**,** 1352-1357.

Guan, B., Zhan, R., Lin, H. & Huang, Z. 2014. Review of state of the art technologies of selective catalytic reduction of NOx from diesel engine exhaust. *Applied Thermal Engineering,* 66**,** 395-414.

Guerra, G., Daniel, C., Rizzo, P. & Tarallo, O. 2012. Advanced materials based on polymer cocrystalline forms. *Journal of Polymer Science Part B: Polymer Physics,* 50**,** 305-322.

Gui, H., Ji, S., Zhang, T., Zhao, Y. & Guo, Q. 2020. Nanofibrous, hypercrosslinked polymers with multiscale pores through post-crosslinking of emulsion-templated syndiotactic polystyrene aerogels. *European Polymer Journal,* 135**,** 109880.

Guillard, C., Bui, T.-H., Felix, C., Moules, V., Lina, B. & Lejeune, P. 2008. Microbiological disinfection of water and air by photocatalysis. *Comptes Rendus Chimie,* 11**,** 107-113.

Guo, H., Meador, M. A. B., McCorkle, L., Quade, D. J., Guo, J., Hamilton, B. & Cakmak, M. 2012. Tailoring properties of cross-linked polyimide aerogels for better moisture resistance, flexibility, and strength. *ACS applied materials & interfaces,* 4**,** 5422-5429.

Guo, Y., Guo, S., Ren, J., Zhai, Y., Dong, S. & Wang, E. 2010. Cyclodextrin functionalized graphene nanosheets with high supramolecular recognition capability: Synthesis and host-guest inclusion for enhanced electrochemical performance (ACS Nano (2010) 4 (4001-4010)). *ACS Nano,* 4**,** 5512.

Gupta, N., Bansal, P. & Pal, B. 2015. Metal ion-TiO2 nanocomposites for the selective photooxidation of benzene to phenol and cycloalkanol to cycloalkanone. *Journal of Experimental Nanoscience,* 10**,** 148-160.

Gurkan, Y. Y., Turkten, N., Hatipoglu, A. & Cinar, Z. 2012. Photocatalytic degradation of cefazolin over N-doped TiO2 under UV and sunlight irradiation: Prediction of the reaction paths via conceptual DFT. *Chemical Engineering Journal,* 184**,** 113-124.

Gutierrez-Urbano, I., Villen-Guzman, M., Perez-Recuerda, R. & Rodriguez-Maroto, J. M. 2021. Removal of polycyclic aromatic hydrocarbons (PAHs) in conventional drinking water treatment processes. *Journal of Contaminant Hydrology,* 243**,** 103888.

Haarstrick, A., Kut, O. M. & Heinzle, E. 1996. TiO2-assisted degradation of environmentally relevant organic compounds in

wastewater using a novel fluidized bed photoreactor. *Environmental science & technology,* 30**,** 817-824.

Haoli, Q., Guobang, G. & Song, L. 2007. Preparation of nitrogen-doped titania and its photocatalytic activity. *Rare Metals,* 26**,** 254-262.

Herrmann, J.-M. 1999. Heterogeneous photocatalysis: fundamentals and applications to the removal of various types of aqueous pollutants. *Catalysis today,* 53**,** 115-129.

Herrmann, J.-M. 2005. Heterogeneous photocatalysis: state of the art and present applications In honor of Pr. RL Burwell Jr.(1912–2003), Former Head of Ipatieff Laboratories, Northwestern University, Evanston (Ill). *Topics in catalysis,* 34**,** 49-65.

Herrmann, J.-M., Duchamp, C., Karkmaz, M., Hoai, B. T., Lachheb, H., Puzenat, E. & Guillard, C. 2007. Environmental green chemistry as defined by photocatalysis. *Journal of hazardous materials,* 146**,** 624-629.

Hewer, T. L. R., Souza, E. C. C. d., Martins, T., Muccillo, E. N. d. S. & Freire, R. S. 2011. Influence of neodymium ions on photocatalytic activity of TiO2 synthesized by sol–gel and precipitation methods. *Journal of Molecular Catalysis A: Chemical,* 336**,** 58-63.

Hinojosa-Reyes, M., Arriaga, S., Diaz-Torres, L. & Rodríguez-González, V. 2013. Gas-phase photocatalytic decomposition of ethylbenzene over perlite granules coated with indium doped TiO2. *Chemical engineering journal,* 224**,** 106-113.

Hjeresen, D. L., Kirchhoff, M. M. & Lankey, R. L. 2002. Green chemistry: Environment, economics, and competitiveness. *Corporate Environmental Strategy,* 9**,** 259-266.

Hoffmann, N. 2008. Photochemical reactions as key steps in organic synthesis. *Chemical reviews,* 108**,** 1052-1103.

Hosseini-Sarvari, M. & Valikhani, A. 2021. Boron-doped TiO 2 (B-TiO 2): visible-light photocatalytic difunctionalization of alkenes and alkynes. *New Journal of Chemistry,* 45**,** 12464-12470.

Hosseini, S. M., Ghiaci, M., Kulinich, S. A., Wunderlich, W., Farrokhpour, H., Saraji, M. & Shahvar, A. 2018. Au-Pd@ g-C3N4 as an efficient photocatalyst for visible-light oxidation of benzene to phenol: experimental and mechanistic study. *The Journal of Physical Chemistry C,* 122**,** 27477-27485.

Hou, D., Goei, R., Wang, X., Wang, P. & Lim, T. 2012. Preparation of carbon-sensitized and Fe–Er codoped TiO2 with response

surface methodology for bisphenol A photocatalytic degradation under visible-light irradiation. *Applied Catalysis B: Environmental,* 126.

Hou, Q., Zheng, Y., Chen, J.-F., Zhou, W., Deng, J. & Tao, X. 2011. Visible-light-response iodine-doped titanium dioxide nanocrystals for dye-sensitized solar cells. *Journal of Materials Chemistry,* 21**,** 3877-3883.

Hu, M., Meng, F., Li, N., Zhang, S. & Ma, J. 2022. Insight Into the CuOx Interacts with Oxygen Vacancies on the Surface of Black-TiO2 for NO Oxidation. *Catalysis Letters,* 152**,** 2869-2879.

Hu, Y., Cao, Y., Wang, P., Li, D., Chen, W., He, Y., Fu, X., Shao, Y. & Zheng, Y. 2012. A new perspective for effect of Bi on the photocatalytic activity of Bi-doped TiO2. *Applied Catalysis B: Environmental,* 125**,** 294-303.

Hu, Y., Li, D., Zheng, Y., Chen, W., He, Y., Shao, Y., Fu, X. & Xiao, G. 2011. BiVO4/TiO2 nanocrystalline heterostructure: a wide spectrum responsive photocatalyst towards the highly efficient decomposition of gaseous benzene. *Applied Catalysis B: Environmental,* 104**,** 30-36.

Huang, G. & Zhu, Y. 2007. Synthesis and photocatalytic performance of ZnWO4 catalyst. *Materials Science and Engineering: B,* 139**,** 201-208.

Huang, J. & Wan, Q. 2009. Gas sensors based on semiconducting metal oxide one-dimensional nanostructures. *Sensors,* 9**,** 9903-9924.

Huang, J., Wang, X., Hou, Y., Chen, X., Wu, L., Wang, X. & Fu, X. 2008. Synthesis of functionalized mesoporous TiO2 molecular sieves and their application in photocatalysis. *Microporous and mesoporous materials,* 110**,** 543-552.

Iacovino, R., Rapuano, F., Caso, J. V., Russo, A., Lavorgna, M., Russo, C., Isidori, M., Russo, L., Malgieri, G. & Isernia, C. 2013. β-cyclodextrin inclusion complex to improve physicochemical properties of pipemidic acid: Characterization and bioactivity evaluation. *International Journal of Molecular Sciences,* 14**,** 13022-13041.

Ibhadon, A. O. & Fitzpatrick, P. 2013. Heterogeneous photocatalysis: recent advances and applications. *Catalysts,* 3**,** 189-218.

Ibram, G., Polkampally, P., Gupta, A., Sekhar, P., Kalathur, R., Gadhe, P. & Sundararajan, G. 2013. Preparation and

characterization of Fe-doped TiO 2 powders for solar light response and photocatalytic applications.

Ide, Y., Nakamura, N., Hattori, H., Ogino, R., Ogawa, M., Sadakane, M. & Sano, T. 2011. Sunlight-induced efficient and selective photocatalytic benzene oxidation on TiO 2-supported gold nanoparticles under CO 2 atmosphere. *Chemical Communications,* 47**,** 11531-11533.

Ioannides, T. & Verykios, X. E. 1996. Charge transfer in metal catalysts supported on doped TiO2: a theoretical approach based on metal–semiconductor contact theory. *Journal of Catalysis,* 161**,** 560-569.

Irie, H., Watanabe, Y. & Hashimoto, K. 2003. Carbon-doped anatase TiO2 powders as a visible-light sensitive photocatalyst. *Chemistry Letters,* 32**,** 772-773.

Jaimy, K., Safeena, V., Ghosh, D., Hebalkar, N. & Warrier, K. 2012. Photocatalytic activity enhancement in doped titanium dioxide by crystal defects. *Dalton transactions (Cambridge, England : 2003),* 41**,** 4824-32.

Janczarek, M. & Kowalska, E. 2017. On the origin of enhanced photocatalytic activity of copper-modified titania in the oxidative reaction systems. *Catalysts,* 7**,** 317.

Javadian, H., Angaji, M. T. & Naushad, M. 2014. Synthesis and characterization of polyaniline/γ-alumina nanocomposite: a comparative study for the adsorption of three different anionic dyes. *Journal of Industrial and Engineering Chemistry,* 20**,** 3890-3900.

Jiang, D., Zhao, H., Zhang, S. & John, R. 2004. Kinetic study of photocatalytic oxidation of adsorbed carboxylic acids at TiO2 porous films by photoelectrolysis. *Journal of Catalysis,* 223**,** 212-220.

Jiang, X., Zhang, Y., Jiang, J., Rong, Y., Wang, Y., Wu, Y. & Pan, C. 2012. Characterization of oxygen vacancy associates within hydrogenated TiO2: a positron annihilation study. *The Journal of Physical Chemistry C,* 116**,** 22619-22624.

Jonidi Jafari, A. & Moslemzadeh, M. 2020. Synthesis of Fe-Doped TiO2 for Photocatalytic Processes under UV-Visible Light: Effect of Preparation Methods on Crystal Size—A Systematic Review Study. *Comments on Inorganic Chemistry,* 40**,** 327-346.

Joseph, A. M., Nagendra, B., Shaiju, P., Surendran, K. & Gowd, E. B. 2018. Aerogels of hierarchically porous syndiotactic

polystyrene with a dielectric constant near to air. *Journal of Materials Chemistry C,* 6**,** 360-368.

Joyce-Pruden, C., Pross, J. K. & Li, Y. 1992. Photoinduced reduction of aldehydes on titanium dioxide. *The Journal of Organic Chemistry,* 57**,** 5087-5091.

Kamaei, M., Rashedi, H., Dastgheib, S. M. M. & Tasharrofi, S. 2018. Comparing photocatalytic degradation of gaseous ethylbenzene using N-doped and pure TiO2 nano-catalysts coated on glass beads under both UV and visible light irradiation. *Catalysts,* 8**,** 466.

Kamat, P. V. 2012. Manipulation of charge transfer across semiconductor interface. A criterion that cannot be ignored in photocatalyst design. *The journal of physical chemistry letters,* 3**,** 663-672.

Kamiya, M., Nakamura, K. & Sasaki, C. 1994. Inclusion effects of cyclodextrins on photodegradation rates of parathion and paraoxon in aquatic medium. *Chemosphere,* 28**,** 1961-1966.

Kansal, S. K., Sood, S., Umar, A. & Mehta, S. K. 2013. Photocatalytic degradation of Eriochrome Black T dye using well-crystalline anatase TiO2 nanoparticles. *Journal of Alloys and Compounds,* 581**,** 392-397.

Karunakaran, C. & Dhanalakshmi, R. 2008. Semiconductor-catalyzed degradation of phenols with sunlight. *Solar energy materials and solar cells,* 92**,** 1315-1321.

Khan, H. & Swati, I. 2016. Fe3+-doped Anatase TiO2 with d-d Transition, Oxygen Vacancies and Ti3+ Centers: Synthesis, Characterization, UV-vis Photocatalytic and Mechanistic Studies. *Industrial & Engineering Chemistry Research,* 55.

Khlyustova, A., Sirotkin, N., Kusova, T., Kraev, A., Titov, V. & Agafonov, A. 2020. Doped TiO 2: The effect of doping elements on photocatalytic activity. *Materials Advances,* 1**,** 1193-1201.

Kim, T. H., Go, G.-M., Cho, H.-B., Song, Y., Lee, C.-G. & Choa, Y.-H. 2018. A novel synthetic method for N Doped TiO2 Nanoparticles through plasma-assisted electrolysis and photocatalytic activity in the visible region. *Frontiers in chemistry,* 6**,** 458.

Konstantinou, I. K. & Albanis, T. A. 2004. TiO2-assisted photocatalytic degradation of azo dyes in aqueous solution: kinetic and mechanistic investigations: a review. *Applied Catalysis B: Environmental,* 49**,** 1-14.

Ku, Y., Lee, W.-H. & Wang, W.-Y. 2004. Photocatalytic reduction of carbonate in aqueous solution by UV/TiO2 process. *Journal of Molecular Catalysis A: Chemical,* 212**,** 191-196.

Kuipers, N. & Beenackers, A. 1993. Non-fickian diffusion with chemical reaction in glassy polymers with swelling induced by the penetrant: a mathematical model. *Chemical engineering science,* 48**,** 2957-2971.

Lair, A., Ferronato, C., Chovelon, J.-M. & Herrmann, J.-M. 2008. Naphthalene degradation in water by heterogeneous photocatalysis: an investigation of the influence of inorganic anions. *Journal of Photochemistry and Photobiology A: Chemistry,* 193**,** 193-203.

Lannoy, A., Kania, N., Bleta, R., Fourmentin, S., Machut-Binkowski, C., Monflier, E. & Ponchel, A. 2016. Photocatalysis of Volatile Organic Compounds in water: Towards a deeper understanding of the role of cyclodextrins in the photodegradation of toluene over titanium dioxide. *Journal of colloid and interface science,* 461**,** 317-325.

Lazar, M. A., Varghese, S. & Nair, S. S. 2012. Photocatalytic water treatment by titanium dioxide: recent updates. *Catalysts,* 2**,** 572-601.

Lee, G.-H., Lee, M. S., Lee, G.-D., Kim, Y.-H. & Hong, S.-S. 2002. Catalytic combustion of benzene over copper oxide supported on TiO2 prepared by sol-gel method. *Journal of Industrial and Engineering Chemistry,* 8**,** 572-577.

Lee, j. h. & Yang, Y. 2006a. Synthesis of TiO2 nanoparticles with pure brookite at low temperature by hydrolysis of TiCl4 using HNO3 solution. *Journal of Materials Science,* 41**,** 557-559.

Lee, J. H. & Yang, Y. S. 2006b. Synthesis of TiO 2 nanoparticles with pure brookite at low temperature by hydrolysis of TiCl 4 using HNO 3 solution. *Journal of materials science,* 41**,** 557-559.

Lee, Y.-J., Kang, J.-K., Park, S.-J., Lee, C.-G., Moon, J.-K. & Alvarez, P. J. 2020. Photocatalytic degradation of neonicotinoid insecticides using sulfate-doped Ag3PO4 with enhanced visible light activity. *Chemical Engineering Journal,* 402**,** 126183.

León, A., Reuquen, P., Garín, C., Segura, R., Vargas, P., Zapata, P. & Orihuela, P. A. 2017. FTIR and raman characterization of TiO2 nanoparticles coated with polyethylene glycol as carrier for 2-methoxyestradiol. *Applied Sciences (Switzerland),* 7.

Levenspiel, O. 1998. *Chemical reaction engineering*, John wiley & sons.

Lhomme, L., Brosillon, S. & Wolbert, D. 2008. Photocatalytic degradation of pesticides in pure water and a commercial agricultural solution on TiO2 coated media. *Chemosphere,* 70**,** 381-386.

Li, F., Li, X., Ao, C., Lee, S. & Hou, M. 2005. Enhanced photocatalytic degradation of VOCs using Ln3+–TiO2 catalysts for indoor air purification. *Chemosphere,* 59**,** 787-800.

Li, F., Li, X. & Hou, M. 2004. Photocatalytic degradation of 2-mercaptobenzothiazole in aqueous La3+–TiO2 suspension for odor control. *Applied Catalysis B: Environmental,* 48**,** 185-194.

Li, H., Hao, Y., Lu, H., Liang, L., Wang, Y., Qiu, J., Shi, X., Wang, Y. & Yao, J. 2015. A systematic study on visible-light N-doped TiO2 photocatalyst obtained from ethylenediamine by sol–gel method. *Applied Surface Science,* 344**,** 112-118.

Li, J., Xu, Y., Ding, Z., Mahadi, A. H., Zhao, Y. & Song, Y.-F. 2020a. Photocatalytic selective oxidation of benzene to phenol in water over layered double hydroxide: A thermodynamic and kinetic perspective. *Chemical Engineering Journal,* 388**,** 124248.

Li, W., Linkun, X., Zhou, L., Ochoa-Lozano, J., Li, C. & Chai, X. 2020b. A systemic study on Gd, Fe and N co-doped TiO2 nanomaterials for enhanced photocatalytic activity under visible light irradiation. *Ceramics International,* 46.

Li, Y., Li, M., Xu, P., Tang, S. & Liu, C. 2016. Efficient photocatalytic degradation of acid orange 7 over N-doped ordered mesoporous titania on carbon fibers under visible-light irradiation based on three synergistic effects. *Applied Catalysis A: General,* 524**,** 163-172.

Liang, C.-H., Hou, M., Zhou, S.-G., Li, F.-b., Liu, C.-S., Liu, T., Gao, Y.-X., Wang, X.-G. & Lü, J.-L. 2007. The effect of erbium on the adsorption and photodegradation of orange I in aqueous Er3+-TiO2 suspension. *Journal of hazardous materials,* 138**,** 471-8.

Lin, Y.-H., Chou, S.-H. & Chu, H. 2014. A kinetic study for the degradation of 1, 2-dichloroethane by S-doped TiO2 under visible light. *Journal of nanoparticle research,* 16**,** 1-12.

Linsebiger, A., Lu, G. & Tatas Jr, J. 1995. Photocatalysis: fundamentals and application to the removal of various types of aqueous pollutants. *Chem. Rev.,* 95**,** 735.

Linsebigler, A. L., Lu, G. & Yates Jr, J. T. 1995a. Photocatalysis on TiO2 surfaces: principles, mechanisms, and selected results. *Chemical reviews,* 95**,** 735-758.

Linsebigler, A. L., Lu, G. & Yates, J. T., Jr. 1995b. Photocatalysis on TiO2 Surfaces: Principles, Mechanisms, and Selected Results. *Chem. Rev. (Washington, D. C.),* 95**,** 735-58.

Liu, C., Chen, W., Sheng, Y. & Li, L. Atrazine degradation in solar irradiation/S-doped titanium dioxide treatment. 2009 3rd International Conference on Bioinformatics and Biomedical Engineering, 2009. IEEE, 1-4.

Long, L.-Y., Weng, Y.-X. & Wang, Y.-Z. 2018. Cellulose aerogels: Synthesis, applications, and prospects. *Polymers,* 10**,** 623.

Lopes Colpani, G., Zanetti, J. T., Cecchin, F., Dal'Toé, A., Fiori, M. A., Moreira, R. D. F. P. M. & Soares, C. 2018. Carboxymethyl-β-cyclodextrin functionalization of TiO2 doped with lanthanum: Characterization and enhancement of photocatalytic activity. *Catalysis Science and Technology,* 8**,** 2636-2647.

Lopez, T., Sanchez, E., Bosch, P., Meas, Y. & Gomez, R. 1992. FTIR and UV-Vis (diffuse reflectance) spectroscopic characterization of TiO2 sol-gel. *Materials chemistry and physics,* 32**,** 141-152.

Lu, P., Wu, F. & Deng, N. 2004. Enhancement of TiO2 photocatalytic redox ability by β-cyclodextrin in suspended solutions. *Applied Catalysis B: Environmental,* 53**,** 87-93.

Luciani, G., Imparato, C. & Vitiello, G. 2020. Photosensitive hybrid nanostructured materials: The big challenges for sunlight capture. *Catalysts,* 10**,** 103.

Magesan, P., Ganesan, P. & Umapathy, M. 2016. Ultrasonic-assisted synthesis of doped TiO2 nanocomposites: characterization and evaluation of photocatalytic and antimicrobial activity. *Optik,* 127**,** 5171-5180.

Maldotti, A., Andreotti, L., Molinari, A., Tollari, S., Penoni, A. & Cenini, S. 2000. Photochemical and photocatalytic reduction of nitrobenzene in the presence of cyclohexene. *Journal of photochemistry and photobiology A: chemistry,* 133**,** 129-133.

Mancuso, A., Morante, N., De Carluccio, M., Sacco, O., Rizzo, L., Fontana, M., Esposito, S., Vaiano, V. & Sannino, D. 2022a.

Solar driven photocatalysis using iron and chromium doped TiO2 coupled to moving bed biofilm process for olive mill wastewater treatment. *Chemical Engineering Journal,* 450**,** 138107.

Mancuso, A., Navarra, W., Sacco, O., Pragliola, S., Vaiano, V. & Venditto, V. 2021a. Photocatalytic Degradation of Thiacloprid Using Tri-Doped TiO2 Photocatalysts: A Preliminary Comparative Study. *Catalysts,* 11**,** 927.

Mancuso, A., Sacco, O., Sannino, D., Pragliola, S. & Vaiano, V. 2020a. Enhanced visible-light-driven photodegradation of Acid Orange 7 azo dye in aqueous solution using Fe-N co-doped TiO2. *Arabian Journal of Chemistry,* 13**,** 8347-8360.

Mancuso, A., Sacco, O., Sannino, D., Venditto, V. & Vaiano, V. 2020b. One-step catalytic or photocatalytic oxidation of benzene to phenol: Possible alternative routes for phenol synthesis? *Catalysts,* 10**,** 1424.

Mancuso, A., Sacco, O., Vaiano, V., Sannino, D., Pragliola, S., Venditto, V. & Morante, N. 2021b. Visible light active Fe-Pr co-doped TiO2 for water pollutants degradation. *Catalysis Today,* 380**,** 93-104.

Mancuso, A., Vaiano, V., Antico, P., Sacco, O. & Venditto, V. 2022b. Photoreactive polymer composite for selective oxidation of benzene to phenol. *Catalysis Today*.

Marami, M. B., Farahmandjou, M. & Khoshnevisan, B. 2018. Sol–gel synthesis of Fe-doped TiO2 nanocrystals. *Journal of electronic Materials,* 47**,** 3741-3748.

Marcı, G., Addamo, M., Augugliaro, V., Coluccia, S., Garcıa-López, E., Loddo, V., Martra, G., Palmisano, L. & Schiavello, M. 2003. Photocatalytic oxidation of toluene on irradiated TiO2: comparison of degradation performance in humidified air, in water and in water containing a zwitterionic surfactant. *Journal of Photochemistry and Photobiology A: Chemistry,* 160**,** 105-114.

Massima Mouele, E. S., Dinu, M., Cummings, F., Fatoba, O. O., Zar Myint, M. T., Kyaw, H. H., Parau, A. C., Vladescu, A., Francesconi, M. G. & Pescetelli, S. 2020. Effect of calcination time on the physicochemical properties and photocatalytic performance of carbon and nitrogen co-doped tio2 nanoparticles. *Catalysts,* 10**,** 847.

Mazierski, P., Mikolajczyk, A., Bajorowicz, B., Malankowska, A., Zaleska-Medynska, A. & Nadolna, J. 2018. The role of

lanthanides in TiO2-based photocatalysis: A review. *Applied Catalysis B: Environmental,* 233**,** 301-317.

Mensitieri, G., Larobina, D., Guerra, G., Venditto, V., Fermeglia, M. & Pricl, S. 2008. Chloroform sorption in nanoporous crystalline and amorphous phases of syndiotactic polystyrene. *Journal of Polymer Science Part B: Polymer Physics,* 46**,** 8-15.

Milano, G., Venditto, V., Guerra, G., Cavallo, L., Ciambelli, P. & Sannino, D. 2001. Shape and volume of cavities in thermoplastic molecular sieves based on syndiotactic polystyrene. *Chemistry of materials,* 13**,** 1506-1511.

Moitzheim, S., Balder, J. E., Poodt, P., Unnikrishnan, S., De Gendt, S. & Vereecken, P. M. 2017. Chlorine doping of amorphous TiO2 for increased capacity and faster Li+-ion storage. *Chemistry of Materials,* 29**,** 10007-10018.

Molinari, R. & Poerio, T. 2010. Remarks on studies for direct production of phenol in conventional and membrane reactors. *Asia-Pacific Journal of Chemical Engineering,* 5**,** 191-206.

Monteiro, R. A., Miranda, S. M., Vilar, V. J., Pastrana-Martínez, L. M., Tavares, P. B., Boaventura, R. A., Faria, J. L., Pinto, E. & Silva, A. M. 2015. N-modified TiO2 photocatalytic activity towards diphenhydramine degradation and Escherichia coli inactivation in aqueous solutions. *Applied Catalysis B: Environmental,* 162**,** 66-74.

Morales, U., Escudero, C., Rivero, M., Ortiz, I., Manríquez, J. & Hernández, J. M. 2017. Coupling of the electrochemical oxidation (EO-BDD)/photocatalysis (TiO 2 -Fe-N) processes for degradation of acid blue BR dye. *Journal of electroanalytical chemistry,* 808**,** 180-188.

Mottola, S., Mancuso, A., Sacco, O., De Marco, I. & Vaiano, V. 2022. Production of hybrid TiO2/β-CD photocatalysts by supercritical antisolvent micronization for UV light-driven degradation of azo dyes. *The Journal of Supercritical Fluids,* 188**,** 105695.

Mousavi, M., Habibi-Yangjeh, A. & Pouran, S. R. 2018. Review on magnetically separable graphitic carbon nitride-based nanocomposites as promising visible-light-driven photocatalysts. *Journal of Materials Science: Materials in Electronics,* 29**,** 1719-1747.

Mugundan, S., Praveen, P., Sridhar, S., Prabu, S., Mary, K. L., Ubaidullah, M., Shaikh, S. F. & Kanagesan, S. 2022. Sol-gel synthesized barium doped TiO2 nanoparticles for solar

photocatalytic application. *Inorganic Chemistry Communications,* 139**,** 109340.

Nakata, K. & Fujishima, A. 2012. TiO2 photocatalysis: Design and applications. *Journal of photochemistry and photobiology C: Photochemistry Reviews,* 13**,** 169-189.

Narayanan, N. & Deepak, N. 2018. Praseodymium–A Competent Dopant for Luminescent Downshifting and Photocatalysis in ZnO Thin Films. *Zeitschrift für Naturforschung A,* 73**,** 441-452.

Ndabankulu, V. O., Maddila, S. & Jonnalagadda, S. B. 2019. Synthesis of lanthanide-doped TiO2 nanoparticles and their photocatalytic activity under visible light. *Canadian Journal of Chemistry,* 97**,** 672-681.

Nevskaia, D. M., Castillejos-Lopez, E., Muñoz, V. & Guerrero-Ruiz, A. 2004. Adsorption of aromatic compounds from water by treated carbon materials. *Environmental science & technology,* 38**,** 5786-5796.

Nguyen, V.-H., Smith, S. M., Wantala, K. & Kajitvichyanukul, P. 2020. Photocatalytic remediation of persistent organic pollutants (POPs): a review. *Arabian Journal of Chemistry,* 13**,** 8309-8337.

Nithyaa, N. & Jaya, N. 2018. Structural, Optical, and Magnetic Properties of Gd-Doped TiO2 Nanoparticles. *Journal of Superconductivity and Novel Magnetism,* 31.

Noguchi, H., Nakajima, A., Watanabe, T. & Hashimoto, K. 2002. Removal of bromate ion from water using TiO2 and alumina-loaded TiO2 photocatalysts. *Water science and technology,* 46**,** 27-31.

Ohkubo, K., Kobayashi, T. & Fukuzumi, S. 2011. Direct oxygenation of benzene to phenol using quinolinium ions as homogeneous photocatalysts. *Angewandte Chemie,* 123**,** 8811-8814.

Omrania, N., Nezamzadeh-Ejhieha, A. & Alizadehb, M. 2019. Brief study on the kinetic aspect of photodegradation of sulfasalazine aqueous solution by cuprous oxide/cadmium sulfide nanoparticles. *catalyst,* 17**,** 24.

Ou, H.-H. & Lo, S.-L. 2007. Effect of Pt/Pd-doped TiO2 on the photocatalytic degradation of trichloroethylene. *Journal of Molecular Catalysis A: Chemical,* 275**,** 200-205.

Padmanabhan, N. T. & John, H. 2020. Titanium dioxide based self-cleaning smart surfaces: A short review. *Journal of Environmental Chemical Engineering,* 8**,** 104211.

Pallotti, D. K., Passoni, L., Maddalena, P., Di Fonzo, F. & Lettieri, S. 2017. Photoluminescence mechanisms in anatase and rutile TiO2. *The Journal of Physical Chemistry C,* 121**,** 9011-9021.

Palmisano, G., Yurdakal, S., Augugliaro, V., Loddo, V. & Palmisano, L. 2007. Photocatalytic Selective Oxidation of 4-Methoxybenzyl Alcohol to Aldehyde in Aqueous Suspension of Home-Prepared Titanium Dioxide Catalyst. *Advanced Synthesis & Catalysis,* 349**,** 964-970.

Panta, P. & Bergmann, C. 2015. Raman spectroscopy of iron oxide of nanoparticles (Fe3O4). *J. Mater. Sci. Eng,* 5.

Papadam, T., Xekoukoulotakis, N. P., Poulios, I. & Mantzavinos, D. 2007. Photocatalytic transformation of acid orange 20 and Cr (VI) in aqueous TiO2 suspensions. *Journal of Photochemistry and Photobiology A: Chemistry,* 186**,** 308-315.

Papp, J., Soled, S., Dwight, K. & Wold, A. 1994. Surface acidity and photocatalytic activity of TiO2, WO3/TiO2, and MoO3/TiO2 photocatalysts. *Chemistry of materials,* 6**,** 496-500.

Park, H. & Choi, W. 2005. Photocatalytic conversion of benzene to phenol using modified TiO2 and polyoxometalates. *Catalysis Today,* 101**,** 291-297.

Park, J. E., Kim, E. J., Park, M.-J. & Lee, E. S. 2019. Adsorption Capacity of Organic Compounds Using Activated Carbons in Zinc Electrowinning. *Energies,* 12**,** 2169.

Parnicka, P., Mazierski, P., Grzyb, T., Lisowski, W., Kowalska, E., Ohtani, B., Zaleska-Medynska, A. & Nadolna, J. 2018. Influence of the preparation method on the photocatalytic activity of Nd-modified TiO2. *Beilstein Journal of Nanotechnology,* 9**,** 447-459.

Parrino, F., Bellardita, M., García-López, E., Marcì, G., Loddo, V. & Palmisano, L. 2018. Heterogeneous photocatalysis for selective formation of high-value-added molecules: Some chemical and engineering aspects. *ACS Catalysis,* 8**,** 11191-11225.

Parthasarathi, R., Subramanian, V., Sathyamurthy, N. & Leszczynski, J. 2007. Solvation of H3O+ by Phenol: Hydrogen Bonding vs π Complexation. *The Journal of Physical Chemistry A,* 111**,** 2-5.

Patil, S. B., Basavarajappa, P. S., Ganganagappa, N., Jyothi, M., Raghu, A. & Reddy, K. R. 2019. Recent advances in non-metals-doped TiO2 nanostructured photocatalysts for visible-light driven hydrogen production, CO2 reduction and air

purification. *International Journal of Hydrogen Energy,* 44**,** 13022-13039.

Pattanaik, P. & Sahoo, M. 2014. TiO2 photocatalysis: progress from fundamentals to modification technology. *Desalination and Water Treatment,* 52**,** 6567-6590.

Pekala, R. 1989. Organic aerogels from the polycondensation of resorcinol with formaldehyde. *Journal of materials science,* 24**,** 3221-3227.

Petraccone, V., Ruiz de Ballesteros, O., Tarallo, O., Rizzo, P. & Guerra, G. 2008. Nanoporous polymer crystals with cavities and channels. *Chemistry of Materials,* 20**,** 3663-3668.

Piątkowska, A., Janus, M., Szymański, K. & Mozia, S. 2021. C-, N- and S-doped TiO2 photocatalysts: a review. *Catalysts,* 11**,** 144.

Pichat, P., Herrmann, J. M., Courbon, H., Disdier, J. & Mozzanega, M. N. 1982. Photocatalytic oxidation of various compounds over TiO2 and other semiconductor oxides; Mechanistic considerations. *The Canadian Journal of Chemical Engineering,* 60**,** 27-32.

Pierre, A. C. & Pajonk, G. M. 2002. Chemistry of aerogels and their applications. *Chemical Reviews,* 102**,** 4243-4266.

Pincock, J. A., Pincock, A. L. & Fox, M. A. 1985. Controlled oxidation of benzyl ethers on irradiated semiconductor powders. *Tetrahedron,* 41**,** 4107-4117.

Pomilla, F., García-López, E., Marcì, G., Palmisano, L. & Parrino, F. 2021. Heterogeneous photocatalytic materials for sustainable formation of high-value chemicals in green solvents. *Materials Today Sustainability,* 13**,** 100071.

Prajapati, B., Kumar, S., Kumar, M., Chatterjee, S. & Ghosh, A. K. 2017. Investigation of the physical properties of Fe: TiO 2-diluted magnetic semiconductor nanoparticles. *Journal of Materials Chemistry C,* 5**,** 4257-4267.

Qi, H.-P. & Wang, H.-L. 2020. Facile synthesis of Pr-doped molecularly imprinted TiO2 mesocrystals with high preferential photocatalytic degradation performance. *Applied Surface Science,* 511**,** 145607.

Qian, R., Zong, H., Schneider, J., Zhou, G., Zhao, T., Li, Y., Yang, J., Bahnemann, D. W. & Pan, J. H. 2019. Charge carrier trapping, recombination and transfer during TiO2 photocatalysis: An overview. *Catalysis Today,* 335**,** 78-90.

Qin, H.-L., Gu, G.-B. & Liu, S. 2008. Preparation of nitrogen-doped titania with visible-light activity and its application. *Comptes Rendus Chimie,* 11**,** 95-100.

Rajalakshmi, S., Pitchaimuthu, S., Kannan, N. & Velusamy, P. 2017. Enhanced photocatalytic activity of metal oxides/β-cyclodextrin nanocomposites for decoloration of Rhodamine B dye under solar light irradiation. *Applied Water Science,* 7**,** 115-127.

Ramalingam, R. 2017. Surface and Electrochemical Characterization of N-Fe-doped- TiO2 Nanoparticle Prepared by Hydrothermal and Facile Electro-Deposition Method for Visible Light Driven Pollutant Removal. *International Journal of Electrochemical Science,* 12**,** 797-811.

Ramalingam, R. J., Arunachalam, P., Radhika, T., Anju, K., Nimitha, K. & Al-Lohedan, H. 2017. Surface and Electrochemical Characterization of N-Fe-doped-TiO2 Nanoparticle Prepared by Hydrothermal and Facile Electro-Deposition Method for Visible Light Driven Pollutant Removal. *Int. J. Electrochem. Sci,* 12**,** 797-811.

Ramandi, S., Entezari, M. H. & Ghows, N. 2017. Sono-synthesis of solar light responsive S–N–C–tri doped TiO2 photo-catalyst under optimized conditions for degradation and mineralization of diclofenac. *Ultrasonics sonochemistry,* 38**,** 234-245.

Ramya, R., Krishnan, P. S., Neelaveni, M., Gurulakshmi, M., Sivakumar, T. & Shanthi, K. 2019. Enhanced visible light activity of pr–tio2 nanocatalyst in the degradation of dyes: effect of Pr doping and TiO2 morphology. *Journal of Nanoscience and Nanotechnology,* 19**,** 3971-3981.

Ranjit, K. & Viswanathan, B. 1997. Photocatalytic reduction of nitrite and nitrate ions over doped TiO2 catalysts. *Journal of Photochemistry and Photobiology A: Chemistry,* 107**,** 215-220.

Reda, S., Khairy, M. & Mousa, M. 2017. Photocatalytic activity of nitrogen and copper doped TiO2 nanoparticles prepared by microwave-assisted sol-gel process. *Arabian Journal of Chemistry*.

Reischauer, S. & Pieber, B. 2021. Emerging concepts in photocatalytic organic synthesis. *Iscience,* 24**,** 102209.

Reszczynska, J., Esteban, D. A., Gazda, M. & Zaleska, A. 2014. Pr-doped TiO2. The effect of metal content on photocatalytic activity. *Physicochemical Problems of Mineral Processing,* 50**,** 515--524.

Reszczyńska, J., Grzyb, T., Wei, Z., Klein, M., Kowalska, E., Ohtani, B. & Zaleska-Medynska, A. 2016. Photocatalytic activity and luminescence properties of RE3+–TiO2 nanocrystals prepared by sol–gel and hydrothermal methods. *Applied Catalysis B: Environmental,* 181**,** 825-837.

Ribeiro, A. R. & Umbuzeiro, G. d. A. 2014. Effects of a textile azo dye on mortality, regeneration, and reproductive performance of the planarian, Girardia tigrina. *Environmental Sciences Europe,* 26**,** 1-8.

Ribeiro, E., Ladeira, C. & Viegas, S. 2017. EDCs mixtures: a stealthy hazard for human health? *Toxics,* 5**,** 5.

Ricci, P. C., Carbonaro, C. M., Stagi, L., Salis, M., Casu, A., Enzo, S. & Delogu, F. 2013. Anatase-to-rutile phase transition in TiO2 nanoparticles irradiated by visible light. *The Journal of Physical Chemistry C,* 117**,** 7850-7857.

Rodríguez, P. A. O., Pecchi, G. A., Casuscelli, S. G., Elias, V. R. & Eimer, G. A. 2019. A simple synthesis way to obtain iron-doped TiO2 nanoparticles as photocatalytic surfaces. *Chemical Physics Letters,* 732**,** 136643.

Sacco, O., Vaiano, V., Daniel, C., Navarra, W. & Venditto, V. 2018a. Removal of phenol in aqueous media by N-doped TiO2 based photocatalytic aerogels. *Materials Science in Semiconductor Processing,* 80**,** 104-110.

Sacco, O., Vaiano, V., Daniel, C., Navarra, W. & Venditto, V. 2019. Highly robust and selective system for water pollutants removal: How to transform a traditional photocatalyst into a highly robust and selective system for water pollutants removal. *Nanomaterials,* 9**,** 1509.

Sacco, O., Vaiano, V., Han, C., Sannino, D. & Dionysiou, D. D. 2015. Photocatalytic removal of atrazine using N-doped TiO2 supported on phosphors. *Applied Catalysis B: Environmental,* 164**,** 462-474.

Sacco, O., Vaiano, V., Rizzo, L. & Sannino, D. 2018b. Photocatalytic activity of a visible light active structured photocatalyst developed for municipal wastewater treatment. *Journal of Cleaner Production,* 175**,** 38-49.

Salam, A., Venditti, R. A., Pawlak, J. J. & El-Tahlawy, K. 2011. Crosslinked hemicellulose citrate–chitosan aerogel foams. *Carbohydrate Polymers,* 84**,** 1221-1229.

Sangari, N. U. 2018. Role of β-cyclodextrin in enhanced photocatalytic decolorization of metanil yellow dye with TiO2. *Asian Journal of Chemistry,* 30**,** 2294-2298.

Sannino, D., Vaiano, V., Ciambelli, P., Carotenuto, G., Di Serio, M. & Santacesaria, E. 2013. Enhanced performances of grafted VOx on titania/silica for the selective photocatalytic oxidation of ethanol to acetaldehyde. *Catalysis Today,* 209**,** 159-163.

Sannino, D., Vaiano, V., Ciambelli, P., Hidalgo, M. C., Murcia, J. J. & Navío, J. A. 2012. Oxidative dehydrogenation of ethanol over Au/TiO2 photocatalysts. *Journal of Advanced Oxidation Technologies,* 15**,** 284-293.

Sannino, D., Vaiano, V., Isupova, L. A. & Ciambelli, P. 2011. Photo-Fenton oxidation of acetic acid on supported LaFeO3 and Pt/LaFeO3 perovskites. *Chemical Engineering Transactions,* 25**,** 1013-1018.

Sasirekha, N., Basha, S. J. S. & Shanthi, K. 2006. Photocatalytic performance of Ru doped anatase mounted on silica for reduction of carbon dioxide. *Applied Catalysis B: Environmental,* 62**,** 169-180.

Schmidt, R. J. 2005. Industrial catalytic processes—phenol production. *Applied Catalysis A: General,* 280**,** 89-103.

Schneider, J., Matsuoka, M., Takeuchi, M., Zhang, J., Horiuchi, Y., Anpo, M. & Bahnemann, D. W. 2014. Understanding TiO2 photocatalysis: mechanisms and materials. *Chemical reviews,* 114**,** 9919-9986.

Sclafani, A. & Herrmann, J. 1996. Comparison of the photoelectronic and photocatalytic activities of various anatase and rutile forms of titania in pure liquid organic phases and in aqueous solutions. *The Journal of Physical Chemistry,* 100**,** 13655-13661.

Seifvand, N. & Kowsari, E. 2016. Synthesis of mesoporous Pd-doped TiO2 templated by a magnetic recyclable ionic liquid for efficient photocatalytic air treatment. *Industrial & Engineering Chemistry Research,* 55**,** 10533-10543.

Selvam, K. & Swaminathan, M. 2010. Au-doped TiO2 nanoparticles for selective photocatalytic synthesis of quinaldines from anilines in ethanol. *Tetrahedron Letters,* 51**,** 4911-4914.

Senthurchelvan, R., Wang, Y., Basak, S. & Rajeshwar, K. 1996. Reduction of hexavalent chromium in aqueous solutions by polypyrrole: II. Thermodynamic, kinetic, and mechanistic aspects. *Journal of the Electrochemical Society,* 143**,** 44.

Serra-Gómez, R., Tardajos, G., González-Benito, J. & González-Gaitano, G. 2012. Rhodamine solid complexes as fluorescence probes to monitor the dispersion of cyclodextrins in polymeric nanocomposites. *Dyes and Pigments,* 94**,** 427-436.

Shao, G.-S., Zhang, X.-J. & Yuan, Z.-Y. 2008. Preparation and photocatalytic activity of hierarchically mesoporous-macroporous TiO2− xNx. *Applied Catalysis B: Environmental,* 82**,** 208-218.

Sharma, V. K. & Chenay, B. V. 2005. Heterogeneous photocatalytic reduction of Fe (VI) in UV-irradiated titania suspensions: effect of ammonia. *Journal of applied electrochemistry,* 35**,** 775-781.

Sharotri, N., Gupta, S. & Sud, D. 2022. Visible light responsive S-Doped TiO2 nanoparticles: synthesis, characterization and photocatalytic degradation of pollutants. *Nanotechnology for Environmental Engineering,* 7**,** 503-515.

Sharotri, N. & Sud, D. 2017. Visible light responsive Mn-S-co-doped TiO2 photocatalyst–Synthesis, characterization and mechanistic aspect of photocatalytic degradation. *Separation and Purification Technology,* 183**,** 382-391.

Shekofteh-Gohari, M., Habibi-Yangjeh, A., Abitorabi, M. & Rouhi, A. 2018. Magnetically separable nanocomposites based on ZnO and their applications in photocatalytic processes: a review. *Critical Reviews in Environmental Science and Technology,* 48**,** 806-857.

Shen, J.-H., Chuang, H.-Y., Jiang, Z.-W., Liu, X.-Z. & Horng, J.-J. 2020. Novel quantification of formation trend and reaction efficiency of hydroxyl radicals for investigating photocatalytic mechanism of Fe-doped TiO2 during UV and visible light-induced degradation of acid orange 7. *Chemosphere,* 251**,** 126380.

Shi, Z., Lai, H., Yao, S. & Wang, S. 2012. Photocatalytic Activity of Fe and Ce Co-doped Mesoporous TiO2 Catalyst under UV and Visible Light. *Journal of the Chinese Chemical Society,* 59.

Shimizu, K.-i., Akahane, H., Kodama, T. & Kitayama, Y. 2004. Selective photo-oxidation of benzene over transition metal-exchanged BEA zeolite. *Applied Catalysis A: General,* 269**,** 75-80.

Shin, C. H., Bugli, G. & Djega-Mariadassou, G. 1991. Preparation and characterization of titanium oxynitrides with high specific surface areas. *Journal of solid state chemistry,* 95**,** 145-155.

Shin, E., Jin, S., Kim, J., Chang, S.-J., Jun, B.-H., Park, K.-W. & Hong, J. 2016. Preparation of K-doped TiO2 nanostructures by wet corrosion and their sunlight-driven photocatalytic performance. *Applied Surface Science,* 379**,** 33-38.

Shiraishi, Y. & Hirai, T. 2008. Selective organic transformations on titanium oxide-based photocatalysts. *Journal of Photochemistry and Photobiology C: Photochemistry Reviews,* 9**,** 157-170.

Shriram, B. & Kanmani, S. 2014. Ozonation of textile dyeing wastewater-a review. *Centre for Environmental Studies, Anna University,* 15**,** 46-50.

Siddiqui, M. A. & Jaiswal, P. Photocatalytic Behavior of Ferroelectric Materials: Comparative Study of BaTiO3 and Ag-loaded BaTiO3 for Wastewater Treatment. IOP Conference Series: Materials Science and Engineering, 2021. IOP Publishing, 012031.

Šihor, M., Reli, M., Vaštyl, M., Hrádková, K., Matějová, L. & Kočí, K. 2019. Photocatalytic Oxidation of Methyl Tert-Butyl Ether in Presence of Various Phase Compositions of TiO2. *Catalysts,* 10**,** 35.

Silva, A. M., Silva, C. G., Dražić, G. & Faria, J. L. 2009. Ce-doped TiO2 for photocatalytic degradation of chlorophenol. *Catalysis Today,* 144**,** 13-18.

Silva, M. J., Gomes, J., Ferreira, P. & Martins, R. C. 2022. An Overview of Polymer-Supported Catalysts for Wastewater Treatment through Light-Driven Processes. *Water,* 14**,** 825.

Singh, K., Harish, S., Kristy, A. P., Shivani, V., Archana, J., Navaneethan, M., Shimomura, M. & Hayakawa, Y. 2018. Erbium doped TiO2 interconnected mesoporous spheres as an efficient visible light catalyst for photocatalytic applications. *Applied Surface Science,* 449**,** 755-763.

Singh, S., Kapoor, D., Khasnabis, S., Singh, J. & Ramamurthy, P. C. 2021. Mechanism and kinetics of adsorption and removal of heavy metals from wastewater using nanomaterials. *Environmental Chemistry Letters,* 19**,** 2351-2381.

Singh, S., Mahalingam, H. & Singh, P. K. 2013. Polymer-supported titanium dioxide photocatalysts for environmental remediation: A review. *Applied Catalysis A: General,* 462**,** 178-195.

Smirniotis, P. G., Boningari, T. & Inturi, S. N. R. 2018. Single-step synthesis of N-doped TiO2 by flame aerosol method and the

effect of synthesis parameters. *Aerosol Science and Technology,* 52**,** 913-922.

Sobana, N., Muruganandam, M. & Swaminathan, M. 2008. Characterization of AC–ZnO catalyst and its photocatalytic activity on 4-acetylphenol degradation. *Catalysis Communications,* 9**,** 262-268.

Song, L., Zhao, X., Cao, L., Moon, J.-W., Gu, B. & Wang, W. 2015. Synthesis of Rare Earth Doped TiO2 Nanorods as Photocatalysts for Lignin Degradation. *Nanoscale,* 7.

Sood, S., Umar, A., Mehta, S. K. & Kansal, S. K. 2015. Highly effective Fe-doped TiO2 nanoparticles photocatalysts for visible-light driven photocatalytic degradation of toxic organic compounds. *Journal of colloid and interface science,* 450**,** 213-223.

Sorrentino, A., Rega, S., Sannino, D., Magliano, A., Ciambelli, P. & Santacesaria, E. 2001. Performances of V2O5-based catalysts obtained by grafting vanadyl tri-isopropoxide on TiO2-SiO2 in SCR. *Applied Catalysis A: General,* 209**,** 45-57.

Sortino, S., Giuffrida, S., De Guidi, G., Chillemi, R., Petralia, S., Marconi, G., Condorelli, G. & Sciuto, S. 2001. The Photochemistry of Flutamide and its Inclusion Complex with β-Cyclodextrin. Dramatic Effect of the Microenvironment on the Nature and on the Efficiency of the Photodegradation Pathways¶. *Photochemistry and photobiology,* 73**,** 6-13.

Spadavecchia, F., Cappelletti, G., Ardizzone, S., Ceotto, M., Azzola, M., Lo Presti, L., Cerrato, G. & Falciola, L. 2012. Role of Pr on the Semiconductor Properties of Nanotitania. An Experimental and First-Principles Investigation. *The Journal of Physical Chemistry C,* 116**,** 23083–23093.

Stylidi, M., Kondarides, D. I. & Verykios, X. E. 2004. Visible light-induced photocatalytic degradation of Acid Orange 7 in aqueous TiO2 suspensions. *Applied Catalysis B: Environmental,* 47**,** 189-201.

Su, R., Kesavan, L., Jensen, M. M., Tiruvalam, R., He, Q., Dimitratos, N., Wendt, S., Glasius, M., Kiely, C. J. & Hutchings, G. J. 2014. Selective photocatalytic oxidation of benzene for the synthesis of phenol using engineered Au–Pd alloy nanoparticles supported on titanium dioxide. *Chemical Communications,* 50**,** 12612-12614.

Su, Y., Xiao, Y., Li, Y., Du, Y. & Zhang, Y. 2011. Preparation, photocatalytic performance and electronic structures of visible-

light-driven Fe–N-codoped TiO2 nanoparticles. *Materials Chemistry and Physics,* 126**,** 761-768.

Sun, H., Bai, Y., Jin, W. & Xu, N. 2008. Visible-light-driven TiO2 catalysts doped with low-concentration nitrogen species. *Solar Energy Materials and Solar Cells,* 92**,** 76-83.

Sun, J., Kang, X.-J., Ma, Y.-Q., Chen, L.-Q., Wang, Y. & Gu, Z.-Z. 2011. The study of adsorption characteristics of electrospun polymer nanofibers for benzenes in water. *Water Science and Technology,* 64**,** 528-533.

Sun, P., Zhang, J., Liu, W., Wang, Q. & Cao, W. 2018. Modification to LH kinetics model and its application in the investigation on photodegradation of gaseous benzene by nitrogen-doped TiO2. *Catalysts,* 8**,** 326.

Tanarungsun, G., Kiatkittipong, W., Assabumrungrat, S., Yamada, H., Tagawa, T. & Praserthdam, P. 2007. Liquid phase hydroxylation of benzene to phenol with hydrogen peroxide catalyzed by Fe (III)/TiO2 catalysts at room temperature. *Journal of Industrial and Engineering Chemistry,* 13**,** 444-451.

Theivasanthi, T. & Alagar, M. 2013. Titanium dioxide (TiO2) nanoparticles XRD analyses: an insight. *arXiv preprint arXiv:1307.1091*.

Tieng, S., Azouani, R., Chhor, K. & Kanaev, A. 2011. Nucleation− Growth of TiO2 Nanoparticles Doped with Iron Acetylacetonate. *The Journal of Physical Chemistry C,* 115**,** 5244-5250.

Tomita, O., Abe, R. & Ohtani, B. 2011. Direct synthesis of phenol from benzene over platinum-loaded tungsten (VI) oxide photocatalysts with water and molecular oxygen. *Chemistry Letters,* 40**,** 1405-1407.

Ulson, S. M. d. A. G., Bonilla, K. A. S. & de Souza, A. A. U. 2010. Removal of COD and color from hydrolyzed textile azo dye by combined ozonation and biological treatment. *Journal of hazardous materials,* 179**,** 35-42.

Vaiano, V., Matarangolo, M., Sacco, O. & Sannino, D. 2017a. Photocatalytic treatment of aqueous solutions at high dye concentration using praseodymium-doped ZnO catalysts. *Applied Catalysis B: Environmental,* 209**,** 621-630.

Vaiano, V., Sacco, O. & Sannino, D. 2019. Electric energy saving in photocatalytic removal of crystal violet dye through the simultaneous use of long-persistent blue phosphors, nitrogen-

doped TiO2 and UV-light emitting diodes. *Journal of cleaner production,* 210**,** 1015-1021.

Vaiano, V., Sacco, O., Sannino, D. & Ciambelli, P. 2015a. Nanostructured N-doped TiO2 coated on glass spheres for the photocatalytic removal of organic dyes under UV or visible light irradiation. *Applied Catalysis B: Environmental,* 170**,** 153-161.

Vaiano, V., Sacco, O., Sannino, D. & Ciambelli, P. 2015b. Photocatalytic removal of spiramycin from wastewater under visible light with N-doped TiO2 photocatalysts. *Chemical engineering journal,* 261**,** 3-8.

Vaiano, V., Sacco, O., Sannino, D., Ciambelli, P., Longo, S., Venditto, V. & Guerra, G. 2014. N-doped TiO2/s-PS aerogels for photocatalytic degradation of organic dyes in wastewater under visible light irradiation. *Journal of Chemical Technology & Biotechnology,* 89**,** 1175-1181.

Vaiano, V., Sacco, O., Sannino, D., Navarra, W., Daniel, C. & Venditto, V. 2017b. Influence of aggregate size on photoactivity of N-doped TiO2 particles in aqueous suspensions under visible light irradiation. *Journal of Photochemistry and Photobiology A: Chemistry,* 336**,** 191-197.

Vaiano, V., Sacco, O., Sannino, D., Stoller, M., Ciambelli, P. & Chianese, A. 2016. Photocatalytic removal of phenol by ferromagnetic N-TiO2/SiO2/Fe3O4 nanoparticles in presence of visible light irradiation. *Chemical Engineering Transactions,* 47**,** 235-240.

Vaiano, V., Sarno, G., Sacco, O. & Sannino, D. 2017c. Degradation of terephthalic acid in a photocatalytic system able to work also at high pressure. *Chemical Engineering Journal,* 312**,** 10-19.

Velusamy, P., Pitchaimuthu, S., Rajalakshmi, S. & Kannan, N. 2014. Modification of the photocatalytic activity of TiO2 by β-Cyclodextrin in decoloration of ethyl violet dye. *Journal of Advanced Research,* 5**,** 19-25.

Venditto, V., Pellegrino, M., Califano, R., Guerra, G., Daniel, C., Ambrosio, L. & Borriello, A. 2015. Monolithic polymeric aerogels with VOCs sorbent nanoporous crystalline and water sorbent amorphous phases. *ACS applied materials & interfaces,* 7**,** 1318-1326.

Verhoeven, J. W. 1996. Glossary of terms used in photochemistry. *Pure Appl. Chem.,* 68**,** 2223-2286.

Verma, S., Nasir Baig, R., Nadagouda, M. N. & Varma, R. S. 2017. Hydroxylation of Benzene via C–H activation using bimetallic CuAg@ g-C3N4. *ACS sustainable chemistry & engineering,* 5**,** 3637-3640.

Villaverde, J. & Morillo, E. 2011. Remediation of contaminated soils and long-term risk assessment of organic residues by using cyclodextrins. John Wiley & Sons, Inc.: Hoboken, NJ.

Vitiello, G., Clarizia, L., Abdelraheem, W., Esposito, S., Bonelli, B., Ditaranto, N., Vergara, A., Nadagouda, M., Dionysiou, D. D. & Andreozzi, R. 2019. Near UV-Irradiation of CuOx-Impregnated TiO2 Providing Active Species for H2 Production Through Methanol Photoreforming. *ChemCatChem,* 11**,** 4314-4326.

Wang, D., Wang, M. & Li, Z. 2015. Fe-based metal–organic frameworks for highly selective photocatalytic benzene hydroxylation to phenol. *Acs Catalysis,* 5**,** 6852-6857.

Wang, G., Dai, J., Luo, Q. & Deng, N. 2021. Photocatalytic degradation of bisphenol A by TiO2@aspartic acid-β-cyclodextrin@reduced graphene oxide. *Separation and Purification Technology,* 254.

Wang, G., Wu, F., Zhang, X., Luo, M. & Deng, N. 2006. Enhanced photodegradation of bisphenol A in the presence of β-cyclodextrin under UV light. *Journal of Chemical Technology & Biotechnology: International Research in Process, Environmental & Clean Technology,* 81**,** 805-811.

Wang, H., Li, X., Zhao, X., Li, C., Song, X., Zhang, P. & Huo, P. 2022. A review on heterogeneous photocatalysis for environmental remediation: From semiconductors to modification strategies. *Chinese Journal of Catalysis,* 43**,** 178-214.

Wang, J., Limas-Ballesteros, R., Lopez, T., Moreno, A., Gomez, R., Novaro, O. & Bokhimi, X. 2001. Quantitative determination of titanium lattice defects and solid-state reaction mechanism in iron-doped TiO2 photocatalysts. *The Journal of Physical Chemistry B,* 105**,** 9692-9698.

Wang, Q., Xu, S. & Shen, F. 2011. Preparation and characterization of TiO2 photocatalysts co-doped with Iron (III) and lanthanum for the degradation of organic pollutants. *Applied Surface Science - APPL SURF SCI,* 257**,** 7671-7677.

Wang, S. & Peng, Y. 2010. Natural zeolites as effective adsorbents in water and wastewater treatment. *Chemical engineering journal,* 156**,** 11-24.

Wang, Y. Y., Xie, H., Zhang, W., Tang, Y. B. & Chen, F. Y. Preparation and photocatalytic activity of Fe-Ce-N tri-doped TiO2 catalysts. Advanced Materials Research, 2013. Trans Tech Publ, 1276-1282.

Weber, M. & Weber, M. 2010. Phenols. *Phenolic resins: a century of progress.* Springer.

Willner, I. & Eichen, Y. 1987. Titanium dioxide and cadmium sulfide colloids stabilized by. beta.-cyclodextrins: tailored semiconductor-receptor systems as a means to control interfacial electron-transfer processes. *Journal of the American Chemical Society,* 109**,** 6862-6863.

Willner, I., Eichen, Y. & Willner, B. 1994. Supramolecular semiconductor receptor assemblies: Improved electron transfer at TiO2-β-cyclodextrin colloid interfaces. *Research on Chemical Intermediates,* 20**,** 681-700.

Wojtaszek, K., Wach, A., Czapla-Masztafiak, J., Tyrala, K., Sá, J., Yıldız Özer, L., Garlisi, C., Palmisano, G. & Szlachetko, J. 2019. The influence of nitrogen doping on the electronic structure of the valence and conduction band in TiO2. *Journal of synchrotron radiation,* 26**,** 145-151.

Wu, H.-D., Wu, S.-C., Wu, I.-D. & Chang, F.-C. 2001. Novel determination of the crystallinity of syndiotactic polystyrene using FTIR spectrum. *Polymer,* 42**,** 4719-4725.

Wu, J. C. S. & Chen, C.-H. 2004. A visible-light response vanadium-doped titania nanocatalyst by sol–gel method. *Journal of Photochemistry and Photobiology A: Chemistry,* 163**,** 509-515.

Wu, Y., Zhang, J., Xiao, L. & Chen, F. 2010a. Properties of carbon and iron modified TiO2 photocatalyst synthesized at low temperature and photodegradation of acid orange 7 under visible light. *Applied Surface Science,* 256**,** 4260-4268.

Wu, Y., Zhang, J., Xiao, L. & Chen, F. 2010b. Properties of carbon and iron modified TiO 2 photocatalyst synthesized at low temperature and photodegradation of acid orange 7 under visible light. *Applied Surface Science,* 256**,** 4260-4268.

Xia, H., Sun, K., Sun, K., Feng, Z., Li, W. X. & Li, C. 2008. Direct spectroscopic observation of Fe (III)− Phenolate complex formed from the reaction of benzene with peroxide species on

Fe/ZSM-5 at room temperature. *The Journal of Physical Chemistry C,* 112**,** 9001-9005.

Xiao, Q., Si, Z., Yu, Z. & Qiu, G. 2007. Sol–gel auto-combustion synthesis of samarium-doped TiO2 nanoparticles and their photocatalytic activity under visible light irradiation. *Materials Science and Engineering: B,* 137**,** 189-194.

Xin, F., Zhang, H., An, W., Sun, L., Hao, A. & Li, Y. 2012. Vesicles prepared from inclusion complexes between cyclodextrins and ethyl benzoate. *Journal of dispersion science and technology,* 33**,** 1-4.

Xing, M., Wu, Y., Zhang, J. & Chen, F. 2010. Effect of synergy on the visible light activity of B, N and Fe co-doped TiO 2 for the degradation of MO. *Nanoscale,* 2**,** 1233-1239.

Xiong, L. & Tang, J. 2021. Strategies and challenges on selectivity of photocatalytic oxidation of organic substances. *Advanced Energy Materials,* 11**,** 2003216.

Xu, B., Chen, Z., Han, B. & Li, C. 2017. Glycol assisted synthesis of MIL-100 (Fe) nanospheres for photocatalytic oxidation of benzene to phenol. *Catalysis Communications,* 98**,** 112-115.

Xu, J., Ao, Y., Fu, D. & Yuan, C. 2009. Synthesis of Gd-doped TiO2 nanoparticles under mild condition and their photocatalytic activity. *Colloids and Surfaces A: Physicochemical and Engineering Aspects,* 334**,** 107-111.

Xu, Z. & Yu, J. 2011. Visible-light-induced photoelectrochemical behaviors of Fe-modified TiO 2 nanotube arrays. *Nanoscale,* 3**,** 3138-3144.

Yadav, R., Anju, Chundawat, T. S. & Vaya, D. Photocatalytic degradation of malachite green dye by using β-cyclodextrin based nanocomposites. AIP Conference Proceedings, 2021. AIP Publishing LLC, 020071.

Yan, T., Long, J., Chen, Y., Wang, X., Li, D. & Fu, X. 2008. Indium hydroxide: A highly active and low deactivated catalyst for photoinduced oxidation of benzene. *Comptes Rendus Chimie,* 11**,** 101-106.

Yanqing, Z., Erwei, S., Suxian, C., Wenjun, L. & Xingfang, H. 2000. Hydrothermal preparation and characterization of brookite-type TiO2 nanocrystallites. *Journal of materials science letters,* 19**,** 1445-1448.

YASAR, A. & YOUSAF, S. 2012. Solar assisted photo Fenton for cost effective degradation of textile effluents in comparison to AOPs. *Global Nest Journal,* 14**,** 477-486.

Ye, X., Cui, Y., Qiu, X. & Wang, X. 2014. Selective oxidation of benzene to phenol by Fe-CN/TS-1 catalysts under visible light irradiation. *Applied Catalysis B: Environmental,* 152**,** 383-389.

Yen, C.-C., Wang, D.-Y., Chang, L. S. & Shih, H. 2011. Characterization and photocatalytic activity of Fe- and N-co-deposited TiO2 and first-principles study for electronic structure. *Journal of Solid State Chemistry,* 184.

Yuan, J., Wang, E., Chen, Y., Yang, W., Yao, J. & Cao, Y. 2011. Doping mode, band structure and photocatalytic mechanism of B–N-codoped TiO2. *Applied surface science,* 257**,** 7335-7342.

Yuzawa, H., Aoki, M., Otake, K., Hattori, T., Itoh, H. & Yoshida, H. 2012. Reaction mechanism of aromatic ring hydroxylation by water over platinum-loaded titanium oxide photocatalyst. *The Journal of Physical Chemistry C,* 116**,** 25376-25387.

Zakoshansky, V. 2007. The cumene process for phenol-acetone production. *Petroleum Chemistry,* 47**,** 273-284.

Zakria, H. S., Othman, M. H. D., Kamaludin, R., Kadir, S. H. S. A., Kurniawan, T. A. & Jilani, A. 2021. Immobilization techniques of a photocatalyst into and onto a polymer membrane for photocatalytic activity. *RSC advances,* 11**,** 6985-7014.

Zama, K., Fukuoka, A., Sasaki, Y., Inagaki, S., Fukushima, Y. & Ichikawa, M. 2000. Selective hydroxylation of benzene to phenol by photocatalysis of molybdenum complexes grafted on mesoporous FSM-16. *Catalysis Letters,* 66**,** 251-253.

Zangeneh, H., Zinatizadeh, A., Habibi, M., Akia, M. & Isa, M. H. 2015. Photocatalytic oxidation of organic dyes and pollutants in wastewater using different modified titanium dioxides: A comparative review. *Journal of Industrial and Engineering Chemistry,* 26**,** 1-36.

Žerjav, G., Scandura, G., Garlisi, C., Palmisano, G. & Pintar, A. 2020. Sputtered vs. sol-gel TiO2-doped films: Characterization and assessment of aqueous bisphenol A oxidation under UV and visible light radiation. *Catalysis Today,* 357**,** 380-391.

Zhang, G., Yi, J., Shim, J., Lee, J. & Choi, W. 2011a. Photocatalytic hydroxylation of benzene to phenol over titanium oxide entrapped into hydrophobically modified siliceous foam. *Applied Catalysis B: Environmental,* 102**,** 132-139.

Zhang, J., Chen, X., Shen, Y., Li, Y., Hu, Z. & Chu, J. 2011b. Synthesis, surface morphology, and photoluminescence properties of anatase iron-doped titanium dioxide nano-

crystalline films. *Physical Chemistry Chemical Physics,* 13**,** 13096-13105.

Zhang, P., Gong, Y., Li, H., Chen, Z. & Wang, Y. 2013. Selective oxidation of benzene to phenol by FeCl 3/mpg-C 3 N 4 hybrids. *Rsc Advances,* 3**,** 5121-5126.

Zhang, T., You, L. & Zhang, Y. 2006. Photocatalytic reduction of p-chloronitrobenzene on illuminated nano-titanium dioxide particles. *Dyes and pigments,* 68**,** 95-100.

Zhang, W., Zhou, L., Shi, J. & Deng, H. 2017. Fabrication of novel visible-light-driven AgI/g-C3N4 composites with enhanced visible-light photocatalytic activity for diclofenac degradation. *Journal of Colloid and Interface Science,* 496**,** 167-176.

Zhang, W., Zhou, L., Shi, J. & Deng, H. 2018a. Synthesis of Ag3PO4/G-C3N4 composite with enhanced photocatalytic performance for the photodegradation of diclofenac under visible light irradiation. *Catalysts,* 8**,** 45.

Zhang, W., Zhou, L., Shi, J. & Deng, H. 2018b. Synthesis of Ag3PO4/G-C3N4 composite with enhanced photocatalytic performance for the photodegradation of diclofenac under visible light irradiation. *Catalysts,* 8.

Zhang, W. F., He, Y. L., Zhang, M. S., Yin, Z. & Chen, Q. 2000. Raman scattering study on anatase TiO2 nanocrystals. *Journal of Physics D: Applied Physics,* 33**,** 912-916.

Zhang, X. & Lei, L. 2008. Effect of preparation methods on the structure and catalytic performance of TiO2/AC photocatalysts. *Journal of hazardous materials,* 153**,** 827-833.

Zhang, X., Li, X. & Deng, N. 2012. Enhanced and selective degradation of pollutants over cyclodextrin/TiO 2 under visible light irradiation. *Industrial and Engineering Chemistry Research,* 51**,** 704-709.

Zhang, X., Wu, F. & Deng, N. 2010. Degradation of paracetamol in self assembly β-cyclodextrin/TiO2 suspension under visible irradiation. *Catalysis Communications,* 11**,** 422-425.

Zhang, X., Wu, F. & Deng, N. 2011c. Efficient photodegradation of dyes using light-induced self assembly TiO2/β-cyclodextrin hybrid nanoparticles under visible light irradiation. *Journal of Hazardous Materials,* 185**,** 117-123.

Zhang, X., Wu, F., Wang, Z., Guo, Y. & Deng, N. 2009. Photocatalytic degradation of 4,4′-biphenol in TiO2 suspension in the presence of cyclodextrins: A trinity

integrated mechanism. *Journal of Molecular Catalysis A: Chemical,* 301**,** 134-139.

Zhang, Y. & Park, S.-J. 2019. Stabilizing CuPd bimetallic alloy nanoparticles deposited on holey carbon nitride for selective hydroxylation of benzene to phenol. *Journal of Catalysis,* 379**,** 154-163.

Zhang, Z., Zhao, C., Duan, Y., Wang, C., Zhao, Z., Wang, H. & Gao, Y. 2020. Phosphorus-doped TiO2 for visible light-driven oxidative coupling of benzyl amines and photodegradation of phenol. *Applied Surface Science,* 527**,** 146693.

Zheng, Y., Erwei, S., Suxian, C., Wenjun, L. & Hu, X. 2000. Hydrothermal Preparation and Characterization of Brookite-Type TiO2 Nanocrystallites. *Journal of Materials Science Letters,* 19**,** 1445-1448.

Zhong, Z., Li, M., Fu, J., Wang, Y., Muhammad, Y., Li, S., Wang, J., Zhao, Z. & Zhao, Z. 2020. Construction of Cu-bridged Cu2O/MIL (Fe/Cu) catalyst with enhanced interfacial contact for the synergistic photo-Fenton degradation of thiacloprid. *Chemical Engineering Journal,* 395**,** 125184.

Zhou, Y., Chen, C., Guo, K., Wu, Z., Wang, L., Hua, Z. & Fang, J. 2020. Kinetics and pathways of the degradation of PPCPs by carbonate radicals in advanced oxidation processes. *Water Research,* 185**,** 116231.

Zhu, D. & Zhou, Q. 2019. Action and mechanism of semiconductor photocatalysis on degradation of organic pollutants in water treatment: A review. *Environmental Nanotechnology, Monitoring & Management,* 12**,** 100255.

Zuorro, A., Lavecchia, R., Monaco, M. M., Iervolino, G. & Vaiano, V. 2019. Photocatalytic degradation of azo dye reactive violet 5 on Fe-doped titania catalysts under visible light irradiation. *Catalysts,* 9**,** 645.